Design, Synthesis, and Characterization of Transition Metal Compounds Using Binucleating and Bifunctional Ligands: Strategies for the Multi-Electron Reduction of Small Molecules

A dissertation,
submitted to the faculty of
the University of Minnesota,
by

Christopher M. Zall

In partial fulfillment of the requirements
for the degree of
Doctor of Philosophy

Connie C. Lu, Advisor

January, 2014

Acknowledgments

I would like to thank everyone who has been a part of my life during my time here at the University of Minnesota. In and out of lab, you have helped to make this a rich and fulfilling experience. Connie, thanks for welcoming me into the group and for teaching me what it means to be a synthetic inorganic chemist. Thanks to everyone in the Lu group; it has been a privilege to work with you and a pleasure to be your labmate. To all the collaborators who have contributed to the work in this thesis: Keying, Laura G., Danylo, Christine, Allison, Mike, Laura C., Victor, Eckhard, Andreas, and Bernd - thanks for the hard work and the helpful discussions. And finally, Kelsey, thanks for putting up with me throughout the process and for keeping me sane along the way!

Abstract

The work described in this thesis focuses on two strategies to promote multi-electron redox within simple inorganic systems. The first involves electronic coupling between two mid-to-late first-row transition metals in the form of strong metal-metal bonds. The second involves tethering a redox-active cofactor to a mononuclear transition metal site via a bifunctional ligand platform. In Chapter 1, the background and theory relevant to achieving multi-electron reactivity using bimetallic complexes are discussed, with a particular focus on the electronic structure of the coupling between first-row transition metals. In Chapter 2, the electronic structure reinvestigation of two "trigonal lantern" bimetallic complexes is discussed. These complexes, $Fe_2(DPhF)_3$ and $Co_2(DPhF)_3$, (DPhF = N,N'-diphenylformamidinate) contain remarkably short metal-metal distances of 2.23 Å and 2.38 Å, respectively, while also possessing large magnetic moments indicative of strong, ferromagnetic coupling between the two metal centers. The electronic structures of these molecules have been studied by a variety of physical and theoretical methods. The molecules have energetically well-isolated high-spin electronic configurations of $S = 7/2$ and $S = 5/2$, respectively, and fully delocalized $M^{1.5}M^{1.5}$ oxidation states. The strong metal-metal bonding, electronic delocalization, and high-spin states are shown to be interrelated, resulting from the distribution of electrons in a molecular orbital manifold that has very small orbital energy differences, engendered by the weak-field ligands and trigonal coordination geometry.

In Chapter 3, the synthesis and characterization of new bimetallic complexes a new, chelating tris(amidinato)amine are discussed. This ligand provides a similar ligand environment to the original "trigonal lanterns" but also contains a single axial donor that

differentiates the two metal sites. The homobimetallic dicobalt complex of this ligand, Co_2L^{Ph}, has been synthesized and possesses an even shorter Co-Co distance, at 2.29 Å, than $Co_2(DPhF)_3$. In addition, a heterobimetallic iron-cobalt complex, $FeCoL^{Ph}$, has also been prepared that contains the shortest known Fe-Co distance, at 2.18 Å. The positions of the iron and cobalt atoms in this complex were assigned by anomalous dispersion methods; these reveal that the compound is essentially a single species, rather than a mixture of heterobimetallic isomers, and that the cobalt selectively occupies the tetracoordinate "bottom" site, bound to the axial nitrogen donor while the iron occupies the tricoordinate "top" site. Both Co_2L^{Ph} and $FeCoL^{Ph}$ possess high-spin electronic configurations and strong metal-metal bonds. While the asymmetric ligand environment creates a distinct polarization of the molecular orbitals and oxidation states, the metal-metal bonding is largely unaffected and is qualitatively similar to that observed in $Fe_2(DPhF)_3$ and $Co_2(DPhF)_3$.

In Chapter 4, the design and coordination chemistry of a bifunctional ligand system containing a reversible organic hydride donor group is presented. This ligand tethers a redox-active phenanthridinium group to a phosphine donor in order to facilitate bifunctional reactivity, in which the hydride donor and an appended metal center react cooperatively to activate and reduce substrates. Palladium dichloride complexes containing two such ligands have been prepared: these can be cleanly interconverted between hydride-"loaded" and -"unloaded" forms by reaction with hydride acceptors and donors. In addition, lower-coordinate palladium complexes have been studied that can react with dihydrogen (H_2) and show intriguing exchange of the hydrides between positions at the metal and ligand.

Table of Contents

List of Tables

Chapter 1

Chapter 2

Chapter 3

Chapter 4

List of Figures

Chapter 1

Chapter 2

Chapter 3

List of Symbols and Abbreviations

°	degree
18-crown-6 (18-c-6)	1,4,7,10,13,16-hexaoxacyclooctadecane
A	hyperfine coupling constant
Å	angstrom
avg	average
B	magnetic field
Bn	benzyl
BNAH	1-benzyl-1,4-dihydropyridine
br	broad
C	celsius
C_6D_6	deuterated benzene
C_6H_6	benzene
CASPT2	complete active space second order perturbation theory
CASSCF	complete active space self consistent field
$CDCl_3$	deuterated chloroform
CH_3CN	acetonitrile
$CHCl_3$	chloroform
cm	centimeter
cm^{-1}	wavenumber
CV	cyclic voltammetry
d	density
d	doublet
D	zero-field splitting
DCM	dichloromethane
dd	doublet of doublets
DFT	density functional theory
dt	doublet of triplets
E/D	rhombicity
E°	standard electrode potential
EBO	effective bond order
EPR	electron paramagnetic resonance
ESI-MS	electron spray ionization mass spectrometry
Et_2O	diethyl ether
EtOAc	ethyl acetate
FBO	formal bond order
Fc	ferrocene
g	gram
g	anisotropic *g* factor
G	Gauss
g_{eff}	effective g factor
GHz	gigahertz
HCl	hydrochloric acid
hrs	hours

I	nuclear spin quantum number
^{i}Pr	isopropyl
J	coupling constant
K	Kelvin
kcal	kilocalorie
keV	kiloelectron volt
KBn	benzylpotassium
LMCT	ligand to metal charge transfer
m	multiplet
M	molarity
m/z	mass-to-charge ratio
Me	methyl
MeOH	methanol
mes	mesityl
mg	milligram
MHz	megahertz
min	minute
mL	milliliter
MLCT	metal to ligand charge transfer
mm	millimeter
mM	millimolar
mmol	millimole
MO	molecular orbital
mol	mole
m_s	electron spin quantum number
mV	millivolts
mT	millitesla
NA	nicotinamide
NAD^+	nicotinamide adenine dinucleotide
NADH	dihydronicotinamide adenine dinucleotide
NEt_3	triethylamine
NHE	normal hydrogen electrode
NIR	near infrared
nm	nanometers
NMR	nuclear magnetic resonance
Ph	phenyl
pKa	pK for association
ppm	parts per million
q	quartet
r	covalent ratio
reflns	reflections
rt	room temperature
s	singlet
s	second
S	spin state

s^{-1}	frequency
SQUID	superconducting quantum interference device
T	temperature
t	triplet
T	Tesla
$TBAPF_6$	tetrabutylammonium hexafluorophosphate
THF	tetrahydrofuran
THF- d_8	deuterated tetrahydrofuran
tren	tris(2-aminoethyl)amine
UV	ultraviolet
V	volts
V	volume
vis	visible
vs.	versus
W	width
Z	number of independent structures in unit cell
δ	chemical shift
δ	isomer shift
ΔE_Q	quadrupole splitting
Δf'	Real component of the anomalous scattering factor
Δf''	Imaginary component of the anomalous scattering factor
ΔG°	Gibbs free energy
ε	molar absorptivity
θ	degrees of data collection
η	Hapticity
λ	wavelength
λ_{max}	maximum absorbance wavelength
μ	bridging
μ	absorption coefficient
μ_B	Bohr magnetons
μ_{eff}	effective magnetic moment
μL	microliter
μM	micromolar
π	pi
σ	sigma

Chapter 1

Introduction

1.1 Bio-inspired Strategies for Small Molecule Activation

Perhaps the greatest challenge facing humanity in the early decades of the 21st Century is the need to accommodate the energy demands of a growing and industrializing world population despite a finite supply of fossil fuel resources and increasing concern about their role in destabilizing the global climate. There is a significant role for chemists in addressing these issues, particularly in the development of efficient methods for the production of fuels and other value-added chemical feedstocks from renewable, abundant molecules such as carbon dioxide (CO_2), dinitrogen (N_2), and water. Conversion of these precursors to useful molecules such as methanol (CH_3OH), ammonia (NH_3) and hydrogen (H_2) will require catalysts that are capable of mediating the transfer of multiple electron equivalents, composed of inexpensive materials, and simple enough to be synthesized on a large scale. Models for such catalysts may be found in Nature, where highly efficient metalloenzymes have evolved to catalyze these reactions. These enzymes and their biosynthesis are complex, and their direct application towards the production of commodity chemicals and fuels is unlikely to be economically viable. However, the factors governing their reactivity have been closely studied and in many cases traced back to the architecture of the primary and secondary coordination spheres of the enzymes' inorganic active sites. By building structural models of these active sites using synthetic inorganic complexes, new catalysts have been developed that can display similar reactivity and in some cases comparable efficiency.

The work described herein focuses on two approaches to developing small inorganic catalysts in which the structures have been even further simplified, so that the

fundamental concepts underlying their reactivity can be isolated and studied. Despite their structural simplicity, these families of complexes retain key aspects of their biological templates, abstracted into general design principles and reactivity patterns. The first approach is inspired by the multinuclear nature of the primary coordination sphere of many metalloenzymes, wherein multiple first-row transition metals are coupled together to effect multi-electron redox chemistry. The simplified systems in this project are bimetallic complexes of first-row metals, using ligands designed to enforce strong metal-metal bonding interactions to make up for the lack of a finely tuned protein environment. The second approach described in this thesis is inspired by the secondary coordination spheres of certain enzymes, in which ancillary cofactors assist in either activation of substrates, redox chemistry, or both. In this project, we have developed ligands containing redox-active pyridinium cofactors capable of mediating hydride transfer reactions. By positioning these groups in close proximity to the metal center, we hope to facilitate cooperative reactivity in which substrates bound to the metal are activated towards hydride transfer with the ligands.

The relationship between these approaches and some of the enzyme designs that inspired them is shown in Figure 1.1. The H_2-activating enzymes [Fe-Fe]- and [Ni-Fe]-hydrogenase are shown on the left side of Figure 1.1.[1,2] The dinuclear nature of these active sites allows them to span a number of redox states without significant charge buildup on either metal. These active sites also contain Lewis basic sites in the secondary coordination sphere that are believed to facilitate the heterolytic cleavage of H_2 to protons and a metal-bound hydride. Intriguingly, there is a third known type of hydrogenase,

[Fe]-hydrogenase, or Hmd, that has only a single iron at the center of its active site.[3] In this enzyme, H_2 cleavage also occurs heterolytically, but the hydride binds not at the metal but at a redox-active guanylylpyridinol heterocycle in the secondary coordination sphere.

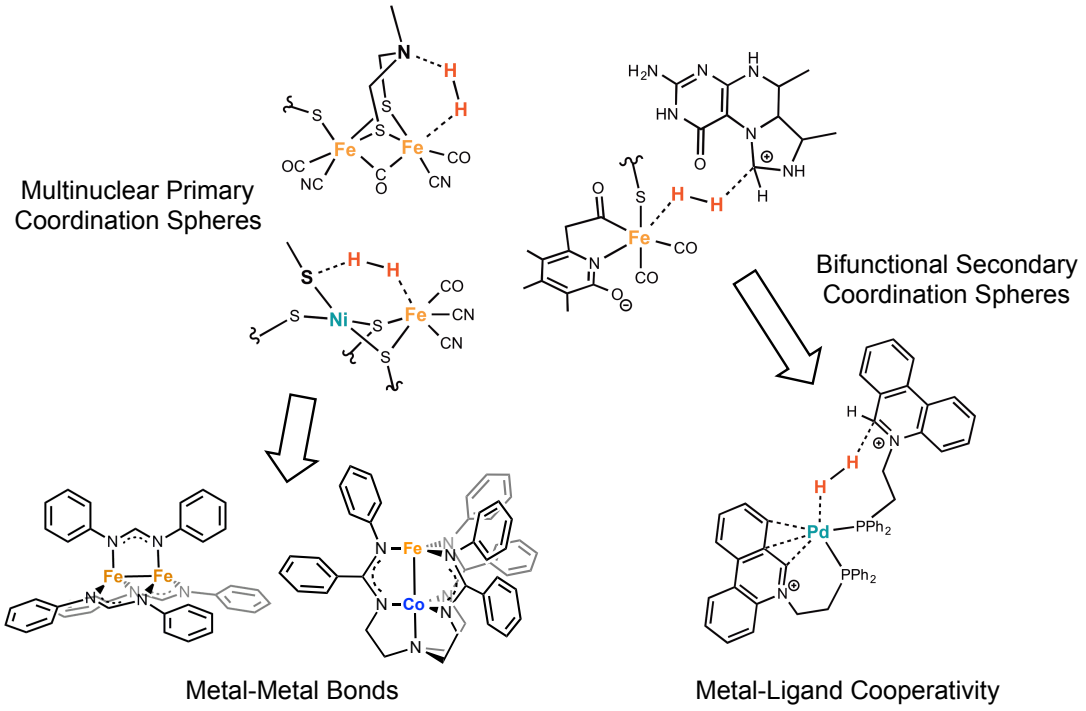

Figure 1.1 Molecules described in this thesis and their inspiration in metalloenzyme active sites. Proposed transition states for activation of H_2 in [Fe-Fe], Hmd, and [Ni-Fe] hydrogenases are shown and compared to the bimetallic and bifunctional systems described in this work.[1-3]

We are attempting to mimic these aspects of the enzymes within the simpler architectures shown in the bottom of Figure 1.1. In the first approach, rather than attempting to directly model the complex, dinuclear cores of [Fe-Fe]- and [Ni-Fe]-hydrogenase, we are using strong metal-metal bonding interactions to couple pairs of mid-to late first-row transition metals in low-coordinate, low-valent environments. Since strong bonding interactions between such metals are rare, we have focused on trigonal

frameworks that maximize the bond order and engender new and unusual electronic structures. In the second approach, we have developed a new ligand that tethers a redox-active phenanthridinium heterocycle to a phosphine donor. This ligand positions a reversible hydride donor within the secondary coordination sphere of a metal complex. This allows cooperative activation of H_2 and stores its electron equivalents in the form of organic hydrides that can later be transferred to substrates.

The primary goal of this work is to understand and control these features of the primary and secondary coordination spheres when they are removed from the finely-tuned biological model systems. The work has focused on developing broadly-extensible methodologies for the activation of small molecules, rather than optimization of specific reactions. For this reason, we have opted to use general frameworks that can be applied to a variety of transition metals, based on modular ligand designs. Within each platform, we have conducted detailed structural and electronic studies and broad surveys of reactivity to develop structure-function relationships. The bimetallic systems described herein have been the most well-studied and form the basis of Chapters 2 and 3 of this thesis. The remainder of Chapter 1 is devoted to a discussion of the fundamentals of small-molecule activation and metal-metal bonding relevant to this work. Finally, the bifunctional metal-ligand systems are discussed in Chapter 4.

1.1.1: Background and Motivation for Small Molecule Activation

According to a recent estimate by the US Energy Information Administration (EIA), global energy consumption is expected to increase by almost 50% between 2011 and 2035, from 530 to 770 quadrillion BTUs, driven largely by a 66% increase in the developing world. These projections anticipate a near-doubling (90% increase) of renewable energy consumption, yet global carbon dioxide emissions are still projected to increase by 36% in this time period.[4] These numbers are in constant flux due to the recent expansion of oil and natural gas production from unconventional "tight oil" sources. As this production has increased, the prospects for renewable energy development have become more uncertain, and the more recent EIA 2013 Annual Energy Outlook projects that domestic consumption of renewable energy will only increase from 2.08 to 2.68 quadrillion BTUs over the same 2011-2035 time period, providing less than 2.5% of the total anticipated domestic energy use.[5]

The advanced extraction techniques fueling the recent boom in oil and gas production are controversial, and their environmental impact and long-term production viability are not yet clear. However, given the inherently finite quantity of fossil fuel resources, production capacity cannot indefinitely keep pace with economic and population growth. Moreover, there is ever-mounting evidence that anthropogenic CO_2 emissions contribute to global climate change.[6,7] Because CO_2 persists in the atmosphere for centuries, its emissions are cumulative, and the longer the delay in reducing CO_2 emissions, the more drastic the reduction that will eventually be needed in order to stabilize atmospheric concentrations.[8-10] There is thus a clear and urgent need for the

development of low-carbon technologies that can compete on price and scale with current energy sources.

One of the primary areas where progress is needed is in the development of efficient catalysts for the production of energy-rich small molecules for fuels and chemical feedstocks. Such catalysts are not energy sources themselves, but in many cases they are needed to enable the use of energy sources or to replace current carbon-intensive processes. Efficient electrocatalysts for the synthesis of fuels such as hydrogen and methanol, for example, could provide a means to store transient solar energy when coupled to photovoltaic devices. Solar energy is more than abundant enough to meet all projected energy demands, but it requires a storage mechanism due to the diurnal nature of solar radiation.[10] Converting the electricity produced by solar devices to chemical energy in the form of high-energy molecules could provide a storage mechanism with energy densities orders of magnitude higher than batteries,[11] with the simplest such conversion being the electrochemical reduction of protons to hydrogen (Eqn 1.1). Coupling this reaction to the electrochemical oxidation of water (Eqn 1.2) would provide a complementary half-reaction to provide the protons and electrons.

$$2\,H^+ + 2\,e^- \rightarrow H_2 \qquad \text{(Eqn 1.1)}$$

$$H_2O \rightarrow 2\,H^+ + 2\,e^- + \tfrac{1}{2}\,O_2 \qquad \text{(Eqn 1.2)}$$

Although the energy density per unit mass of hydrogen is enormous, it is difficult to store and transport; for these reasons, another desirable fuel is methanol (CH_3OH), which can be produced through the reduction of CO_2 by six protons and six electrons (Eqn 1.3).

$$CO_2 + 6\,H^+ + 6\,e^- \rightarrow CH_3OH + H_2O \qquad \text{(Eqn 1.3)}$$

Methanol is currently produced by a combination of steam reforming of methane (Eqn 1.4) and hydrogenation of the resulting carbon monoxide (CO) (Eqn 1.5).

$$CH_4 + H_2O \rightarrow CO + 3\,H_2 \qquad \text{(Eqn 1.4)}$$

$$CO + 2\,H_2 \rightarrow CH_3OH \qquad \text{(Eqn 1.5)}$$

This process is inherently inefficient, as it requires overoxidation followed by reduction; moreover, the steam reforming step is energy-intensive and uses non-renewable methane as a feedstock, making the process carbon-intensive. Using CO_2 as an alternative precursor – ideally directly with protons and electrons (Eqn 1.3) or with H_2 produced by water-splitting (Eqns 1.1, 1.2, and 1.5) would make this a potentially near-carbon-neutral fuel.

Another long-sought objective is an efficient catalyst for the conversion of atmospheric N_2 to ammonia. Ammonia is immensely important as a fertilizer and chemical precursor; by the year 2010, its annual production had grown to around 140 million metric tons produced worldwide.[12] This production has dramatically impacted agricultural productivity and, hence, the ability to support the growing global population. It is estimated that the number of humans supported per hectare of arable land has more than doubled, from 1.9 to 4.3 persons, between 1908 to 2008.[13] It has been suggested that, with agricultural yields that prevailed in the year 1900, today's croplands could support only around 40% of the world's current population.[14] The use of synthetic nitrogen-based fertilizers, ammonia in particular, has played a primary role in the increased productivity. Thus, after accounting for other increases in productivity, the use of these fertilizers is believed to have supported approximately 27% of the world's

population since 1908.[13] However, this industrialization comes with an enormous energy cost. Ammonia is industrially produced via the reaction of dinitrogen with three equivalents of H_2 (Eqn 1.6). This reaction is exothermic, but the extremely strong N-N triple-bond in dinitrogen makes it very difficult to achieve kinetically.

$$N_2 + 3\,H_2 \rightarrow 2\,NH_3 \qquad \text{(Eqn 1.6)}$$

Industrially, the reaction is promoted with an iron or ruthenium catalyst in what is known as the Haber-Bosch process. The high temperatures and pressures used (typically >400 °C and between 200-300 atm) make it an inherently demanding process.[15] More significantly, the hydrogen used in this reaction is produced from fossil fuels *via* steam reforming, producing enormous quantities of emitted carbon dioxide. It would be far better from an environmental standpoint to find a catalyst that could produce NH_3 from protons and electrons (Eqn 1.7) or, alternatively, to use H_2 that is produced electrolytically *via* water-splitting.

$$N_2 + 6\,e^- + 6\,H^+ \rightarrow 2\,NH_3 \qquad \text{(Eqn 1.7)}$$

However, while numerous catalysts can be used to generate H_2 from water, none is currently scalable to the enormous industrial scale required for use as an input in the Haber-Bosch process. Even less promising is the current state of catalysts for ammonia production using protons and electrons. Only two such catalysts are known. Both are mononuclear molybdenum catalysts; the first produces 7 to 8 equivalents of NH_3,[16] while the second produces 12 equivalents.[17]

1.1.2 Multi-Electron Redox and Thermodynamics of Small Molecule Activation

A large part of the difficulty in the reduction of small molecules like CO_2 and N_2 is the multi-electron nature of these reactions. As shown in Eqns 1.3 and 1.7, reduction of these species to useful products like methanol and ammonia requires six equivalents of protons and electrons each. This is obviously not a feasible process for a single metal center to mediate in a single step, as it would imply enormous charge buildup. An alternative strategy is to deliver the protons and electrons in a stepwise, sequential fashion; this is the approach used by the successful molybdenum-based catalysts for N_2 reduction. However, this stepwise approach entails a series of unstable intermediates that can produce unwanted byproducts through homocoupling or dissociation of the activated substrates. In addition to these kinetic issues, there are thermodynamic costs to the stepwise approach. For instance, the one-electron reduction of CO_2 to form the $CO_2^{\bullet-}$ radical anion has a large and energetically costly reduction potential of -1.9 V (vs NHE). On the other hand, the reductions of CO_2 by two electrons and two protons to form either formic acid, HCO_2H, or the dehydrated products CO and H_2O, have much milder reduction potentials of -0.61 V and -0.53 V, respectively.[18] This trend continues with the further addition of protons and electrons, with the more reduced products becoming even more thermodynamically favorable. A similar situation exists for the reduction of dinitrogen; in that case, the reaction becomes closer to thermoneutral with more reductive equivalents until, with the full addition of six electrons and six protons, the reaction becomes thermodynamically favorable. This is represented graphically in Figure 1.2.[19]

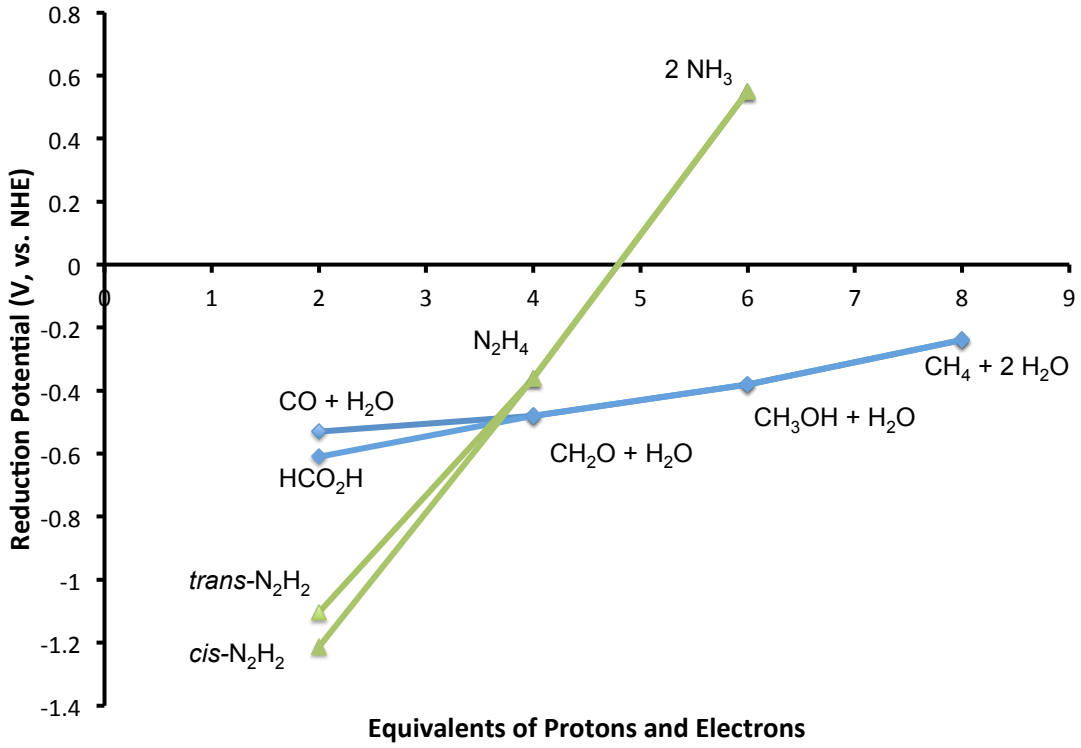

Figure 1.2 Reduction potentials of products from reduction of CO_2 (blue, diamonds) and N_2 (green, triangles). All potentials are for aqueous reactions, pH 7, vs. NHE.[19,20]

There are thus kinetic and thermodynamic advantages to maximizing the number of electron equivalents that can be transferred simultaneously. Metal complexes that can undergo reversible multi-electron reactions are therefore desirable for the development of catalysts for these processes. Unfortunately, the enormous scale entailed in the production of these commodity chemicals will require catalysts that are based on inexpensive, abundant metals. First-row transition metals would be ideal, as they are earth-abundant, inexpensive, and relatively environmentally benign in comparison to second- and third-row metals. However, these first-row metals are much more prone to one-electron redox couples than their second- and third-row counterparts. Two strategies that are emerging to address this issue are to use multinuclear complexes that combine

the redox capacities of multiple metal centers, or to use bifunctional systems in which the ligand can participate in redox as well. Neither idea is particularly new; the challenge is in ensuring that the interactions, either between two or more metals or between metal and ligand, are cooperative. The challenges in metal-ligand cooperativity are discussed in Chapter 4. The following discussion focuses on developing cooperative metal-metal interactions, with a particular focus on covalent metal-metal bonds.

1.2 Multinuclear Clusters and Metal-Metal Interactions

As discussed above, one attractive solution to the problem of achieving multi-electron redox reactions is to use multinuclear compounds in which two or more metal centers are coupled together. Indeed, most of the enzymes that perform multi-electron redox are multinuclear clusters: the [Fe-Fe] and [Ni-Fe] hydrogenases, as well as the Ni-Fe cluster in CODH and the FeMo cofactor in nitrogenase, have been discussed previously. There are a vast number of additional examples, notably including the Mn_4CaO_4 cluster in Photosystem II[21,22], which catalyzes the four-electron oxidation of two water molecules to form O_2, and the iron and copper centers in cytochrome oxidase, which catalyze the reverse reaction.[23] In most cases, the collective role of the metal clusters are known; however, the role of each individual metal ion or of the interactions between various metal pairs are often unclear. More significantly, these interactions are finely controlled by the protein environment, with results that are difficult to replicate in simplified synthetic models. The greater structural complexity in multinuclear complexes than in conventional, mononuclear systems is reflected in a greater diversity of reaction

outcomes. The metals can react cooperatively or independently, in large part determined by the distances between the metal centers and the coordination geometries around them[24] and also potentially by the electronic coupling between the two, which can be highly structure-dependent.[25] Thus, slight structural changes can greatly affect the modes of reactivity. One approach to simplifying these systems is to ensure that only one of the metals can interact with the substrate. However, even with this approach, productive coupling of the metal centers can be a challenging task. This is probably best exemplified by the work of Bosnich and coworkers. Seeking to create a broadly-extensible platforms for "two-metal two-electron reductions" where the substrate is bound to only one metal, the authors created binucleating ligand frameworks with two contiguous metal-binding sites, as shown in Figure 1.3.[26,27] These ligands cleverly provide asymmetric four- and six-coordinate metal environments; thus, only one metal is coordinatively unsaturated and able to bind substrates. The designs also facilitated electronic communication between the metals. It was thus hoped that introduction of a two-electron oxidant would result in oxidation of both metals. Reaction with a variety of oxidants showed that either metal could be oxidized. For instance, as shown in Figure 1.3, a dicobalt complex could be oxidized at the four-coordinate metal site through reaction with $FeCp_2^+$ or NO^+ or at the six-coordinate site through reaction with O_2. However, in no case was oxidation of *both* metals observed. Similar results were observed for other metal pairs and oxidants. Strikingly, even when placed in close proximity to a high-valent V^{5+}=O moiety, a Fe(II) site was not oxidized to Fe(III). The authors concluded that structural changes associated with the oxidation of the first metal were deactivating the second metal towards electron

transfer.

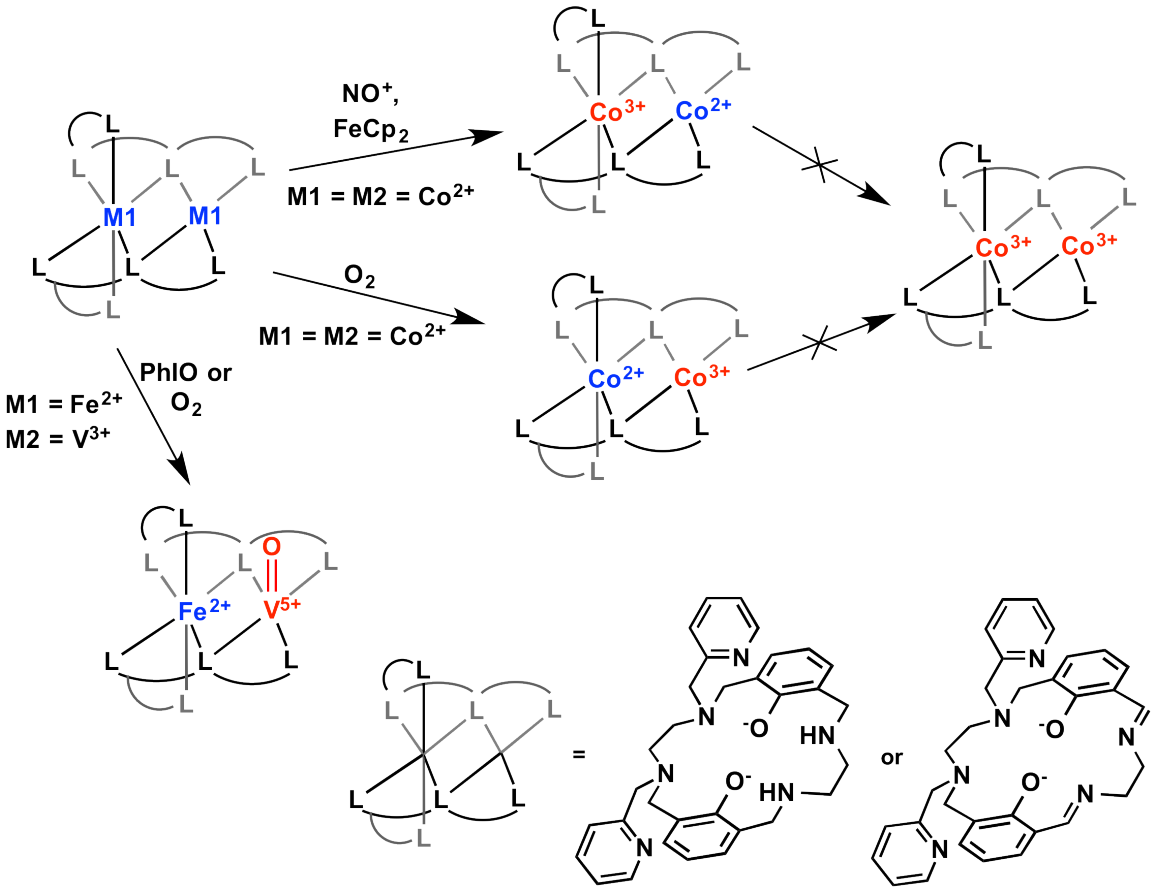

Figure 1.3. Selected binuclear complexes prepared by Bosnich *et al.* and their pronounced resistance to oxidation of both metals. A variety of other bimetallic pairs were synthesized, including CoZn, CoCu, CoNi, and CoMn, wherein M' is in the four-coordinate site.[26,27]

Later, an asymmetric ligand was prepared that replaced one of the bridging arms of the previous systems with a simple bridging hydroxide. Dicobalt complexes with this flexible, asymmetric platform were shown to undergo two-electron oxidations in which both metal sites were oxidized.[28,29] This was taken as support for the hypothesis that the mutual-deactivation observed in the initial systems was due to geometrical rearrangements in the rigid ligand backbone that deactivated the second metal to oxidation. However, the lessened chelating ability of this ligand led to oligomerization

when other metal pairs were synthesized, and the system was not broadly-extensible.[30] The variability of these systems and the mutual-deactivation process emphasize that achieving bimetallic reactivity is not a simple matter of designing platforms that combine two metals in close proximity. The results are rarely the sum of their parts, and productive reactivity requires that the metals be coupled cooperatively. It is not often clear how to ensure cooperativity in weakly-coupled systems, but an alternative could be to instead maximize the electronic coupling between the metals, in the form of a direct metal-metal bond. In this limit of strong electronic coupling, the electrons from the two metals are fully paired and could be expected to transfer concurrently, avoiding complications due to one-electron processes. Indeed, M-M bonds have been shown to facilitate promising multi-electron redox reactions. However, such examples have been largely limited to complexes of second- and third-row metals. Attempts to achieve similar multi-electron reactivity with first-row metals have been hampered by interrelated issues stemming from the fundamentally weaker bonds between 3d orbitals. The following sections briefly describe the theory and scope of metal-metal bonding, promising applications to multi-electron redox, the difficulties in achieving similar results with first-row metals, and our strategies for addressing these issues.

1.2.1 Electronic Structure of "Traditional" Metal-Metal Bonds

The foundational moment in the field of metal-metal bonding was the crystallographic study by Cotton *et al.* of the trirhenium and dirhenium chloride clusters $Rh_3Cl_{12}^{3-}$ and $Rh_2Cl_8^{2-}$, in 1963 and 1964, respectively; these molecules are shown in

Figure 1.4.[31,32] The rhenium ions in these clusters are separated by very short distances and were correctly interpreted as having covalent bonding interactions between the metal centers.

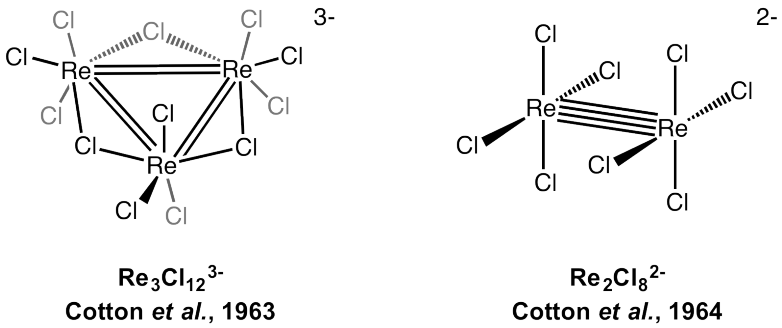

Figure 1.4. Rhenium clusters discovered by Cotton *et al.* with direct M-M multiple bonds.[31,32]

These back-to-back discoveries led to a rapid and fruitful search for other examples of metal-metal bonding, with thousands of such compounds known by 1990.[33] The rhenium compounds were not the first compounds structurally shown to have direct metal-metal bonds: Brosset, for instance, showed in 1935 that the distance between the two tungsten atoms in the dinuclear $[W_2Cl_9]^{3-}$ ion is so short that the metals "are, apparently, within these pairs, in some way bound together."[33,34] However, such reports remained sporadic and were not considered a general phenomenon in inorganic chemistry. More remarkable than the discovery of the direct M-M bonding interaction itself, then, was the realization by Cotton that the short distances between the metals resulted from *multiple* bonding between the electronically unsaturated metal atoms, arising from the overlap of multiple metal *d* orbitals, akin to the multiple bonding in unsaturated organic molecules. Moreover, such an analysis of the rhenium dimer suggested that its metal-metal bond was in fact a *quadruple* bond.[32] Such a bond order is

physically impossible between *p*-block elements, which have a maximum bond order of only three, from one σ- and two π-bonds. As shown in Fig. 5, however, the additional *d* orbitals within the transition metals allow an extra set of in-phase bonding interactions, between the d_{xy} orbitals of the metals, that gives rise to an additional bonding orbital of δ-type symmetry.

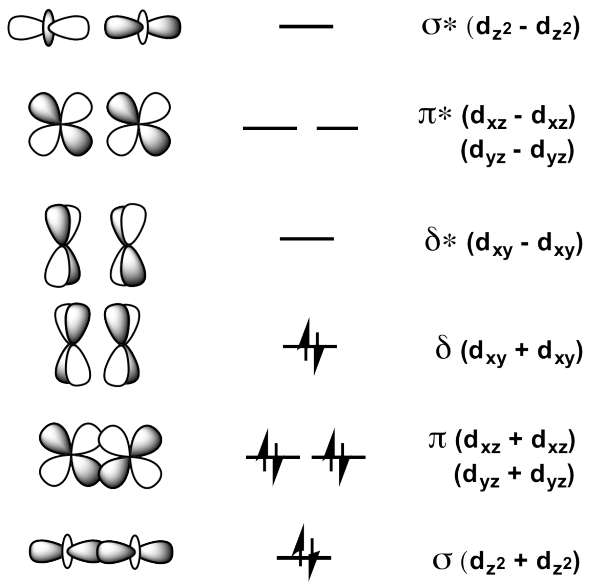

Figure 1.5 Molecular orbital interactions leading to quadruple bonding in the $Re_2Cl_8^{2-}$ dianion.[35]

The crucial early evidence for the quadruple bonding in $Re_2Cl_8^{2-}$ was the eclipsed geometry of the equatorial Cl^- ligands. Without the δ-bond, there would be no electronic influence on the conformation, due to the non-directional nature of the σ-bond and the degeneracy of the two π-bonds, and the chloride ligands would be able to relax to the less sterically encumbered staggered configuration. In order to achieve the electronically favorable δ-bond, however, the d_{xy} orbitals of the metals must overlap, which forces the less sterically-preferred eclipsed geometry.[32,36] Indeed, the discovery of Mo_2Cl_6, shown

in Figure 1.6a, and its ditungsten analogue, W_2Cl_6, showed that this geometry is a consequence of the δ-bond.[37] These complexes, with two fewer *d* electrons than $Re_2Cl_8^{2-}$, have the same σ- and π-type bonds but do not have a delta bond, and their halide ligands are free to rotate freely around the triple bond, resulting in a staggered conformation.

Multiple bonds were subsequently discovered in a wide variety of bimetallic systems. There are a large number of bimetallic complexes for metals of Groups 6-9, which contain stable electron counts between [d^6] through [d^{14}], and far fewer of later metals. This is summarized in Table 1.1, which is adapted from Ref. 35 and depicts the number of non-organometallic bimetallic compounds with an M_2^{n+} core reported in the literature as of 2003. With the exception of dichromium compounds, there is an obvious dearth of bimetallic complexes of first-row transition metals. This important class of bimetallic compounds has grown significantly since 2005. The difficulties in making these compounds and the strategies that have enabled chemists to overcome them are a major subject of this thesis and will be discussed more in depth later in this chapter.

Table 1.1 Number of crystallographically characterized compounds with M_2^{n+} cores of transition metals from Groups 5-10 as of 2003.[35]

V 11	*Cr* >500	*Mn* 0	*Fe* 3	*Co* 8	*Ni* 9
Nb 7	*Mo* >1,100	*Tc* >50	*Ru* >500	*Rh* >1,500	*Pd* 3
Ta 0	*W* >110	*Re* >550	*Os* 70	*Ir* 9	*Pt* >100

Within complexes of second- and third-row metals, however, there are a large number of complexes, particularly among metal pairs from Group 6 through Group 9. A thorough discussion of these bimetallics and their electronic structures is outside the

scope of this work, but there are a few features worth mentioning: their general structural similarities, their conserved pattern of M-M bonding, and their applications in small-molecule catalytic transformations. These aspects are interrelated and are a result of the strong bonding and closed-shell configurations of these metal pairs. The vast majority of these complexes are of "tetragonal" symmetry, with four equatorial ligand donors around each metal center, as in $Re_2Cl_8^{2-}$. The use of bidentate, bridging ligands has greatly facilitated the synthesis of new bimetallics, and compounds with four such bridging groups have become the archetypical bimetallic structural motif, known as "paddlewheel" or "lantern" compounds. Variation in these ligands, particularly their donor strength, has played a large role in tuning the structural and electronic properties of the known bimetallics and enabling the synthesis of new bimetallic pairs.

Despite such variation in metal pairs and ligand sets, however, the simple bonding picture shown in Fig. 5 is general enough to describe the M-M interactions in most bimetallics, with adjustment for the total d-electron count. These bonds are most commonly described using their formal bond order (FBO), defined as one half of the difference between the number of bonding and antibonding electrons in their ground electronic configuration. Within the tetragonal framework, this can easily be predicted simply from the total electron count of the two metals, $[d]^n$. As demonstrated in Figure 1.6, this value increases with increasing d electron count, as the additional electrons fill the bonding orbitals first, up to a maximum FBO of four, from a $[d]^8$ configuration, as in $Re_2Cl_8^{2-}$ or the dimolybdenum(II) carboxylate shown in Figure 1.6b. With electron counts higher than eight, the electrons begin to fill antibonding orbitals, lowering the bond order,

as in the single bond of the [d^{14}] dirhodium(II) carboxylates, shown in Figure 1.6d.

The bonding pattern in Figure 1.6 explains the prevalence of metal pairs from Groups 6 through 9 in Table 1.1. These metals contain stable electron counts between $[d]^6$ through $[d]^{14}$ that correspond to strong quadruple through single M-M bonds; bonding in earlier metals is possible but rare, due to the instability of low-valent oxidation states in these metals. With metals of Group 10 and later, there is typically no formal M-M bonding, with the rare exception of Pd and Pt dimers in high-valent (3+) oxidation states. More subtle effects can lead to intermetallic attractions in metal systems with higher electron counts, as in the well-known "aurophilic" interactions between gold dimers and in dipalladium(II) paddlewheel complexes, where a similar attraction has been attributed to excited state interactions. These are distinct from true covalent bonding, however, and are outside the scope of this discussion.

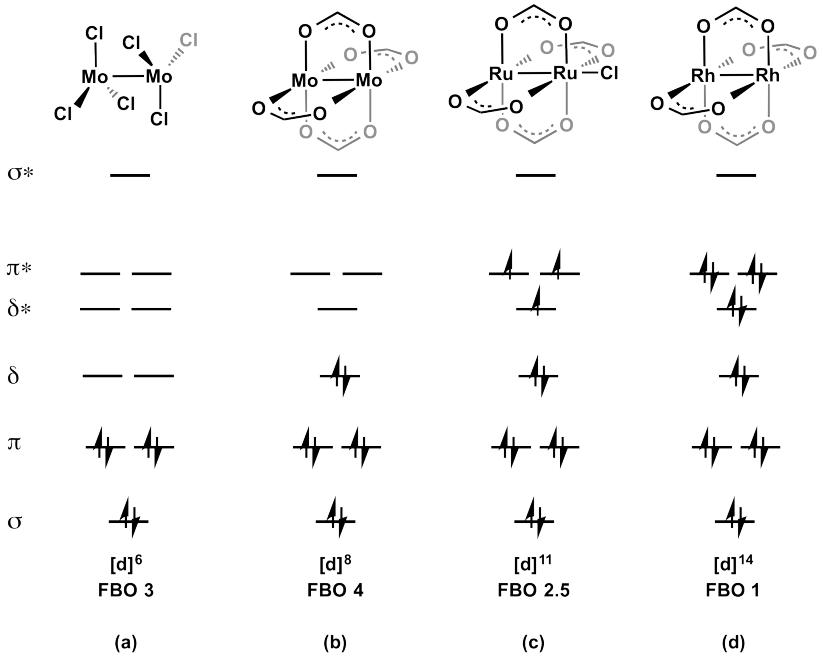

Figure 1.6. Variation in formal bond order (FBO) within a consistent molecular orbital manifold for second-row transition metal bimetallics. The bond order increases with d-electron count up to a maximum of four, then decreases as antibonding orbitals are populated.

An interesting case is that of the diruthenium(II,III) mixed-valent compounds, such as the tetracarboxylate chloride compound shown in Figure 1.6c. Due to the "accidental degeneracy" of the δ* and π* orbitals, these orbitals remain only half filled, giving an $S = 3/2$ ground state. The intermediate spin state does not affect the formal bond order, as the electrons populate M-M antibonding orbitals in both the intermediate-spin and low-spin configurations, giving the same FBO of 1.5. However, since there is more significant M-M overlap in the π* orbitals than in the δ*, the presence of one extra π* and one fewer δ* electrons makes the Ru-Ru bond weaker than it would presumably be in the low-spin configuration. The less common diruthenium(II,II) analogues are even more complicated: the ordering and occupation number of the δ* and π* orbitals depend strongly on the donor strength, with dramatic effects on the Ru-Ru bond distance and spin state. However, these diruthenium complexes are the exception that proves the rule; it is the accidental degeneracy of the π* and δ* orbitals that create the complexity. In contrast, virtually all other M-M bonded bimetallics of second- and third-row metals have low-spin, closed-shell electronic configurations, with few complications from higher spin states or low-lying excited states.

The large number of examples, strong bonding, and simple electronic picture for M-M bonds between second- and third-row metals has allowed chemists to finely tune their electronic properties. The resulting studies have been intriguing and inspiring on a fundamental level, as they have broadened our understanding of chemical bonding, pushing the limits of strength and complexity. They have also provided challenges and test cases for theoretical treatments of electronic structure. From a practical standpoint,

though, the most tantalizing application for these complexes is in redox chemistry and related transformations of small molecules.

1.2.2: Reactivity of M-M bonds Between Second- or Third-row Metals

The strong, predictable bonding observed in bimetallic compounds of second- and third-row metals offers several advantages for reactivity when compared to mononuclear compounds. At the simplest level, it provides a stable platform for combining and coupling multiple metal centers, which can then delocalize charge buildup and minimize the changes in oxidation state during a reaction. In addition, the same structural motif provides a conserved, strong bonding motif over a variety of electron counts, suggesting that these molecules could be able to undergo multi-electron redox changes without the large structural rearrangements often observed in multi-electron redox of mononuclear systems. Moreover, the M-M bonding is not simply conserved upon oxidation or reduction; it is strengthened or weakened in a predictable way that can be advantageous for reversible reactions. For instance, in complexes of later, electron-rich metals, oxidation of the bimetallic core results in removal of electrons from the M-M antibonding orbitals. This results in an increase in the M-M bond order, which can provide a stabilizing effect on otherwise high-energy intermediates. In bimetallics of the early metals, the reverse occurs: oxidation of the M-M core weakens the bonding by removing electrons from bonding orbitals. Paradoxically, this can have a similarly beneficial effect on certain types of reactions. For these earlier metals, oxidized M=E bonds such as oxo or nitride moieties are much stronger and more stable than those of later metals. The

strength of these bonds can actually provide a bottleneck in catalysis, as it can be difficult to break them and return to the original M-M catalyst resting state. In such systems, the weakened M-M bond in the overall M-M=E unit can provide a necessary destabilization of the otherwise-inert M=E moiety, and the stronger M-M bond in the reduced form can provide a driving force to return to the starting complex. This effect was demonstrated recently by Berry *et al*., who reported the four-electron oxidation of a quadruply-bonded ditungsten core to form a tungsten-oxo species, shown in Figure 1.7.[38]

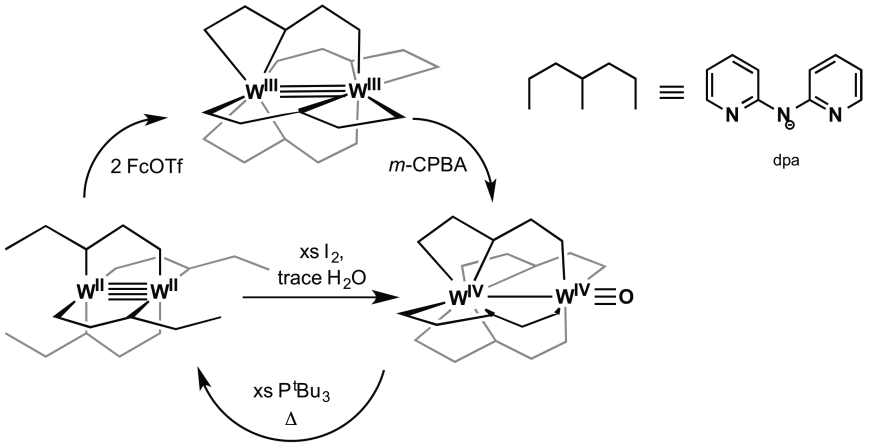

Figure 1.7 Oxidation chemistry of tungsten dipyridylamidate dimers.[38]

This four-electron oxidation, which can be achieved in one step or through two two-electron oxidations, cleaves the original W-W bond and forms a tungsten-oxo triple bond. In mononuclear complexes of tungsten, such species are typically inert, dead-end reaction products, due to the stability of the tungsten-oxo bond; yet in this case the product remains reactive enough to oxidize tri-*tert*-butylphosphine and re-form the original ditungsten core. The regeneration of the strong W-W quadruple bond helps to drive this reaction.[38] The net reaction in this case is not particularly noteworthy; however, as a general methodology, it is easy to see how it could be applied to other, more

significant reactions. For example, mononuclear molybdenum complexes have in two cases been shown to split dinitrogen to form mononuclear molybdenum-nitride products.[39,40] However, these nitride moieties are relatively inert and do not react with protons to form ammonia. Destabilization of the Mo-N bond by an ancillary metal atom might prove to be a productive way to induce reactivity and turnover in such cases.

In later transition metal systems, oxidized M=E moieties tend to be high-energy intermediates, and the metal-metal bond can instead provide a necessary stabilization. The most notable examples of this phenomenon are the dirhodium catalysts used for carbene and related group transfer insertions into C-H and C=C bonds. These compounds, structurally simple paddlewheel complexes with carboxylate and amidate ligands, are the best-known and most well studied bimetallic catalysts. They react with diazo-organic precursors to generate highly electrophilic carbene intermediates that can insert into even unactivated C-H bonds, as shown in Figure 1.8.[41] Functionalization of unactivated C-H bonds is a noteworthy reaction in its own right, but the dirhodium catalysts are even more remarkable due to their high selectivity. Chemoselectivity is crucial in C-H insertion reactions due to the large number of C-H bonds in most potential substrates. The dirhodium catalysts are, in general, highly selective for insertion into tertiary over secondary or primary C-H bonds, They can also be made highly enantioselective if chiral groups are introduced in the backbone of the ligands, which has enabled their application in complex organic syntheses.[42-44]

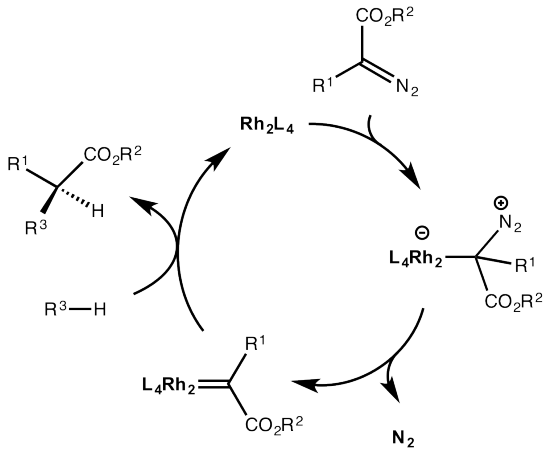

Figure 1.8. General catalytic cycle for dirhodium-catalyzed C-H insertion using a diazoalkane. L = carboxylate or amidate.[41]

The selectivity of the dirhodium catalysts is attributable to the stability of the dirhodium-carbene intermediate, which is conferred by the second rhodium center. Carbene complexes with early metals are known, but they tend to be unreactive to C-H insertions. On the other hand, several mononuclear late-metal complexes, mostly of copper and silver, are able to effect C-H insertions through the decomposition of diazo precursors, but these suffer from poor selectivity due to their extremely reactive carbene intermediates.[41] The dirhodium complexes are in the "sweet spot," generating carbene intermediates that are electrophilic enough to insert into unactivated C-H bonds but stable enough to do so selectively. This stability can be tuned by the choice of bridging ligand, with more electron-rich ligands showing less reactivity and more selectivity; however, the crucial stabilization in these complexes comes from the second rhodium center and the metal-metal bonding. This second metal atom is often described as an "electron reservoir," donating and accepting electron density as needed; this is often depicted through an "arrow-pushing" mechanism in which the Rh-Rh bond breaks and forms during the catalytic cycle, as shown in Figure 1.9.[45] A more physically correct view of the

interactions between the metals and the carbene, however, is that of a three-center, four-electron bond, with the bonding delocalizing through M=M=C sigma and pi orbitals. The carbene fragment has a filled lone pair and an empty *p* orbital. The lone pair donates into the Rh-Rh σ-bonding manifold, stabilizing the filled σ orbital and destabilizing the empty σ*. The empty *p* orbital, meanwhile, can accept electron density from the filled π* antibonding orbital of the dirhodium unit. This effect strengthens the M-M bonding, and recent theoretical analyses have suggested that both the Rh-Rh and Rh-C interactions are best viewed as double bonds.[46,47] Thus, rather than the Rh-Rh bond *breaking* upon binding to the carbene, as the "arrow-pushing" description in Figure 1.9a would suggest, it is *strengthened*, through two new stabilizing effects.

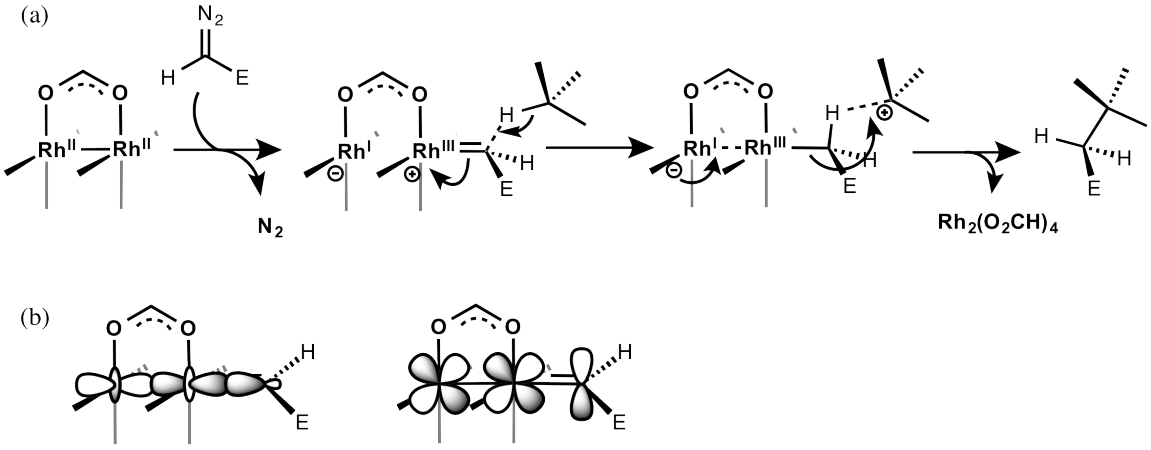

Figure 1.9. Two electronic descriptions of the dirhodium carbene intermediate in C-H insertion reactions. (a) "Arrow-pushing" mechanism involving Rh-Rh bond cleavage. (b) Frontier orbital interactions between dirhodium and carbene fragments.[45-47]

This system provides a noteworthy example of a metal-metal bond acting to stabilize high-energy metal-ligand multiply-bonded intermediates. In some similar systems, highly electrophilic M-M=E intermediates can be generated through redox

reactions, such as dirhodium nitrenes used for intermolecular C-H amination reactions, which are entirely analogous to the carbene systems discussed above but are generated by oxidation of a sulfamate ester bound to the dirhodium unit, as shown in Figure 1.10a.[46] The Berry group has investigated similar diruthenium nitride intermediates generated thermally or photolytically from the corresponding azides. These species are highly electrophilic and immediately insert into nearby C-H bonds of the ligand (Figure 1.10b).[48,49] Removing such C-H groups has allowed the extension of this chemistry to intermolecular N-atom transfer, with the initial report using PPh_3 as a substrate (Figure 1.10c).[50]

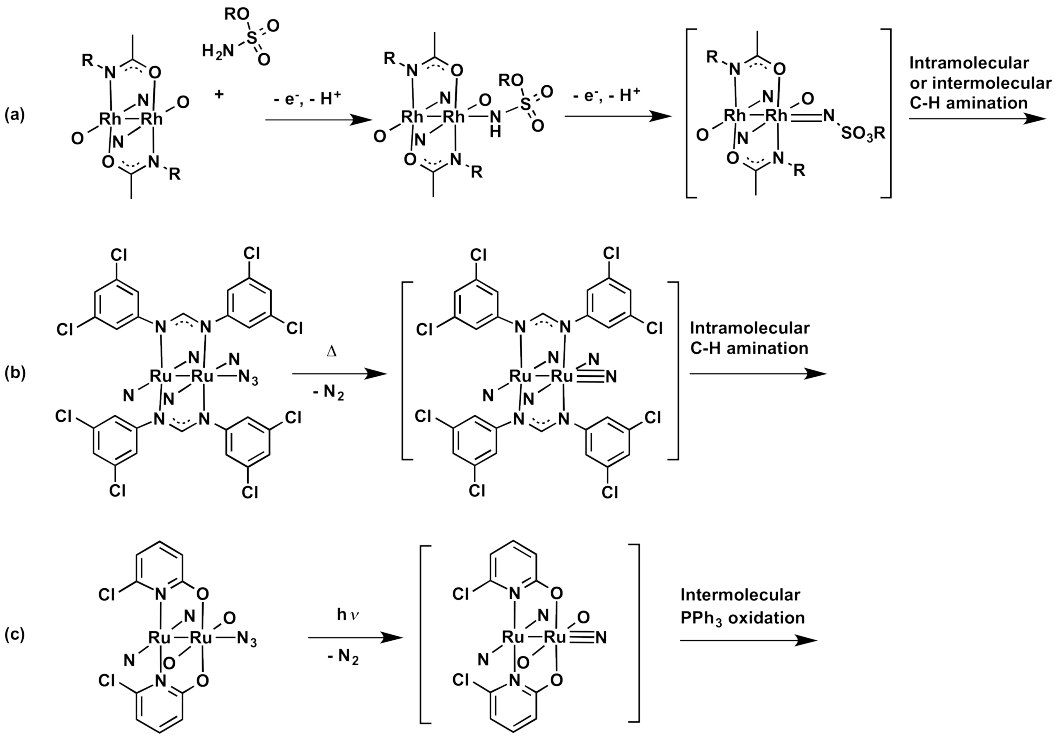

Figure 1.10. Reactions of metal-ligand multiply-bonded species in dirhodium and diruthenium systems.[46,48-50]

It is apparent in the work discussed so far that most of the research into the reactivity of metal-metal bonds has focused on the chemistry of axially-bound, metal-

ligand multiply-bonded species. This is largely due to the prevalence of paddlewheel-type structures in the literature, in which only the axial positions of the metals are open for substrate binding. With lower coordination numbers, more interesting substrate activation modes, and entirely different catalytic processes, are possible. One of the most interesting examples of such reactivity is another dirhodium system developed by Nocera and coworkers.[51-53] In this system, the dirhodium complex $Rh_2(dfpma)_3$ converts in two-electron steps between Rh(0,0), Rh(0,II), and Rh(II,II) states for overall four-electron chemistry, as shown in Figure 1.11. The oxidation reactions involve oxidative addition of two equivalents of HX and elimination of one equivalent of H_2 per metal. In each step, one rhodium atom converts between trigonal bipyramidal Rh(0)L and octahedral $Rh(II)X_2$ geometries. Each of the two-electron steps is made reversible by the ability of the system to photolytically eliminate X•, which is trapped either by an added radical scavenger or by the THF solvent. This reversibility allows the system to work photocatalytically, operating between the Rh(0,0) and Rh(0,II) states to convert HBr into H_2.[54]

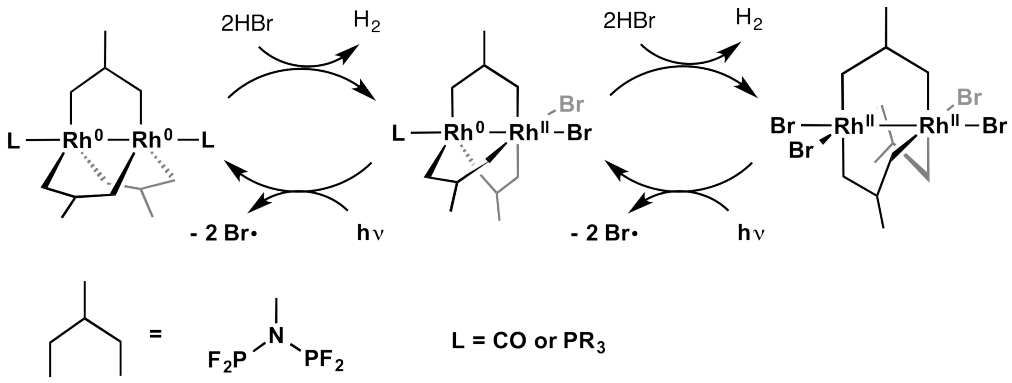

Figure 1.11. H_2 production from hydrohalic acid solutions mediated by $Rh_2(dfpma)_3$.[53,54]

The Rh-Rh bond plays a crucial role in this reaction. It remains a strong single bond throughout the process, providing structural stability despite the unusual, strained ligand geometries. Perhaps more importantly, despite the variation in oxidation states and geometries, the σ* M-M antibonding orbital remains the LUMO throughout the reaction. This is crucial because, when a halide ligand is in the axial position, there is significant M-X antibonding character admixed into this LUMO. Thus, photoexcitation of an electron into this orbital causes dissociation of the axial X group. Since this orbital framework is conserved throughout the process, photoexcitation can reduce the Rh(II,II) state by four electrons back to Rh(0,0).[53]

The strong bonding and conserved electronic frameworks are crucial in all of the reactions described above. These factors are also essential to the rational development of new complexes and new catalysts. Extension of this chemistry to complexes of first-row metals would be valuable, as such metals are much more earth-abundant, economically viable, and environmentally benign. However, there are many more challenges in the chemistry of metal-metal bonds between first-row metals. These challenges include difficulties in synthetically accessing such species and in the theoretical understanding of the bonding in the complexes that are known. Both these problems are rooted in the fundamental difficulty in developing M-M bonds between first-row metals, which is that such bonds are inherently weaker than their second- and third-row analogues, due to their smaller 3d orbitals. The development of catalysts based on first-row M-M bonds will require strong and predictable bonding in order to rationally tune their properties.

1.2.3 Bonds Between First-Row Metals: Electronic Structure of Dichromium Systems

The most obvious issue in the study of metal-metal bonds between first-row metals is that there are far fewer well-characterized examples than there are for second and third-row bimetallics. Until very recently, chromium was the only metal for which a significant number of examples had been structurally characterized. As a result, much of the current knowledge is based on lessons learned from dichromium systems. Fortunately, many of the lessons learned from these complexes appear broadly applicable to other first-row metals. They explain not only why the M-M bonding tends to be weaker in these compounds, but also which factors can be manipulated in order to increase the bond strength and which theoretical methods give accurate descriptions of the electronic structure.

Even within the large number of crystallographically characterized dichromium compounds, there is very little structural diversity. Almost all known dichromium structures up until around 2005 were paddlewheel complexes or closely related tetragonal species. However, within this structural series, there is a striking range of apparent bond strengths, with Cr-Cr separations ranging from 1.83 to 2.7 Å. This is by far the largest variation in bond distances between any isostructural series of any element.[55] At a first glance, there would be little reason to suspect that these compounds would have significantly different M-M bonds than their isoelectronic dimolybdenum and ditungsten analogues, which have well-established quadruple bonds. However, the earliest discovered compounds showed quite weak bonding: the structure of the tetraacetate, $Cr_2(O_2CCH_3)_4(H_2O)_2$, was the first to be solved, with a Cr-Cr distance of 2.362(1) Å.

This distance is significantly longer than the its dimolybenum analogue (Mo-Mo: 2.100 Å), despite the smaller size of the Cr ion.[55]

Early configuration-interaction calculations provided insight into the surprisingly weak bonding. They found that in the dichromium tetraformate, $Cr_2(O_2CH)_4$, the lowest energy configuration is the expected $(\sigma)^2(\pi)^4(\delta)^2$ pattern, which corresponds to a formal quadruple bond; however, this configuration accounts for only 12% of the overall wavefunction.[56] The rest are higher-energy configurations in which electrons are excited to higher-energy orbitals, such as the excitation of π electrons to δ* orbitals to form a $(\sigma)^2(\pi)^2(\delta)^2(\delta^*)^2$ configuration (8% of the wavefunction) and two δ electrons to δ* orbitals to form $(\sigma)^2(\pi)^4(\delta^*)^2$ (5% of the wavefunction). The excited electrons in these configurations retain the same spin as in the ground configuration and thus have no effect on the magnetic properties. However, in these configurations, electrons are moved from M-M bonding orbitals to M-M antibonding orbitals, which lowers the bond order. These effects are prominent in complexes of first-row metals due to the small energy differences between the orbitals, which allow electron correlation effects, such as the Coulombic repulsion between the electrons, to become more noticeable.

Theoretical modeling of these multiconfigurational ground states thus require methods that explicitly treat electron correlation. The process of explicitly including these excited configurations in the calculations is called configuration interaction (CI). This process is a conceptually simple but can be computationally intensive. Methods that further allow the form of the molecular orbitals to vary as the weights of the configurations are varied are termed multiconfigurational self-consistent-field (MC-SCF)

calculations. These give much more meaningful results. With these techniques, one can describe the bonding interactions using "effective bond order" (EBO), which includes the contributions of the higher-energy configurations to the overall bond order. In $Cr_2(O_2CH)_4$, for example, the formal bond order (FBO) is 4, from the $(\sigma)^2(\pi)^4(\delta)^2$ leading configuration, but once the higher energy configurations are included, the EBO is only 1.1, from the overall occupancies of $(\sigma)^{1.47}(\pi)^{2.44}(\delta)^{1.18}(\delta^*)^{0.82}(\pi^*)^{1.56}(\sigma^*)^{0.53}$. The calculated EBO thus neatly quantifies and explains the weak Cr-Cr bonding. It is a semantic difference whether to refer primarily to the FBO or the EBO when describing these bonds, but the convention of synthetic chemists is to refer to the FBO. Thus, the dichromium paddlewheel complexes are typically said to have quadruple bonds, regardless of the EBO.

The prominence of the multiconfigurational wavefunctions in first-row bimetallics is the result of the weak splitting energies between M-M bonding and antibonding orbitals; these in turn are partly due to the weak overlap between the small 3d orbitals and partly due to the weaker M-L splitting energies for first-row metals. One way to compensate for this is to increase the metal-ligand splitting energies by using more strongly-donating ligands. As with bimetallic compounds of second- and third-row metals, the donor strength of the bridging ligands affects the M-M bond strength; in dichromium compounds, this effect is particularly dramatic. The effects can be seen in both the bond distances and the calculated EBOs. Changing the weakly-donating carboxylate ligands in $Cr_2(O_2CH)_4$ to the more basic amidinate analogue, $Cr_2(HN_2CH)_4$, more than doubles the calculated EBO, from 1.1 to 2.6; the Cr-Cr distance shrinks

accordingly, from 2.30 to 1.93Å.[56]

In addition, while it had long been known that the strength of donors in the axial positions could affect the Cr-Cr distance, it was shown only fairly recently that the axial ligands can have an effect comparable to that of the equatorial donors. The first and only dichromium carboxylate compound characterized without axial coordination has a "supershort" Cr-Cr distance of 1.9662(5) Å, compared to 2.3892(2) Å for the same compound with two CH_3CN donors.[57] This experimental result has caused some consternation, however, as it casts uncertainty on earlier calculations on the carboxylate compounds. Most of these had used models without axial coordination, but none had predicted that the effect of the axial donors would be anywhere near as large. For example, the aforementioned calculations performed on $Cr_2(O_2CH)_4$ predicted a bond distance of 2.30 Å, near the experimental distance of 2.360(2) Å for the bis-aquo complex, $Cr_2(O_2CH)_4(H_2O)_2$. Subsequent studies found that even when "heavy corrections for CI" were made, traditional Hartree-Fock calculations failed to accurately reproduce the Cr-Cr distance; similar results were found with density functional theory (DFT) calculations, which predicted Cr-Cr distances of around 2.3 Å for $Cr_2(O_2CH)_4$.[55,58,59] Only complete active space self-consistent field (CASSCF) calculations combined with second order perturbation theory (CASPT2) correctly predicted that a carboxylate without axial coordination would have a Cr-Cr distance less than 2 Å.[59] This method has become the most reliable theoretical treatment of systems with degeneracies or near-degeneracies and other static correlation effects. Since full geometry optimizations with these techniques can be enormously computationally

intensive, however, most studies instead perform geometry optimizations using DFT methods and only apply CASSCF and CASPT2 calculations for analysis of the molecular orbitals and ground state energies, respectively. With recent advances in DFT methods, this approach has proven to be fairly reliable. However, care must be taken that the DFT-derived geometries are close to those found by experiment, as studies comparing various density functionals have found that the M-M distances predicted for transition metal dimers can vary substantially based on the choice of functional, with significant margins of error even (sometimes especially) with the more modern functionals.[60,61]

1.2.4 Low-Coordinate Dichromium Compounds: Maximizing the Bond Order

Within the past decade, there has been a striking resurgence of interest in dichromium systems. This was initiated by the report by Power *et al.* in 2005 of a low-coordinate, organometallic dichromium(I,I) complex with an exceptionally short Cr-Cr distance of 1.8351(4) Å.[62] It was immediately recognized that this short separation was the result of complete pairing of the d^5 Cr(I) centers to give a $(\sigma)^2(\pi)^4(\delta)^4$ ground state – in other words, a quintuple bond! Such a bond order is not possible in the paddlewheel complexes, where one d_{x2-y2} orbital on each metal is primarily metal-ligand antibonding and lies at too high of an energy to be populated by M-M bonding electrons. With the lower coordination number of the Power complex, the orbitals are all at much closer energies, and these d_{x2-y2} orbitals become available to make a fifth M-M bond. This remarkable bonding motif was subsequently confirmed by CASSCF/CASPT2 calculations and found to have a smaller - but still substantial - EBO of 3.52.[63]

Following this result, there was a flurry of reports using low-coordinate frameworks to make ever-shorter Cr-Cr bonds, with several examples shown in Figure 1.12.[64-68] These set successive records for the shortest metal-metal bond distance in a structurally-characterized compound, with the current shortest distance found in a guanidinate dimer reported by Kempe *et al.* in 2009; at 1.729(1) Å, it has an only slightly longer Cr-Cr distance than the gas-phase dinuclear Cr_2 dimer (1.68 Å), which is believed to possess a sextuple bond.[69]

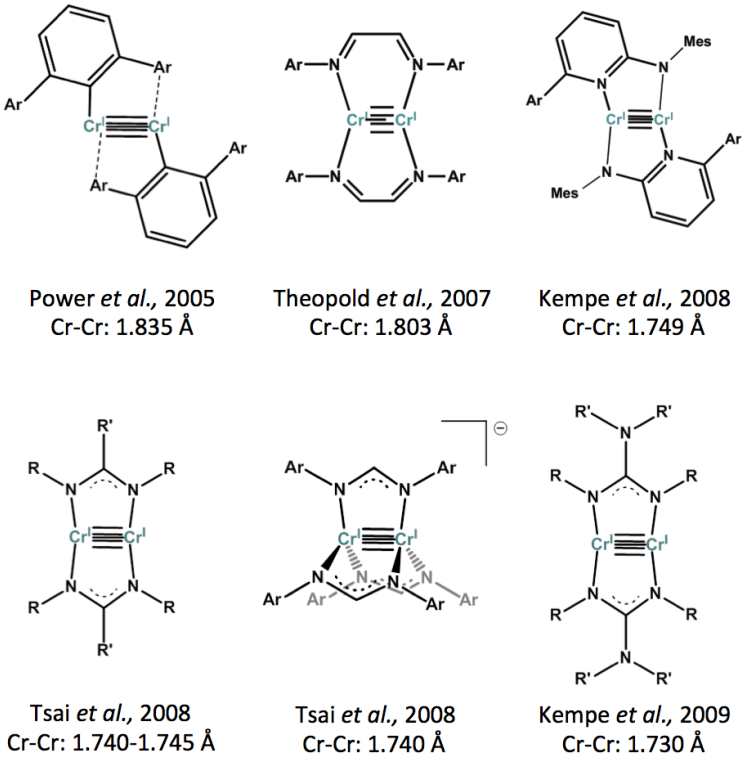

Figure 1.12. Low-coordinate dichromium(I,I) compounds possessing quintuple bonds.[62,64-68]

1.2.5 Metal-Metal Bonding Between First-Row Metals Later Than Chromium

There are far fewer examples of metal-metal bonding between first-row metals later than chromium. To the extent that they are known and show M-M bonding, the paddlewheel complexes between later metals appear to follow the general trends

observed for dichromium compounds. For example, axial coordination weakens the bonding, while strong bridging ligands strengthen it. However, since the maximum possible bond order is lower with the later metals, these factors can make the difference between the presence or absence of a bond. This is demonstrated in Figure 1.13, which compares the paddlewheel carboxylate and amidinate compounds for both chromium and cobalt. A similar effect is observed in the diiron paddlewheel complexes: the carboxylate compex $Fe_2(O_2CAr^{tol})_4(4\text{-}^t\text{Bu-py})_2$ (where O_2CAr^{tol} is 2,6-di[*p*-tolyl]benzoate) has a long Fe-Fe distance of 2.823 Å indicative of no bonding, while the amidinate complex $Fe_2(DPhF)_4$ has a shorter Fe-Fe bond of 2.46 Å, comparable to the distance in metallic iron.[70]

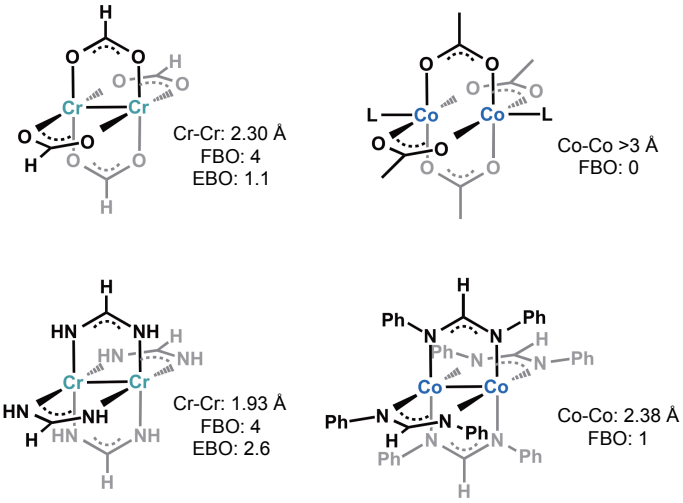

Figure 1.13. Selected dichromium and dicobalt paddlewheel complexes showing effect of donor strength on M-M bond. EBOs have not been calculated for the dicobalt complexes.[56,70]

As was the case with dichromium compounds, significant progress has been made in recent years in the isolation of diiron and dicobalt complexes with strong bonds, due to the use of low-coordination numbers and strongly donating ligands. Several such

examples are shown in Figure 1.14, along with the more traditional tetra-amidinate compounds.[71-77] There is far greater structural diversity in these complexes than for the quintuply-bonded dichromium systems. Moreover, it is readily apparent that no one factor, such as donor strength, can explain the observed metal-metal distances. Rather, there are significant differences between complexes even with similar ligands or geometries. The diiron and dicobalt terphenyl compounds reported by Nguyen and Power, for instance, are direct analogues of the quintuply bonded chromium(I) dimer, yet they have Fe-Fe and Co-Co distances significantly longer than the paddlewheel amidinate complexes. This is the opposite of the trend within dichromium compounds.[71-73] However, similar low-coordinate, low-valent compounds show extremely short distances when coordinated by guanidinate ligands.[76,77]

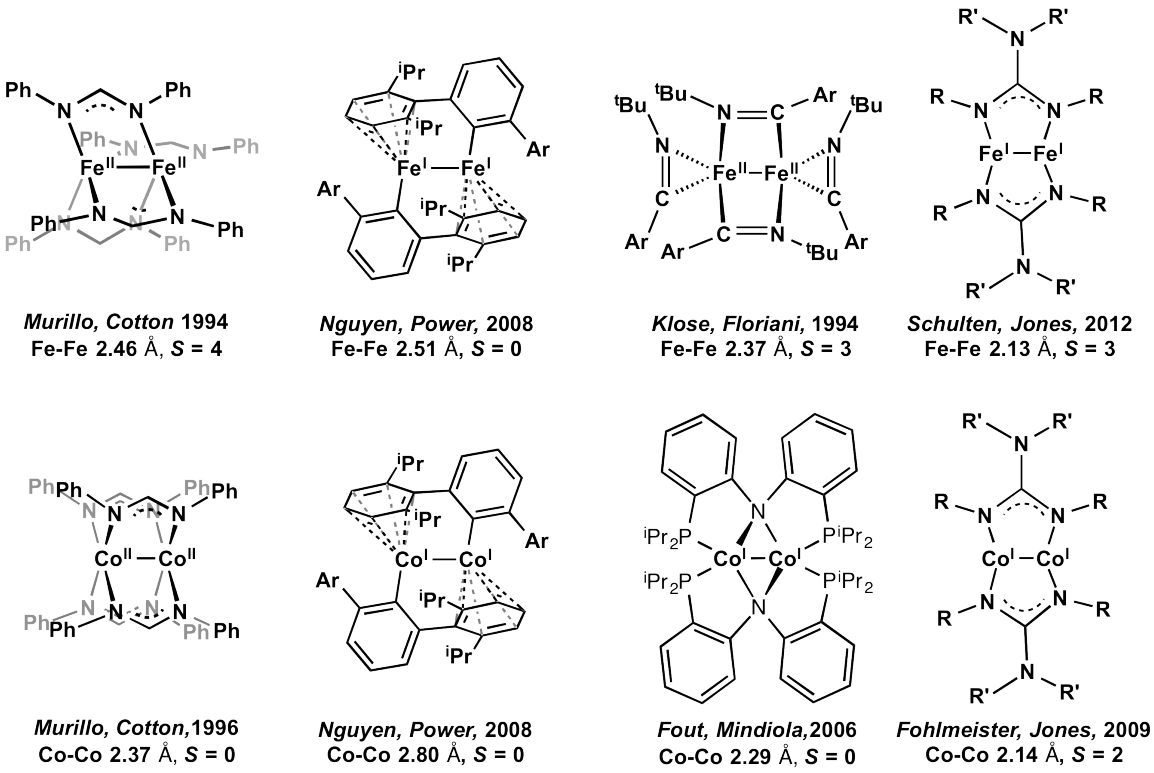

Figure 1.14. Selected examples of strong Fe-Fe and Co-Co bonding.[71-77]

The structural trends are even less clear when comparing diiron and dicobalt compounds compounds. In the tetra-amidinate systems, the dicobalt compound, surprisingly, has a shorter M-M bond; in many other comparisons, the diiron distances are shorter. Meanwhile, in the guanidinate systems, the distances are essentially identical. More strikingly, while the terphenyl and guanidinate compounds are essentially isostructural when iron is substituted for cobalt, in the diiron tetra-amidinate $Fe_2(DPhF)_4$, there is an unusual distortion away from idealized D_{4h} symmetry. This distortion, and its relation to the Fe-Fe bonding, were not understood for more than 15 years, until a recent theoretical re-examination of this molecule by Berry and Timmer.[78]

Finally, the most dramatic, and perhaps the most perplexing, differences are in the overall spin states of these complexes. Whereas the dichromium systems are all low-spin, the diiron and dicobalt complexes show a range from low- to intermediate- to high-spin compounds. Surprisingly few generalities can be made about these spin state differences, other than that the diiron systems appear more prone to higher-spin states than the dicobalt examples. There does not appear to be a clear correlation between M-M bond distance and spin state. For instance, two of the complexes with the shortest Co-Co bonds, reported by Jones and Mindiola, are both dicobalt(I,I) systems, but Jones' is high-spin ($S = 2$) while Mindiola's is low-spin ($S = 0$).[75,77] Similarly, the tetragonal and trigonal "lantern" complexes $Co_2(DPhF)_4$ and $Co_2(DPhF)_3$, reported by Cotton *et al.* contain nearly identical Co-Co distances, but the former is diamagnetic, while the latter was found to be highly paramagnetic.[72,79] There is likewise no clear correspondence between the spin state and the choice of weak- or strong-field ligands. The complexes

reported by Jones *et al.* use weak-field guanidinate ligands and are both high-spin.[76,77] This is more or less as might be expected from ligand field theory; yet the even weaker-field amidinate donors give a low-spin state in the case of the dicobalt paddlewheel, $Co_2(DPhF)_4$.[72] The complexes reported by Power use strong-field organometallic donors, and while the dicobalt complex is diamagnetic, as expected, the diiron complex shows paramagnetism that is not fully understood; it was originally described as a singlet, and this paramagnetism was attributed to impurities, but subsequent theoretical treatments support an open-shell configuration.[73]

Prediction of the magnetic behavior of bimetallics with late first-row metals is clearly not as straightforward as that of monometallic compounds or bimetallics with second- and third-row metals. In fact, the very coexistence of strong metal-metal bonding with highly paramagnetic ground states, as seen in several of these examples, is rather extraordinary, since direct M-M bonding seemingly implies pairing of electrons and would be expected to result in antiferromagnetic coupling. One of the major goals of the research described in this thesis is to understand the nature and origin of these high-spin metal-metal bonds. At the time this research was begun, many of the compounds in Figure 1.14 were not yet reported, and highly-paramagnetic metal-metal bonding was an exceptionally rare phenomenon. As the field of first-row metal-metal bonds has rapidly expanded, this motif has been observed more often, and understanding it has become even more essential.

1.2.6 Trigonal Lantern Diiron and Dicobalt Compounds

As a starting point for exploring this unusual bonding motif, we chose to conduct a detailed reinvestigation of the electronic structure of the first reported molecules to show the phenomenon: the "trigonal lantern" compounds $Fe_2(DPhF)_3$ and $Co_2(DPhF)_3$. These compounds were originally reported by Cotton, Murillo, and coworkers in 1994 and 1996, respectively.[80,81] They combine exceptionally short M-M bonds of 2.23 Å and 2.38 Å, respectively, with highly paramagnetic electronic configurations; the diiron complex was shown to have a high-spin, $S = 7/2$ ground state[82] while the magnetic data on $Co_2(DPhF)_3$ was inconclusive but suggested an $S = 5/2$ ground state with a low-lying $S = 3/2$ excited state.[79] The structure of the diiron complex is shown in Figure 1.15; the dicobalt complex is structurally analogous.

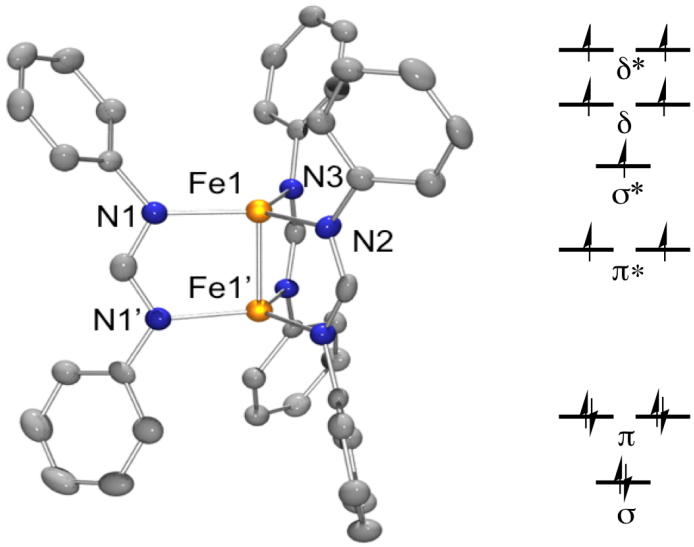

Figure 1.15. Solid-state structure of $Fe_2(DPhF)_3$ with thermal ellipsoids drawn at the 50% probability level. Hydrogen atoms are omitted for clarity. At right is the molecular orbital description proposed by Cotton, Murillo, *et al.* for this compound.[82,83]

The short M-M distances and highly paramagnetic behavior were rationalized according to a molecular orbital picture, based on *ab intio* calculations, that assigned to

$Fe_2(DPhF)_3$ a $(\sigma)^2(\pi)^4(\pi^*)^2(\sigma^*)^1(\delta)^2(\delta^*)^2$ ground configuration, consistent with both the high-spin, $S = 7/2$ state and a formal bond order of 1.5.[83] This motif is shown on the right side of Figure 1.15. The dicobalt analogue would then have two more electrons filling the π^* orbitals, lowering the spin state to $S = 5/2$ and the bond order to 0.5. The details of these studies and the origin of the M-M bonding are discussed in more depth in Section 2.1.2. However, a number of issues were left unresolved by these initial reports. For instance, while the diiron complex appeared to have a well-established high-spin ground state, the data for the dicobalt was less conclusive. In addition, the mixed-valent or delocalized-valent character of the formally M^IM^{II} oxidation states in the molecules were not established. The M-M bonding motif proposed for these molecules implies delocalized, $M^{1.5}M^{1.5}$ valences, but these were not verified experimentally. More generally, there is a dearth of spectroscopic information on these molecules, which is disappointing, considering the novelty of their electronic structure.

From a theoretical perspective, there are also open questions about the nature of the metal-metal interactions and about their initial theoretical characterization. Contemporary quantum mechanical methods had difficulty describing the structure and bonding in low-spin dichromium compounds, and the even more extreme amount of degeneracy and multireference character expected for the paramagnetic trigonal lanterns presents a more significant challenge for such methods. Modern, multiconfigurational calculations would provide a more accurate and detailed picture of the electronic structure. Even more fundamentally, the validity of applying a molecular orbital-based description of metal-metal bonding to the interactions between the metals, as opposed to

one based on exchange-coupling, is a matter of some dispute. Even Cotton had reservations about using an MO-based approach for these molecules,[83] and an alternate, exchange-coupling description was offhandedly proposed for $Fe_2(DPhF)_3$ by Berry and Timmer in their analysis of the similarly high-spin Fe-Fe bonding in $Fe_2(DPhF)_4$.[78]

Exchange-coupling models are far more commonly used to describe the interactions between open-shell ions of late first-row metals, largely due to the lack of clear metal-metal bonding in most enzymatic and synthetic clusters. These descriptions are not mutually exclusive, but there is rarely confusion about which method to apply in any given case. In general, exchange-coupling descriptions are used when the M-M interactions are indirect or weak and the magnetic behavior is interesting, while molecular-orbital-based descriptions of M-M bonding are used when the interactions are strong and direct and result in a closed-shell system. Intermediate cases, or those in which there is direct electronic communication between the metals but interesting magnetic behavior is observed, are rare, and in such cases it is often not clear which description is more appropriate. In the cases of $Fe_2(DPhF)_3$ and $Co_2(DPhF)_3$, there are obviously direct interactions between the metals, but, given their unusual magnetic behavior and our interest in obtaining a detailed understanding of their electronic structure, the exchange-coupling model cannot be dismissed out of hand. In fact, it can be shown that both the molecular orbital and exchange-coupling formalisms can adequately predict the bonding and the spin states in these molecules, and, moreover, that these models are essentially two different descriptions of the same underlying phenomenon. This is explained in more detail in Section 2.2.3 but requires a description of the origins of exchange-coupling.

1.2.7 Interactions Between Open-shell Metal Ions with Weak-field Ligands

Unlike compounds of second- and third-row metals, which have a preference for low-spin, closed-shell electronic configurations essentially regardless of their ligand donors, many first-row metal ions have a well-known distinction between high-spin and low-spin states that is determined by the coordination environment. With weak-field donors, such as the anionic carboxylates and amidinates commonly used as bridging ligands in bimetallic systems, high-spin states are often preferred. Similar weak-field ligands are also very common donors in metalloproteins. In multinuclear complexes of open-shell metals, the spins of the individual metal ions can interact in a number of ways. Although these coupling interactions often referred to as "magnetic interactions," because their effects are most visible in the magnetic properties of the cluster, their origins are in the exchange of electrons between the two metal ions, rather than the direct interactions of the metals' magnetic fields. These interactions are thus most commonly understood in the formalism of exchange coupling. In this formalism, the metal ions are treated as discrete, localized centers of spin density that interact either ferromagnetically, in which their individual spins align parallel to each other, giving a larger total spin, or antiferromagnetically, in which their spins align antiparallel and cancel. This is described quantitatively by the Heisenberg-Dirac-Van Vleck Hamiltonian, Eqn 1.8:

$$\hat{H} = -2J\,(\boldsymbol{S}_1 \cdot \boldsymbol{S}_2) \qquad \text{(Eqn 1.8)}$$

Here, $\boldsymbol{S}_1$ and $\boldsymbol{S}_2$ are the spins of the individual metal ion, and J is the coupling constant describing the energy of the interaction between them. Although conventions vary, in this work $J > 0$ describes a ferromagnetic interaction and $J < 0$ describes an

antiferromagnetic interaction. These outcomes are depicted pictorially in Figure 1.16.

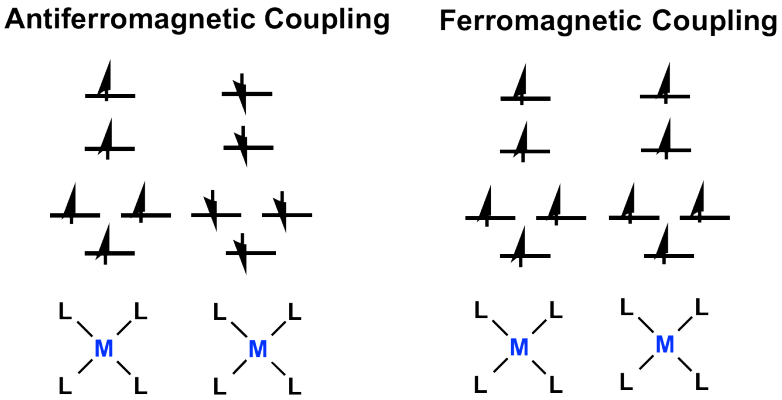

Figure 1.16. Electronic orientations in antiferromagnetic (left) and ferromagnetic (right) coupling scenarios.

These interactions are the result of electronic contact between orbitals containing unpaired spin density. In the simplest form, that of direct exchange, the contacts are directly between the *d* orbitals of two metals in close contact. In this case, in order to allow delocalization of an electron from an orbital on the first metal center to another half-filled orbital on the second, the Pauli exclusion principle requires the electrons in these orbitals to be of opposite spin, leading to antiferromagnetic coupling of the metals, as shown in Figure 1.17. This delocalization of electrons is stabilizing, and these interactions are often referred to as incipient or weak bonding; the same logic applies to cases of full M-M bonding, which can be thought of as the limit of strong antiferromagnetic coupling *via* direct exchange.[84]

More often, however, the distances between the metals are too long to allow direct exchange, and the electronic communication is mediated by bridging ligands, in a process known as superexchange. In this latter case, the electronic contact is the result of partial delocalization of the unpaired spin density onto the ligand orbitals; one such

possible interaction is shown in Figure 1.17. For an electron to delocalize from the ligand p orbital onto a half-filled metal d orbital requires that this ligand-based electron be aligned antiparallel to the spin of the metal-based electrons, which are arbitrarily assigned as "spin-up." The second ligand-based electron must therefore be "spin-up," and in order for it to delocalize onto the second metal center, the electrons on the second metal must be "spin-down." Thus, interaction of two metals with the same, filled ligand orbital requires the metals to have their spins mutually antiparallel, or antiferromagnetically coupled.

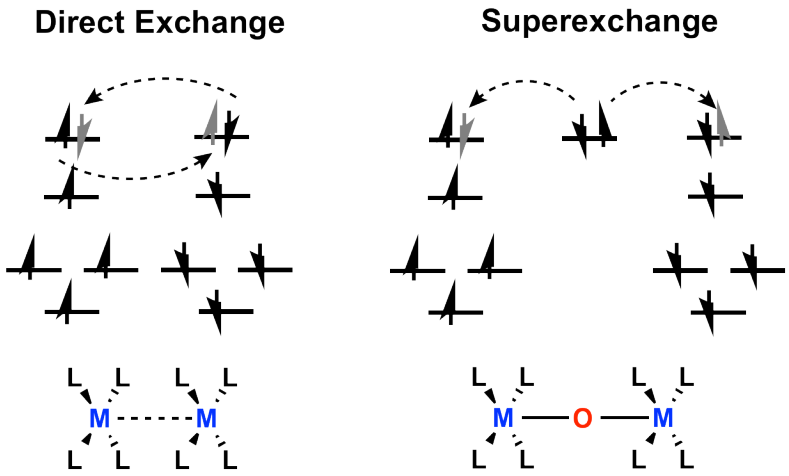

Figure 1.17. Qualitative depiction of electron interactions in direct exchange and superexchange.

The strength of these interactions can range from strong to weak or nonexistent, depending on the nature of the ligands, the length of the bridging group, and the geometry of the system, which determines the orbital overlap leading to the interaction. In fact, whether the coupling is ferromagnetic or antiferromagnetic is also determined by orbital overlap considerations, described in the Goodenough-Kanamori rules, which have been paraphrased in the following form:[84]

1. When the two ions have lobes of localized orbitals pointing toward each other in such a way that the orbitals would have a reasonably large overlap integral, the exchange is antiferromagnetic.
2. When the orbitals are arranged in such a way that they are expected to be in contact but have a zero overlap integral, the exchange is ferromagnetic (but usually weaker than the corresponding antiferromagnetic exchange).

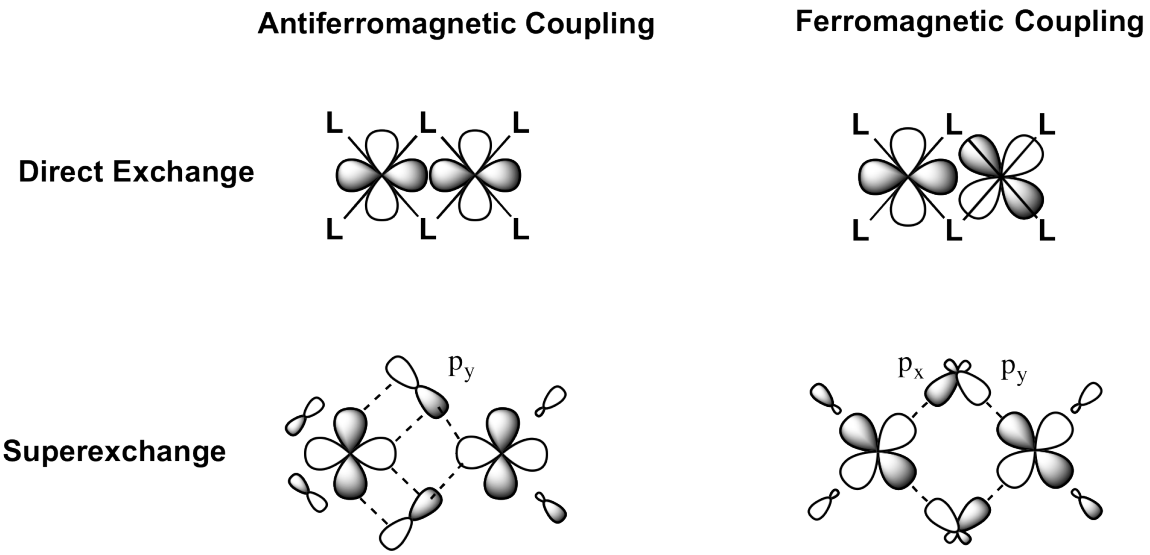

Figure 1.18. Example orbital interactions leading to ferromagnetic and antiferromagnetic coupling between two metals.[84]

Examples of these rules as applied in direct and superexchange pathways are shown pictorially in Figure 1.18. In general, systems in which there is direct orbital overlap favor antiferromagnetic coupling, with direct overlap between metal orbitals being a stronger interaction than ligand-mediated pathways. This logic suggests that a metal-metal bonded system should be strongly and *inherently* antiferromagnetically coupled, through a direct coupling mechanism, but that an antiferromagnetically coupled system is not necessarily metal-metal bonded. In this sense, a metal-metal bond can be considered the limit of strong antiferromagnetic coupling. Ferromagnetic coupling, on the other hand, results from indirect interactions through orthogonal orbitals; it is therefore

usually a much weaker interaction, and there is no obvious mechanism for metal-metal bonding to enforce strong ferromagnetic coupling, or *vice versa*.

1.2.8: Strongly Ferromagnetic Interactions in Mixed-Valent Systems: Double-Exchange

In fact, there are two ways to enforce strongly-ferromagnetic interactions. The first and most common is to couple the metals via a ligand radical. This strategy does not tend to involve significant M-M interactions and is thus not relevant to the complexes described in Sections 1.2.5 and 1.2.6. The second is the result of direct exchange of an electron between two metals and is quite relevant. This phenomenon, known variously as spin-dependent delocalization or double-exchange, can occur when an electron is fully delocalized between half-filled orbitals on two different metal ions.[84,85] Because this type of delocalization typically occurs between two metals with different oxidation states, the phenomenon has been traditionally tied to mixed-valency, although this does not necessarily need to be the case.[78] Nevertheless, it has found the most application in explaining the ferromagnetic coupling between certain $Fe^{II}Fe^{III}$ mixed-valent pairs, including both natural[86] and mutant[87] [FeS] clusters and many synthetic model systems[85,88-92] and it is easiest to explain within this context.

As shown in Figure 1.19, a mixed-valent $Fe^{II}Fe^{III}$ pair can be thought of as two Fe^{III} ions with an "extra" electron to be distributed between them. If the Fe centers are otherwise equivalent, and there is direct orbital overlap between them, the electron should be free to delocalize between the two, as shown on the left side of Figure 1.19.[85] This delocalization is a stabilizing, resonance-like interaction and favors delocalized-valent

oxidation states of $Fe^{2.5}Fe^{2.5}$. However, it is only possible when the Fe spins are aligned parallel to one another. In that case, both high-spin Fe^{III} ions have their d orbital shells half-filled and coupled ferromagnetically (all α spin); the "extra" or "itinerant" electron is therefore of β spin and can freely delocalize. If, instead, the Fe^{III} spins are aligned antiparallel (Figure 1.19, right), then the electron must change its spin from β to α upon moving from one center to the other, to avoid violating the Pauli exclusion principle. This creates a barrier to delocalization that traps the metals in localized $Fe^{II}Fe^{III}$ valences. Another way of stating this is that, in the antiferromagnetic arrangement, the Pauli principle requires that the *α-spin* electron, rather than the β-spin electron, be the one that delocalizes from FeA to FeB; this leaves FeA with an electronic configuration (4α, 1β) that violates Hund's rule and is higher in energy than the preferred $M_S = 5/2$ spin projection. There is thus a significant energy cost to delocalization in the antiferromagnetic arrangement.[84]

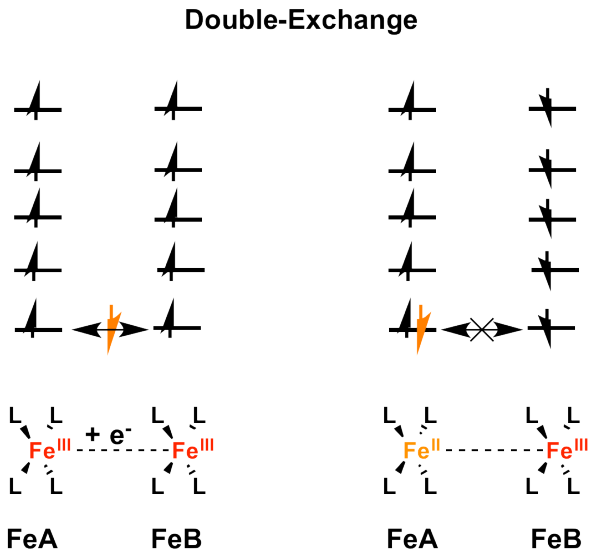

Figure 1.19. Double-exchange between an $Fe^{II}Fe^{III}$ pair, showing the easy delocalization when the metals are coupled ferromagnetically (left) and trapped state when they are antiferromagnetically coupled (right).

Since the delocalization is stabilizing, there is a difference in energy between the delocalized and "trapped" states that favors the delocalized (ferromagnetic) form. This is a resonance energy, with the difference between the symmetric (ferromagnetic) and antisymmetric (antiferromagnetic) spin combinations given by Eqn 1.9.[84]

$$\Delta E^{s,a} = 2B(S + ½) \qquad \text{(Eqn 1.9)}$$

Here, B is the double-exchange parameter, a new coupling constant that quantifies the favorability of delocalization. There are, of course, other factors that affect the spin energetics, such as the other direct-exchange and superexchange interactions: these are treated according to the usual Heisenberg-Dirac-Van Vleck Hamiltonian (Eqn 1.8), giving an overall equation for the energy difference between spin states, Eqn 1.10:[88]

$$E^{s,a}(S) = -JS(S + 1) \pm B(S + ½) \qquad \text{(Eqn 1.10)}$$

J is the usual coupling constant due to Heisenberg exchange, and if $J < 0$, there is a competition between the double-exchange and Heisenberg exchange terms, where stronger Heisenberg exchange interactions will favor antiferromagnetic coupling and stronger double-exchange will favor ferromagnetic coupling. If $J > 0$, then the system is already predisposed to ferromagnetic coupling, and the effect of double-exchange is merely to increase the strength of the coupling. In practice, it is difficult to experimentally distinguish the relative contributions of the first and second terms in Eqn 1.10, and Eqn 1.8 can be used to describe the entire system. In that case, the contributions of B are included in the value of J, and an overall coupling constant is determined that does not differentiate the influences of double-exchange and Heisenberg exchange.

While the double-exchange mechanism can explain some strong ferromagnetic

interactions through the formalism of exchange coupling, it is not necessarily distinct from the MO-based description of metal-metal bonding that Cotton *et al.* used to rationalize the high-spin states of $Fe_2(DPhF)_3$ and $Co_2(DPhF)_3$. The application of the double-exchange formalism to these molecules, and the correspondence between this description and the MO-based one, is made in Chapter 2, Section 2.13.

1.2.9 Comparison of Exchange-Coupling and Molecular Orbital Formalisms: Can MO Theory be Used to Describe High-Spin Bimetallics?

In practice, the exchange-coupling model is rarely invoked to describe complexes with significant amounts of metal-metal bonding. Such systems are typically analyzed through a molecular orbital formalism, in which the spin state of the bimetallic system is considered as a whole, rather than as the combination of two individual spins. In such an analysis, the spin state of a complex is determined by the population of the M-M bonding and antibonding molecular orbitals, with the relative energetics of electron pairing versus orbital splitting determining the number of unpaired electrons, exactly as in the ligand field analysis of a conventional mononuclear metal ion. This approach, while less amenable to spectroscopic and magnetic characterization, has the advantage of being a more tractable description of the bonding and is more easily analyzed by theoretical methods. However, its applicability to bonds between first-row metals with weak-field ligands is somewhat controversial.

The difference between exchange-coupling and molecular orbital treatments of spin interactions is similar to that between valence-bond (VB) and MO treatments of chemical bonds. In VB theory, the bond is a perturbation on an otherwise localized

picture of the interacting atoms; the electrons are presumed to be localized around individual atoms, except in the specific cases where they are involved in bonding. In MO theory, the electrons are treated as inherently delocalized. In most cases, both models give descriptions of the bonding that are qualitatively accurate, and the choice of a description is largely based on its utility: VB descriptions are simpler and more useful in describing the properties of atoms, while MO theory gives a more informative view of bonds. VB is more useful in explaining, for example, the linear geometry of a carbon atom in an alkyne, while MO theory is more useful in describing the electronic origins and reactivity of its triple bond. The fundamental differences between the analyses become more apparent when quantitative predictions are needed. The VB treatment of chemical bonding is far superior in cases of weak interactions and large interatomic distances, where a localized, atomic view is qualitatively more appropriate and where MO theory quantitatively over-predicts bond strengths unless perturbations are made to account for electron correlation. On the other hand, while VB analysis gives a qualitatively acceptable description of stronger bonding interactions, it is quantitatively less precise in such cases, not accounting for effects such as ionization.[56]

The prediction of spin energetics using exchange-coupling and MO formalisms is similar. The former considers the unpaired spin density to be essentially localized on individual metals, then introduces intermetallic interactions that account for any delocalization. MO models, on the other hand, start with a delocalized picture of the electrons but can account for localization through nonbonding or polarized molecular orbitals. Qualitatively, both methods can give useful descriptions of magnetic

interactions. Exchange-coupling models are generally more useful in explaining spectroscopic and magnetic data, and they are also more informative in describing atomic properties, such as oxidation states, for each metal. MO analysis can be much more useful in describing the nature of a metal-metal bond.

Compared with the difference between VB and MO models of bonding, the quantitative differences between the exchange-coupling and MO models of spin interactions are more dramatic, and there are more cases in which only one is useful. MO descriptions, for example, are very cumbersome in describing weak interactions between two distant metals, while exchange-coupling models do not give particularly useful descriptions of strong, direct covalent bonding in conventional M-M systems. In one sense this is not a fair comparison, as exchange-coupling models are only intended to account for the energetic differences between the possible spin states, while MO models account for the entirety of the bonding. However, a similar situation is encountered in the quantitative prediction of spin energetics using exchange-coupling and MO-based spin Hamiltonians, which compare only the relative energies of the various spin states, rather than the total electronic energy of a system. A direct comparison of the spin energetics predicted by both approaches has been made for a two-electron dinuclear system as a function of two key parameters, the orbital interaction energy (β, Hückel integral) and the electron pairing energy (U_0).[85] This found that both methods give essentially identical energies for the singlet and triplet states when β is large and U_0 is small. However, only the exchange Hamiltonian gave accurate results in the opposite case, when the interaction energies are weak relative to the pairing energy. As described by Blondin and Girerd,[85]

> For transition-metal ions of the first line in low oxidation states or of the second or third line and when those metal ions are very close to each other, $\beta/U_0 >> 1$ is expected to

> be valid. For such cases, U_0 is small (diffuseness of the orbitals) and β is large. This limit corresponds to a metal-metal bond situation.
>
> On the other hand, one can remark… that MO theory fails in the limit $\beta/U_0 << 1$. The gap between the $1^1\Gamma_g$ (MO) and the $^3\Gamma_u$ states is large, in contradiction with the vanishing gap expected from the exact calculation and experimentally observed. This limit corresponds to electron-exchange phenomenon.

Based on this analysis, the authors conclude that "MO theory is in fact contained in" the exchange-coupling model, and that the latter model can accurately describe the interactions in bimetallic systems regardless of the strength of the interaction. On the other hand, MO theory is said to be applicable in cases of strong metal-metal bonding but fails in the case of weaker interactions between the *3d* orbitals of first-row metals. It was assumed that first-row metals do not participate in strong metal-metal bonding.

The assertion that the exchange-coupling model accurately describes stronger M-M interactions does not appear to always hold true for systems with more than two exchanging electrons. Notably, several systems are known that have intermediate spin states with a strong temperature dependence, such as the $S = 3/2 \leftrightarrow S = 1/2$ equilibrium in some diruthenium(II,III) paddlewheel complexes[93] and an $S = 2 \leftrightarrow S = 4$ equilibrium discovered in a much more recent triiron complex.[94] These intermediate spin states and their thermal behavior cannot be rationalized strictly in terms of ferro- or antiferromagnetic coupling between localized centers of spin density, but they are readily explained by a simple Boltzmann population of the *d* electrons within a delocalized MO bonding manifold.

Unfortunately, it is not clear *a priori* which description is most apt in the analysis of the trigonal lantern systems. The strong orbital overlap inherent in their M-M bonding would favor an MO description, but the smaller, less diffuse 3*d* orbitals and weak orbital

splittings of the first-row metals may complicate this analysis. We have chosen to use a primarily MO-based description, as it is more amenable to theoretical analysis and provides a much more tractable account of the bonding. It is worth emphasizing that the differences between these approaches are only relevant to the relative energies of the various spin states, not the total electronic energy of the system. Any significant disagreements between the models can be easily settled by comparison with the experimental magnetic behavior. Conversely, if both models are consistent with the experimental data, then the differences in approach are not important.

As described in sections 2.1.2 and 2.1.3, both MO formalisms and double-exchange formalisms can be used to explain the high-spin states of $Fe_2(DPhF)_3$ and $Co_2(DPhF)_3$; moreover, these approaches can be qualitatively seen as two different descriptions of the same phenomenon. The descriptions should thus differ, if at all, only in their quantitative predictions of the energy gap between the high-spin ground states and the lower-spin excited states. Preliminary data reported by Cotton *et al.* suggest that $Fe_2(DPhF)_3$ is an octet at both low and high temperatures,[82] and measurement of the spin energetics should thus not be feasible. However, $Co_2(DPhF)_3$ was reported to have a low-lying quartet excited state accessible at room temperature.[79] The temperature-dependence of the magnetism in this case would provide a valuable experimental measurement of the spin energetics that could validate the theoretical models.

1.3 Chapter Summaries

We are interested in developing general platforms that enable strong bonding

between first-row metals. Ideally, these platforms would allow direct comparison of the bonding interactions between various metal pairs within isostructural series. This has led us to reinvestigate and extend the chemistry of trigonal lantern tris-amidinate compounds. We are interested in understanding the nature of the M-M interactions in these complexes and whether this motif can be a general way to enforce strong bonding between mid-to-late first-row metals. We also sought to determine whether their strong bonding and low-coordinate geometries offered potential applications in multi-electron redox chemistry and small-molecule reactivity. The following two chapters describe our investigations along these lines.

Chapter 2 is an account of our reinvestigation of the previously reported complexes $Fe_2(DPhF)_3$ and $Co_2(DPhF)_3$. In these studies, a new synthetic route is reported for each compound; these allow their isolation in high purity suitable for spectroscopic and physical measurements. Spectroscopic and magnetic measurements are reported which definitively assign the bimetallic cores as having $M^{1.5}M^{1.5}$ delocalized valences and high-spin ground states energetically well-separated from the lower-spin excited states. These experimental studies are paired with high-level theoretical analyses based on multiconfigurational *ab initio* calculations that rationalize the electronic structure. Finally, the reactivity of $Fe_2(DPhF)_3$ towards small-molecule oxidants is described, revealing a highly reducing diiron core that nonetheless shows a surprising selectivity towards reaction with molecules containing radical character.

In Chapter 3, the trigonal lantern motif is extended to a new set of trigonal lantern compounds. These use a chelating ligand design that allows synthesis of both

homobimetallic and heterobimetallic compounds *via* a stepwise metallation procedure. The trigonal structure and high-spin electronic framework of the original trigonal lanterns are conserved in these compounds, and these result in strong metal-metal bonds. The isolation and characterization of a heterobimetallic iron-cobalt compound is particularly noteworthy, as it shows not only the shortest Fe-Co bond in the literature, but a delocalized, high-spin electronic structure that is exceptionally rare among heterobimetallic compounds with M-M' bonds.

Chapter 4 describes much more recent work on a different approach to the multi-electron activation of small molecules, using ligands that position hydride donor groups in the secondary coordination sphere of a metal. These are designed to facilitate activation and reduction of substrates through metal-ligand cooperativity. The design and synthesis of these ligands and their coordination chemistry with palladium are described. Also discussed are their reactions with hydride donors and acceptors and their redox chemistry with hydrogen and hydrogenation substrates.

Chapter 2

Reinvestigation of High-Spin Metal-Metal Bonds in Diiron and Dicobalt "Trigonal Lantern" Compounds

In part from:

Zall, C. M.; Zherebetskyy, D.; Dzubak, A. L.; Bill, E.; Gagliardi, L.; Lu, C. C. A Combined Spectroscopic and Computational Study of a High-Spin *S*= 7/2 Diiron Complex with a Short Iron–Iron Bond. *Inorg. Chem.* **2012**, *51*, 728–736.

and

Zall, C. M.; Clouston, L. J.; Young, V. G., Jr; Ding, K.; Kim, H. J.; Zherebetskyy, D.; Chen, Y.-S.; Bill, E.; Gagliardi, L.; Lu, C. C. Mixed-Valent Dicobalt and Iron-Cobalt Complexes with High-Spin Configurations and Short M-Co Bonds. *Inorg. Chem.* **2013**, *52*, 9216-9228.

2.1 Overview

The "trigonal lantern" diiron and dicobalt complexes $Fe_2(DPhF)_3$, **1**, and $Co_2(DPhF)_3$, **2**, originally reported by Cotton, Murillo, *et al.* are unusual in featuring a combination strong metal-metal bonds between late first-row transition metals and high-spin electronic ground states. In order to better understand this bonding picture, these compounds have been resynthesized and studied by a host of physical and theoretical methods. These results shed light on several features of the complexes important to their M-M bonding, including the temperature independence of their spin state, delocalization of their oxidation states into formally $M^{1.5}M^{1.5}$ mixed-valent cores, and the molecular orbital basis of their bonding, which is revealed by high-level calculations to be well-described by the simple picture originally proposed by Cotton *et al.* The reactivity patterns of **1** have also been studied; despite its highly reduced nature, the diiron core is unreactive to many singlet small molecules and common oxidative addition substrates. On the other hand, it is extremely reactive towards one-electron oxidants and radical small molecules such as O_2 and NO, forming cluster compounds that retain the original Fe-Fe unit and demonstrate its one-electron oxidation.

2.2 Introduction

The study of metal-metal bonds is of longstanding interest to chemists for both theoretical and practical reasons. Using such bonds to couple the reactivity of two metal centers is a promising approach to achieving multielectron small-molecule redox chemistry. In particular, productive coupling of two first-row metals *via* metal-metal

bonding would be advantageous, considering the low cost of these metals and their greater propensity towards one-electron redox couples (e.g. $Fe^{II/III}$, $Cu^{I/II}$). However, there are far fewer examples of non-organometallic metal-metal bonds between first-row metals than their second- and third-row analogues, due in large part to the weaker overlap between 3d orbitals. Yet, within this smaller sample size, there is a remarkable diversity of electronic structures. Understanding the factors governing these interactions is essential to the rational development of these systems for catalysis and other applications.

2.2.1 Strong Bonding in the "Trigonal Lantern" Complexes of Diiron and Dicobalt

One of the most interesting classes of compounds is the "trigonal lantern" family of diiron and dicobalt amidinate complexes, comprising $Fe_2(DPhF)_3$, $Co_2(DPhF)_3$, (where DPhF = N,N'-diphenylformamidinate) and their benzamidinate analogues. These compounds were first reported by Cotton, Murillo, *et al.* in the mid-1990s,[1-4] as discussed in section 1.2.6. The most notable structural feature of these complexes is their extremely short metal-metal distances: in **1**, the iron-iron separation is 2.2318(8) Å,[1] while the Co-Co distance in **2** is 2.385(1) Å.[5] At the time it was reported, the former distance was the shortest iron-iron bond known. The benzamidinate analogues $M_2(DPhBz)_3$ of both complexes were reported shortly thereafter[3,4] and feature even shorter distances of 2.18 and 2.31 Å, respectively. The shorter distances in the benzamidinates are attributable to the extra steric pressure of the phenyl group in the bridgehead position of the ligand. This steric effect compresses their N-C-N angles from 121-122° to 115-120°, forcing a shorter M-M distance. The electronic differences between the complexes are believed to be

minimal, and therefore more attention has been paid to the original formamidinate species. The structure of **1** is shown in Figure 2.1; the structure of **2** is entirely analogous.

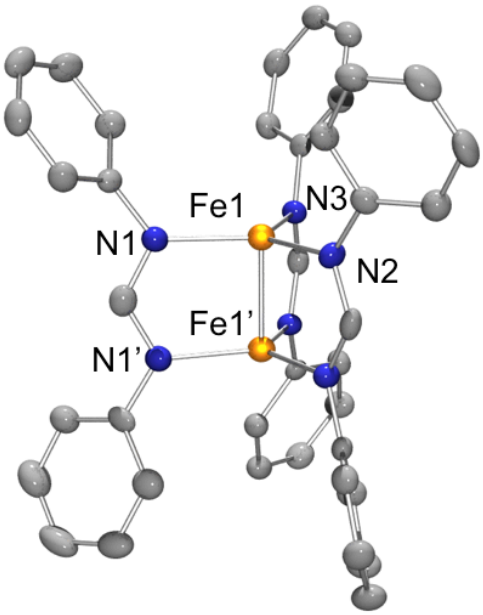

Figure 2.1. Solid-state structure of **1** at 50% probability level. Compound **2** is isostructural. Hydrogen atoms have been omitted for clarity. Selected bond distances (Å) and angles (°) for **1**:[3] Fe1-Fe1', 2.2318(8); Fe1-N1, 2.033(2); Fe1-N2, 2.025(2); Fe1-N3, 2.017(2); N1-Fe1-N2, 132.6(1); N1-Fe1-N3, 111.08(1); N2-Fe1-N3, 116.18(9); N1-Fe1-Fe1', 92.29(6); N2-Fe1-Fe1', 90.98(6); N3-Fe1-Fe1', 89.77(7). For **2**:[4] Co1-Co2, 2.385(1); Co1-N1, 1.932(5); Co1-N2, 1.935(5); Co1-N3, 1.959(6); N1-Co1-N2, 125.1(2); N1-Co1-N3, 119.2(2); N2-Co1-N3, 115.6(2); N1-Co1-Co2, 90.32(2); N2-Co1-Co2, 90.06(2); N3-Co1-Co2, 91.30(2).

Since these early reports, there has been only one complex reported with a shorter diiron distance, a dibridged bis-guanidinate reported by Jones *et al.* in 2012, at Fe-Fe = 2.1270(9) Å.[6] A few dicobalt compounds have shorter Co-Co distances, notably including the tetragonal lantern complex $Co_2(DPhF)_4$, which is only very slightly shorter at 2.3735(9) Å,[7] and a pair of dibridged amidinate and guanidinate complexes reported by Jones and coworkers, with exceptionally short distances of 2.140(1) Å and 2.1345(7) Å, respectively.[8] Several of these complexes were discussed in Section 1.2.4. Nevertheless,

the bond distances **1** and **2** remain remarkably short compared to most of the complexes reported in the literature.

2.2.2 Molecular Orbital Analysis of M-M Bonding in the Trigonal Lanterns

In addition to possessing remarkably short M-M distances, the trigonal lantern complexes also show highly paramagnetic electronic configurations. An $S = 7/2$ ground state was assigned for the diiron complex, **1**, based on its high-*g* EPR resonance ($g_\perp = 7.99$) and its large room-temperature effective magnetic moment ($\mu_{eff} = 7.94\ \mu_B$).[3] The magnetic behavior of dicobalt **2** was more complex and somewhat problematic. The room-temperature magnetic moment was initially reported as 4.65 μ_B[2] and later revised to 5.2 μ_B.[4] These latter values, which fall well short of the spin-only value of 5.92 μ_B expected for an $S = 5/2$ system, were interpreted as representing a ground-state $S = 5/2$ but with a low-lying $S = 3/2$ state, although this assignment was occasionally reversed in later descriptions.[4] Details or plots of the EPR spectrum and variable-temperature magnetic susceptibility for **2** were not reported, but these data were apparently recorded and were described as being consistent with this assignment.[2] Finally, in a theoretical study of the truncated model, $Co_2(HNCHNH)_3$, *ab initio* multireference configuration interaction (MRCI) calculations were performed on the three lowest-lying states: the $^6A_2$" sextet, the $^4A_1$' quartet, and a $^2A_2$' doublet. The sextet state was found to be lowest in energy, with the quartet lying next lowest, less than 1000 cm^{-1} above the ground state.[9] As the last paper in a series on these compounds, this theoretically-derived description as a ground-state sextet and low-lying quartet has become the accepted electronic configuration for **2**.[10]

The same calculations also provided a molecular orbital picture that explains both the metal-metal bonding and the open-shell configurations of the molecules. This MO analysis is explained largely through contrast between the trigonal lanterns and the more conventional tetragonal paddlewheel complexes. It begins with a comparison of the monometallic ML_3 and ML_4 fragments that form one half of each structure. As shown in Figure 2.2, in the square planar ML_4 fragment, the $d_{x^2-y^2}$ orbital lies at much higher energy than the other four d orbitals, as a result of its direct overlap with the four ligand donors in a strongly antibonding interaction. The trigonal fragment, on the other hand, has one fewer donor, leading to less overall M-L splitting. The $d_{x^2-y^2}$ orbital in particular is significantly lowered, as it not only loses a direct M-L antibonding interaction; it also has the remaining three M-L interactions arranged in an orientation with much less direct overlap. The d_{xy} orbital, meanwhile, is significantly destabilized in the new orientation, and the two orbitals become degenerate at an intermediate energy. The trigonal arrangement thus has more degeneracy and lower overall orbital splitting energies than the tetragonal one.

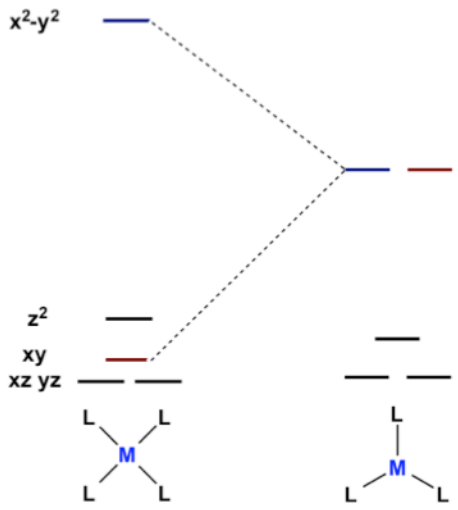

Figure 2.2. Molecular orbital diagram for monometallic fragments of tetragonal and trigonal lantern structures.

When two of the monometallic fragments are brought together to form the bimetallic structure, the d_{x2-y2} orbital in the tetragonal system starts at much higher energy and does not gain significant stabilization from M-M bonding. Thus, there is only one δ/δ* pair at an energy relevant to M-M bonding. In contrast, the trigonal lantern has two sets of degenerate δ/δ* pairs that, being still primarily M-L antibonding, are at relatively high, but still accessible, energy. This energy is comparable to that of the π* and σ* orbitals resulting from the antibonding combinations of d_{xz}, d_{yx}, and d_{z2} orbitals. The resulting MO manifolds are shown in Figure 2.3 for the tetragonal and trigonal dicobalt lanterns, $Co_2(DPhF)_4$ and $Co_2(DPhF)_3$. In the tetragonal lantern, the larger orbital splittings cause the electrons to pair conventionally, giving an $S = 0$ state with a single bond from the $(\sigma)^2(\sigma^*)^0$ pair, analogous to the isoelectronic dirhodium(II) paddlewheels. In $Co_2(DPhF)_3$, however, after the filled set of $(\sigma)^2(\pi)^4$ bonding MOs, the remaining orbitals have much smaller energy gaps, apparently less than the pairing energy; they are thus filled in a high-spin fashion, leaving the σ*, δ, and δ* orbitals half-filled. There is thus a formal bond order (FBO) of 0.5, from the $(\sigma^2)(\sigma^*)^1$ pair, and an $S = 5/2$ spin from the five unpaired electrons. This analysis also easily explains the stronger bonding and higher spin in $Fe_2(DPhF)_3$. With two fewer electrons, the π* orbitals become half-filled, increasing the bond order to 1.5, from one $(\sigma)^2(\sigma)^1$ and two $(\pi)^2(\pi^*)^1$ half-bonds, and giving a spin of 7/2, from the seven unpaired electrons in the π*, σ*, δ, and δ* orbitals. In both molecules, the high-spin states are crucial to the M-M bonding: if the orbitals were populated in a low-spin manner, the π* and σ* orbitals would be filled, leaving only the weak-to-nonexistent stabilization of a half δ bond. For $Fe_2(DPhF)_3$ this would be a $(\delta)^1$

configuration and for $Co_2(DPhF)_3$ it would be $(\delta)^2(\delta^*)^1$.

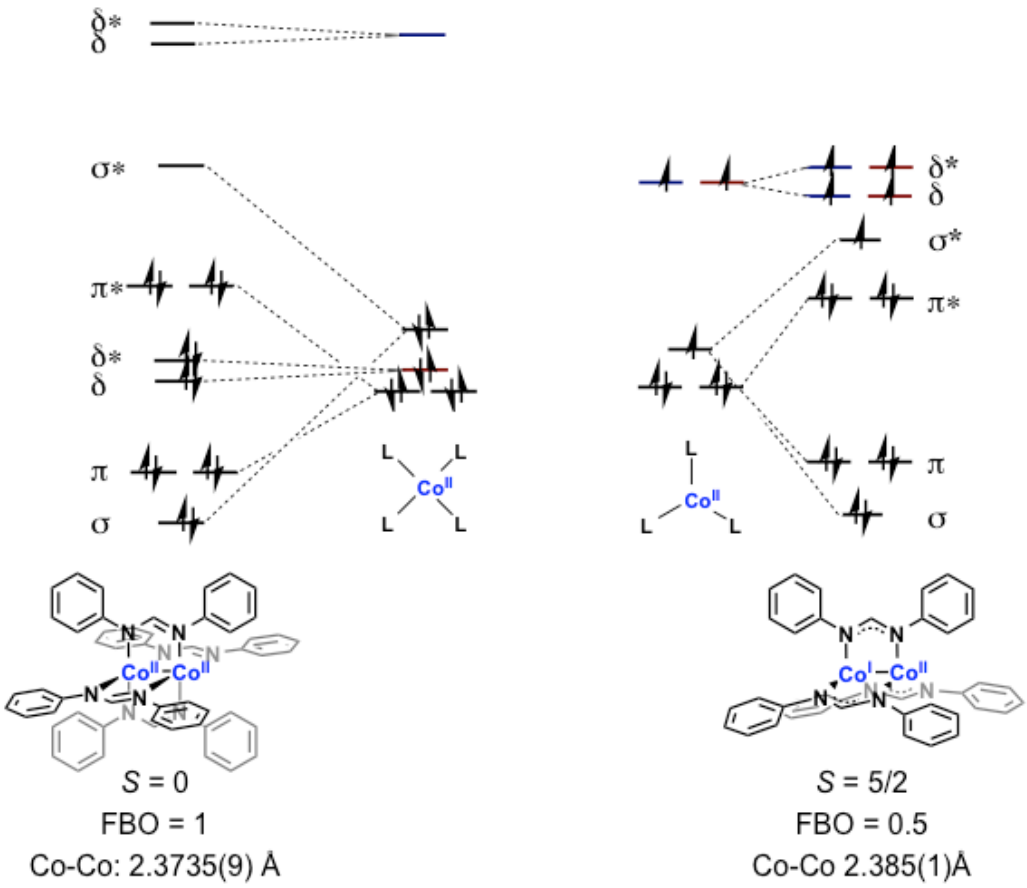

Figure 2.3. Molecular orbital diagram, with d-electron population, for $Co_2(DPhF)_4$ and $Co_2(DPhF)_3$ formed by combination of their monometallic fragments. Predicted spin states and formal bond orders (FBO) are given for each molecule.

2.2.3 Double-Exchange Formalism for M-M Interactions in the Trigonal Lanterns

It is also worth noting that there is a second model for the ferromagnetism of **1** and **2**. This is the formalism of double-exchange, as described in Section 1.2.8. The case of the dicobalt is easier to depict through this formalism. The system can be thought of as two high-spin Co^{II} atoms with an "extra" electron to be shared between them. If the two Co sites are equivalent, this electron has two half-filled, degenerate d_{z^2} orbitals it could

occupy, and, due to the short Co-Co distance, it should be free to delocalize between them. This delocalization is stabilizing. However, the electron is only able to freely delocalize when the Co atoms are coupled ferromagnetically. If their spins are instead aligned antiparallel, the "extra" electron cannot transfer between them without changing its spin, creating a barrier to delocalization and trapping the system as an antiferromagnetically coupled, mixed-valent $Co^{I}Co^{II}$ pair. This is shown on the left side of Figure 2.4.

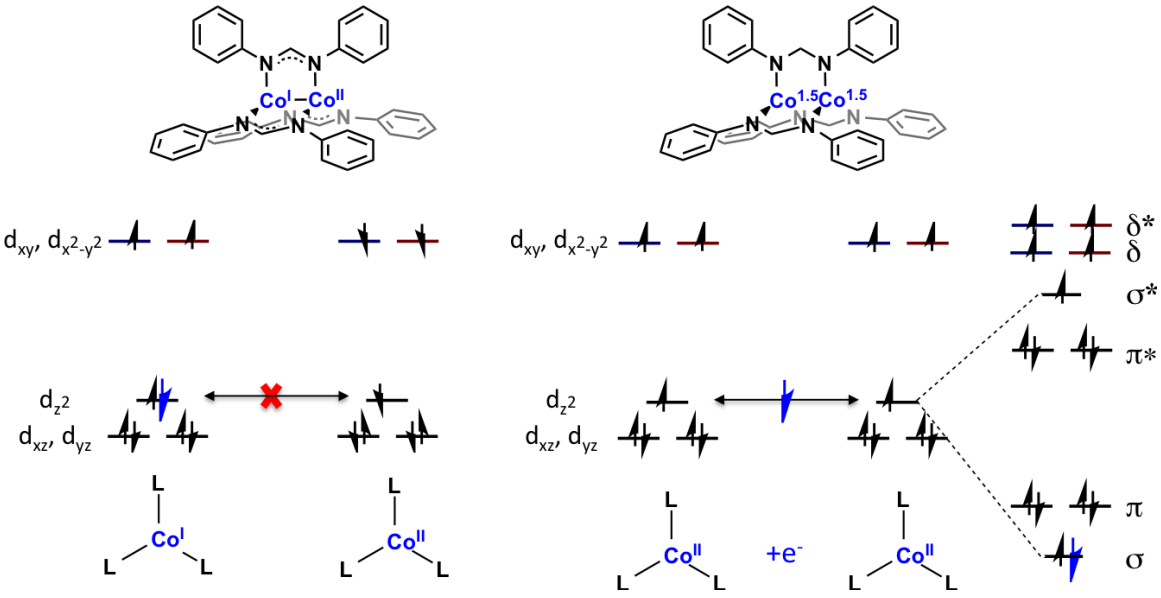

Figure 2.4. Double-exchange model of the electronic structure of $Co_2(DPhF)_3$. On the left side, the spins of the Co ions are mutually antiparallel; this creates a barrier to delocalization of the "extra" electron and a trapped $Co^{I}Co^{II}$ state. If the spins are parallel, the electron can freely delocalize, creating a resonance stabilization through the d_{z^2} orbitals analogous to a metal-metal σ-bond.

The difference in energy between the delocalized and "trapped" states is a resonance energy that differentiates the symmetric and antisymmetric spin combinations, favoring the symmetric (ferromagnetic) combination. If the system is otherwise disposed towards antiferromagnetic coupling in the absence of this effect, there is a competition,

giving spin-ladder energetics according to Eqn 2.1.

$$E^{s,a}(S) = -\tfrac{1}{2}JS(S+1) \pm B(S+1/2) \quad \text{(Eqn 2.1)}$$

Here, J is the usual coupling constant due to Heisenberg exchange, and B is the double-exchange parameter that quantifies the favorability of delocalization, as explained in section 1.2.8. The difference in energy due to the exchanging electron is therefore given by the difference between the symmetric and antisymmetric spin components (Eqn 2.2):

$$\Delta E^{s,a} = 2B(S+\tfrac{1}{2}) \quad \text{(Eqn 2.2)}$$

This is equal to $6B$ for the $S = 5/2$ $Co_2(DPhF)_3$. Thus the difference in energy under the double-exchange formalism is quantified by the spin and the parameter B, which is the resonance energy gained from delocalization.

In reality, the same factors that favor a large value of B – in other words, factors that favor delocalization, most notably good spatial and energetic overlap between the metal orbitals – will also favor strong metal-metal bonding. Thus, the only molecules known to display double-exchange-based ferromagnetic coupling also have relatively short metal-metal distances and could alternatively be described using a metal-metal bonding formalism. In fact, occasionally both conventions are used interchangeably, with the resonance energy $2B(S+\tfrac{1}{2})$ taken to be equal to the orbital splitting energy between the metal-metal bonding and antibonding combinations through which the electron is delocalizing.[11,12] This correspondence is valid because the resonance stabilization due to delocalization turns out to be equal to β, the resonance integral between the orbitals through which delocalization takes place.[13] This is the same resonance integral used in Hückel MO theory. The larger the overlap between the orbitals, the larger the value of β

and the greater the energy due to delocalization.

The pathway for delocalization of the "extra" or itinerant electron in $Co_2(DPhF)_3$ is between the d_{z^2} orbitals of the two Co atoms, and it is a stabilizing interaction involving the sharing of an electron across an in-phase combination of metal orbitals. It can therefore be thought of as analogous to a metal-metal bond, albeit one involving only one bonding electron delocalizing between two half-filled orbitals. This is functionally equivalent to the description of $Co_2(DPhF)_3$ as having a $(\sigma)^2(\sigma^*)^1$-based Co-Co half-bond. This analogy is made explicitly on the far right side of Figure 2.4.

It should also be stressed that delocalization of electrons between two high-spin metals will only very rarely lead to double-exchange. Obviously, most direct bonding or exchange-coupling interactions between metals lead to antiferromagnetic coupling. The double-exchange interaction occurs only when there are three electrons shared between a pair of orbitals, or, put another way, an "extra" electron to be delocalized between two half-filled orbitals. In the MO framework, this is equivalent to having a filled bonding and half-filled antibonding pair of orbitals, for a net half-bond. In cases where there are only two electrons to be distributed between two orbitals, the interaction is antiferromagnetic, since the electrons in this case must be of opposite spins to exchange. This is equivalent to a single bond in the MO framework, in which the electrons must be of opposite spin to pair in the lowest energy orbital.[13] In the other case of a half-bonding interaction, where there is only one electron to be shared between two orbitals, there should be no influence on the coupling, as there is no other electron with which it can exchange. Thus, the double-exchange model predicts strong ferromagnetic coupling only

in cases that could also be described as half-bonding interactions, with three electrons in two orbitals. Even in such cases, the double-exchange competes with other factors, such as superexchange and vibronic coupling, that can lead to antiferromagnetic interactions.[14]

A description of the Fe-Fe interactions in $Fe_2(DPhF)_3$ can be made using the double-exchange formalism. In this case there are three itinerant electrons rather than one, as drawn in Figure 2.5. The right half of Figure 2.5 again shows the analogy between the three exchanging electrons in the double-exchange model and the $(\sigma)^2(\sigma^*)^1$ and two $(\pi)^2(\pi^*)^1$ half-bonds in the MO formalism.

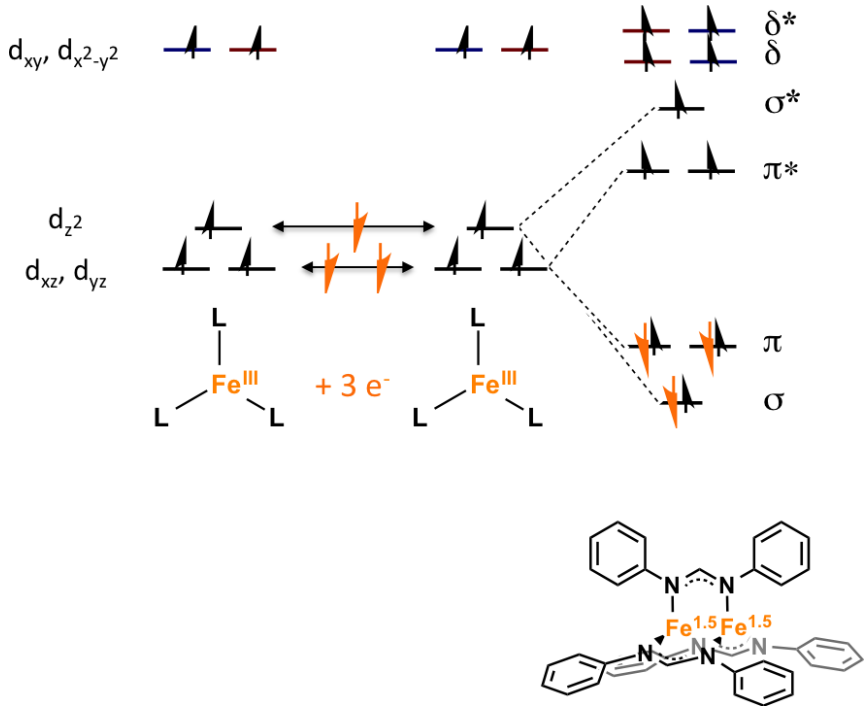

Figure 2.5. Double-exchange and molecular orbital models for ferromagnetic coupling in **1**. The three "itinerant" electrons in this case delocalize through the d_{z^2}, d_{xz}, and d_{yz} orbitals and are functionally equivalent to the β-spin electrons that form the σ and π half-bonding interactions in the MO formalism.

Whereas the single itinerant electron in $Co_2(DPhF)_3$ implies an exchange between formally one-electron mixed-valent Co^ICo^{II} resonance forms, the three itinerant

electrons in $Fe_2(DPhF)_3$ imply formally Fe^0Fe^{III} resonance forms, a three-electron form of mixed valency that appears physically dubious. However, the rapid delocalization inherent in double-exchange implies that these resonance structures are not really meaningful descriptions of the oxidation states in either complex; rather, the electrons are equally distributed over both centers, for fully delocalized $Fe^{1.5}Fe^{1.5}$ and $Co^{1.5}Co^{1.5}$ oxidation states.

Both the double-exchange and MO-based descriptions of the metal-metal interactions in **1** and **2** thus provide reasonable explanations of the high-spin states and the strong bonding. There is a direct correspondence between these explanations, in that they both attribute the spin states and bonding to the delocalization of β-spin electrons through the same overlapping metal orbitals. However, the formalisms are not equivalent. The exchange-coupling formalism treats the metal centers as inherently localized, whereas the MO formalism is inherently delocalized. Thus, the MO model can easily account for high, low, or intermediate spin states based on the orbital splitting energies. The exchange-coupling model, however, in general predicts only ferromagnetic or antiferromagnetic combinations of the localized atomic spins, or high- and low-spin states, based on the relative values of *B* and *J*. Intermediate-spin ground states can be predicted at very particular ratios of *J/B*, but these cases are exceptionally rare and should be distinguishable by the thermal accessibility of a number of low-lying spin states.[14,15] For this reason, metal-metal bonded complexes with intermediate spins and thermally dependent magnetic behavior have been the most obvious cases in which the exchange-coupling and MO formalisms do not agree. For instance, a variety of well-known

diruthenium(II,III) complexes have thermally-dependent equilibria between low-spin, S = 1/2 states and intermediate, S = 3/2 spins.[16] Two much more recently reported triiron compounds characterized by Betley *et al.*[17] have intermediate spins with similar thermally-dependent equilibria between S = 2 and S = 4 spins. These are easily explained as a result of electron populations within a delocalized molecular orbital manifold. They are not, however, easily rationalized in terms of ferromagnetic or antiferromagnetic coupling between localized spins on each metal, and attempts to model the temperature dependence of their magnetism using spin Hamiltonians based on this formalism have not been successful. On the other hand, the magnetic data were easily modeled using a simple Boltzmann distribution corresponding to a thermal equilibrium between electron populations within a delocalized molecular orbital manifold.[17] In this respect, the previous reports[2] suggesting that $Co_2(DPhF)_3$ has an intermediate S = 3/2 spin with a low-lying S = 5/2 excited state are intriguing, as this suggests a possible means to distinguish the two formalisms. Even if the assignment is reversed and S = 5/2 is the ground state, as has alternately been proposed,[4] the temperature dependence of its magnetism should be quite informative.

2.2.4 Reinvestigation of Diiron and Dicobalt Trigonal Lanterns

In addition to the magnetism of these complexes, there are details regarding the bonding and electronic structure in the trigonal lanterns that were either not addressed in the early studies or that rely on unproven assumptions. One perplexing issue, for instance, is why the Co-Co distances in $Co_2(DPhF)_4$ and $Co_2(DPhF)_3$ are essentially identical, despite the

predicted bond order being twice as strong for the former than the latter. It is unlikely to be a steric effect, since the ligands in the two molecules are the same, and since the $DPhF^-$ anion has been shown to support Co-Co distances of up to 2.885(1) Å in similar geometries.[4] Clearly, there are nuances in the electronic structure that are not captured with simple predictions of formal bond order. Multiconfigurational calculations that integrate other excited-state configurations into the wavefunction would provide better insight into the bonding interaction. In addition, the electronic structure descriptions from both MO and double-exchange formalisms assume that the bimetallic cores are delocalized, $M^{1.5}M^{1.5}$, rather than mixed-valent $M^{I}M^{II}$, yet this has not been demonstrated experimentally.

More significantly, the generality of this high-spin bonding motif is unproven. In other words, it is not clear whether a trigonal arrangement of weak-field ligands will consistently lead to a MO framework like that in Figure 2.3, or if it is specific only to these diiron and dicobalt species. The simplicity of the MO picture suggests that it ought to be generally extensible to other metals, electron counts, and donor sets. However, the field of M-M bonding between first-row metals is full of edge cases and deviations from the rule. For instance, although the electronic structure of paddlewheel complexes is well-conserved for second- and third-row metals, this appears to hold for only a few of the known first-row paddlewheel compounds. The tetragonal dicobalt species, $Co_2(DPhF)_4$, for instance, conforms to the typical bonding pattern, but its diiron analogue, $Fe_2(DPhF)_4$, does not. The electronic structure of this molecule, which has a highly distorted structure, a longer Fe-Fe distance than $Fe_2(DPhF)_3$, and a high-spin, $S = 4$, ground state, was not

understood until a recent theoretical reinvestigation by Berry and Timmer.[12] In this study, the distortion was attributed to a Jahn-Teller effect, and the high-spin state was found to be the result of double-exchange from a pair of $(\sigma)^2(\sigma)^1$ and $(\delta)^2(\delta)^1$ half-bonds. In order to rationally design catalysts or build molecular magnets based on first-row bimetallics, it will be necessary to have a more complete understanding of their electronic structures and be able to predict such anomalies.

Even within the trigonal lantern framework, the known dichromium(I,II) and (I,I) tris-amidinate analogue of **1** and **2** are low-spin,[18] as described in Section 1.2.4. This suggests that the high-spin M-M bonding motif is not applicable for complexes with earlier metals and lower electron counts. Whether it can be extended to other pairs of late metals, or to heterobimetallic complexes, is a major focus of work in our laboratory and is the subject of Chapter 3. Before we sought to extend this motif to new metal combinations, however, we decided to reinvestigate the previously-reported **1** and **2**. We were interested in characterizing their electronic properties and their reactivity towards small molecules. This chapter describes our work towards this end. Two new synthetic routes to these complexes are described, as well as their characterization by a variety of spectroscopic, physical, and theoretical techniques. The theoretical and physical measurements described in this chapter rely heavily on collaborations with the groups of Prof. Laura Gagliardi at the University of Minnesota for multiconfigurational calculations and of Dr. Eckhard Bill at the Max Planck Institute for Chemical Energy Conversion for advanced magnetic measurements. Finally, a brief, but informative, survey of their reactivity towards small molecules is also discussed.

2.3 Results and Discussion

2.3.1 Synthesis of the diiron trigonal lantern, $Fe_2(DPhF)_3$

Synthetic access to diiron structures using amidinate ligands has proven to be a more difficult and complicated endeavor than would be ordinarily assumed, especially compared to bimetallic amidinates with other metals. One challenge is simply to control the chemoselectivity of the reaction, as a wide variety of possible structures can be produced. This is illustrated in Figure 2.6, which shows the number of disparate structures that can be synthesized with amidinate ligands using only slightly different synthetic approaches. In these reactions, the precise choice of starting materials and reaction conditions is crucial to the outcome. The products in Figure 2.6 were all discovered in attempts to produce the paddlewheel complex, $Fe_2(DPhF)_4$. The simplest conceivable reaction, of deprotonated amidinate with $FeCl_2$, instead produces the monometallic iron(III) tris-amidinate complex, $Fe(DPhF)_3$, and its reduced anion, $Li(THF)_4$•$Fe(DPhF)_3$ (Figure 2.6a).[19] To prevent the formation of this product, the neutral iron dichloride bis-amidine adduct, $FeCl_2(HDPhF)_2$, was used as a precursor and deprotonated with two equivalents of methyllithium per Fe. When the deprotonation was performed in Et_2O at 0° C, this resulted in an orange precipitate, which, upon redissolving in THF, gave the desired yellow paddlewheel complex, $Fe_2(DPhF)_4$ (Figure 2.6b).[20] Oddly, if the same reaction is conducted at -78° C in toluene, a highly distorted structure is obtained in which only two of the amidinate ligands bridge the iron centers, while the other two chelate in a κ^2 fashion to a single iron center (Figure 2.6c).[21] While this is an unusual geometry for amidinate-bridged systems, it is similar to carboxylate-

bridged diiron complexes studied as models for the active sites of ribonucleotide reductase, soluble methane monooxygenase, and other diiron enzymes, and these "windmill" structures are known to interconvert with the paddlewheel forms based on a variety of factors.[22-26]

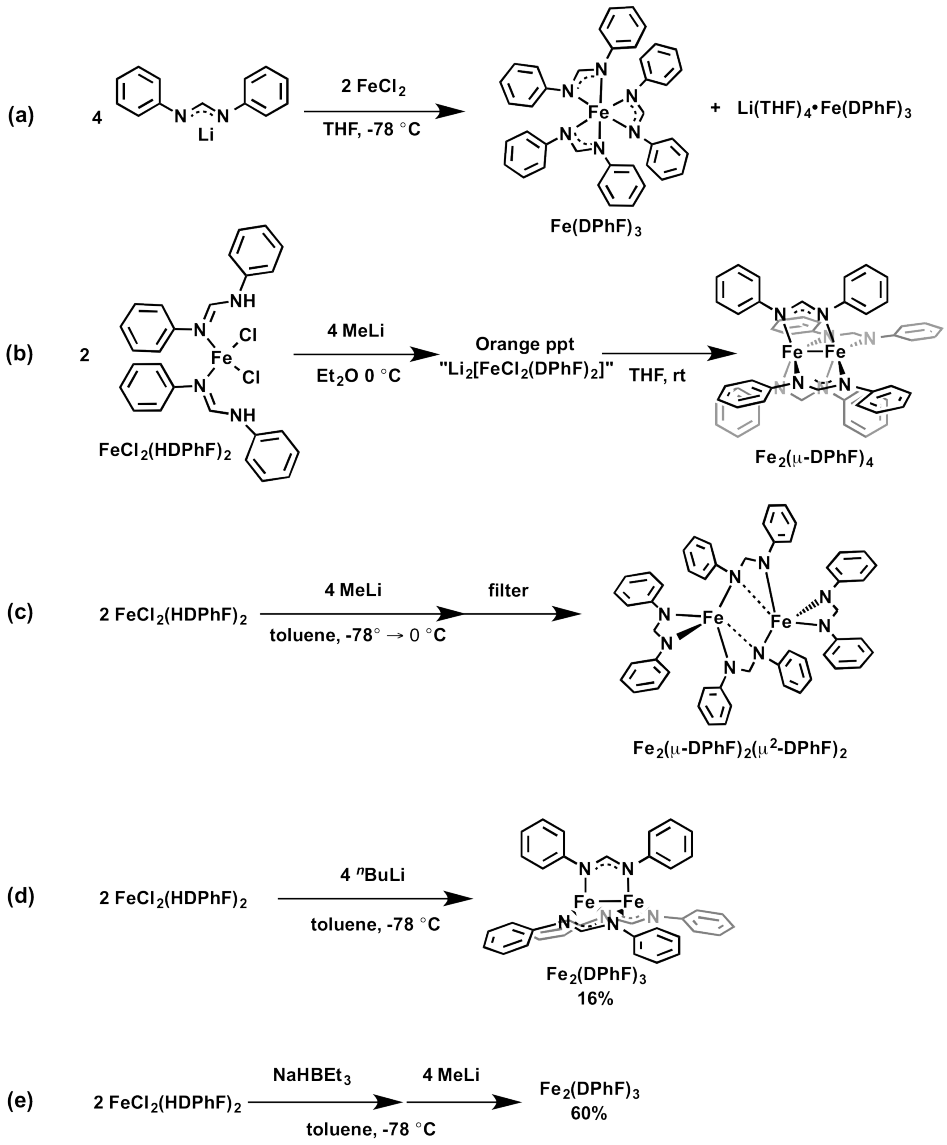

Figure 2.6. Synthetic routes to iron-formamidinate complexes reported in the literature.[1,3,19-21]

More remarkably, the diiron trigonal lantern $Fe_2(DPhF)_3$, **1**, was accidentally discovered early in the attempted synthesis of the paddlewheel complex, when butyllithium was used instead of methyllithium to deprotonate the ligands (Figure 2.6d).[1] The product was isolated in ~16% yield after crystallization. The unusual reaction, which involves the loss of one bridging ligand and reduction of the diiron system from a formally Fe_2^{4+} to a formally Fe_2^{3+} core, was rationalized as the result of coordination of butyllithium to one of the iron centers, followed by β-hydride elimination, and subsequent deprotonation of one of the neutral amidines by the hydride to give H_2. With this insight, a later synthesis for the tri-bridged complex (Figure 2.6e) was devised using redox-innocent methyllithium and a discrete hydride source, $NaHBEt_3$, giving a higher (~60%) reported yield.[3] The presumed balanced reaction is shown in Eqn (1).

$$2FeCl_2(HDPhF)_2 + 4MeLi + NaHBEt_3 \rightarrow Fe_2(DPhF)_3 + 4MeH + 0.5H_2 + 4LiCl + NaDPhF + BEt_3$$

Eqn (1)

In our attempts to resynthesize **1**, we have found that this latter route successfully produces **1**, but in low (5-10%) yield, and only after extensive purification. $Fe_2(DPhF)_3$ appears to be only a minor component of the crude reaction product by ^1H NMR spectroscopy; the rest is a mixture of diamagnetic borane and paramagnetic, oxidized iron-containing species (*vide infra*). Interestingly, in small-scale reactions, the earlier reported route in Figure 2.6d, using four equivalents of butyllithium and no borohydride, proved much more effective. The crude products from these reactions show substantially more $Fe_2(DPhF)_3$ and can be easily purified by filtering, washing with Et_2O, and crystallizing. Crystalline yields are typically 25-50 mg after isolation (30-35%), higher

than the 16% described in the initial report, which based on a 40 mg isolated yield.[1] Unfortunately, this reaction does not scale reliably to the preparation of larger quantities of **1**; on scales of 100-500 mg, the reaction does not appear to produce **1** at all: none is observed in the crude material by ^{1}H NMR, and no **1** is obtained from crystallization.

Surprisingly, we have found that the the most reliable method for preparation of **1** has been the reaction of 2 equivalents of $FeCl_2(HDPhF)_2$ with three equivalents of butyllithium; this is the same reaction as in Figure 2.6d but simply using less than stoichiometric base. Surprisingly, despite the substoichiometric amount of base, this reaction routinely produces **1** in high purity and comparable yield (35%) to the original literature method. This result is particularly surprising when it is noted that even the original four equivalents of butyllithium are insufficient for a balanced stoichiometry. As shown in Eqn (2), five equivalents of base are needed for a balanced reaction: four to deprotonate the ligands and an additional equivalent to act a hydride donor. Nevertheless, the reaction using three equivalents of BuLi is actually more effective than using four or five, since it is more reliable and can be scaled up: the products remain pure and can be obtained in the same 35% yield when the reaction is scaled up to yield 175-350 mg of crystalline product.

$$2\ FeCl_2(HDPhF)_2 + 5\ BuLi \rightarrow Fe_2(DPhF)_3 + 4\ BuH + 0.5\ H_2 + 4\ LiCl + LiDPhF + Butene$$

Eqn (2)

The reason that this unusual substoichiometric amount of BuLi is effective remains unclear; with such a complicated series of elementary steps required to form the bimetallic from these simple precursors, mechanistic proposals are necessarily speculative. However, a possible partial explanation is suggested by the observation

that, upon filtering the toluene solution of the crude reaction mixture, an orange precipitate is removed, which is not observed when larger amounts of BuLi are used. Moreover, the orange precipitate can be isolated following filtration and dissolved in THF to cleanly form the yellow tetragonal diiron complex, $Fe_2(\mu\text{-}DPhF)_4$. Following this observation, some of the failed, larger-scale attempts to form **1** using 4 equiv. BuLi were re-examined and, indeed, in several cases showed significant amounts of $Fe_2(\mu\text{-}DPhF)_4$ as a contaminant that had previously been unidentified.

Thus, the effectiveness of the substoichiometric reaction appears to result from its precipitation of an orange byproduct that, with larger amounts of BuLi, appears to go on to form soluble $Fe_2(\mu\text{-}DPhF)_4$ in competition with $Fe_2(DPhF)_3$. This orange byproduct appears to be the same species reported as an intermediate in the synthesis of the diiron paddlewheel, $Fe_2(\mu\text{-}DPhF)_4$;[20,21] in that case, the orange precipitate crashes out of Et_2O upon reaction of $FeCl_2(HDPhF)_2$ with methyllithium and goes on to form $Fe_2(\mu\text{-}DPhF)_4$ upon redissolution in THF (Figure 2.6b). This highly paramagnetic orange species was suggested to be deprotonated $[FeCl_2(DPhF)_2]^{2-}$, based on its insolubility in Et_2O and toluene and its rapid dissolution in THF to form $Fe_2(\mu\text{-}DPhF)_4$. When this byproduct is removed, the crystallization of $Fe_2(DPhF)_3$ is greatly facilitated, allowing bulk crystallization of pure material from the crude reaction mixtures. Pure $Fe_2(DPhF)_3$ is bright yellow, unlike the light brown products described in previous reports.[1,27] Contamination with oxidized species can result in a brown or burgundy color; these oxidized species probably explain the complications in previous attempts to obtain analytical data on this compound. $Fe_2(DPhF)_3$ is extremely sensitive to oxygen and protic

or halogenated solvents, and a great deal of precaution must be taken to prevent its oxidation. However, under a well-maintained inert atmosphere, this compound is thermally stable and can be stored for extended periods in the solid state.

2.3.2 Resynthesis of $Co_2(DPhF)_3$, ***2***

The reported synthesis of the dicobalt trigonal lantern, $Co_2(DPhF)_3$, is essentially identical to the synthesis of its iron analogue, using methyllithium and sodium triethylborohydride.[4] Unfortunately, in our attempts to resynthesize this compound, this route has proven unreliable: although we have been able to observe $Co_2(DPhF)_3$ as the major product in these reactions, we have been unable to isolate it in adequate purity from the initial product mixture. Moreover, the alternative routes that proved effective for $Fe_2(DPhF)_3$, involving reaction with only butyllithium and no borohydride, are entirely unsuccessful when applied to the dicobalt synthesis. Instead, a new strategy was developed, which produces $Co_2(DPhF)_3$ from the direct reduction of its tetragonal dicobalt(II,II) analogue, $Co_2(DPhF)_4$ (Figure 2.7).

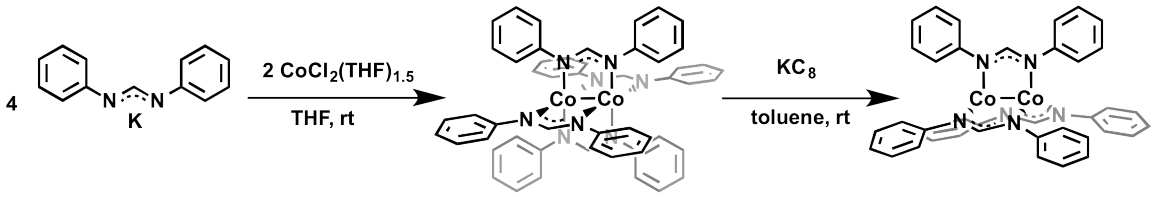

Figure 2.7. New synthetic procedure for **2**.

The synthesis of $Co_2(DPhF)_4$ has previously been reported:[7] the literature synthesis involves deprotonation of the cobalt dichloride bis-amidine compound, $CoCl_2(HDPhF)_2$, with methyllithium, analogous to the synthesis of the diiron paddlewheel complex, in Figure 2.6b. We have found that it can instead be formed from

reaction of $CoCl_2(THF)_{1.5}$ with the anionic formamidinate potassium salt, K(THF)DPhF. This direct metallation route was traditionally avoided because the lithium formamidinate salt, LiDPhF, reacts with $CoCl_2$ to form the monometallic cobalt(III) tris-amidinate, $Co(DPhF)_3$, as reported for the iron complex (Figure 2.6a).[5,7,28] However, we find that this reaction gives the bimetallic paddlewheel complex in good yield when the potassium salt is used. This direct route is more economical and more convenient, and the ^{1}H NMR spectrum of diamagnetic $Co_2(DPhF)_4$ is identical regardless of which route is used. Reduction of $Co_2(DPhF)_4$ with potassium graphite, KC_8, results in a color change from yellow to a red-brown solution. Prolonged stirring of the reaction mixture results in decomposition, indicated by a blue color change. Thus the solution must be filtered within approximately one hour and immediately dried or concentrated and set to crystallize at low temperature. However, with this precaution, the crude product is very pure, as assessed by combustion analysis and by ^{1}H NMR, which shows a highly paramagnetically-shifted spectrum identical to the species produced by the literature synthesis of $Co_2(DPhF)_3$.

This reaction is a novel approach to the synthesis of trigonal lantern species. The amidinate groups in $Co_2(DPhF)_4$ have previously been shown to be quite labile, as demonstrated by their susceptibility towards abstraction reactions. Specifically, the salt metathesis of $Co_2(DPhF)_4$ with $AgPF_6$ has been shown to proceed, with presumed loss of 0.5 equivalents of $[Ag(DPhF)]_2$, to give the trigonal dicobalt(II,II) salt, $[Co_2(DPhF)_3(CH_3CN)_2]PF_6$.[4] This complex is an oxidized and axially coordinated analogue of $Co_2(DPhF)_3$, but its Co···Co separation of 2.885(1) Å is too long to have any

significant Co-Co bonding. However, the loss of a ligand upon *reduction*, as observed here, had not previously been observed. In fact, very different electrochemical behavior has been reported for the benzamidinate analogue, $Co_2(DPhBz)_4$, which differs only in the substitution of Ph for H in the bridgehead position of the amidinate group (DPhBz = N,N'-dphenylbenzamidinate).

$Co_2(DPhBz)_4$ reportedly shows a quasi-reversible reduction at -1.64 V (vs. SCE) in CH_2Cl_2; the EPR spectrum of the product, formed by controlled potential electrolysis of $Co_2(DPhBz)_4$, showed an axial signal corresponding to an S = ½ system, presumed to represent anionic $[Co_2(DPhBz)_4]^-$.[29] As discussed below, this is inconsistent with the EPR signatures we observe for $Co_2(DPhF)_3$, which we form by reduction of $Co_2(DPhF)_4$ in toluene. The most obvious explanation for this discrepancy is the difference in solvent. It is possible that the more polar CH_2Cl_2 solvent stabilizes the reduced, anionic paddlewheel compound; the insolubility of K(DPhF) in toluene, on the other hand, could drive the formation of the neutral trigonal species. We have also observed that $Co_2(DPhF)_3$ is unstable in CH_2Cl_2, and it is also possible that the previously-reported EPR signal results from one of its as-yet uncharacterized decomposition products, rather than the anionic paddlewheel compound. As with its diiron analogue, $Co_2(DPhF)_3$ is extremely sensitive to oxygen, moisture, and halogenated solvents, and samples used for spectroscopic and magnetic studies were freshly crystallized and harvested just prior to each experiment.

*2.3.3 Solid-State Structures of **1** and **2***

The solid-state structures of both $Fe_2(DPhF)_3$, **1**, and $Co_2(DPhF)_3$, **2**, were reported previously.[1,2] The structure of **1** is shown in Figure 2.1. Aside from their extremely short metal-metal separations, the most interesting structural features of these complexes are the arrangements of the three amidinate groups around the metal-metal core. In both **1** and **2**, these ligands bridge the two metals with roughly three-fold symmetry around the metal-metal axis. In **1**, which crystallizes in the space group C2/c, there is a C_2 rotation axis that bisects the molecule perpendicular to the Fe-Fe axis, making the two iron atoms equivalent by symmetry. In the dicobalt complex, which crystallizes in P-1, there is no such crystallographically-imposed symmetry; nevertheless, the molecular structure of **2** is fairly symmetric: the structure has only slight deviations from C_3 symmetry along the Co-Co axis, with N-Co-N angles close to 120°. On the other hand, in the diiron complex, **1**, the molecule is considerably distorted from three-fold symmetry about the Fe-Fe axis, with N-Fe-N angles varying as much as 22°, from narrow angles of 111.08(9)° and 116.18(9)° to a much larger angle of 132.6(1)°. Since this distortion could be an indication of an electronic effect, it was the subject of close scrutiny by Cotton *et al.*, who performed calculations showing that the potential energy surface for changing these N-M-N angles is very shallow. Thus, they suggested, there is little to no electronic basis for the distortion from three-fold symmetry, and it was attributed to crystal packing effects.

In resynthesizing **1**, we obtained a new solid-state structure of $Fe_2(DPhF)_3$, which contains a different crystal packing arrangement due to the incorporation of ½ C_6H_6 per

$Fe_2(DPhF)_3$. In addition, it crystallizes in the triclinic P-1 space group, causing a loss of the molecular C_2 symmetry axis from the original structure. Despite these differences, most features of the two structures are nearly identical. Notably, the metal-metal bond distance of 2.230(1) Å is identical within error to the previous value. The only significant difference between the two structures is in the smaller range of N-Fe-N angles, which in the new structure vary only 12°, from 113.7 to 125.7°, in line with the angles observed in $Co_2(DPhF)_3$. These results support the idea that the distortions from C_3 symmetry are the result of crystal packing forces and do not have an electronic basis. A comparison of important structural parameters for all three compounds is given in Table 2.1.

Table 2.1. Selected bond lengths (Å) and angles (°) for **1** and **2**[2,4,30]

Structure	$Fe_2(DPhF)_3$	$Fe_2(DPhF)_3$•½(C_6H_6)	$Co_2(DPhF)_3$•(C_7H_8)
M−M, Å	2.231(3)	2.230(1)	2.385(1)
M−N, Å	2.033(3)	2.035(4)	1.932(5)
	2.033(3)	2.024(3)	1.955(5)
	2.025(3)	2.006(4)	1.959(5)
	2.025(3)	2.006(4)	1.957(5)
	2.018(3)	1.989(4)	1.978(5)
	2.018(3)	1.988(3)	1.983(5)
N−M−N, °	132.7(1)	125.7(2)	125.1(2)
	132.7(1)	125.2(2)	119.2(2)
	116.2(1)	121.0(2)	115.6(2)
	116.2(1)	117.3(2)	120.1(2)
	111.1(1)	116.8(2)	114.8(2)
	111.1(1)	113.7(2)	124.7(2)
N−M−M, °	92.3(1)	91.5(1)	88.19(2)
	92.3(1)	90.7(1)	88.24(2)
	90.1(1)	91.2 (1)	87.07(2)
	90.1(1)	91.3(1)	90.06(2)
	89.8(1)	92.2(1)	90.32(2)
	89.8(1)	90.0(1)	91.30(2)
N−C−N, °	122.59	122.2(4)	121.6(6)
	122.59	122.2(4)	122.7(6)
	121.27	122.1(4)	122.4(6)

*2.3.4 NMR Spectra of **1** and **2***

The trigonal symmetry of **1** and **2** is more clearly visible in their solution ^{1}H NMR spectra, which were not previously reported by Cotton *et al*. The spectra of both compounds are consistent with solution-averaged D_{3h} symmetry (Figures 2.8 and 2.9, respectively). In addition, the spectra for both compounds are highly paramagnetically shifted and broadened. In **1**, the broadening is much more pronounced, and only three peaks are visible, at 12.6 ppm, -18.6 ppm, and an extremely broad peak at approximately -40 ppm (δ, *vs.* TMS). Integration of these signals gives a 2:1:2 ratio, respectively, suggesting their identity as the *meta*, *ortho*, and *para* protons on the phenyl rings. The signal for the bridgehead-*H* of the formamidinate groups is presumably broadened and/or shifted beyond visibility. Spectra taken in THF-d_8 and benzene-d_6 are essentially identical.

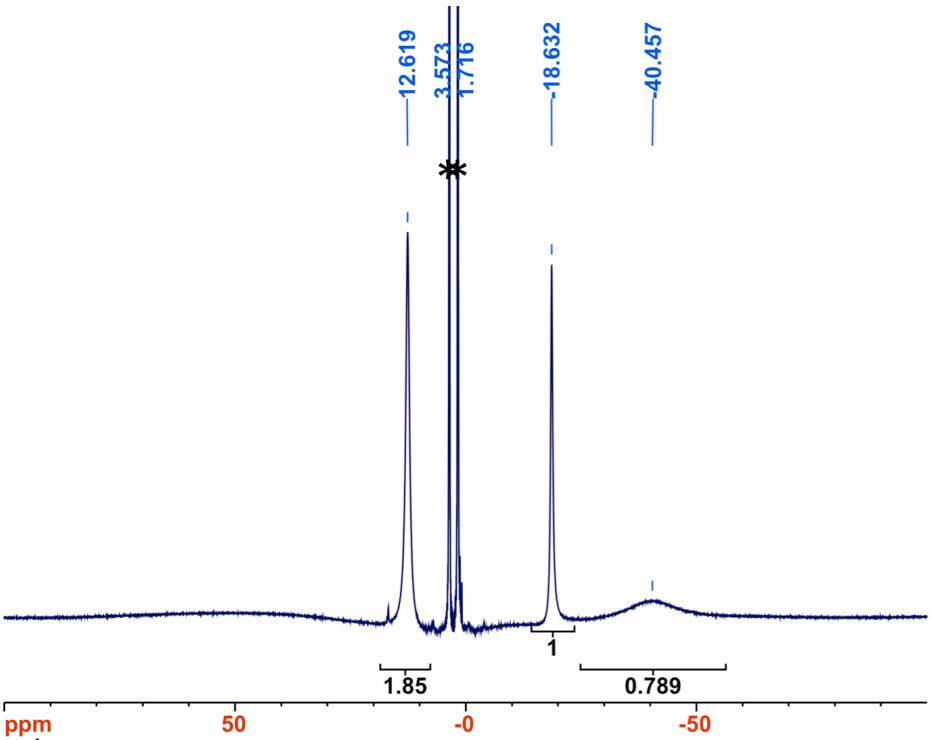

Figure 2.8. ^{1}H NMR spectrum of **1** (500 MHz, THF-d_8). The residual solvent peaks are marked with an asterisk.

The peaks in the spectrum of **2** are significantly sharper but still highly paramagnetically shifted. Similar peaks for the phenyl substituents are visible at 13.0, -26.2, and -50.2 ppm; in addition, the peak corresponding to the bridgehead-*H* is visible at a much more downfield shift, 175.1 ppm (C_6D_6, δ *vs*. TMS). Overall, the NMR spectra of **1** and **2** are consistent with their having trigonally symmetric, highly paramagnetic cores in solution.

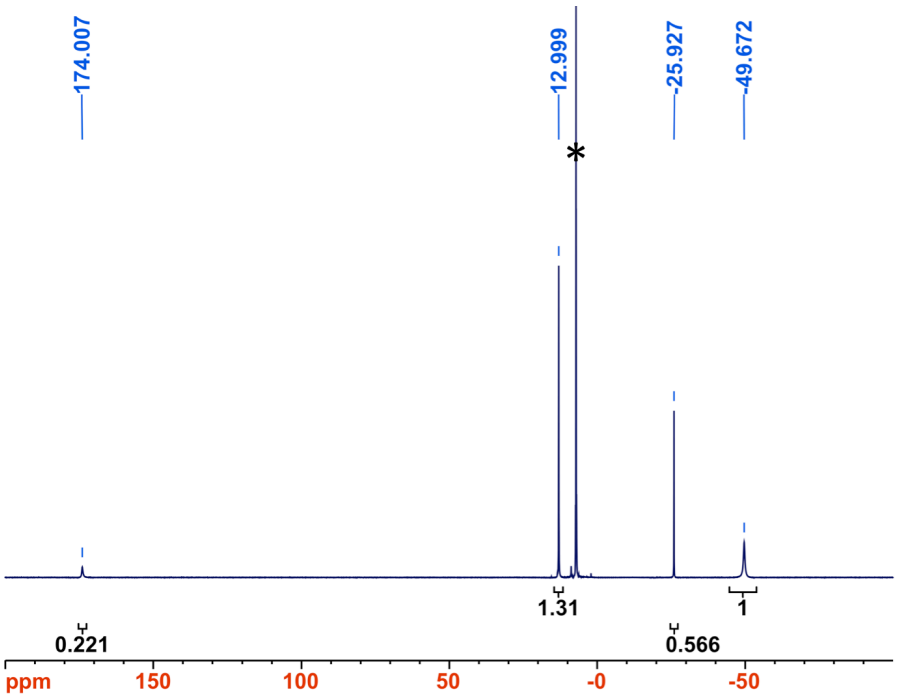

Figure 2.9. ^{1}H NMR spectrum of **2** (500 MHz, C_6D_6). The residual solvent peak is marked with an asterisk.

2.3.5 UV-Vis-NIR Spectra of $Fe_2(DPhF)_3$:

As with the NMR spectroscopy, the electronic absorption spectra of **1** and **2** were not reported by Cotton *et al.* The electronic absorption spectrum of **1** is dominated by an intense UV absorption at 280 nm (ε = 63,000 $M^{-1}cm^{-1}$) with a strong shoulder at approximately 350 nm (ε = 13,000 $M^{-1}cm^{-1}$), accounting for the bright yellow

character of the molecule (Figure 2.10a). Given the intensity of these features and the donor properties of the amidinate ligands, these are likely either ligand-based $\pi \rightarrow \pi^*$ transitions or ligand-to-metal charge-transfer bands. In addition to these features, several lower energy, very low intensity absorptions are visible in the Vis-NIR region, between 650 and 1250 nm. The extinction coefficients of these transitions are orders of magnitude smaller than the UV absorptions and are shown on a separate scale, in Figure 2.10b.

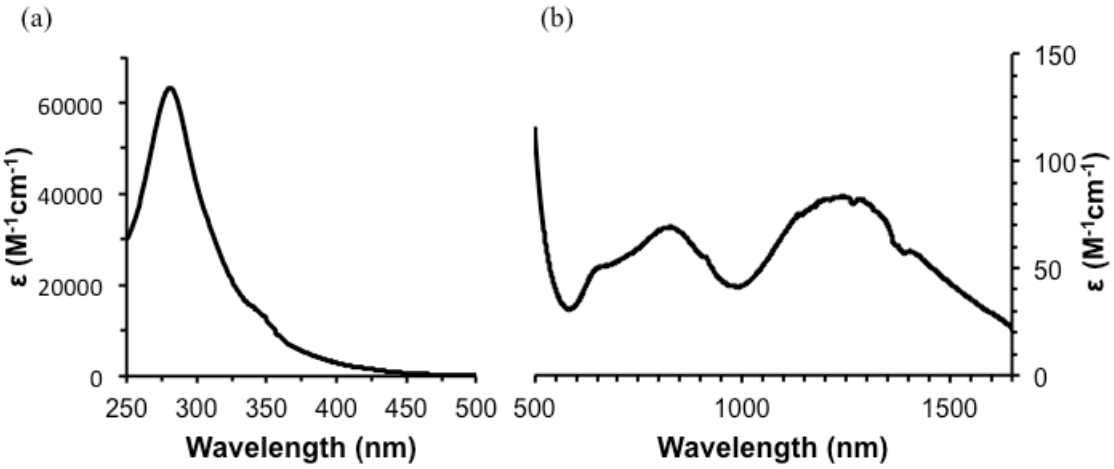

Figure 2.10. UV-Vis-NIR absorption spectra of **1** in THF at two different concentrations, showing UV-Visible region (7.1 μM, a) and Visible-Near-IR region (6.7 mM, b)

The transitions in the visible-NIR region are in the energy range expected for transitions between M-M-based molecular orbitals. There are three major features visible in this range, at 650 nm (ε = 50 $M^{-1}cm^{-1}$), 800 nm (ε = 70 $M^{-1}cm^{-1}$), and 1,250 nm (ε = 80 $M^{-1}cm^{-1}$), and a small shoulder at 700 nm (ε = 50 $M^{-1}cm^{-1}$). The qualitative MO diagram proposed by Cotton *et al.* for this complex[9] suggests that several metal-based transitions are possible within the diiron core. Assuming idealized D_{3h} symmetry, the selection rules for spin- and electric-dipole-allowed transitions are shown, with this qualitative MO picture, in Figure 2.11.

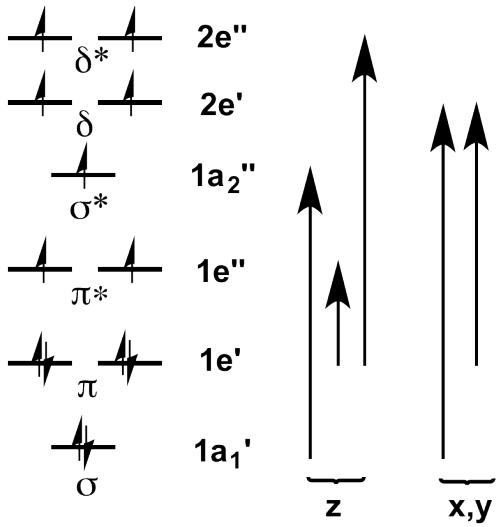

Figure 2.11. The allowed electronic transitions in **1** based on D_{3h} selection rules.

Within this high-spin manifold, transitions are spin-allowed only from the doubly occupied bonding orbitals to the singly occupied antibonding orbitals. Nevertheless, numerous such transitions are possible, from the σ to both σ* and δ orbitals, and from the π to π*, δ, and δ* orbitals. Given that these transitions are fully allowed, the extremely low extinction coefficients seen in $Fe_2(DPhF)_3$ are surprising. One possible explanation for the discrepancy is the Franck-Condon principle: since the transitions are all from Fe-Fe bonding to antibonding orbitals, the Fe-Fe distances are expected to differ significantly between the ground and excited states, which could diminish the overlap of vibrational wavefunctions necessary for the electronic transitions and modulate the intensity of the absorptions.

2.3.6 Electronic absorption spectra of $Co_2(DPhF)_3$

Despite the quite different color of red-brown **2** from bright-yellow **1**, the two bimetallics have qualitatively similar absorption spectra. As with **1**, the spectrum of **2** is

dominated by an intense feature in the UV region (λ_{max} 284 nm, ε 62,000 $M^{-1}cm^{-1}$) nearly identical to that in **1** (Figure 2.12a). The insensitivity of this feature to the identity of the metal strongly suggests that it is an intra-ligand π→π* transition, rather than a charge-transfer band. The shoulder present at 350 nm in **1** is absent in **2**, while other ill-defined shoulders are present at higher and lower energies. These features may be charge-transfer derived, but they are not resolved enough to merit discussion.

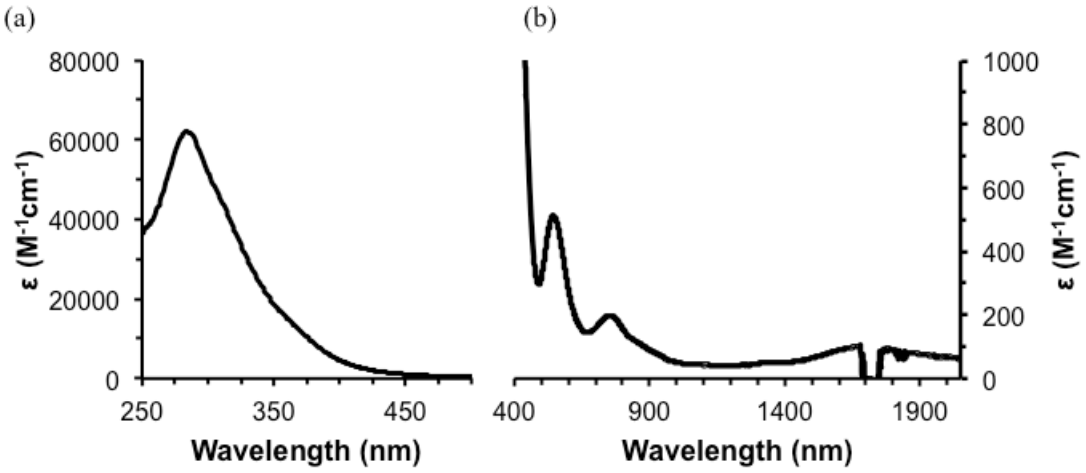

Figure 2.12. UV-Vis-NIR absorption spectra of **2** in THF at two different concentrations, showing UV-Visible region (33 μM, a) and Visible-Near-IR region (4 mM, b)

As with **1**, the Vis-NIR region shows some lower-intensity absorptions within the energy range relevant to M-M bonding (Figure 2.12b). Two are well-defined, at 545 nm (ε = 530 $M^{-1}cm^{-1}$) and 752 nm (ε = 200 $M^{-1}cm^{-1}$), while a third absorption far into the near-infrared is obscured: interference with a strong background absorption between 1650-1750 nm causes imperfect subtraction and prevents accurate measurement of the peak position and intensity; an approximate extrapolation suggests a λ_{max} ~ 1700 nm and ε ~ 125 $M^{-1}cm^{-1}$. While this spectrum is qualitatively similar to that of **1**, there are some

quantitative differences. The extinction coefficients of these transitions, ranging from ~ 500 to ~100 $M^{-1}cm^{-1}$, are larger than in **1** and in the range of spin-allowed but Laporte-forbidden d-d transitions within conventional mononuclear transition metal complexes. They are still significantly lower than would be ordinarily be expected for spin- and symmetry-allowed transitions between M-M bonding orbitals, however. As with **1**, the discrepancy between the M-M bond distances in the ground and excited states may partly explain this, through the Franck-Condon principle.

More notably, the lowest energy feature in **2** is significantly red-shifted into the near-IR region, compared to the analogous feature in **1**, while the higher-energy absorption at 545 nm is blue-shifted by ~3000 cm^{-1} relative to the highest-energy metal-based transition in **1**. Assuming that these features have their origins in transitions between M-M bonding orbitals, the red-shift in the near-IR absorption would be consistent with a change in the lowest-energy allowed transition from $\pi \rightarrow \pi^*$ to $\pi^* \rightarrow \delta$, as the π^* orbitals in **2** are expected to be filled. The apparent higher-energy shift for the peak at 545 nm is more mysterious, as there is no obvious reason to expect a *larger* energy gap between two sets of orbitals in **2** than **1**. One possible explanation would be that this peak does not represent a blue shift from one of the lower-energy peaks in **1**, but rather a red shift from a transition at even higher energy that could be obscured by the trailing edge of the strong UV absorption. A possible candidate for this transition is the $\sigma \rightarrow \sigma^*$ excitation, as this transition should be fully allowed, should have the largest orbital splitting in both complexes, and should show a pronounced decrease in energy from the extremely short Fe-Fe distance in **1** to the significantly longer Co-Co distance in **2**.

Admittedly, however, these assignments are purely speculative. A more meaningful discussion of the electronic transitions will be made in the context of the electronic structure calculations, discussed later in the chapter.

*2.3.7 Magnetic Behavior of **1***

As mentioned in the introduction, the highly paramagnetic electronic configurations of **1** and **2** are particularly noteworthy, given the tendency of most metal-metal bonding interactions to couple antiferromagnetically. Room temperature magnetic susceptibility studies of **1** were previously reported, with a μ value of 7.81 B.M., corresponding to a spin of 7/2. Low-temperature EPR measurements also indicated an S = 7/2 spin for this spectrum in toluene glass at 10 K.[3] We obtain an essentially identical spectrum for **1** in toluene at 2.5 K, shown in Figure 2.13. The spectrum is consistent with the axial symmetry of **1** with $g_x = g_y >> g_z$, and confirms the octet ground state. The effective *g*-values of 7.93 and 1.98 are nearly identical to the expected values of 8 for the *x*,*y* component and 2 for the *z* component of the $m_s = \pm ½$ transition in an ideal, axial $S = 7/2$ system ($g_{Fe} = 2$, $E/D = 0$). Moreover, the fact that signals are observed only between this $m_s = \pm ½$ Kramers doublet suggests a large zero-field splitting term ($D >> h\nu$). Under this condition, the shape of the spectrum is independent of the value of the zero-field splitting. Due to the straightforward nature of this spectrum and its exact match with the previously reported spectrum, we have not attempted to extract parameters by fitting the data.

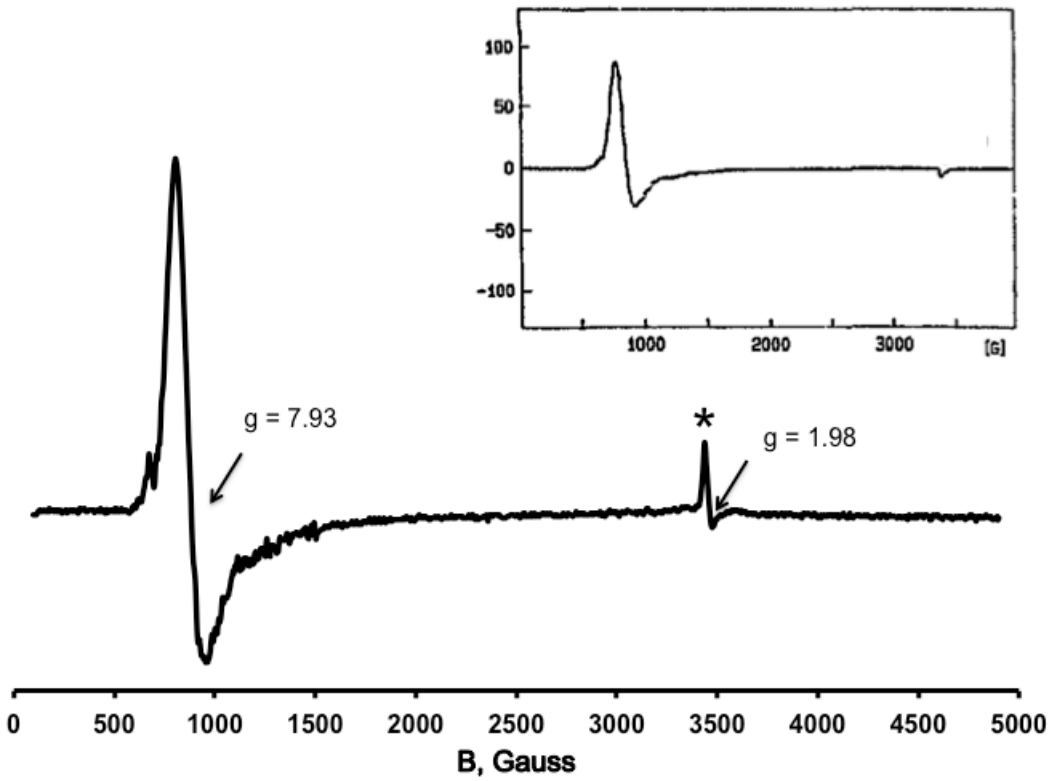

Figure 2.13. X-band EPR spectrum (dX″/dB) of **1** in toluene glass (1.0 mM, 2.5 K, frequency = 9.647 GHz, modulation to 1 G, power = 0.06 mW). An asterisk denotes the signal from a contaminant within the cavity of the instrument. Inset: original EPR spectrum reported by Cotton *et al* (toluene solution, 10 K).[3]

To further probe the ground and excited state magnetic behavior of **1**, magnetic susceptibility measurements were performed on solid samples with variable temperature (VT) and variable temperature and field (VTVH) using superconducting quantum interfering device (SQUID) susceptometry. These measurements were performed at the Max Planck Institute for Chemical Energy Conversion in the group of Dr. Eckhard Bill. The data are shown in Figure 2.14; these results confirm the S = 7/2 ground state and establish that it is energetically well-isolated from the other spin states. From 30 to 290 K, the effective magnetic moment is temperature independent at 7.4 μ_B. Below 30 K, the magnetic moment drops sharply. These data were fit using the JulX program; since this

program allows a maximum single spin of only $S = 5/2$, a two-spin model was used for the diiron core, with values $S_1 = 3/2$ and $S_2 = 2$ for formally high-spin Fe(I) and Fe(II), respectively; otherwise, the iron centers were treated as equivalent. A fixed, strongly ferromagnetic coupling constant, $J = 300$ cm^{-1} was used to enforce the qualitatively observed $S = 7/2$ spin. This value was sufficient to simulate the temperature-independence of the magnetism at higher temperatures, but it should be stressed that this already quite large value is a *minimum* value of the true interaction energy; any higher value would also be consistent with the temperature independence. The drop in magnetization at lower temperatures is consistent with either zero-field splitting effects or with intermolecular antiferromagnetic interactions. Fitting the remaining parameters gave an isotropic $g_{Fe} = 1.86$ and zero-field splitting parameter $D = 19.1$ cm^{-1} for both iron centers. The *g*-value is lower than the ideal value of 2.0 but was consistent for measurements of three different crystalline samples. A similar *g*-value of 1.9 was recently measured by Betley *et al.* for a high-spin triiron(II,II,II) cluster.[17] The *D* value corresponds to a zero-field splitting of the ground state octet according to $D_{7/2} = 8.2$ cm^{-1}, as can be seen from the spin projection coefficient ($D_{7/2} = 0.1429\ D_1 + 0.2857\ D_2$).[31]

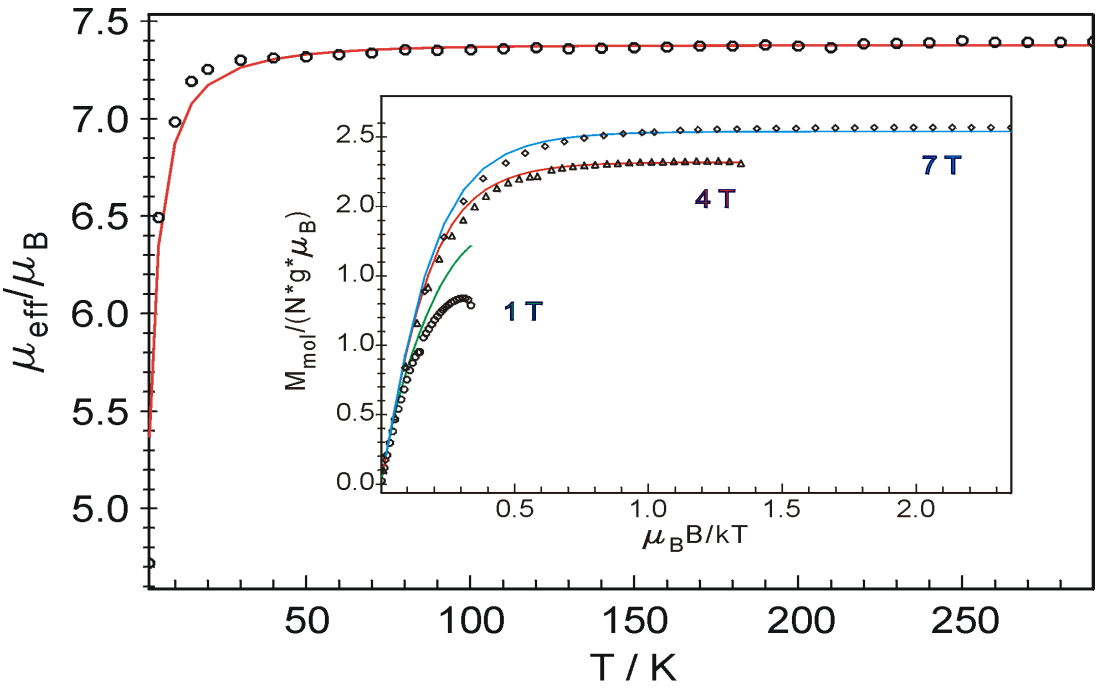

Figure 2.14. Temperature dependence of the effective magnetic moment, μ_{eff}, of $Fe_2(DPhF)_3$ (shown in open circles, 1 T, 2 to 290 K). The solid line represents the best fit. Inset: Isofield VTVH Magnetization of $Fe_2(DPhF)_3$ as a function of $\mu_B B/kT$ (1, 4, and 7 T; 2 to 290 K with corresponding simulation curves). The data were corrected for χ_{TIP} of 0.375 x 10^{-3} emu. Intermolecular coupling was considered by introducing a Weiss constant, θ, of −0.286 K to obtain a consistent fit of the low temperature data recorded at different fields. See text for simulation parameters.

The inset in Figure 2.14 shows the VTVH dependence of the magnetization of $Fe_2(DPhF)_3$. The nonoverlapping isofield curves of the magnetization as a function of B/T are indicative of substantial zero-field splitting, which prevents magnetic saturation, and fitting of these data can give values that are much more reliable than those from a single field measurement.[13] Accordingly, global fitting of the data gave a nearly identical $g_{Fe} = 1.87$, no rhombicity ($E/D = 0$), and $D = +10$ cm^{-1} for both iron centers. The large, positive zero-field splitting parameter is characteristic of high-spin iron centers and assigns the $m_s = \pm ½$ state as the ground energy level, consistent with the EPR spectrum.

Altogether, the magnetization data are consistent with the assignment of the ground state in **1** as a well-isolated octet, with no significant population of other spin states at room temperature. The large, axial zero-field splitting is consistent with the trigonal symmetry of **1** also observed in the EPR spectrum, and its positive sign identifies the $m_s = \pm ½$ as the ground energy level.

*2.3.8 Spin State and Magnetic Behavior of **2***

As described in the introduction, the previously reported magnetic characterization of **2** was more complex than for **1** and somewhat problematic. While highly paramagnetic, the spin state was not found to be well-isolated. Room temperature magnetic susceptibility measurements initially found a μ_{eff} of 4.65 μ_B for **2**, a value significantly lower than the expected spin-only value of 5.92 μ_B. for an $S = 5/2$ spin, and lower even than the expected 4.90 μ_B for an $S = 3/2$ system. Nevertheless this value, and "some preliminary SQUID measurements" were described as being "all consistent with an electronic configuration of ground state $S = 5/2$ with a thermally accessible $S = 3/2$ state."[2] The room-temperature μ_{eff} value was later revised to, which was interpreted in alternating accounts to reflect an $S = 3/2$ ground state with $S = 5/2$ excited state[4] and *vice versa*;[9] however, further variable-temperature measurements were not reported. The low-temperature EPR spectrum was not shown but was also described as being consistent with a ground $S = 5/2$ spin state with a low-lying quartet excited state.[2] This became the accepted model for the paramagnetism in **2** based largely on theoretical work;[9] however, this was based on a truncated model using fairly limited calculations. Moreover,

experimental evidence for this configuration remains limited, and the unsteady progression towards this consensus highlights the difficulty in obtaining reliable analytical data for these trigonal lantern compounds, which are difficult to synthesize and extremely sensitive to the laboratory atmosphere.

To clarify and further explore the magnetic behavior of **2**, we measured its variable temperature and VTVH magnetic susceptibility, again in collaboration with the Eckhard Bill group. The data are shown in Figure 2.15. From ~30 to 290 K, the effective magnetic moment, μ_{eff}, is essentially constant at 6.92 μ_B. This is significantly higher than the previously reported room temperature value of 5.2 μ_B,[4] which had led to speculation about a low-lying quartet excited state. In fact, the temperature independence of the magnetic moment observed here indicates that the ground spin state is energetically well-isolated and rules out any significant population of excited states up to room temperature. The μ_{eff} value of 6.92 is in fact significantly larger than the expected spin-only value of 5.92 μ_B for an $S = 5/2$ system. Despite this deviation, the spectrum could be simulated by modeling the system as a single $S = 5/2$ spin; refinement of the data gave a good fit, with the larger-than-expected value of μ_{eff} being accounted for in a large g-value of 2.33. This value, while quite different from the expected value of 2.0, is not unprecedented for low-valent Co ions in multimetallic clusters: for instance, a similar g-value of 2.29 was found in a Cr-Cr-Co trimetallic complex.[32] Intermolecular antiferromagnetic interactions are not expected to contribute significantly to the magnetism, since the closest intermolecular Co-Co contacts observed in the crystal packing are all greater than 8.5 Å. Rather, a relatively large zero-field splitting parameter accounts for the drop in magnetism below

~30 K. This was refined as $D = 5.4$ cm^{-1} and $E/D = 0$; although these values are not often reliable when obtained from VT susceptibility at a single applied field, in this case the fit was quite sensitive to the value of D. Significantly higher values of D caused the drop in magnetism to occur at temperatures higher than what is observed in the experimental spectrum, and *vice versa*. The large zero-field splitting term is also evident in the VTVH data (not fit), as the non-overlapping isofield curves indicate a lack of saturation up to an applied field of 7 T.

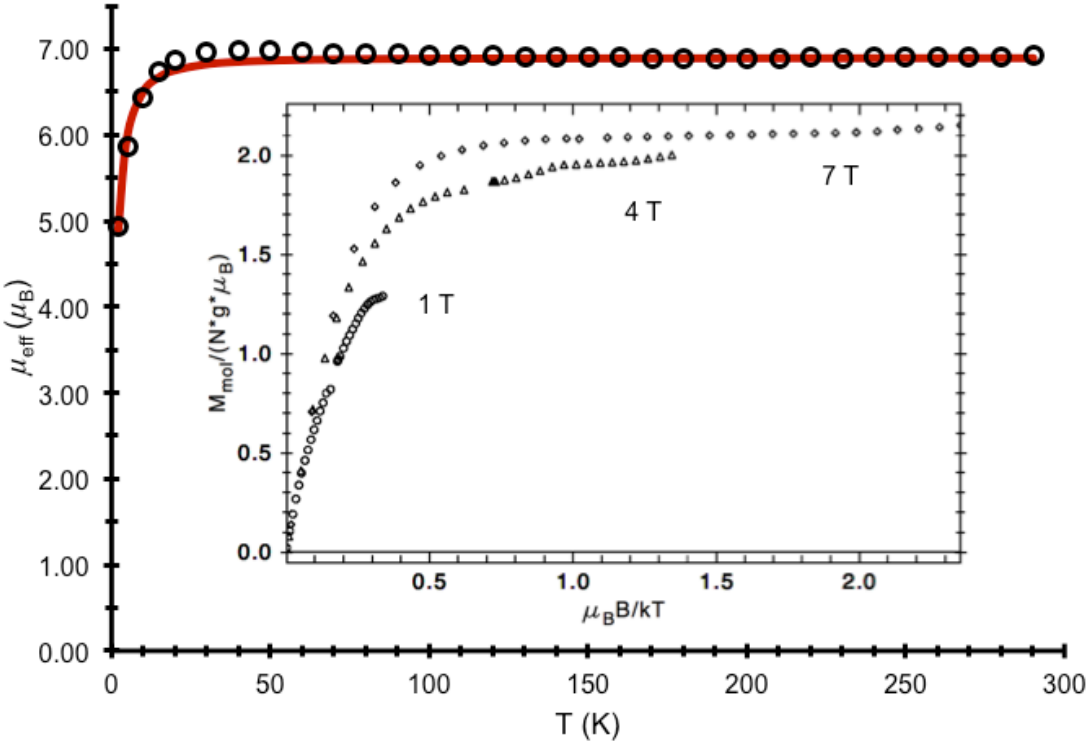

Figure 2.15. Temperature dependence of the effective magnetic moment, μ_{eff}, of $Co_2(DPhF)_3$ (shown in open circles, 1 T, 2 to 290 K). The solid line represents the best fit. Inset: Isofield VTVH Magnetization of $Co_2(DPhF)_3$ as a function of μ_BB/kT (1, 4, and 7 T; 2 to 290 K). The data were corrected for χ_{TIP} of 0.375 x 10^{-3} emu. See text for simulation parameters.

The use of a single $S = 5/2$ spin in these fits implies strong, ferromagnetic coupling between the two cobalt centers. Identical fits are obtained if the system is modeled using two localized $S = 1$ and 3/2 spins, for formally high-spin Co(I) and Co(II) centers, with $J \geq 200$ cm^{-1}. As in the case of **1**, this already quite large coupling constant is a *minimum* value for the true strength of the ferromagnetic interaction. In order to confirm the ground spin state of **2**, and because the unexpectedly large *g*-values in these susceptibility measurements could be an indication of magnetic impurities, we next examined **2** by EPR spectroscopy.

The X-band EPR spectra we have obtained from pure **2** in frozen toluene solution (20 K, 1.0 mM) are qualitatively similar to that of **1**, in showing an axial signal with $g_x = g_y >> g_z$ (Figure 2.16). The g_{eff} values of around 6 and 2 are as expected for the $m_s = \pm ½$ Kramers doublet for an ideal axially-symmetric $S = 5/2$ system, pinpointing this as the ground-state configuration. No hyperfine coupling is observed to the I = 5/2 ^{59}Co nucleus; presumably this is obscured by the broad lineshapes in both features. As in the case of **1**, the observation of only these two features suggests a large axial zero-field splitting term (D >> hν). The data were simulated using an $S = 5/2$ spin and constraining the g_x- and g_y-values to be equal. The best fit of the data gave $g = (2.243, 2.243, 2.12)$, with a fixed $D = 9$ cm^{-1} and a small rhombicity term, $E/D = 0.0509$; any value of D > 2 was found to be consistent with the experimental spectrum.

Additionally, no evidence for an $S = 3/2$ excited state is observed in these pure samples. However, in spectra taken on crude or partially decomposed samples of **2**, a broad feature at $g \approx 4.3$ is observed, which could explain the earlier report of such an

excited state; the signal is presumably the result of an S = 3/2 Co(II) impurity, whether from starting material, a byproduct, or, more likely considering the extreme air-sensitivity of **2**, a one-electron oxidized decomposition product.

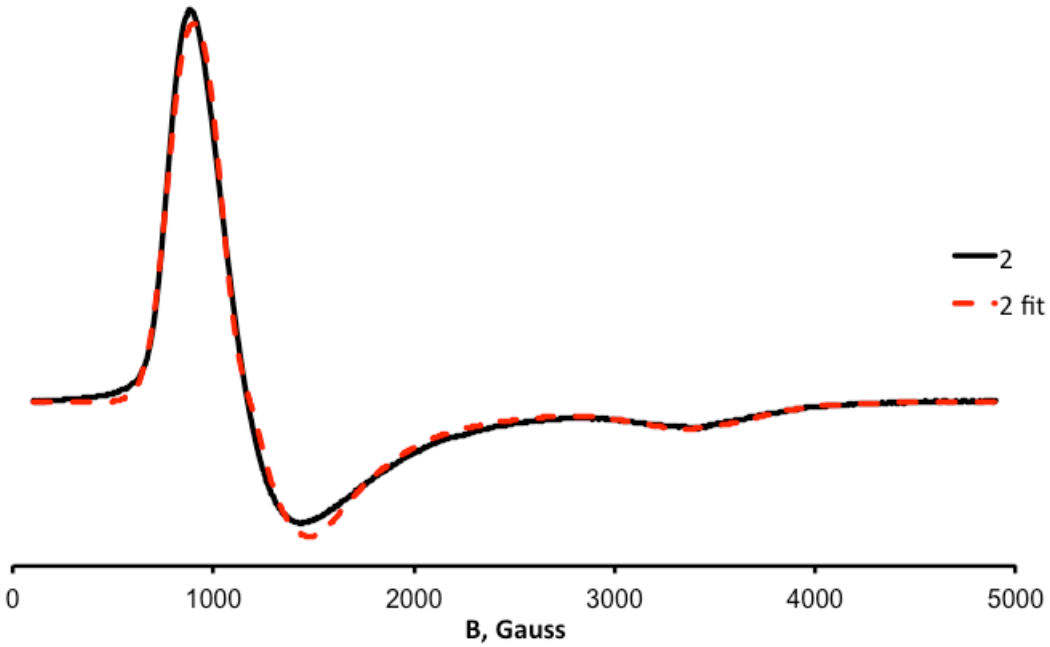

Figure 2.16. X-band EPR spectrum (dX″/dB) of **2** in toluene glass shown as solid, black line (1.0 mM, 20.0 K, frequency = 9.646 GHz, modulation to 10 G, power = 2.01 mW). The spectrum was simulated (shown as dashed grey line) by adopting S = 5/2 with the following anisotropic values: g = (2.243, 2.243, 2.12); line widths, W = (172.6, 172.6, 700); zero-field splitting parameters D = 5.40 cm^{-1}, E/D = 0.0509 (D value fixed).

Altogether, the combined EPR and magnetic susceptibility data for **1** and **2** are consistent with both molecules having energetically well-isolated ground states with the maximum possible spin multiplicity: S = 7/2 in the case of **1** and S = 5/2 in the case of **2**. The ferromagnetic coupling between the metals in both molecules is thus quite strong, as no contributions from lower-spin states are observable up to room temperature. This corresponds to coupling constants of 200 – 300 cm^{-1} at the very least, suggesting that they

may be better described as having a single overall spin resulting from a delocalized M_2^{3+} core, rather than as two localized spins coupled *via* an exchange interaction. These descriptions are equivalent with respect to the magnetic data.

*2.3.9 Mixed-Valency and Electronic Delocalization: Mossbauer Spectroscopy of **1***

Both the MO model and double-exchange explanations for the high-spin nature of **1** and **2** require that the formally mixed valent M(I,II) cores be highly delocalized, *i.e.* $M^{1.5}M^{1.5}$ Neither X-ray crystallography nor NMR spectroscopy show any significant differences between the two metal sites in **1** or **2** that would correspond to a firmly-localized $M^{I}M^{II}$ mixed-valent state, or Class I mixed valent in the Robin-Day classification system.[33] However, a localized, Class I system would not be expected with the identical donor sets surrounding both iron centers. The more relevant distinction is between Class III, in which the molecule is fully delocalized and the metal sites are indistinguishable, and Class II "partial delocalization."[33] The timescale and resolution of NMR and X-ray diffraction would not be sufficient to distinguish a fully delocalized core from one delocalizing on a slower timescale. FT-IR spectroscopy operates at a much faster timescale and has proven to be useful technique in distinguishing mixed-valent complexes at the Class II-III border, with electron-transfer rate constants in the range of 10^{11}-10^{13} s^{-1}.[34] However such analysis requires that the spectrum have well-defined vibrational modes that are sensitive to the metal environment. The spectrum of **1** is relatively simple, as shown in Figure 2.17, which could suggest a molecule with equivalent iron centers. However, without definitive assignments of the observed bands

to the iron-centered vibrational modes of the molecule, no conclusions about the iron chemical environments can reasonably drawn from this data.

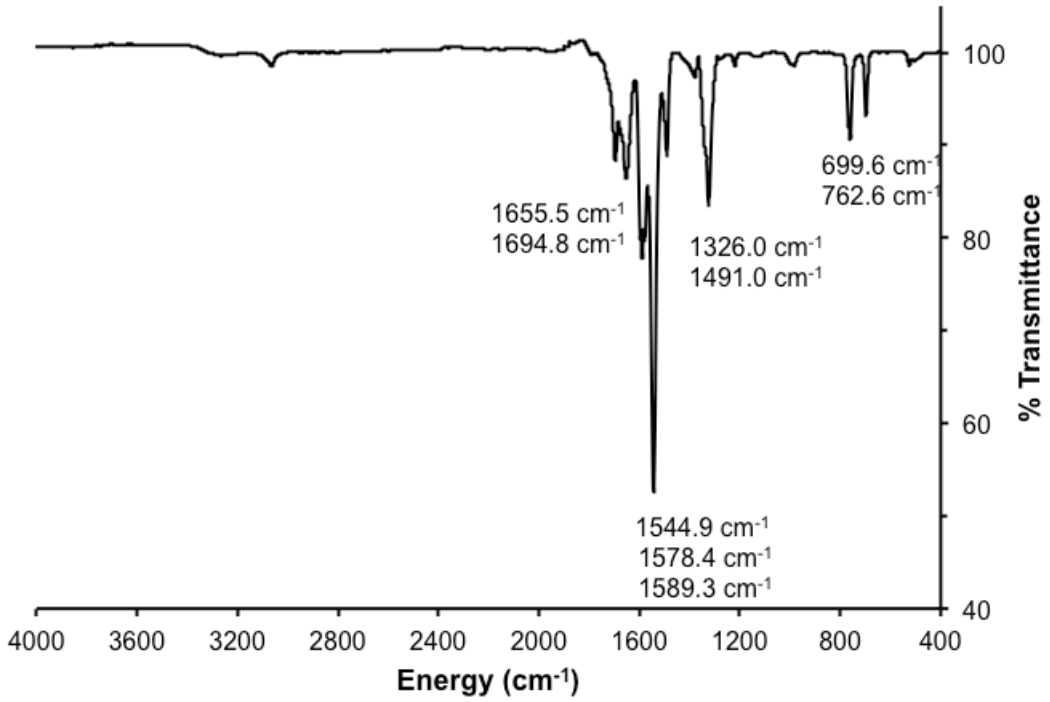

Figure 2.17. Solution-phase FT-IR spectrum of **1** (THF, KBr cell). Subtraction of the signal for the THF background results in the somewhat irregular baseline and low intensity of the C-H stretching region (2900-3250 cm^{-1}). Frequencies for the major vibrational features are labeled.

For a technique that is sensitive to the iron oxidation state and operates on a more rapid timescale, we turned to ^{57}Fe Mössbauer spectroscopy. Spectra collected at 4.2 K with applied fields of 3 - 7 T are shown in Figure 2.18. The most notable feature of these spectra is the observation of a six-line signal, corresponding to only a single iron environment. This indicates that the iron sites are equivalent on the Mössbauer timescale (10^7 s^{-1}). Consequently, the electron exchange rate must be very fast, and these data suggest that **1** should be considered a fully delocalized mixed-valent complex. The spectra were globally fitted with a fixed, isotropic $g_{7/2} = 2.0$; this yielded zero-field

splitting parameters $D_{7/2} = 8.2$ cm^{-1} and $E/D_{7/2} = 0$, in line with those obtained from SQUID measurements. The Mössbauer parameters obtained from the fit are $\delta = 0.65$ mm s^{-1} and $\Delta E_Q = +0.32$ mm s^{-1}.

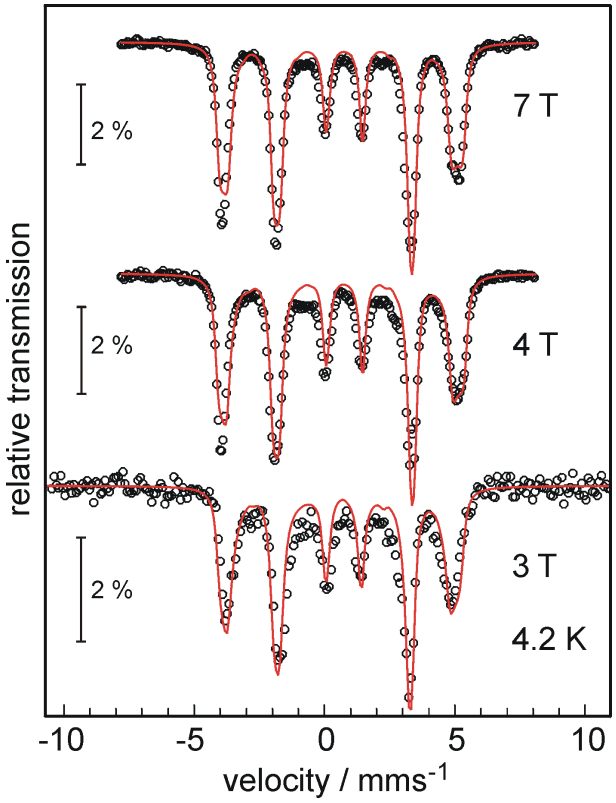

Figure 2.18. Applied field Mössbauer spectra of $Fe_2(DPhF)_3$ recorded at 4.2 K with fields of 3, 4, and 7 T. The solid lines represent spin-Hamiltonian simulations for S = 7/2 with $g_{7/2}$ = (2.0, 2.0, 2.0) fixed, $D_{7/2} = 8.2$ cm^{-1}, $E/D_{7/2} = 0$, and with Mössbauer parameters $\delta = 0.65$ mm s^{-1}, $\Delta E_Q = +0.32$ mm s^{-1}, asymmetry parameter $\eta = 0$, line width = 0.26 mm s^{-1}, and magnetic hyperfine coupling constants $A_{xx}/g_N\beta_N = -11.59$ T; $A_{yy}/g_N\beta_N = -10.59$; $A_{zz}/g_N\beta_N = -30.81$ T. The spin projection coefficients in the ionic limit of Fe(I), $S_1 = 3/2$, and Fe(II), $S_2 = 2$ would be $A_{Fe(I)} = 2.333 \cdot A$, and $A_{Fe(II)} = 1.751 \cdot A$, respectively, i.e. the local A values for the iron sites are about twice the total spin values given here.

At the time of this initial report, there were very few examples of similar low-coordinate, low-valent, high-spin iron compounds with which to compare these parameters. Holland *et al.* had reported data for a family of high-spin, three-coordinate

Fe(II) compounds with β-diketiminate ligands, which had isomer shifts ranging from 0.48 to 0.74 mm s^{-1} and $|\Delta E_Q|$ values between 1.11 and 1.74 mm s^{-1}.[35] For a high-spin Fe(I) complex in the same system, a slightly lower isomer shift of 0.44 mm s^{-1} with ΔE_Q = 2.02 mm s^{-1} was reported.[36] An Fe(I)(μ-N_2)Fe(I) sandwich complex was reported by Peters *et al.* with δ = 0.53 mm s^{-1} and ΔE_Q = +0.89 mm s^{-1}.[37] The isomer shift in **1** is notably higher than in the Fe(I) examples and within the range of the Fe(II) species. This was taken to be consistent with assignment of an Fe(1.5) oxidation state. The quadrupole splitting value of **1** is much lower than in these examples, which is perhaps due to the weak-field ligand set.

For further comparison, simulated Mössbauer parameters were calculated by DFT methods using the ORCA program, using a DFT-optimized geometry discussed in more detail below.[38] Four different functionals were surveyed, including both local functional and hybrid methods: B2PLYP, BP86, TPSSh, and B3LYP.[39,40] For the isomer shift, all of the functionals gave predictions within 0.20 mm s^{-1} of the experimental value, but the predictions are uniformly lower than experiment. The range of simulated quadrupole splittings is much wider (from −0.45 to 0.26 mm s^{-1}), but these values are near zero, as is observed experimentally. The best agreement between theory and experiment was found for the B2PLYP functional, with δ = 0.49 mm s^{-1} and ΔE_Q = 0.26 mm s^{-1}, where Δ = 0.15 and 0.14 mm s^{-1}, respectively; yet the wide variation of the values predicted by the different functionals does not inspire confidence in any of them. The results are summarized in Table 2.2.

Table 2.2. Calculated hyperfine parameters of $Fe_2(DPhF)_3$ relevant to Mössbauer spectroscopy for different DFT functionals (B2PLYP, BP86, TPSSh, B3LYP).

Functional	exp	B2PLYP[1]	BP86[1]	TPSSh[1]	B3LYP[1]	B3LYP[2]
δ, mm/s	0.65	0.49	0.45	0.48	0.49	0.51
ΔE_Q, mm/s	0.32	0.26	−0.45	−0.17	−0.27	−0.25

[1]Input geometry from a PBE/SV(P) optimization. [2]Input geometry from a B3LYP/TZV(P) optimization.

Since this initial report, several other iron-containing bimetallics and trimetallics have been studied by Mössbauer spectroscopy; some have been reported in the literature,[17,41-43] while others have been more recently synthesized and characterized in our laboratory. Many of these complexes will be described more fully in Chapter 3. In general, the isomer shift of 0.65 mm s^{-1} in **1** is higher than most $Fe^{1.5}$ and Fe^{I} centers but lower than most Fe^{II} centers, although there is substantial overlap between these values, and in many cases the oxidation state of the reference molecule is not clear. The ΔE_Q value for **1**, at 0.32 mm s^{-1}, is far lower than virtually all other reference compounds, which generally have more polarized M-M bonding interactions. Thus, the Mössbauer parameters observed for **1** are seemingly consistent with an $Fe^{1.5}Fe^{1.5}$ delocalized valence; the isomer shift is on the high end, and the ΔE_Q is far lower, both of which may be attributed to the symmetric, low-coordinate ligand environment and the non-polar nature of the Fe-Fe bond.

A more qualitative feature of these spectra of **1** that was unappreciated at the time was the broad, asymmetric, and unresolved signals observed at temperatures above 4.2 K. Even with applied fields of 4 T, and even at temperatures as low as 12 K, the spectra are poorly resolved, as shown in Figure 2.19. At 80 K, the spectrum appears to be a broad, asymmetric quadrupole doublet. This broadening may be due to the large spin and

intermolecular coupling, and fits of the data at these temperatures are poor. This effect has now been seen in other Mössbauer spectra containing high-spin Fe centers and appears to be a general phenomenon in such species.

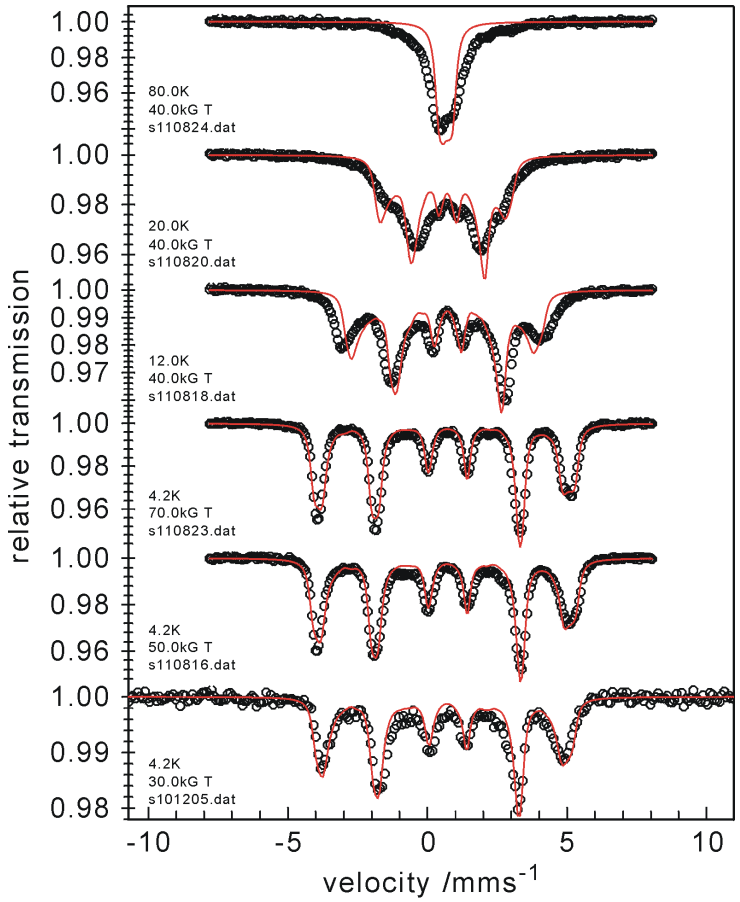

Figure 2.19. Applied field Mössbauer spectra of $Fe_2(DPhF)_3$ recorded at 4.2, 12.0, 20.0 and 80.0K with fields of 3 to 7 T. The solid lines spin Hamiltonian simulations for S = 7/2 with $g_{7/2}$ = (2.0, 2.0, 2.0) fixed, $D_{7/2}$ = 8.2 cm-1, $E/D_{7/2}$ = 0, and with Mössbauer parameters δ = 0.65 mm s^{-1}, ΔE_Q = +0.32 mm s^{-1}, asymmetry parameter η = 0, line width = 0.26 mm s^{-1}, and magnetic hyperfine coupling constants $A_{xx}/g_N\beta_N$ = −11.59 T; $A_{yy}/g_N\beta_N$ = −10.59; $A_{zz}/g_N\beta_N$ = −30.81 T. At temperatures of 20.0 K and 80.0 K, the fitting of the data grows worse perhaps due in part to the large spin and intermolecular coupling.

*2.3.10 Calculated Structure and Spin State of **1***

We have performed geometry optimizations for the lowest doublet, quartet, sextet and octet spin-states using DFT (PBE/def-SV(P)). The full molecular structure of

$Fe_2(DPhF)_3$ was optimized, using the reported crystal structure as a starting point, in contrast to earlier models, which truncated the phenyl substituents on the amidinate ligands to hydrogen atoms.[9] These optimized structures were then used as the geometries for higher level, *ab initio* CASSCF/CASPT2 calculations. Since these *ab initio* calculations are computationally intensive, we sought to constrain the structures with imposed symmetry to reduce the costs of refinement. Although three-fold symmetry would perhaps be a more obvious choice for the trigonal $Fe_2(DPhF)_3$, the MOLCAS program used for the later *ab initio* calculations is limited to symmetry constraints involving D_{2h} and its subgroups. Therefore, we chose to impose C_2 symmetry, which enforces a two-fold rotation axis perpendicular to the Fe-Fe vector; this symmetry element is present in the crystal structure of $Fe_2(DPhF)_3$ as well, making it a more realistic constraint in any case. The relative energies for the various states calculated at these three levels of theory are reported in Table 2.3.

Table 2.3. Calculated relative energies of $Fe_2(DPhF)_3$ for all possible spin states at DFT, CASSCF and CASPT2 levels of theory.

	Irreducible Representation	doublet	quartet	sextet	octet
ΔE_{DFT}, eV	—	2.95	1.65	0.71	0
ΔE_{CASSCF}, eV	A	1.63	1.10	1.30	0
	B	1.44	1.44	0.60	1.26
ΔE_{CASPT2}, eV	A	1.50	1.22	1.17	0
	B	1.53	1.22	0.50	1.18

All methods indicate that the ground state is the octet, as is experimentally observed; this state belongs to the irreducible representation (^{8}A), as previously proposed for the truncated model.[9] Overall, the agreement between theory and experiment is quite good. Selected parameters are shown in Table 2.4. The metal-metal bond distance is

underestimated by ~0.04 Å, in line with the underestimation found in most DFT-optimized M-M bond distances.[44] Otherwise, the predicted bond distances are very close matches to the experimental distances. Interestingly, despite the imposition of C_2 symmetry, the optimized structure is more trigonally symmetric than either experimental structure, as seen in the N-Fe-N distances very close to 120°. This supports the assertion by Cotton *et al*., based on optimization of the truncated model, that the deviations from trigonal symmetry seen in the experimental structures do not have an electronic basis.[9]

Table 2.4. Selected bond lengths (Å) and angles (°) for experimental and DFT-optimized octet $Fe_2(DPhF)_3$ structures.

Structure	$Fe_2(DPhF)_3$	$Fe_2(DPhF)_3$•½(C_6H_6)	$Fe_2(DPhF)_3$ PBE/def-SV(P)
Fe−Fe, Å	2.231(3)	2.230(1)	2.188
Fe−N, Å	2.033(3)	2.035(4)	2.034
	2.033(3)	2.024(3)	2.034
	2.025(3)	2.006(4)	2.034
	2.025(3)	2.006(4)	2.031
	2.018(3)	1.989(4)	2.031
	2.018(3)	1.988(3)	2.031
N−Fe−N, °	132.7(1)	125.7(2)	121.6
	132.7(1)	125.2(2)	121.6
	116.2(1)	121.0(2)	119.4
	116.2(1)	117.3(2)	119.4
	111.1(1)	116.8(2)	118.7
	111.1(1)	113.7(2)	118.7
N−Fe−Fe, °	92.3(1)	91.5(1)	92.2
	92.3(1)	90.7(1)	92.2
	90.1(1)	91.2 (1)	92.0
	90.1(1)	91.3(1)	92.0
	89.8(1)	92.2(1)	91.8
	89.8(1)	90.0(1)	91.8
N−C−N, °	122.59	122.2(4)	121.8
	122.59	122.2(4)	121.7
	121.27	122.1(4)	121.7

*2.3.11 Molecular Orbital Description of **1** from CAS-SCF Calculations*

The CAS calculations were used to obtain a more detailed picture of the bonding in **1**. In these calculations, the 13 3d electrons were allowed to populate an active space of 13 orbitals comprising the ten orbitals from the 3d shell of the two iron atoms and three additional bonding orbitals: one σ- and two π-(Fe-Fe) MOs from the fourth shell of Fe orbitals, used to account for correlation effects. Inspection of the output revealed the ten expected σ, π, and δ bonding and antibonding combinations of the 3d orbitals. The remaining three orbitals are a combination of 4s, 4p, and 4d Fe orbitals. The ^{8}A ground state is primarily single-configurational, with the leading configuration, $(\sigma)^2(\pi)^4(\pi^*)^2(\sigma^*)^1(\delta^2)(\delta^{*2})$, accounting for 73% of the total wavefunction. This electronic configuration reproduces the formal bond order (FBO) of 1.5 originally proposed for the molecule, from the $(\sigma)^2(\sigma^*)^1$ and two $(\pi)^2(\pi^*)^1$ half-bonds. The remaining configurations are composed primarily of excitations from the doubly-occupied π bonding orbitals into the π* antibonding orbitals, with some minor additional excitations from σ into the σ* and 4σ orbitals and from π into the 4π orbitals. The overall ground-state wavefunction is $(\sigma)^{1.85}(\pi)^{3.64}(\pi^*)^{2.30}(\sigma^*)^{1.06}(\delta)^{2.00}(\delta^*)^{2.00}(4\sigma)^{0.10}(4\pi)^{0.06}$, giving an effective bond order of 1.15. This is lowered from the FBO of 1.5; however, because the wavefunction is primarily (73%) single-configurational, this EBO is still substantial, especially for a metal-metal bond between first-row metals. In fact, this value is larger than the EBO calculated for the dichromium carboxylates, which have a formal *quadruple* bond.[45]

This CAS-SCF method does not compute orbital energies directly; rather, the

orbital energies are inferred from their relative occupancies; large differences in electron populations are assumed to correspond to large energy splittings. A molecular orbital energy diagram can be constructed in this manner, as shown in Figure 2.20. This scheme is essentially identical to that determined by Cotton *et al.* from SCF-Xα-SW and *ab initio* CI calculations on the truncated molecule $Fe_2(HNCHNH)_3$. The new, high-level calculations thus seem to confirm the original bonding proposal, in which the strong bonding and high-spin configuration are both due to the trigonal ligand field. The degeneracies and weak orbital splittings engendered by this arrangement cause the orbitals to fill in a high-spin manner; this in turn leaves the π* and σ* antibonding orbitals only half-filled, giving the molecule strong overall bonding through a summation of three half-bonding interactions.

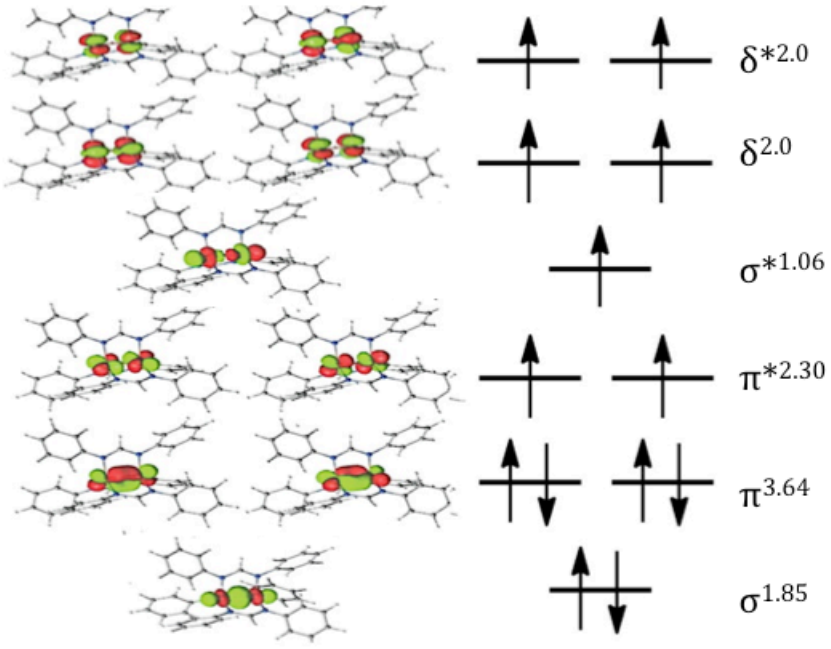

Figure 2.20. Molecular orbitals for **1** as found from CASSCF calculations. The leading electronic configuration is shown pictorially, while the orbital occupancies from the overall wavefunction are listed to the right. Contributions from orbitals in the fourth Fe shell are not shown.

*2.3.12 Excited State Energies and Electronic Transitions Calculated for **1***

While the relative orbital energies shown in Figure 2.20 are useful in understanding the bonding, more quantitative measures of the orbital energies are critical to understanding the absorption spectra and electronic delocalization pathways of **1**.[11] In order to better characterize the electronic transitions and excited-state properties of **1,** the excited-state wavefunctions were determined using CASSCF, their energies were computed with CASPT2, and the oscillator strengths for various transitions were evaluated using the complete active space state interaction method, CASSI. Table 2.5 lists the excitation energies and intensities found for transitions between the ^{8}A ground state and excited states of the same symmetry. Only one such transition was found to have significant intensity: the $\pi \rightarrow \delta$ transition is predicted to occur at 1.66 eV (~13,400 cm^{-1}, or 750 nm) with an oscillator strength of 2.56 x 10^{-4}. However, the energies for the other transitions are informative, despite their low oscillator strengths: notably, the large differences in ΔE (> 1 eV) between $\pi \rightarrow \pi^*$ and $\sigma \rightarrow \pi^*$ transitions suggest that the σ orbital lies significantly lower in energy. This is the lowest possible energy transition from the σ orbital, and at a predicted energy of 20,200 cm^{-1} (495 nm), it would be obscured by the strong UV absorption even if it had significant intensity.

Table 2.5. Spin-Free Excitation Energies of $Fe_2(DPhF)_3$ for Octet Wave Functions Belonging to the *A* Irreducible Representation. All transitions correspond to $^8A \rightarrow {}^8A$.

Transition	ΔE, (CASPT2)		Oscillator	Weight, %
	eV	cm^{-1}	Strength, a.u.	
$\pi \rightarrow \pi^*$	1.42	11,450	0.235×10^{-7}	0.64
$\pi \rightarrow \pi^*$	1.45	11,700	$< 0.1 \times 10^{-7}$	0.63
$\pi \rightarrow \delta$	1.60	12,900	0.788×10^{-5}	0.54
$\pi \rightarrow \delta$	**1.66**	**13,400**	**0.256×10^{-3}**	**0.53**
$\pi \rightarrow \sigma^*$	1.92	15,480	$< 0.1 \times 10^{-7}$	0.51
$\pi \rightarrow \delta^*$	2.06	16,610	0.777×10^{-7}	0.27
$\pi \rightarrow \delta^*$	2.13	17,180	0.118×10^{-6}	0.34
$\sigma \rightarrow \pi^*$	2.51	20,200	0.827×10^{-4}	0.67

Since there are multiple absorptions observed in the visible-NIR spectrum, we expanded the calculations to include transitions between the ^8A ground state and excited states belonging to both *A* and *B* irreducible representations. Only two additional transitions were found to have significant oscillator strengths; these are shown in Table 2.6.

Table 2.6. Selected Spin-Free Excitation Energies of $Fe_2(DPhF)_3$ for Octet Wave Functions Belonging to the *A* and *B* Irreducible Representations. All transitions correspond to $^8A \rightarrow {}^8A$ or $^8A \rightarrow {}^8B$.

Molecular Orbital	State Transition	ΔE, eV (cm^{-1}, rounded)	Oscillator Strength, a.u.	Weight, %
$\pi^A \rightarrow \delta^A$	$^8A \rightarrow {}^8A$	1.661 (13,400)	0.14×10^{-3}	54
$\pi^A \rightarrow \delta^B$	$^8A \rightarrow {}^8B$	1.557 (12,560)	0.13×10^{-3}	45
$\pi^A \rightarrow \delta^{*B}$	$^8A \rightarrow {}^8B$	1.906 (15,370)	0.29×10^{-3}	24

Hence, three significant excitations are predicted at 12,560 cm^{-1} (800 nm), 13,400 cm^{-1} (746 nm), and 15370 cm^{-1} (650 nm). These correspond quite well to the experimentally observed absorptions at 800 nm, the shoulder at 700 nm, and the peak at 650 nm; they are interpreted as $\pi^A \rightarrow \delta^B$, $\pi^A \rightarrow \delta^A$, and $\pi^A \rightarrow \delta^{*B}$ transitions, respectively.

However, no transitions were predicted to have significant intensity in the NIR region, where there is an observed absorption at 1250 nm (0.99 eV or 8,000 cm^{-1}). This band is expected to be the $\pi \rightarrow \pi^*$ transition, as it is the lowest-possible-energy transition within the MO manifold. Two such transitions were found in the initial calculations, but were predicted to occur at ~875 nm with no significant intensity, leading us to refine our techniques.

To better model the full Vis/NIR spectrum of $Fe_2(DPhF)_3$, spin-orbit (SO) coupling was included in the calculations. The most important resulting excitations correspond to transitions from pure (> 99%) octet ground states (A) to octet-dominated excited states (84 to 97 %) with limited mixing of the sextet configurations. Because of the limited mixing, the calculated excited energies with spin-orbit coupling are essentially identical to those obtained from the spin-free calculations. Therefore, the NIR band at 8,000 cm^{-1} is not reproduced by considering spin-orbit coupling.

Another strategy is to increase the active space from the initial treatment of 13 electrons in 13 orbitals, denoted AS(13,13). An attempt to increase the active space by including three additional high-lying MOs, however, was unstable. A stable active space was eventually formed by adding three high-lying MOs while removing the energetically low-lying σ MO and its two electrons to generate an AS(11,15) configuration. This resulted in a low-energy $\pi \rightarrow \pi^*$ transition found at 0.80 eV (~6,500 cm^{-1}). Although this excited energy corresponds reasonably well to the NIR band, the previously well-modeled $\pi \rightarrow \delta/\delta^*$ transition energies shift to lower energies of ~1.00 eV, and consequently, the overall spectrum is worse. Ideally, employing an even larger active

space should result in more accurate excitation energies, but such calculations are too computationally expensive. We therefore present the original AS(13,13) calculations as the most reliable, and we tentatively interpret the NIR band as a $\pi \rightarrow \pi^*$ transition, although we are unable to model this computationally. An overlay of the experimental spectrum and the transitions predicted by the AS(13,13) model is shown in Figure 2.21.

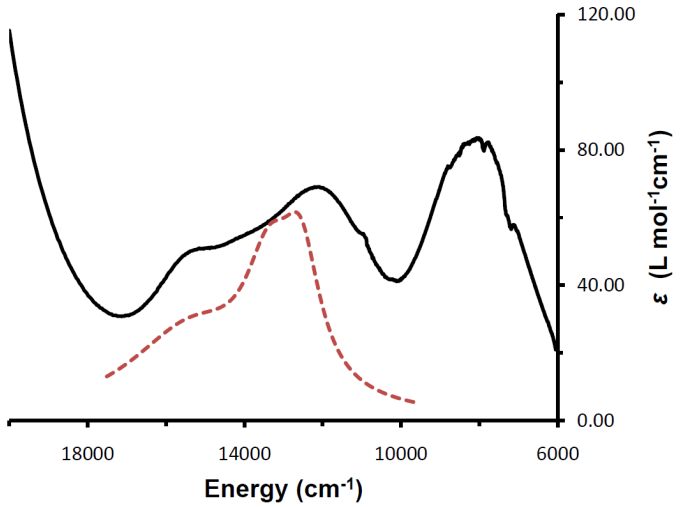

Figure 2.21. Electronic absorption spectrum of $Fe_2(DPhF)_3$ in THF (—, black), with simulated spectrum from AS(13,13) CASSCF/CASPT2 calculations (---) (see Table 6). Experimental λ_{max}, cm^{-1} (ε, L mol^{-1} cm^{-1}) = 15,380 (50), 14,290 sh (50), 12,120 (70), 8,000 (80).

*2.3.13 Calculated Structure and Spin State of **2***

Interestingly, when identical DFT geometry optimizations were performed on the dicobalt analogue, a structure was obtained that is distorted dramatically from three-fold symmetry. Although the experimental structure of **2** is closer to trigonal symmetry than either of the experimental structures of **1**, the initial DFT-optimized structure obtained under imposed C_2 symmetry has a hugely distorted N-Co-N angle of 138.6° and two much smaller angles of ~110°. Moreover, whereas the variation in N-Fe-N angles in **1** has no effect on the Fe-Fe bond distance, in this distorted structure of **2**, the Co-Co

distance is severely underestimated: at 2.245 Å, it is nearly 0.15 Å shorter than the experimentally observed bond. We attempted to correct this distortion by re-optimizing with a structure closer to the experimental one. In order to keep the computational efficiency of the C_2 symmetry constraint while retaining the salient features of the C_1-symmetric experimental structure, we constructed a new molecule by taking one half of the experimental structure and generating new coordinates for the other half based on rotation about a C_2 symmetry axis. The Co-N distances and N-Co-N angles were then fixed and the C_2 symmetry axis retained, but the molecule was otherwise freely optimized. Results of the optimizations for both structures are shown with the experimental values in Table 2.7. Gratifyingly, the Co-Co distance in the symmetry-generated structure lengthened considerably: at 2.302 Å, it is still shorter than the experimental distance by ~0.08 Å, but this is a much more reasonable value.

All levels of theory for both structures give the sextet ^{6}A as the ground state. The next lowest state is the quartet ^{4}A. CASPT2 calculations find this state to be 0.266 eV (2,145 cm^{-1}) higher in energy than the sextet for the original C_2-symmetric structure. Although this is a lower energy gap than for any of the excited spin states found in the diiron complex, it should have no real impact on the observed electronic structure of **2**. At this energy separation, there will be a negligible population (< 0.04% of a given sample) of these excited states at 298 K.

Table 2.7. Selected bond lengths (Å) and angles (°) for experimental and calculated dicobalt structures. The middle column represents the structure optimized directly from the crystal structure coordinates with C_2 symmetry imposed; the last column represents an a structure generated by taking one half of the experimental structure and creating coordinates for the second half by rotation around an imposed C_2 symmetry axis, as described in the text.

Structure	$Co_2(DPhF)_3$	$Co_2(DPhF)_3$, PBE/def-SV(P) C_2	$Co_2(DPhF)_3$, C_2, Symmetry-generated
Co−Co, Å	2.385(1)	2.245	2.302
Co−N, Å	1.955(5)	1.979	1.932
	1.932(5)	1.979	1.955
	1.959(6)	1.976	1.959
	1.978(5)	1.979	1.932
	1.957(5)	1.979	1.955
	1.983(5)	1.976	1.959
N−Co−N, °	125.1(2)	138.6	125.1
	119.2(2)	110.4	119.2
	115.6(2)	110.9	115.6
	120.1(2)	138.6	125.1
	114.8(2)	110.9	119.2
	124.7(2)	110.4	115.6
N−Co−Co, °	88.19	91.3	90.0
	88.24	91.2	92.1
	87.07	91.2	89.5
	90.06	91.3	90.0
	90.32	91.2	92.1
	91.30	91.2	89.5
N−C−N, °	121.6(6)	121.6	122.4
	122.7(6)	121.6	120.3
	122.4(6)	121.6	122.4

2.3.14 Electronic Structure of $Co_2(DPhF)_3$ from CAS-SCF and CAS-PT2 Calculations

Given the similar experimental structures for **1** and **2**, a similar MO manifold can be assumed, and the $S = 5/2$ ground state and longer Co-Co distance in **2** can then be rationalized as the result of filling the π* orbitals with its two additional d electrons. This leaves only 5 unpaired electrons and gives a formal bond order of 0.5, from the $(\sigma)^2(\sigma^*)^1$

combination. Indeed, this was the qualitative reasoning used by Cotton, and the truncated molecule $Co_2(HNCHNH)_3$ was in fact found to have the expected $(\sigma)^2(\pi)^4(\pi^*)^4(\sigma^*)^1(\delta)^2(\delta^*)^2$ configuration by SCF-Xα-SW and *ab initio* CI calculations. However, in our multiconfigurational calculations on untruncated models of **2**, we have found the electronic behavior of these calculated structures to be more complex than for **1**. These complications result from their multiconfigurational character and appear to be related to the overly short Co-Co distances found in the geometry optimizations.

The results of the MO calculations for the "C_2 symmetry-generated" structure that more accurately reproduces the Co-Co bond distance are summarized in Figure 2.22. The leading configuration found by the CASSCF calculations is the expected $(\sigma)^2(\pi)^4(\pi^*)^4$ $(\delta)^2(\delta^*)^2(\sigma^*)^1$, giving a FBO of 0.5; however, this configuration accounts for only 36% of the total wavefunction. The overall orbital occupancies are $(\sigma)^{1.87}(\pi)^{3.76}(\pi^*)^{3.11}(\delta)^{2.89}(\delta^*)^{2.21}(\sigma^*)^{1.03}(4\sigma)^{0.11}(4\pi)^{0.04}$. The σ* is apparently higher in energy than the δ and δ* set, which is reversed from **1**. More importantly, these occupation numbers give an EBO of 1.16 – in other words, the effective bond order is more than double the formal bond order! This striking and counterintuitive prediction results from the fact that the higher energy configurations largely involve exciting electrons out of the M-M *antibonding* π* orbitals and into the formally M-M *bonding* δ orbitals. The π* orbitals, which are formally fully occupied in the leading configuration, have an actual net occupancy of only 3.11 in the overall wavefunction. The δ orbitals, on the other hand, have a formal occupancy of only 2 in the leading configuration but a net occupancy of 2.89. This leads to a significant net *increase* in bond order. It is worth

noting that this EBO, at 1.16, is even larger than the EBO of 1.15 calculated for $Fe_2(DPhF)_3$. This is clearly not an accurate description of the bond strength, which is obviously stronger in **1**, considering the much shorter Fe-Fe distance. The error arises from the fact all bonding interactions are counted equally in the determination of the EBO, whereas the π-bonding in **1** is in reality much more stabilizing than the δ-bonding in **2**. The δ orbitals are primarily metal-ligand antibonding in character and only weakly M-M bonding; thus the EBO is in this case overestimating the "true" strength of the Co-Co bond by counting these towards the bond order. However, these excitations into the δ-bonds do remove electron density from the π* orbitals, which are much more strongly M-M antibonding. Thus, the increase in EBO over the FBO in **2**, while exaggerated, should reflect a meaningful increase in bond strength. These results go a long way towards explaining the existence of the very short Co-Co distance in **2** despite the predicted FBO of only 0.5. It would, for example, explain how the trigonal and tetragonal lanterns, $Co_2(DPhF)_3$ and $Co_2(DPhF)_4$, can have the same experimental Co-Co distance, despite the latter having a predicted FBO twice the strength of the former.

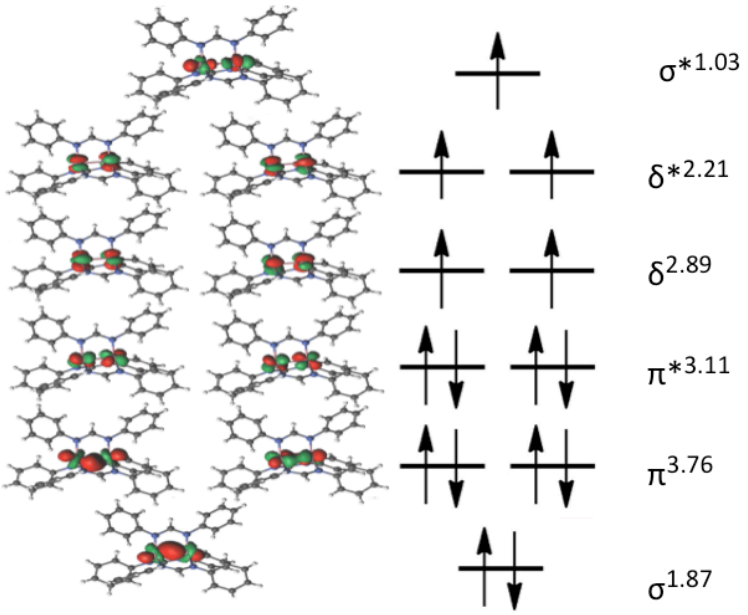

Figure 2.22. Molecular orbitals for more symmetric "C_2 symmetry-generated" structure of **2** as found from CASSCF calculations. The leading electronic configuration is shown pictorially, while the orbital occupancies from the overall wavefunction are listed to the right. Contributions from orbitals in the fourth Co shell are not shown; these provide an additional contribution of 0.075 to the effective bond order, giving a total EBO of 1.16.

The initial C_2-symmetric structure has an even more severely underestimated Co-Co distance and a large distortion away from trigonal symmetry. Its electronic structure is therefore much more suspect and will not be discussed in detail. However, the effect of these distortions on the Co-Co bonding is informative. The MO picture obtained from CASSCF calculations is shown in Figure 2.23. The leading configuration is $(\sigma)^2(\pi)^4(\pi^*)^3(\delta)^3(\delta^*)^2(\sigma^*)^1$, which much more closely resembles the overall wavefunction calculated for the other dicobalt structure. One π* orbital is only half-filled, and one δ orbital is filled. The non-degeneracy of the π* and δ orbital sets is clearly related to the distortion away from trigonal symmetry. The formal bond order thus increases to 1. This configuration represents 55% of the overall wavefunction. There is another configuration

with significant weight (20%): $(\sigma)^2(\pi)^3(\pi^*)^4(\delta_X)^2(\delta^*)^3(\sigma^*)^1$, representing double excitation from the π and δ bonding orbitals to their corresponding antibonding combinations, lowering the overall bond order. The total ground state wavefunction is $(\sigma)^{1.87}(\pi)^{3.63}(\pi^*)^{3.24}(\delta)^{2.74}(\delta^*)^{2.38}(\sigma^*)^{1.03}(4\sigma)^{0.10}(4\pi)^{0.04}$, yielding an EBO of 0.87. In this case the EBO is less than the FBO, but only because the latter has become a single bond.

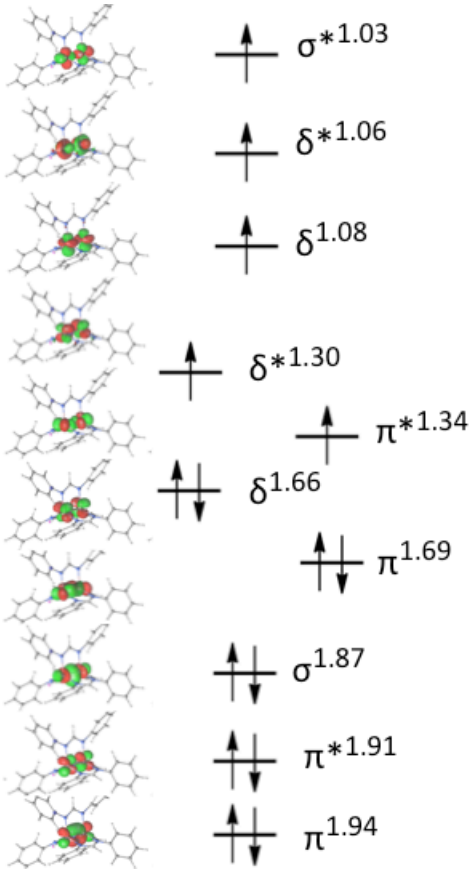

Figure 2.23. Molecular orbitals for asymmetric "C_2" geometry optimization of **2** as found from CASSCF calculations. The leading electronic configuration is shown pictorially, while the orbital occupancies from the overall wavefunction are listed to the right. Contributions from orbitals in the fourth Co shell are not shown.

The electronic structure calculations for both dicobalt geometries thus predict a much stronger Co-Co bonding interaction than originally anticipated. The reasons are different for each structure: in the less symmetric structure, the stronger bonding is

reflected in the formal bond order, as a result of the reordering of the π* and δ orbitals. In the more symmetric structure, the formal bond order remains 0.5, but the overall bonding interaction is strengthened through excited-state interactions. Yet both sets of calculations suggest that the Co-Co interaction involves substantial amounts of π- and δ-bonding in addition to the half-σ-bond originally predicted for the molecule. This result underscores the subtlety of bonding within first-row bimetallics and the utility of multiconfigurational calculations in accurately describing these interactions. In both **1** and **2**, strong bonding is achieved through the sum of many weak interactions. In **1**, this is through the combination of three half-bonding interactions. In **2**, it is the combination of a half-σ-bond with even weaker π- and δ-interactions.

2.3.15 Reactivity Survey of Trigonal Lantern Complexes

Due to the extreme sensitivity of **1** and **2** to air and moisture they are unlikely to become practical catalysts for small or industrial-scale processes. However, we were interested in exploring their amenability to redox chemistry. We therefore conducted a relatively broad survey of their reactivity patterns. This survey was tailored to address several questions regarding the structure-function relationship between the high-spin, metal-metal bonded character and their reactivity. First, we wondered whether the strong M-M bonding would facilitate multielectron redox chemistry, as been seen for some bimetallic complexes of second- and third-row metals.[46,47] In addition, we sought to assess the extent to which the high-spin electronic character would dictate the reactivity. Finally, we were interested in the numerous possible substrate-binding modes afforded by the two low-coordinate metal centers.

Because of the low-valent Fe oxidation states in **1**, we anticipated that it would be more amenable to oxidation than reduction. Indeed, cyclic voltammetry measurements performed in THF with 0.1 M (^{n}Bu)$_4$N•PF$_6$ electrolyte showed no reductive waves within the THF solvent window but a number of overlapping, irreversible oxidations. As shown in Figure 2.24, there are at least five such oxidations between -1.0 V and +0.75 V (vs. Fc/Fc$^+$) when scanning at 50 mV s^{-1}. At higher scan rates these waves remain irreversible but become less resolved. Unfortunately, **1** is unstable and decomposes during these experiments, perhaps from reaction with the PF$_6^-$ electrolyte, causing the solution to turn from bright yellow to brown within a matter of minutes. This is accompanied by the observation of broad oxidation waves overlapping with those of **1**. Thus the electrochemical data on this complex is limited. However, the major features of **1** are consistent from batch to batch and reflect a highly reducing character. Unfortunately, the irreversibility of these features suggests that **1** is unlikely to support reversible multielectron chemistry. Electrochemical data on **2** were not collected, as this compound decomposes rapidly under the measurement conditions. The one-electron oxidized product of **2** has already been reported as the bis-acetonitrile adduct, Co$_2$(DPhF)$_3$(CH$_3$CN)$_2$•PF$_6$; this product is produced not by oxidation of **2**, but from ligand abstraction of Co$_2$(DPhF)$_4$ by AgPF$_6$.[4] Chemical oxidation of **1** was attempted using FcBF$_4$ but in all cases led to a mixture of paramagnetic products that were not isolated or further characterized.

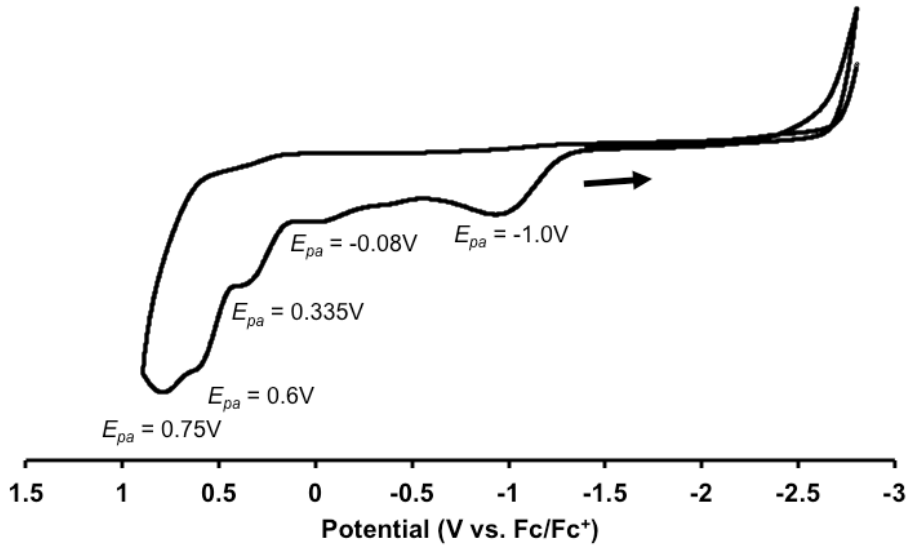

Figure 2.24. Cyclic voltammogram of **1** in 0.1 M (^{n}Bu)$_4$N•PF$_6$ THF. Scan rate is 50 mVs^{-1}.

We anticipated, given the reducing nature of **1** and its apparent reactivity towards halogenated solvents and, potentially, the PF_6^- anion, that it might be reactive towards the oxidative addition of small molecules and common organic substrates. However, **1** was unreactive to oxidative addition of H_2 and similar substrates, like PhX (X = Cl, Br). While disappointing, this result is not surprising, given the high-spin state of **1**. Oxidative addition of H_2 and similar substrates typically proceeds in a concerted fashion and requires both a low-energy, empty orbital and a high-energy, filled orbital on the reactive metal. As shown in Figure 2.25, the low-energy LUMO accepts electron density from the filled σ orbital, while the high-energy HOMO donates into the σ* orbital of the substrate; both effects contribute to the H-H bond breaking and the two M-H bonds forming. In contrast, the high-spin character of **1** ensures that both orbitals are half-filled, inhibiting both interactions and likely preventing the reaction. In this context, it is notable that the [FeFe]-hydrogenases react with hydrogen in a similar diiron(I,II) oxidation state; however, these complexes contain strong-field CO and CN^- ligands that enforce low-

spin states at both iron centers.[48] It is widely accepted that this low-spin state is crucial to the H_2 binding and activation in hydrogenases; **1** is an interesting counter-example that has a high-spin state and, consistent with this theory, does not react with H_2.

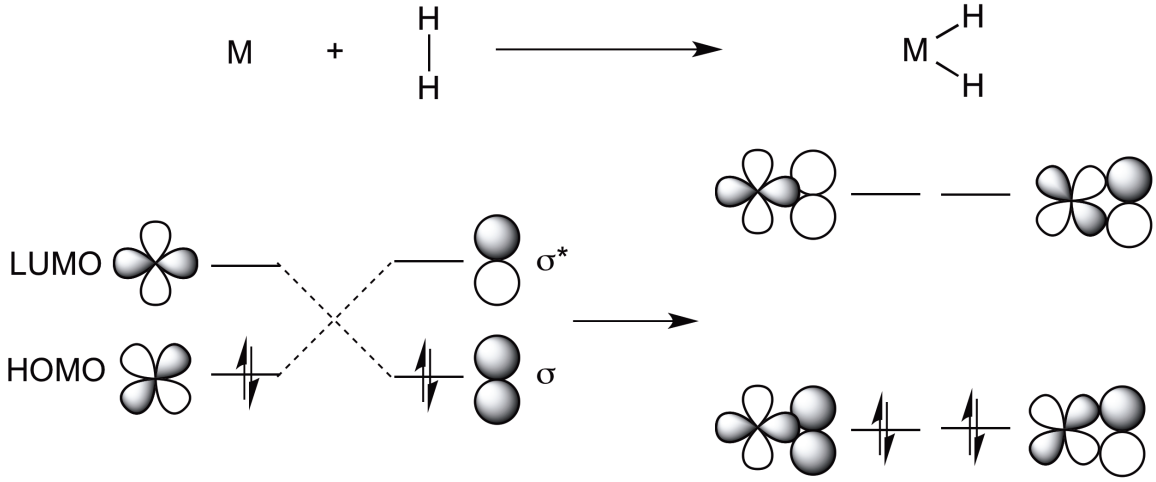

Figure 2.25. Orbital interactions in concerted oxidative addition of H_2 at a metal center. The reaction is facilitated when the metal has a high-lying filled orbital to donate to the σ* orbital on H_2 and a low-lying empty orbital to interact with the σ orbital.

On the other hand, other oxidative addition reactions with some substrates can proceed differently: with electrophiles such as CH_3I, for instance, reactions at metal centers can proceed through heterolytic R-X bond-breaking, in an S_N2-like mechanism. In other cases, R-X bonds can cleave homolytically, with buildup of radical character. **1** does not react with CH_3I, suggesting that despite its reducing character, it is not particularly nucleophilic; this is likely due to the delocalization of charge density between the two iron centers. However, **1** reacts readily with benzyl bromide, a substrate with significant propensity towards radical-like R-X cleavage. This reaction gives a number of diamagnetic and paramagnetic products, as observed by NMR spectroscopy, and thus far none has been isolated. However, a similar set of products is produced by reaction of **1** with the Cl• and Br• sources N-chlorosuccinimide and N-bromosuccinimide (NCS

and NBS, respectively). In the latter case, a green, paramagnetic product was isolated and crystallographically determined to be the mononuclear iron(III) tris-amidinate complex, $Fe(DPhF)_3$. This implies cleavage of the Fe-Fe bond upon reaction with these radical halide sources; combined with the observed decomposition upon reaction with $FcBF_4$, these studies indicate that the diiron core is not stable to oxidation.

1 is also unreactive towards electron-deficient small molecules such as CO_2 and N_2O. However, it reacts readily with small molecules that have radical ground states, such as O_2 and NO. The reaction with O_2 was reported previously by Cotton *et al:*[19] the product, $[Fe_2(DPhF)_3]_2$-μ_4O, **3**, is a tetrairon cluster compound in which the four iron centers form a distorted tetrahedron around a single central O atom. The stoichiometry dictates that each iron is in the (2+) oxidation state, implying a one-electron oxidation of each diiron unit. Interestingly, the original diiron units are relatively intact in the structure, which has a short Fe-Fe distance of 2.845(1) Å within each diiron unit and two longer distances of > 3.15 Å between the two units. However, two of the amidinate ligands rearrange to bridge the two diiron units; there is thus little hope that oxidation can be made reversible by reducing the system back the original diiron units. The molecular structure is shown in Figure 2.26.

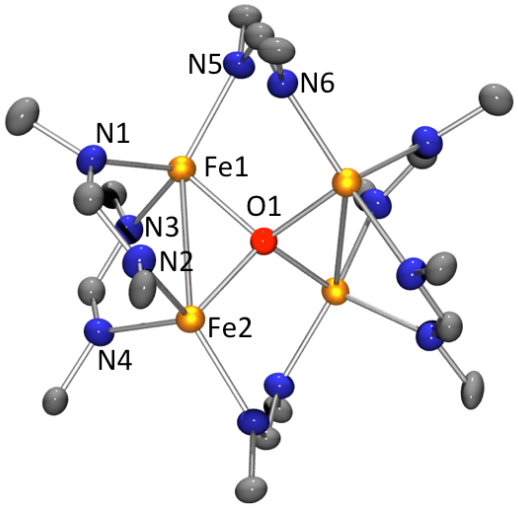

Figure 2.26. Tetrairon core of $[Fe_2(DPhF)_3]_2$-μ_4O, **3**, at 50% probability level. For clarity, hydrogen atoms, phenyl substituents, and toluene solvents have been omitted. Selected bond distances (Å) and angles (°): Fe1-Fe2, 2.845(1); Fe1-O1, 1.952(3); Fe2-O1, 1.955(3); Fe1-N1, 2.048(3); Fe2-N2, 2.056 (3); Fe1-N3, 2.061(3); Fe2-N4, 2.048(3); Fe1-N5, 2.070(3); Fe2-N6, 2.065(3); Fe1-O1-Fe2, 93.5(1); Fe1-O1-Fe1', 109.9(1); Fe1-O1-Fe2', 129.0(1).

Cotton *et al.* originally reported the isolation of **3** through two methods: the reaction of **1** with O_2, *via* addition of solvents that had been exposed to air, and the more direct reaction of $FeCl_2(HDPhF)_2$ with $LiOH{\bullet}H_2O$ and MeLi.[19] We have isolated **3** both as a byproduct in the synthesis of **1** and in reactions with O_2 and air. **3** can be separated from crude reaction mixtures of **1** by washing with methyl tert-butyl ether (MTBE); subsequent crystallization yielded an essentially identical structure to that previously reported for $[Fe_2(DPhF)_3]_2$-μ_4O. We were thus able to determine its ^{1}H NMR and UV-Vis-NIR spectra. It possesses a diagnostic, paramagnetically-shifted ^{1}H NMR spectrum (Figure 2.27) consistent with the crystallographically-observed C_2 symmetry of the molecule. Its absorption spectrum is featureless except for a strong UV-energy absorbance and a moderate ($\varepsilon \approx 450$ $M^{-1}cm^{-1}$) at a λ_{max} of 1350 nm, distinct and red-shifted from the 1250 nm absorption in **1**.

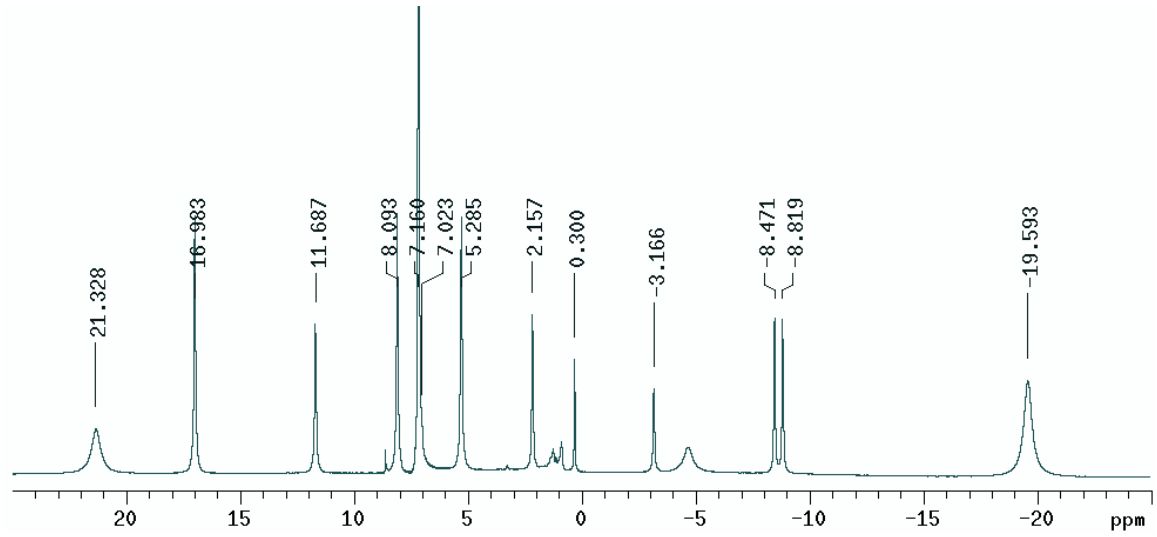

Figure 2.27. ^{1}H NMR spectrum (500 MHz, C_6D_6) of $[Fe_2(DPhF)_3]_2$-μ^4O, **3**.

Since **3** can be produced either through oxidation of **1** or by reaction of the Fe(II) precursor with organolithium reagents and lithium oxides or hydroxides, it is unclear if its formation as a byproduct in the synthesis of **1** is the result of oxidative decomposition or of competitive side-reactions. Our best efforts to exclude O_2 and H_2O have not been able to prevent it from forming in significant amounts, and these amounts do not seem to vary with conditions such as reaction scale or reaction time. We are thus tempted to ascribe its formation to reaction with lithium hydroxides or oxides in the ^{n}BuLi reagent; however, we cannot rule out reaction with adventitious O_2 or H_2O altogether. We have also investigated the small-scale reaction of **1** with controlled amounts of O_2. We have found these reactions to be quite sensitive to the amount of gas added to the reactions. With small amounts of O_2, (~0.25-0.5 equiv per $Fe_2[DPhF]_3$), clean, yellow solutions of **3** are produced; with larger amounts, the solutions turn burgundy and the NMR signal is lost. The product of these reactions is unknown. A more highly oxidized tetrairon species, $Li_2(HDPhF)_2Fe_4O_4(DPhF)_6$, was consistently produced by Cotton *et al.* by reaction of

Fe(III) sources, water, HDPhF, and organolithium reagents;[49] this has a similar burgundy color and is consistent with the higher degree of oxidation, but requires sources of lithium and proton ions that are not provided in these reactions. Presumably, similar polynuclear clusters are produced.

Considering the reducing nature of **1** and the apparent favorability of forming oxo clusters, we investigated the reaction of **1** with the electron-deficient small molecules N_2O and CO_2. These molecules are both environmentally detrimental greenhouse gases formed as waste products of combustion.[50-52] Their reaction with **1** could conceivably give oxo transfer to form **3** and N_2 or CO, respectively, in what would appear to be favorable reactions. Unfortunately, **1** does not react with CO_2 even after extended heating, nor does it react with a mixture of H_2 and CO_2. It does react with large excesses of N_2O to form **3**; however, addition of greater than 1 atm N_2O is needed for appreciable conversion. Stoichiometric amounts of N_2O show no reaction with **1**. Since industrial-grade N_2O invariably contains trace O_2, we attribute the formation of **3** to this impurity.

We have also found that **1** reacts rapidly with the ground-state radical small molecule nitric oxide (NO). The product of this reaction, **4**, is diamagnetic and crystallizes in the monoclinic space group $C_{2/c}$. X-ray diffraction revealed a diiron nitrosyl cluster in which the diiron core is largely intact and the three amidinate groups remain bridging but splay open to accommodate a planar arrangement of three nitrosyl ligands. Each iron has one of these NO ligands bind in a terminal, bent fashion, and the third bridges between the two through the nitrogen atom in a μ-1,1 fashion. The structure is shown in Figure 2.28. The structure has a C_2 rotation axis perpendicular to the Fe-Fe

axis, making one half of the molecule unique. The Fe-Fe separation is 2.4717(5) Å, similar to the distance in metallic iron and indicative of a single bond.[53] This is consistent with the 34-electron count of the diiron core, which is unsaturated by two electrons. The formal assignment of the geometry around each iron is ambiguous: without considering the other iron, it is intermediate between trigonal bipyramidal and square pyramidal ($\tau_5 \approx 0.6$). In the trigonal bypyramid, the equatorial plane would be defined by the terminal and bridging NO groups and the coplanar amidinate nitrogen, with the other two amidinate nitrogens capping the axial positions. In the square pyramid, the base of the pyramid would be defined by the three amidinate nitrogens and the bridging NO, and the apex is defined by terminal NO.

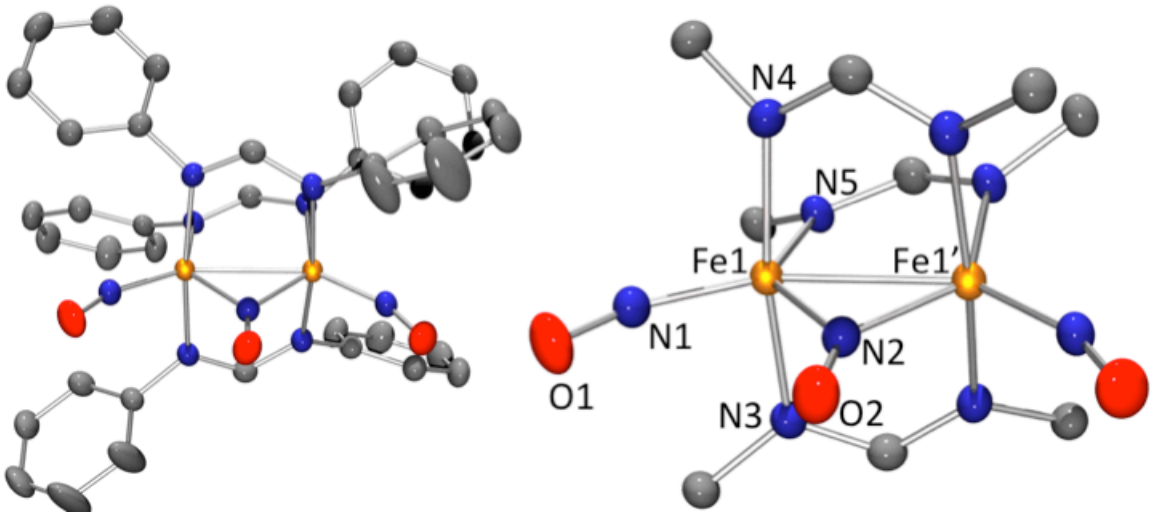

Figure 2.28. Molecular structure (left) and labeled $Fe_2(NO)_3$ core (right) of **4** at 50% probability level. For clarity, hydrogen atoms have been omitted. Selected bond distances (Å) and angles (°): Fe1-Fe1', 2.4717(5); Fe1-N1, 1.679(2); Fe1-N2, 1.803(2); Fe1-N3, 1.996(2); Fe1-N4, 2.040(2); Fe1-N5, 1.994(2); N1-O1, 1.170(2); N2-O2, 1.205(3); O1-N1-Fe1, 157.6(2); O2-N2-Fe1, 136.71(5); N1-Fe1-Fe, 145.62(6); N1-Fe1-N2, 99.07(8) N1-Fe1-N5, 127.18(7); N2-Fe1-N5, 133.54(7); N3-Fe1-N4, 170.35(7); N3-Fe1-N5, 86.08(7); N4-Fe1-N5, 86.02(7).

Since NO ligands have π* electrons very close in energy to metal 3d electrons, these ligands can be very redox-active, with accessible oxidation states ranging from NO^+ to $NO^\bullet$ to NO^-. There are thus a number of possible formulations for the formal oxidation state in **4**. It is extremely unlikely that **1** would oxidize the nitrosyls to NO^+ oxidation states, since the redox potential of NO^+ in nonpolar solvents is around +1.0V vs Fc/Fc^+, while the potential of **1** is -1.0 V.[54] This still leaves possible formulations as $Fe^{I}Fe^{II}(NO^\bullet)_3$, $Fe^{II}{}_2(NO^\bullet)_2(NO^-)$, or $Fe^{III}{}_2(NO^-)_3$. It is common to refer to such complexes through the sum of their metal d and NO π* electrons, in the Enemark-Feltham notation, to emphasize the covalency of these bonds. This would be $\{Fe_2(NO)_3\}^{16}$ for **4**. However, the oxidation states of nitrosyl ligands can also be assigned based on their geometric parameters and their vibrational frequencies. In the case of **4**, the Fe-N and N-O distances for the terminal ligands are very diagnostic of neutral ($NO^\bullet$) groups: the Fe1-N1 distance of 1.679(2) Å is perfectly in line with the range of 1.661(4)-1.695(3) Å found in dinitrosyl iron complexes (DNICs) shown to have ($NO^\bullet$) formulations, and the slightly bent Fe1-N1-O1 angle of 157.6(2)° is similarly in line with these complexes.[55,56] The N1-O1 distance of 1.170(2) likewise fits within the range 1.160(6)–1.178(3) Å found for the N-O distances in the same complexes. It is also much closer to the distance of 1.15 Å for molecular $NO^\bullet$ than the 1.26 Å for NO^- or 1.05 Å for NO^+.[57] The oxidation states of bridging nitrosyl ligands are much more ambiguous, and we cannot distinguish between the $Fe^{I}Fe^{II}(NO^\bullet)_3$, $Fe^{II}{}_2(NO^\bullet)_2(NO^-)$ forms based on structural parameters. In fact, it may not be physically meaningful to attempt to distinguish these oxidation states, considering the covalency of the Fe and NO frontier orbitals. The terminal NO groups can be

confidently assigned as NO$^{\bullet}$ radicals, however, indicating that the binding of the nitrosyls does not involve multi-electron oxidation of the diiron core.

The IR spectrum of **4** is consistent with the assignments based on structural parameters. Metal nitrosyl complexes display rich vibrational spectroscopy. The stretching frequency of free NO is 1870 cm^{-1}, and this value can vary considerably with the electronic properties of the complexes, increasing to 2377 cm^{-1} for NO^{+} and decreasing to 1470 cm^{-1} for NO^{-}. Unfortunately, the ranges of frequencies for metal-bound nitrosyls have large amounts of overlap, and they are not reliable indicators for NO$^{\bullet}$ vs NO^{-} formulations.[57] With this caveat, however, the IR spectrum of **4** is consistent with the assignment of the terminal NO groups as NO$^{\bullet}$ radicals. The spectrum is shown in 2.29, overlaid with the spectrum of **1**. The features due to the $Fe_2(DPhF)_3$ backbone are mostly unchanged, allowing assignment of the NO stretching frequencies to the new features at 1770.7, 1740.0, and 1652.8 cm^{-1}. The first two should be the symmetric and asymmetric modes of the terminal ligands. The third is then the bridging nitrosyl; its stretching frequency is at the high end of the range typically observed for these ligands (1650-1300 cm^{-1}).[57]

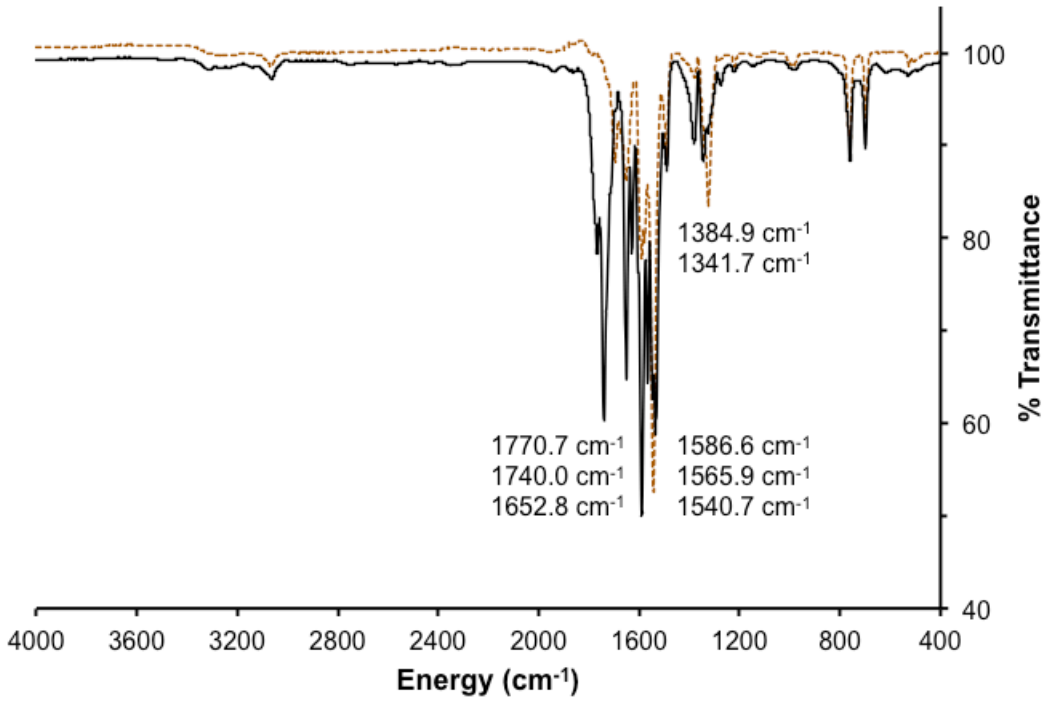

Figure 2.29. Solution-phase FT-IR spectra (THF, KBr cell) of **4** (solid black line) and **1** (dashed gold line). Subtraction of the signal for the THF background results in the somewhat irregular baseline and low intensity of the C-H stretching region (2900-3250 cm^{-1}). Frequencies for the major vibrational features of **4** are labeled; for the frequencies of **1**, see Figure 2.17.

Altogether, the results of this reactivity survey indicate that $Fe_2(DPhF)_3$ is quite reactive, but in a surprisingly selective way. It does not react with molecules showing only singlet character, but reacts rapidly with molecules possessing some radical character. In reactions with halide radicals or similar one-electron oxidants, the diiron core appears unstable and decomposes to a number of products. However, in the case of radical small molecules such as NO and O_2, these reactions result in interesting clusters in which the diiron core is intact but is oxidized by, at most, one electron.

2.4 Conclusions

The trigonal lantern bimetallics $Fe_2(DPhF)_3$, **1**, and $Co_2(DPhF)_3$, **2**, originally reported by Cotton, Murillo, *et al.*[1,3,4] have been reinvestigated in order to understand their unusual combination of strong metal-metal bonds and high-spin electronic ground states. Synthetic routes to these compounds have been developed that reliably give products in high purity and scales suitable for detailed study. This has allowed their electronic structures to be studied by a variety of experimental methods. These results indicate that both molecules have high-spin states well-isolated from lower-spin configurations. Notably, this implies that the spins of these molecules can reasonably be described through either molecular orbital and double-exchange formalisms. In addition, Mössbauer spectroscopy finds only one iron environment in **1**, suggesting strongly delocalized, formally $M^{1.5}M^{1.5}$ mixed-valent cores. Multiconfigurational calculations have also been used in order to study the molecular orbital basis of their bonding. The results from CASSCF calculations suggest that the lowest-energy configurations of **1** and **2** are essentially as predicted by Cotton *et al.*[9] In these configurations, the bonding interactions and high-spin states are found to be interrelated. The trigonal ligand field causes only small orbital energy differences between the π^*, σ^*, δ, and δ^* orbitals; these therefore fill in a high-spin fashion, giving large spin states and minimizing the population of the M-M antibonding orbitals. The multiconfigurational calculations also provide deeper insight into the bonding by revealing the effect of higher-energy configurations on the bond order. In the case of **1**, these configurations lower the bond order by populating M-M antibonding orbitals, a well-known phenomenon in first-row

metals that lowers the effective bond order to 1.15. In the case of **2**, the effects are much more interesting, as the higher-energy configurations actually depopulate the π* orbitals and populate the δ orbitals, leading to an *increased* bond order, through π- and δ-bonding character that was not predicted from qualitative or single-configurational analyses. This effect is highly structure-dependent, with effective bond orders of 0.87 and 1.16 predicted from two different geometry optimizations. These results help to explain the unexpectedly strong bonding observed for this complex. They emphasize the need for multiconfigurational techniques in order to fully understand the bonding in such systems. Finally, they underscore that strong M-M interactions can be created through the combination of several interactions that in isolation would be quite weak. These complexes are not generally considered to have "multiple-bonding" character in the same sense as, *e.g.*, dichromium and dirhenium systems, but their bonds are nevertheless the result of multiple orbital interactions, and these can combine to form unexpectedly strong M-M bonds.

The reactivity patterns of **1** have also been studied; despite its highly reduced nature, the diiron core is unreactive to even highly electron-deficient small molecules and oxidative addition substrates with closed-shell configurations. On the other hand, it is extremely reactive towards one-electron oxidants and oxidative addition substrates with radical character, but the diiron core is not stable to such oxidation. Finally **1** reacts readily with radical small molecules such as O_2 and NO, forming cluster compounds that retain the original Fe-Fe unit but indicate its one-electron oxidation. These results are all consistent with a highly reducing character that is directed to a surprising degree by the

high-spin electronic configuration.

These results suggest that the high-spin, strongly-bonded electronic structure of the trigonal lanterns results from their trigonal ligand fields and their electronic delocalization. In principle, these features should be quite general and could be applied to form bonds between different metal pairs or to the same metal pairs but within a more stable, chelating framework. Our work along both these lines is discussed in Chapter Three.

2.5 Experimental Procedures

2.5.1 Synthetic Considerations.

All manipulations were performed under a dinitrogen atmosphere in a Vacuum Atmosphere glovebox or using standard Schlenk techniques. Standard solvents were deoxygenated by sparging with dinitrogen and dried by passing through activated alumina columns of a SG Water solvent purification system. Deuterated solvents were purchased from Cambridge Isotope Laboratories, Inc., dried over CaH_2, distilled, and stored over activated 4 Å molecular sieves.

*Modified synthesis of $Fe_2(DPhF)_3$, **(1)**:* $FeCl_2(HDPhF)_2$ (750 mg, 1.44 mmol) was dissolved in toluene (90 mL) and cooled to −78°C. *n*-Butyllithium (in hexane, 2.15 mmol) was slowly added dropwise, and the reaction solution was allowed to slowly warm to room temperature over 12 hours. The resulting brown mixture was filtered, giving a light yellow-brown solution. After removal of solvent under vacuum, the dried brown

solid was redissolved in THF, layered with diethyl ether, and left to crystallize at −35° C. Yellow crystals of $Fe_2(DPhF)_3$, which formed after 2 days, were filtered and dried under vacuum. Yield: 175 mg, 35%. ^{1}H NMR (500 MHz, THF-d_8, 23° C): δ = 12.6 (12H, *meta*), −19.6 (6H, *para*), −40 (12H, *ortho*); UV/Vis/NIR (THF): λ_{max}, nm (ε, M^{-1} cm^{-1}) = 280 (63,000), 350 sh (13,000), 650 (50), 700 sh (50), 825 (70), 1250 (80).

Modified synthesis of $Co_2(DPhF)_4$. To a solution of HDPhF (11.0 g, 56.3 mmol) in THF (100 mL) was added benzylpotassium (7.3 g, 56.3 mmol) in THF (25 mL), forming a light yellow solution immediately. The mixture was stirred for 6 h, and solvent was removed under vacuum. The light yellow solid was rinsed with pentane (3 x 5 mL) and dried under vacuum, giving a light yellow crystalline powder (14.8 g, 85% yield). The ^{1}H NMR spectrum of the solid is consistent with K(THF)[DPhF]: ^{1}H NMR (C_6D_6): δ 8.81 (s, N-C*H*-N, 1H), 7.31 (t, *J* = 7.6 Hz, *meta*-C*H*, 4H), 6.96 (m, *ortho*- and *para*-CH, 6H), 3.56 (THF, 4H), 1.39 (THF, 4H). To a solution of K(THF)[DPhF] (4.4 g, 14.3 mmol) in THF (80 mL) was added $CoCl_2(THF)_{1.5}$ (1.5 g, 6.5 mmol). The mixture was stirred at rt for 2 h. The precipitate was filtered through Celite (1 cm) and volatiles were removed under vacuum. The brown-green solid was rinsed with diethyl ether (3 x 5 mL), and then dried under vacuum to give a brown powder (1.9 g, 65 % yield). ^{1}H NMR (C_6D_6, 500 MHz): δ 8.40 (s, N-C*H*-N, 4H), 6.87 (t, *J* = 7.0 Hz, *meta*-C*H*, 16H), 6.82 (t, J = 7.0 Hz, *para*-C*H*, 8H), 6.27 (d, *J* = 7.5 Hz, *ortho*-C*H*, 16H).

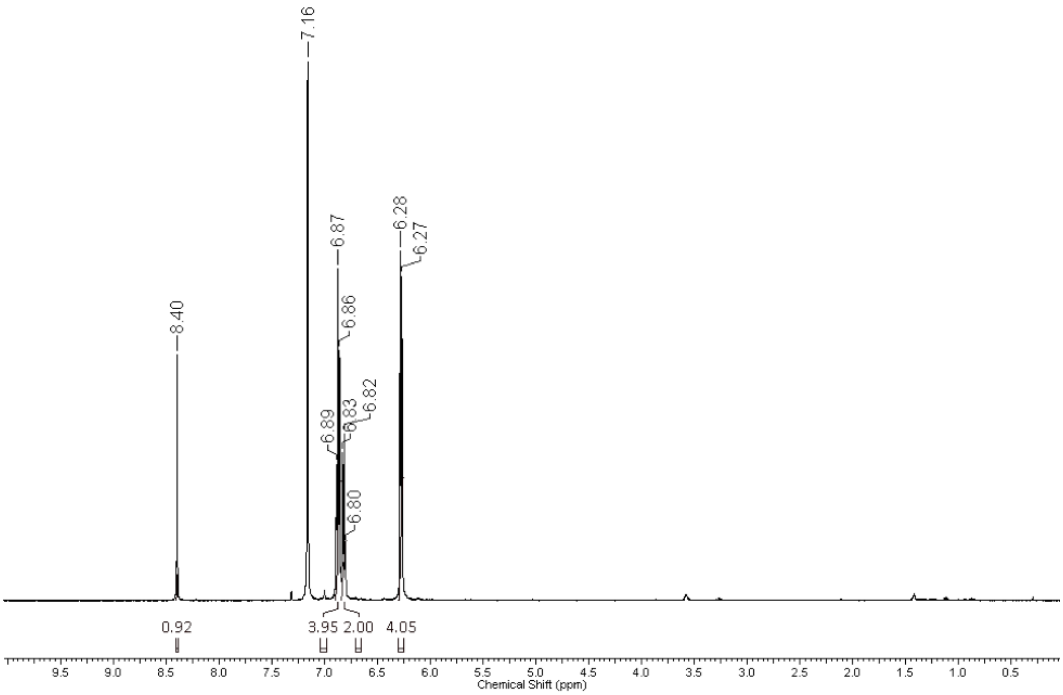

Figure 2.30 ^{1}H NMR spectrum (C_6D_6, 500 MHz) of $Co_2(DPhF)_4$.

*Modified synthesis of $Co_2(DPhF)_3$, (**2**).* To a solution of $Co_2(DPhF)_4$ (1.4 g, 1.5 mmol) in toluene (50 mL), KC_8 (205 mg, 1.5 mmol) was added, resulting immediately in a black precipitate. After 1 h, the mixture was filtered through a Celite plug, reduced to 10 mL, and cooled at −25 °C to give red-brown crystals (662 mg, 60% yield). ^{1}H NMR (C_6D_6, 500 MHz): δ 175.10 (N-C*H*-N, 3H), 13.00 (*meta*-C*H*, 12H), −26.19 (*para*-C*H*, 6H), −50.16 (*ortho*-C*H*, 12H). UV−vis (toluene): λ_{max}, nm (ε, $M^{-1}cm^{-1}$): 545 (530), 752 (200), ~1665 (100). The NIR values are only approximate because of the artifacts created by imperfect subtraction of the solvent background. Anal. Calc'd for $C_{39}H_{33}N_6Co_2$: C 66.58; H 4.73; N 11.94. Found C 66.49; H 4.65; N 11.78.

*Synthesis of [Fe2(DPhF)3]2-μ4O, (**3**). Method a.* This compound can be isolated from the crude reaction mixture from the synthesis of **1** (*vide supra*) by washing with MTBE and filtering. The filtrate is then dried under vaccum, yielding a brown solid. This is

redissolved in benzene, and the red-brown solution set to undergo vapor diffusion with pentanes. After approximately two days, pale yellow crystals are obtained.

Method b. A J-Young NMR tube was charged with a solution of **1** (5 mg, 7 μmol) in C_6D_6 (0.75 ml). The sample was freeze-pump-thawed twice on a high-vacuum line equipped with a small (4.2 mL) gas addition bulb, into which was bled O_2 until the pressure reached 16 mmHg. The bulb was then closed to the O_2 source and opened to the NMR tube, which was frozen in liquid nitrogen. When thawed, the solution turned from bright yellow to pale yellow. The product **3** was observed by NMR but not isolated. ^{1}H NMR (500 MHz, THF-d_8, 23° C): δ = 21.33 (br s, 2H), 16.98 (s, 2H), 11.68 (s, 1H); 8.09 (s, 2H); 7.02 (s, 1H); 5.28 (s, 1H), 2.16 (s, 1H); 0.30 (s, 0.5H); -3.17 (s, 0.5H); 8.47 (s, 1H); -8.82 (s, 1H); -19.59 (br s, 2H). Vis/NIR (THF): λ_{max}, nm (ε, M^{-1} cm^{-1}), 1375 (450).

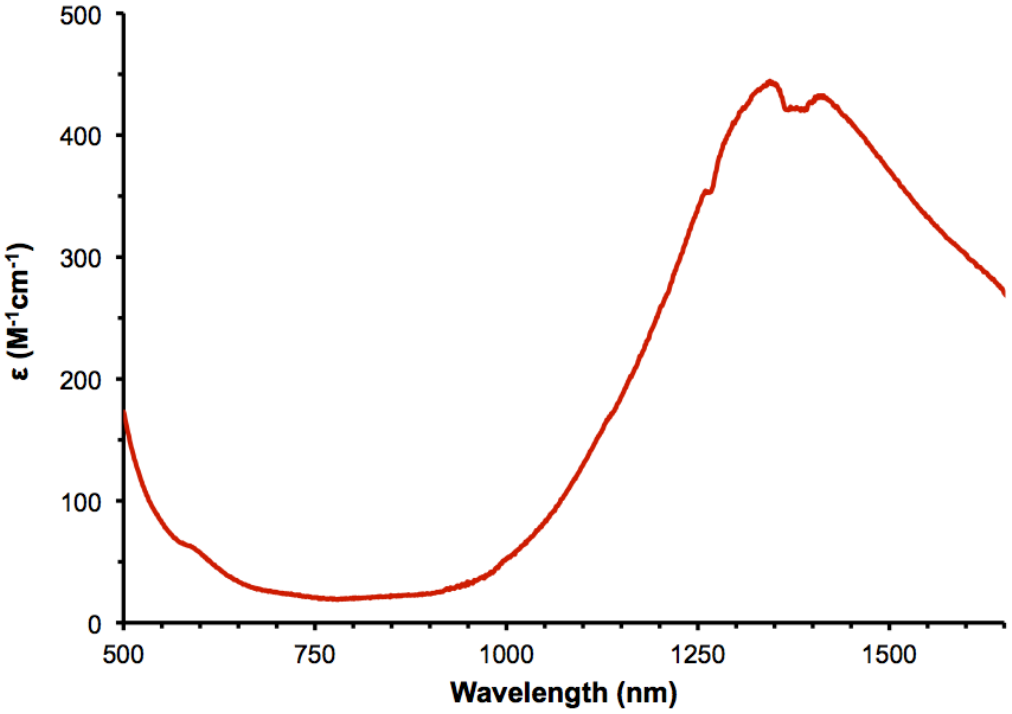

Figure 2.31 Vis-NIR absorption spectrum of **3** (THF, 6.7 mM).

*Synthesis of $Fe_2(NO)_3(DPhF)_3$, (**4**). Method a.* This compound was originally prepared and characterized in the attempted reaction of **1** with NO•BF_4 in THF. In this reaction, **1** (42.5 mg, 0.061 mmol) was dissolved in THF (12 mL) and cooled to -78 °C. NO•BF_4 (14.7 mg, 0.012 mmol) was added, causing the solution to turn dark red-brown. The reaction mixture was allowed to slowly warm to rt over the next 12 hours. The solvent was then removed under vacuum, leaving a black solid. This was dissolved in Et_2O and filtered to remove a purple/black solid; the red-orange filtrate was collected and dried, giving **4** as a brown solid (12 mg, 36%).

Method b. Compound **4** was also prepared more cleanly from the addition of $NO_{(g)}$ (1 atm) to a thick-walled reaction flask containing a solution of **1** (143.5 mg, 0.0206 mmol) in THF (30 mL) at room temperature. The $NO_{(g)}$ source was run through a heat exchanger submerged in a dry ice/acetone bath before addition to the reaction vessel. After 30 mins, during which time the solution had turned dark brown, vacuum was applied to the flask to remove residual $NO_{(g)}$ and solvent, leaving a dark brown solid. This was dissolved in Et_2O and filtered, giving **4** as a red-brown solid (118.2 mg, 73%). ^{1}H NMR (500 MHz, THF-d_8, 23° C): δ = 9.10 (br s, 2H), 7.16 (br s, 2H), 7.10 (br s, 8H); 6.94 (br s, 4H); 6.58 (br s, 4H); 4.34 (br s, 2H).

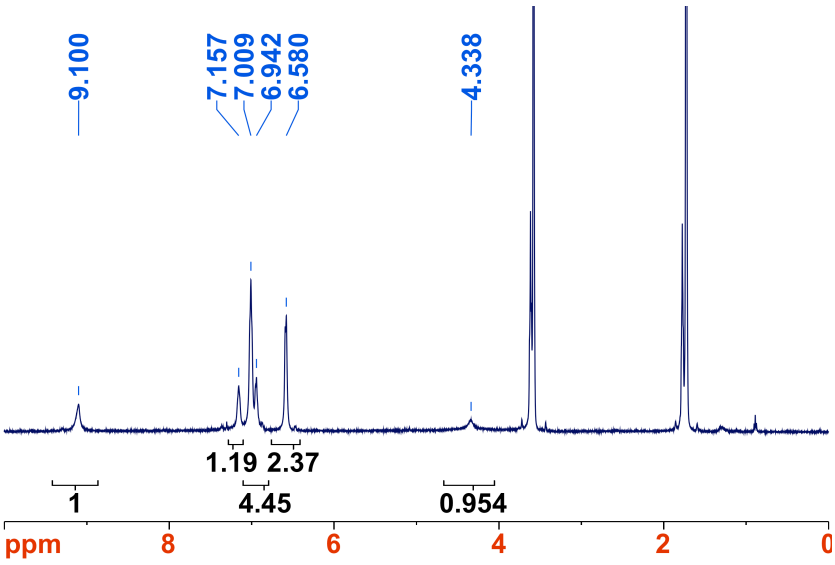

Figure 2.32 ^{1}H NMR (THF-d_8, 500 MHz) of **4**.

2.5.2 X-Ray Crystallographic Data Collection and Refinement of the Structures. Single crystals of **1**•$(C_6H_6)_{0.5}$ and **3**•$(C_6H_6)_{1.5}$ were grown from vapor diffusion of hexane into saturated benzene solutions at room temperature. Single crystals of $Fe_2(DPhF)_3(NO)_3$ were grown by vapor diffusion of pentane into a concentrated THF solution. A thin yellow plate of **1** (0.3x0.3x0.1 mm^3), an orange block of **3** (0.5x0.3x0.3 mm^3), and a brown block of **4** (0.1x0.1x0.1 mm^3) were placed on the tip of a glass capillary and mounted on either a Siemens SMART Platform CCD diffractometer (for **1** and **3**) or a Bruker Apex-II diffractometer (for **4**) for data collection at 173 K. The data collections were carried out using Mo Kα radiation (graphite monochromator). The data intensity was corrected for absorption and decay (SADABS). Final cell constants were obtained from least squares fits of all measured reflections. The structures were solved using SHELXS-97 and refined using SHELXL-97. A direct-methods solution was calculated

which provided most non-hydrogen atoms from the E-map. Full-matrix least squares / difference Fourier cycles were performed to locate the remaining non-hydrogen atoms. All non-hydrogen atoms were refined with anisotropic displacement parameters. Hydrogen atoms were placed in ideal positions and refined as riding atoms with relative isotropic displacement parameters. Crystallographic data are summarized in Table 2.8.

Table 2.8. Crystallographic data for $[Fe_2(DPhF)_3]\bullet 0.5(C_6H_6)$, $[Fe_4O(DPhF)_6]\bullet 1.5(C_6H_6)$, and $Fe_2(NO)_3(DPhF)_3$.

	$[Fe_2(DPhF)_3]\bullet 0.5(C_6H_6)$	$[Fe_4O(DPhF)_6]\bullet 1.5(C_6H_6)$	$Fe_2(NO)_3(DPhF)_3$
chemical formula	$C_{39}H_{33}N_6Fe_2(C_6H_6)_{0.5}$	$C_{78}H_{66}N_{12}Fe_4O(C_6H_6)_{1.5}$	$C_{36}H_{33}N_9O_3Fe_2$
formula weight	736.48	1527.96	727.42
crystal system	Triclinic	Triclinic	Monoclinic
space group	P-1	P-1	C2/c
a (Å)	11.311(2)	14.806(4)	9.9124(6)
b (Å)	11.949(2)	15.394(5)	16.709(1)
c (Å)	13.941(2)	18.906(6)	22.014(1)
α (^{o})	108.301(2)	85.322(4)	90.00
β (^{o})	91.287(2)	86.317(4)	92.067(1)
γ (^{o})	95.540(2)	63.554(3)	90.00
V (Å^3)	1777.7(5)	3844(2)	3643.7(4)
Z	2	2	4
D_{calcd} (g cm^{-3})	1.449	1.233	1.326
λ (Å), μ (mm^{-1})	0.71073, 0.859	0.71073, 0.791	0.71073, 0.836
T (K)	173(2)	173(2)	173(2)
θ range (deg)	1.54 to 27.53	1.08 to 27.56	1.85 to 28.04
reflns collected	6520	17369	4360

unique reflns	3189	11338	3398
data/restraint/parameters	6820 / 0 / 436	17369 / 0 / 919	4360 / 0 / 241
R_1, wR_2 ($I > 2\sigma(I)$)	0.0661, 0.1131	0.0690, 0.1135	0.0348, 0.0743

2.5.3 Physical Measurements.

NMR spectra were collected on a Varian Inova 500 MHz spectrophotometer. Room-temperature visible- and near-infrared absorption data were collected on a Cary-14 spectrophotometer. UV-wavelength absorption spectra were collected on a Cary 300 Bio UV-Visible spectrophotometer. Samples of $Fe_2(DPhF)_3$ and $Co_2(DPhF)_3$ were recrystallized from THF/hexane prior to data collection, then redissolved in THF. Cyclic voltammetry was conducted using a CH Instruments 600 electrochemical analyzer. The one-cell setup utilized a glassy carbon working electrode, platinum wire counter electrode, and Ag/AgNO3 reference electrode in acetonitrile. Analyte solutions were prepared in a THF solution of tetra-^{n}butylammonium hexafluorophosphate (0.1 M) and referenced internally to the $FeCp_2/FeCp_2$ redox couple. Infrared spectroscopy was collected on a Bruker Tensor-37 FTIR using the OPUS 6.5 software, using concentrated THF solutions in a KBr cell. Magnetic susceptibility data were measured from powder samples of solid material in the temperature range 2 - 300 K by using a SQUID susceptometer with a field of 1.0 T (MPMS-7, Quantum Design, calibrated with standard palladium reference sample, error <2%). Multiple-field variable-temperature magnetization measurements were made at 1 T, 4 T, and 7 T in the range 2-300K with the magnetization equidistantly sampled on a 1/T temperature scale. The experimental data were corrected for underlying diamagnetism by use of tabulated Pascal's

constants,[34,35] as well as for temperature-independent paramagnetism. The susceptibility and magnetization data were simulated with our program julX for exchange coupled systems.[36] The simulations are based on the usual spin-Hamilton operator for mononuclear complexes with $S = 7/2$ and $S = 5/2$:

$$\hat{H} = g\beta\vec{\hat{S}}\cdot\vec{B} + D[\hat{S}_z^{\,2} - 1/3S(S+1) + E/D(\hat{S}_x^{\,2} - \hat{S}_y^{\,2})]$$

where g is the average electronic g value, and D and E/D are the axial zero-field splitting and rhombicity parameters. Magnetic moments are calculated after diagonalization of the Hamiltonian from the eigenfunctions using the Hellman-Feyman theorem $\mu_i(B) = \langle\psi_i|(dH)/(dB)|\psi_i\rangle$. Powder summations were done by using a 16-point Lebedev grid.[37] Since our program is not equipped for individual spins larger than 5/2, we reproduced the octet ground state of **1** by adopting ferromagnetic coupling of $S_1 = 3/2$ and $S_2 = 2$ with a exceedingly large exchange coupling constant J = 300 cm^{-1}. This value is a conservative estimate of the true coupling of the mixed-valence iron dimer since the excited states are higher in energy so that thermal population cannot be detected.

Mössbauer data were recorded on an alternating constant-acceleration spectrometer. The minimum experimental line width was 0.24 mm s^{-1} (full width at half-height). The sample temperature was maintained constant in an Oxford Instruments Variox or an Oxford Instruments Mössbauer-Spectromag 2000 cryostat, which is a split-pair superconducting magnet system for applied fields (up to 8 T). The field at the sample is oriented perpendicular to the γ-beam. The ^{57}Co/Rh source (1.8 GBq) was positioned at

room temperature inside the gap of the magnet system at a zero-field position. Isomer shifts are quoted relative to iron metal at 300 K. Magnetic Mössbauer spectra were simulated using the spin-Hamiltonian given in (eq.1). The hyperfine interactions for ^{57}Fe were calculated with the usual nuclear Hamiltonian.[38]

2.5.4 Computational Methods

1 and **2** was studied using density functional theory (DFT) and the complete active space self-consistent field (CASSCF) method,[18] followed by a multi-configurational second-order perturbation theory (CASPT2) method.[39] It has been demonstrated that this strategy is successful in predicting accurate results for ground and electronically excited states of bimetallic systems.[40,41,42,43,44] In all calculations, the symmetry constraints of the C_2 point group were imposed to the system.

DFT calculations. Geometry optimizations of **1** and **2** were performed for the various possible spin states at the DFT level employing the Perdew-Burke-Ernzerhof (PBE) exchange-correlation functional[45] and the TURBOMOLE 6.1 program package.[46]

For **1** and **2**, the initial inputs for the geometry optimizations were the experimental structures. Since, in the case of **2**, this resulted in an underestimated Co-Co distance and N-Co-N angles severely distorted from C_3 symmetry, a new structure was generated. One half of the molecule used the coordinates from the experimental structure as inputs, and the other half of the molecule was constructed by rotating these coordinates around a C_2 symmetry axis. The Co-N and N-Co-N angles were fixed, and the C_2 symmetry constraints imposed, but the structure was otherwise allowed to refine normally. For all

atoms, the double-ζ quality basis sets def-SV(P) were used. DFT calculations were performed with the broken symmetry option (unrestricted calculations) and the resolution-of-the-identity (RI) approximation.[47] Hyperfine parameters were calculated using ORCA program package.[48] For Fe atoms, the CP(PPP) basis set designed by Neese and coworkers for accurate calculations of hyperfine coupling in transition metal compounds was used.[49,50] The all-electron Gaussian basis sets used were those reported by Ahlrichs and coworkers, including TZVP basis set for N atoms and SV(P) for C and H atoms.[51,52] The DFT calculations of the Mössbauer parameters for **1** were performed using four functionals: B3LYP, BP86, TPSSh and B2PLYP for comparison.

CASSCF/CASPT2 Calculations. All CASSCF/CASPT2 calculations were performed with the MOLCAS-7.4 package[53] using the DFT-optimized structures with imposed two-fold symmetry for all possible spin states. The relativistic all-electron ANO-RCC basis sets[54,55] were used for all elements. Since MOLCAS works in subgroups of D_{2h}, all calculations were performed in the C_2 point group to minimize computational cost. For the Fe, Co, and N atoms have basis set of double-ζ quality (ANO-RCC-VDZP) with the following contractions: [5s4p2d1f] for Fe and [3s2p1d] for N were used. The remaining C and H atoms have basis sets of minimal basis quality (ANO-RCC-MB) with a contraction of [2s1p] for C and [1s] for H. Scalar relativistic effects were included by using the Douglas-Kroll-Hess Hamiltonian.[56] The two-electron integral evaluation was simplified by employing the Cholesky decomposition technique.[57,58,59]

The ground- and excited-state wave functions were computed at the CASSCF

theory level, and corresponding energies were computed at the CASPT2 theory level. An imaginary level shift of 0.2 a.u. was used to avoid intruder states.[60] The natural orbital occupation numbers were used for the evaluation of the effective bond order (EBO),[14,17] which is calculated as the difference between the total occupancies of the bonding and antibonding molecular orbitals of the Fe-Fe bond divided by two.

CAS choice. For **1**, a complete active space was used consisting of all 13 valence electrons of both Fe ions distributed over 13 orbitals, denoted as AS (13, 13). This active space was optimized to include all the 3*d* Fe orbitals and three additional bonding orbitals, one σ- and two π-(Fe-Fe) MOs that primarily consist of atomic orbitals in the fourth shell of Fe atoms (for correlation effects between the third and fourth shell orbitals of the Fe atoms). Computations of the excited-state wave functions were performed using AS (13, 13) as well as AS (11, 15). The latter active space excludes the lowest doubly-occupied σ-orbital formed by the $3d_z^2$-orbitals of Fe ions and includes three additional formally empty MOs of the fourth shell. Many electronic states were computed with the (13,13) active space, namely the lowest eight octet states belonging to the *A* irreducible representation, the lowest six octet states belonging to the *B* irreducible representation, and the lowest six *A* and *B* sextet and quartet states. The intensities of the transitions among all the states including spin-orbit coupling were determined by using the complete active space state interaction method, CASSI,[61] which employs an effective one-electron spin-orbit (SO) Hamiltonian, based on the mean field approximation of the two electronic part.[62] To compute SO coupling, a SO Hamiltonian matrix was constructed using the

basis of all 13/13 CASSCF wave functions corresponding to the octet, sextet, and quartet states within 2.2 eV of the ground state. A total of 14 octet, 12 sextet, and 12 quartet states were thus included, giving a total of 232 spin-orbit states. Dynamic correlation energy was introduced in the consideration by substituting the diagonal elements of the Spin-Orbit Hamiltonian matrix by the corresponding CASPT2 energies.

In the case of **2**, a complete active space was used consisting of all 15 valence electrons of both Co ions distributed over 13 orbitals, denoted as AS (15, 13). This active space was optimized to include all the 3d Co orbitals and three additional bonding orbitals, one σ- and two π-(Co-Co) MOs that primarily consist of atomic orbitals of the fourth shell of Co atoms. These three additional orbitals were used in order to take into account correlation effects between the third and fourth shell orbitals of the Co atoms.

Chapter 3

Synthesis and Characterization of New Trigonal Lantern Compounds Using a Tripodal Tris-Amidinate Ligand

In part from:

Zall, C. M.; Clouston, L. J.; Young, V. G., Jr; Ding, K.; Kim, H. J.; Zherebetskyy, D.; Chen, Y.-S.; Bill, E.; Gagliardi, L.; Lu, C. C. Mixed-Valent Dicobalt and Iron-Cobalt Complexes with High-Spin Configurations and Short M-Co Bonds. *Inorg. Chem.* **2013**, *52*, 9216-9228.

3.1 Overview

The trigonal lantern framework of bimetallic complexes coordinated within a trigonal ligand field is extended to new complexes using a tripodal tris(amidinato)amine ligand. By tethering three amidinate donors to an apical amine, this platform offers two distinct metal-binding sites that can be metallated in a stepwise fashion. This enables the controlled synthesis of both homobimetallic and heterobimetallic compounds, as demonstrated by the synthesis of dicobalt and iron-cobalt compounds. The coexistence of high-spin states and strong metal-metal bonding, as seen in the earlier trigonal lantern compounds, is retained in these complexes: their $[Co_2]^{3+}$ and $[FeCo]^{3+}$ cores have high-spin sextet and septet ground states, respectively, and their solid-state structures reveal extremely short metal-metal bond distances of 2.29 Å for Co−Co and 2.18 Å for Fe−Co. The latter is the shortest distance for an iron-cobalt bond to date. In addition, the high-spin electronic configuration is unique among iron-cobalt compounds and possibly among all heterobimetallic compounds that contain metal-metal bonds. There is a surprising regioselectivity in the synthesis of the iron-cobalt compound, allowing isolation of only one of the two possible heterobimetallic isomers. By X-ray anomalous scattering techniques, the metal positions were determined to be $(Fe_{0.94(1)}Co_{0.06(1)})(Co_{0.95(1)}Fe_{0.05(1)})L^{Ph}$, in which the cobalt resides predominantly in the "bottom" metal site, containing the apical donor. Based on spectroscopic data and theoretical calculations, it is proposed that the formal $[FeCo]^{3+}$ core is fully delocalized but that the $[Co_2]^{3+}$ is more polarized.

3.2 Introduction

Given the scarcity of metal-metal bonds between first-row transition metals and their potential for applications in catalysis (*vide supra*), we are interested in developing platforms that can enable the synthesis of bimetallic compounds containing metal-metal bonds between a wide variety of metals. We aim to create a large library of such compounds by systematically varying the metals and donor groups in order to observe their effects on features, such as bond polarity and redox potential, that may have significant effects on reactivity. As part of this pursuit, we are exploring bimetallic complexes of mid- to late-first-row metals coordinated by hard donor atoms, such as nitrogen. Such complexes have significant biological relevance, as the multimetallic active sites of a large number of metalloenzymes contain mid- to late-first-row metals, from manganese through copper. Moreover, the ligand sets used in Nature are usually hard nitrogen and oxygen donors. Such donors have been widely used in the synthesis of bimetallic complexes. However, with first-row metals in conventional geometries, as described in Section 1.2.5, these donor sets typically result in complexes with weak to no metal-metal bonding. Given the ability of the "trigonal lantern" framework to enforce strong metal-metal bonds in diiron and dicobalt complexes, we were interested in testing the generality of this framework, particularly whether it could be extended to mixed-metal, heterobimetallic pairs.

3.2.1 Mixed-Metal Systems and M-M Bond Polarization

Combinations of different metals are prevalent in biology, such as nickel and iron

in the active sites of [Ni-Fe]-hydrogenase[1] and carbon monoxide dehydrogenase;[2,3] iron and molybdenum or vanadium in nitrogenase;[4,5] iron and manganese in some ribonucleotide reductases (RNRs) [6,7] and in the N-oxygenase AurF;[8] iron and zinc or manganese in purple acid phosphatases;[9,10] calcium and manganese in the $CaMn_4O_4$ cluster in the oxygen-evolving center (OEC) of Photosystem II;[11,12] and iron and copper in the active site of cytochrome *c* oxidase.[13] The precise roles of the two metals are not always clear in these enzymes, but they can have profound effects on their reactivity. For instance, the identity of the M' in synthetic $M'Mn_3O_4$ synthetic models of the OEC can dramatically influence the redox potential of the cluster[14,15] and can direct the oxidative reactivity of the cluster.[16] Similarly, the mechanism of O_2 activation at the R2 subunit of RNRs is believed to be different for Fe-Mn than for Fe-Fe active sites.[17] In other cases, the identity of the metal may be important for regulatory purposes, by making a catalytically-inactive state available through oxidation or reduction.[9,18,19] The importance of metal identity and specificity within these enzymes can also be inferred from the extensive regulatory systems that have evolved to control the uptake and delivery of each metal within the cell.[20-22]

Synthetic model complexes can play a crucial role in the process of understanding and exploiting the cooperative interactions between multiple metal centers by providing platforms within which a variety of metals can be combined and their interactions can be studied. Such studies will require ligand frameworks that allow the selective synthesis of a variety of metal pairs. These would ideally form an isostructural series, where the effects of the different metals can be compared without complications. Having identified

low-coordinate, trigonal frameworks as an interesting structural motif in which strong M-M bonding and high-spin states can be enforced between first-row transition metals, we were interested in testing the generality of this motif. One obvious measure of generality is the number of metal pairs, other than diiron and dicobalt, that can be prepared with this motif. Another question of interest is the extent to which the M-M interaction can be polarized and retain the strong bonds and high-spin states.

We envisioned that bond polarization could be induced in at least two ways within the general "trigonal lantern" motif. One is to form bonds between two different metals; another is to use ligands with different donor properties at each metal site. Examples at the limits of either case are well-known in the literature: for instance, combinations of very early metals with very late metals have been well-studied[23-25] and can show interesting reactivity, such as the activation of CO_2 by a [Zr-Co] complex to form a metal-bound CO and a bridging oxo.[26] In our own laboratory, low-valent [Al-Fe] and [Al-Co] complexes were found to activate and functionalize dinitrogen using silyl chloride reagents.[27] These early-late metal pairs are made using ligands with very different donor sets, with "hard" donors coordinating to the early metal and "soft" donors coordinating to the later metal. The bonding in these cases is often considered to be essentially dative, although it may have varying amounts of covalent character.

Bond polarization may also be induced within metals of the same type by using ligands with very different donor properties. At the limits of this approach are the "xenophilic" complexes, in which higher-valent ions coordinated by weak-field ligands are combined with lower-valent metals bound to π-accepting ligands, as in

$[Co(py)_3Co(CO)_4]^+$, *TpFeCo$(CO)_4$, and $Mn(THF)_2[Mn(CO)_5]_2$, where py = pyridine and *Tp is a series of hydrotris(dialkylpyrazolyl)borate derivatives. The M-M interactions in these complexes are so strongly polarized that they are primarily electrostatic in nature. As a result, the bonding is sufficiently weak and ionic in character that the metals dissociate in solution.[28-31]

More interesting electronic situations are found in between these extremes, with more similar metals and donor sets. In such cases the bonding is more covalent, there are more variable spin interactions, and there is more direct relevance to biological and heterogeneous systems. This space has been less well explored, largely due to the difficulty in selectively preparing such complexes. However, there has been a recent renewal of activity in this field using interesting new strategies. For instance, the group of Christine Thomas has pioneered the use of ligands with dissimilar combinations of hard amide and soft phosphine donor groups, originally designed for early/late metal combinations, to prepare homobimetallic and heterobimetallic complexes with mid- and late-first-row metals.[32-35] Diiron and dicobalt complexes have been prepared with these ligands that show relatively short M-M distances: for instance, dicobalt(II,II), dicobalt(I,I) and dicobalt(II,I) species could be prepared and showed Co-Co bonds of 2.60, 2.55, and 2.49 Å, respectively.[35] The dicobalt(I,I) was found to have an intermediate $S = 1$ ground state, while the dicobalt(II,I) was low-spin, with $S = ½$. These molecules showed flexibility in their coordination modes that could complicate interpretation of their bonding: in the dicobalt(II,II) dihalide, the two ligands bridge in an asymmetric fashion, wherein both amide donors coordinate to a single cobalt, while in

the dicobalt(I,I) complex, the ligands rearrange to bridge the metals symmetrically, resulting in identical cobalt environments. Upon oxidation to the dicobalt(I,II) complex, however, the ligands rearrange to again bridge asymmetrically, creating a polar, mixed-valent Co-Co bond. This is shown in Figure 3.1.

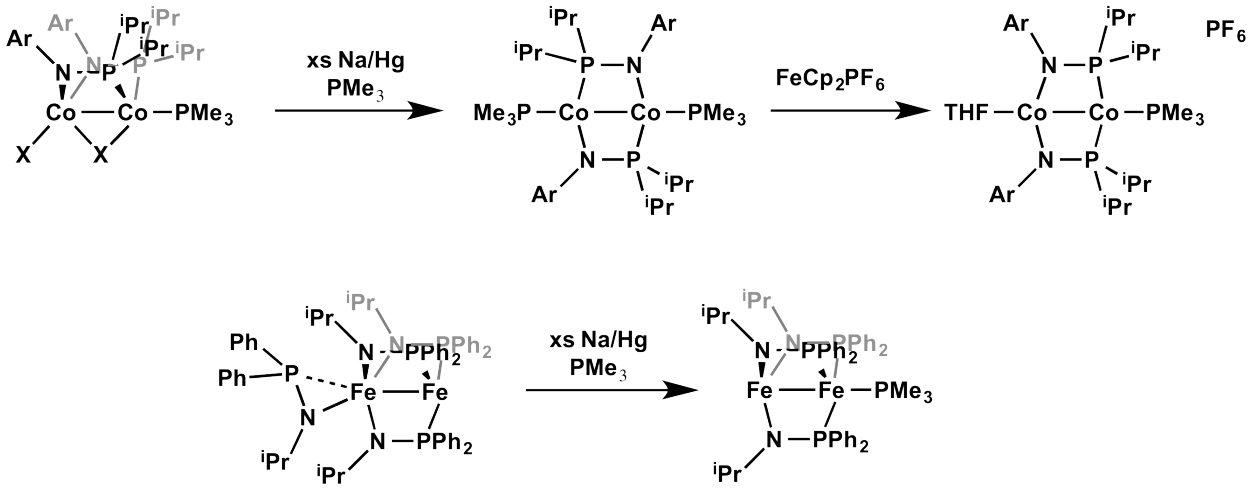

Figure 3.1. Routes to diiron and dicobalt bimetallic complexes using phosphinoamide ligands, as prepared by Thomas *et al*.

Trigonal diiron(II,II) and –(I,II) complexes were also prepared using three phosphinoamide ligands. Two such complexes are shown in Figure 3.1: these have Fe-Fe distances of 2.8684(6) and 2.4645(5) Å for the diiron(II,II) and –(I,II), respectively.[34] These compounds retain the same coordination mode in both oxidation states, in which all three amides coordinate to one Fe and all three phosphines coordinate to the other. However, not all of the diiron complexes are so consistent in their coordination modes; simple variation of the substituents on N and P can cause rearrangement of the diiron(II,II) complex to an asymmetric arrangement of ligands, along with a significant shortening of the Fe-Fe distance to 2.6112(7).[33] The flexibility of the ligands in these systems clearly complicates the comparison of M-M bonding; enforcing a more rigid

geometry would allow more direct conclusions about the role of polarization in these bonds.

At the other end of the spectrum of M-M bond polarization are complexes in which different metals are coordinated by ligands with similar donor groups. Notable work in this area was reported very recently by Betley and Eames, who showed that new heterotrimetallic clusters could be formed by direct substitution of cobalt dihalides into a preassembled triiron core.[36] The structures of these complexes are shown in Figure 3.2: they contain three metals in a trigonal arrangement, coordinated by a hexadentate, hexaanionic ligand, as well as one neutral ligand (pyridine or MeCN) and a halide ligand, giving a formally mixed-valent $[M_2^{II}M^{III}]^{7+}$ core. This trimetallic core is asymmetric in all three molecules, featuring a bimetallic unit with a short M-M distance and delocalized $M^{2.5}M^{2.5}$ oxidation states set apart from a M^{II}-halide center. Interestingly, in this series of $[Fe_3]^{7+}$, $[Fe_2Co]^{7+}$, and $[FeCo_2]^{7+}$ clusters, the M-M distances appear to depend much more strongly on their specific positions in the asymmetric M-M---M core than on the identity of the metal. There is a strong preference for Co to occupy the more strongly bonded positions; however, the M-M distance within this dinuclear unit remains essentially unchanged regardless of the metals occupying these positions, at 2.2955(8) Å for $[Fe_2]^{5+}$, 2.2934(8) Å for $[FeCo]^{5+}$, and 2.2971(5) Å for $[Co_2]^{5+}$.[36,37] On the other hand, the longer M---M' distances vary more substantially, decreasing from 2.65 and 2.73 Å for Fe-Fe to 2.52 and 2.53 Å for Fe-Co. Curiously, the decrease in bond distance on substituting Co for Fe is the opposite of the trend observed in the trigonal lantern systems. However, the most important determinants of bond metrics in this system are

the positions within the asymmetric core; this obscures the effects that are due to metal identity. The effect of the metals on more subtle effects, such as differences in magnetic interactions and bond polarity, are more ambiguous: the M-M interactions between the metals in the strongly-coupled site range from intermediate-spin ($S = 3/2$ for Fe-Fe; $S = 1$ for Fe-Co) to low-spin ($S = 1/2$ for Co-Co), while the weaker M---M interactions change from weak ferromagnetic coupling (for $[Fe_3]^{7+}$) to weak antiferromagnetic coupling (For $[Fe_2Co]^{7+}$ and $[FeCo_2]^{7+}$).[36,37] While these are impressive and intriguing results, the complexity of the asymmetric, trinuclear core prevents a systematic comparison of the M-M' interactions.

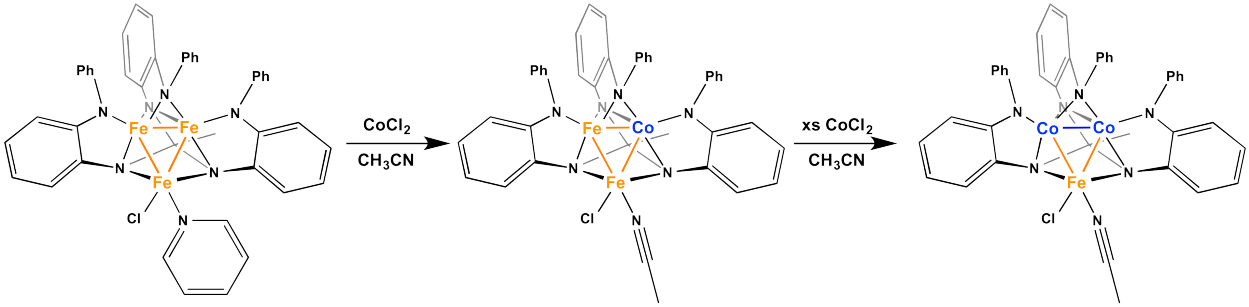

Figure 3.2. Trinuclear complexes prepared by Betley and Eames.[36,37]

3.2.2 Ligand-Directed Synthesis of Bimetallics in the Lu Group

We have been working to develop platforms that allow a direct comparison between an isostructural series of complexes in which the metals and/or the donor sets are varied. To simplify the synthesis and interpretation, we have limited our focus to bimetallic complexes. Rather than rely on self-assembly of the metal pairs and bridging groups, we have designed chelating ligands that control the coordination number and orientation of the donor sets. These frameworks are also designed to facilitate stepwise insertion of the

metals, to maximize the selectivity in synthesizing mixed metal pairs. Through addition of only one equivalent of metal at a time, we can minimize the production of homobimetallic byproducts, *i.e.* M-M-L and M'-M'-L, in the synthesis of M'-M-L; they should also lead to synthetic control over the metal positions, *i.e.* M-M'-L vs M'-M-L. Three of the ligand frameworks used in the Lu Group are shown in Figure 3.3. These are structurally similar in combining three bidentate bridging groups with a tripodal base, either tris(2-aminoethyl)amine ("*tren*"), or N(*o*-$NH_2C_6H_4)_3$, in which the ethylene arms of *tren* are replaced by *o*-phenylene spacers. They differ in the polarity of their bridging groups, however: the tris(amidinato)amine ("*tramen*") ligands, shown at the right of Figure 3.3, contain nitrogen donors with similar charges in both metal binding sites, as in the trigonal lanterns $Fe_2(DPhF)_3$ and $Co_2(DPhF)_3$. The $(py)_3$*tren* ligand, shown in the middle of Figure 3.3, also contains nitrogen donors in both binding sites, but these are differentiated: the top plane of donors features neutral, somewhat π-accepting pyridine donors, while the bottom pocket has hard, anionic amide donors. However, this charge is delocalized to some extent *via* resonance. There is an even greater disparity in the donor sets of the N(*o*-$C_6H_4NCH_2P^iPr_2)_3$ ligand at the right side of Figure 3.3, which features soft phosphine donors in the top pocket and hard amides in the bottom site. These three ligands provide an interesting contrast. Ideally, they would allow the synthesis of a wide variety of metal pairs within all three ligands that can then be used to compare the effects of the different donors on the M-M bonding. In practice, we anticipated that the disparate donor sets of N(*o*-$C_6H_4NCH_2P^iPr_2)_3$ would be better suited for synthesis of early/late metal pairs, while the all-nitrogen-based donors of the *tramen* and $(py)_3$*tren* ligands

would be better suited for mid-to-late metal combinations.

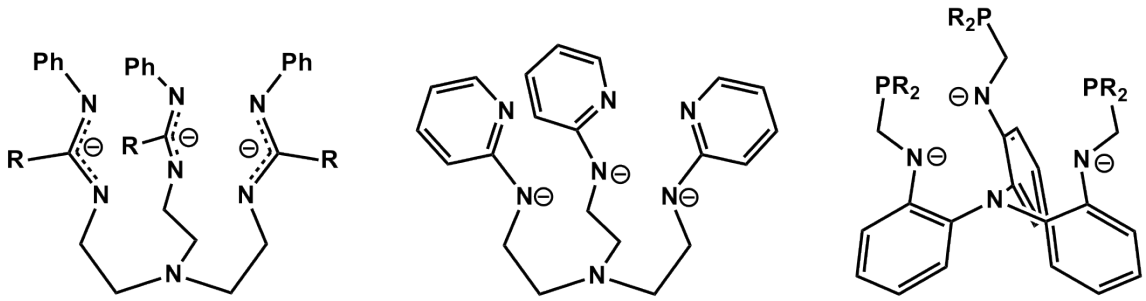

Figure 3.3 Ligand architectures used in the Lu Group.

3.2.3 Homobimetallic and Heterobimetallic Complexes Using Tris(Amidinato)amine Ligands

The work described in this chapter focuses on the research into the coordination chemistry of the new tris(amidinatoethyl)amine ligands L^{Ph} and L^{tBu} (Figure 3.4). These provide three amidinate bridging groups similar to those in the "trigonal lantern" complexes $Fe_2(DPhF)_3$ and $Co_2(DPhF)_3$,[38-41] but do so within a chelating framework that imparts stability and controls the coordination number. More importantly, it provides two metal binding sites that have essentially equal charges but are differentiated by the apical amine donor in the "bottom" binding pocket. With these ligands, we set out to create an isostructural series of different metal combinations within which the effects of metal identity on electronic properties and reactivity could be compared. Using the phenyl-substituted derivative ($[L^{Ph}]^{3-}$), we have been able to isolate and study the dicobalt species, $Co_2(L^{Ph})$ (**1**). By comparing **1** with $Co_2(DPhF)_3$, we show that the addition of an apical amine donor does not significantly perturb the electronic structure of the dicobalt core. We also report a rare iron-cobalt heterobimetallic, $FeCo(L^{Ph})$ (**2**). The isolation of

this complex demonstrates the utility of this ligand architecture for gaining access to heterobimetallics. By comparing **1** to **2**, we show that the swapping of cobalt for iron retains the high-spin, metal-metal bonded configuration of the other trigonal lantern species. We have also, through collaboration with the group of Prof. Laura Gagliardi, examined the electronic structures of **1** and **2** through high-level, multiconfigurational calculations. These accurately predict the spin state and geometry of the complexes, show that the strong bonding is the result of similar orbital interactions to those in the earlier trigonal lanterns, and find subtle but intriguing evidence for a reversal of bond polarization between **1** and **2**, suggesting a competition between ligand effects and metal effects. Finally, X-ray anomalous scattering techniques have been used to assess the positions of Fe and Co within the structure. These results indicate a high selectivity for the isomer shown in Figure 3.4. Attempts to produce the other heterobimetallic isomer, $CoFeL^{Ph}$, have resulted instead in $FeCoL^{Ph}$, suggesting a thermodynamic preference for this isomer, rather than synthetic control, leads to the observed selectivity.

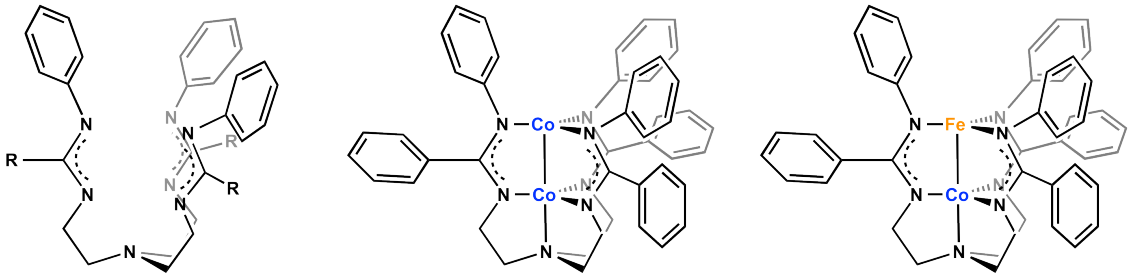

Figure 3.4. Tris(amidinato)amine ligands $[L^R]^{3-}$ and the bimetallic complexes Co_2L^{Ph} (**1**) and $FeCoL^{Ph}$ (**2**)

3.3 Results and discussion

3.3.1 Synthesis of Tris(amidinate)amine Ligands

The tris(amidinato)amine ligands H_3L^{Ph} and H_3L^{tBu} are simple but, to our knowledge, previously unknown. They can be obtained in good yield from a relatively simple three-step procedure, starting from commercially available *tren* and the appropriate acyl chloride, as shown in Figure 3.5. First, benzoyl or pivaloyl chloride (3.4 equiv.) is added to tren in the presence of excess triethylamine to generate the tris(amide)amine species. Second, the amide groups are transformed into imidoyl chloride functionalities using phosphorus pentachloride; since this procedure generates HCl in a closed system, the product is the hydrochloride salt of the tris-imidoyl chloride. The protonation presumably involves hydrogen bonding to the imine groups of the imidoyl chloride moieties, which makes them extremely susceptible to nucleophilic substitution. Accordingly, reaction with a slight excess of aniline proceeds at -78 °C to yield the amidinate functionalities; the initial products are the tetra-protonated HCl salts, after which a basic workup produces the neutral proligands, H_3L^{Ph} and H_3L^{tBu}, in high purity. These can be obtained in multi-gram scale in good overall yield as a hard white solid after drying but are more conveniently handled as the (THF)- or $(Et_2O)_{0.5}$-solvate following recrystallization, from which white microcrystalline powders are obtained.

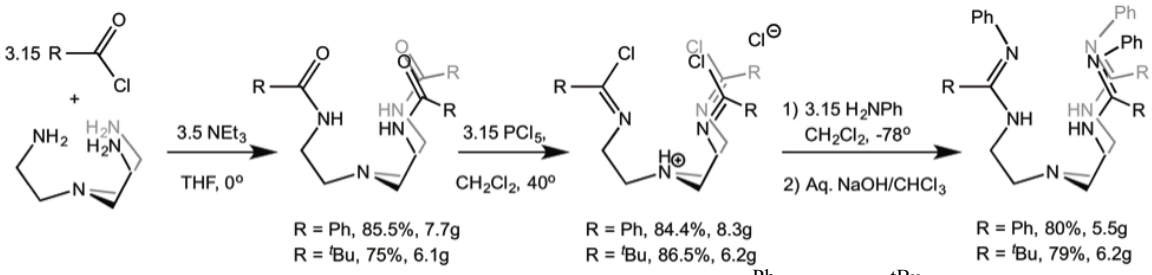

Figure 3.5. Synthesis of tris(amidinato)amine ligands H_3L^{Ph} and H_3L^{tBu}

3.3.2 Synthesis of Monometallic Compounds

The ligands H_3L^{Ph} and H_3L^{tBu} can be easily metallated with a variety of first-row metals to form monometallic complexes. The preferred synthesis is deprotonation with three equivalents of benzylpotassium and addition of one equivalent of the appropriate metal di- or trihalide salt in THF at -78 °C, as shown in Figure 3.6.

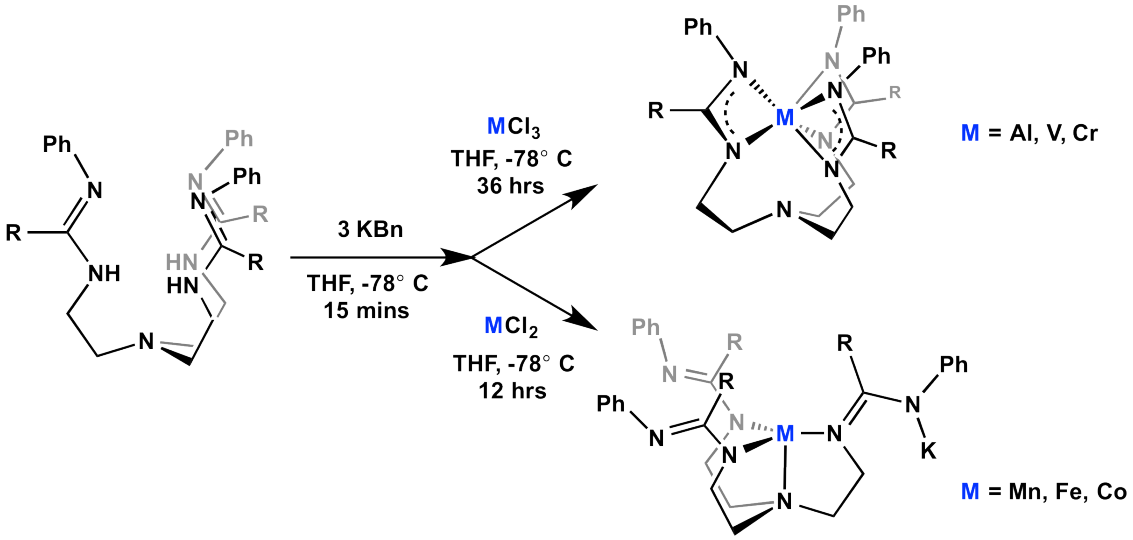

Figure 3.6. Synthesis of monometallic tris-amidinate complexes.

For the early metal(III) compounds $M^{III}L^{Ph}$ and $M^{III}L^{tBu}$, (M^{III} = Al, V, Cr) the products are neutral, highly soluble monometallic species in which the metal coordinates to both planes of donors formed by the three amidinate groups. Because the amidinates must twist significantly in order to accommodate this binding motif, their six donors form a highly distorted trigonal prismatic geometry not all that dissimilar from a distorted octahedron. This was first observed in the ^{1}H NMR spectra; the twisting of each arm makes the protons in the ethylene arms of the *tren* backbone diastereotopic. This effect is not observed for the vanadium and chromium complexes, which are paramagnetic and only three, very broad peaks. However, it can be clearly observed in the diamagnetic

aluminum complex and AlL^{tBu}, as shown in Figure 3.7. One proton from each methylene (H_a and H_b) is oriented between the protons on the other methylene and split into atriplets of doublets (H_a: J = 12.5, J = 3.5 Hz; H_b: J = 12.5, J = 3 Hz), while the other two ($H_{a'}$ and $H_{b'}$) are more isolated and are doublets ($H_{b'}$: J = 12.5 Hz; $H_{a'}$: J = 12.5 Hz).

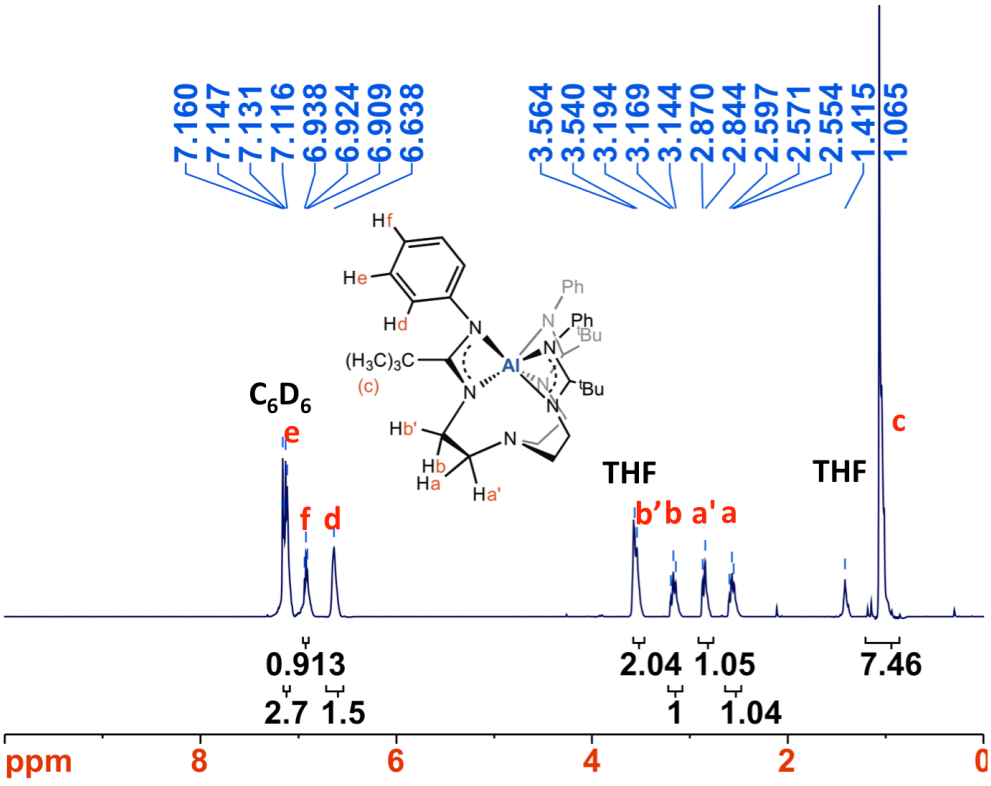

Figure 3.7. ^{1}H NMR spectrum (500 MHz, C_6D_6) of AlL^{tBu}. Binding to both planes of donors is clearly observed in the canting of the *tren* backbone, which makes the methylene protons diastereotopic.

The binding motif is observed more clearly in the solid-state structures of the vanadium and chromium complexes, VL^{tBu} and CrL^{Ph}, respectively (Figure 3.8). Binding of the metals to both planes of amidinate donors is evident in both structures. The other obvious feature of these structures is that the vanadium is heptacoordinate, with bonds to the six donors from the three amidinate groups as well as the apical amine (V1-$N1_{(ap)}$ = 2.235(2)

Å), whereas the chromium center in CrL^{Ph} is only hexacoordinate, due to the much longer Cr-N_{ap} distance of > 3 Å. This difference is consistent with both the greater electron deficiency of vanadium as well as the stability of the Cr(III) ion in the quasi-octahedral, six-coordinate environment.

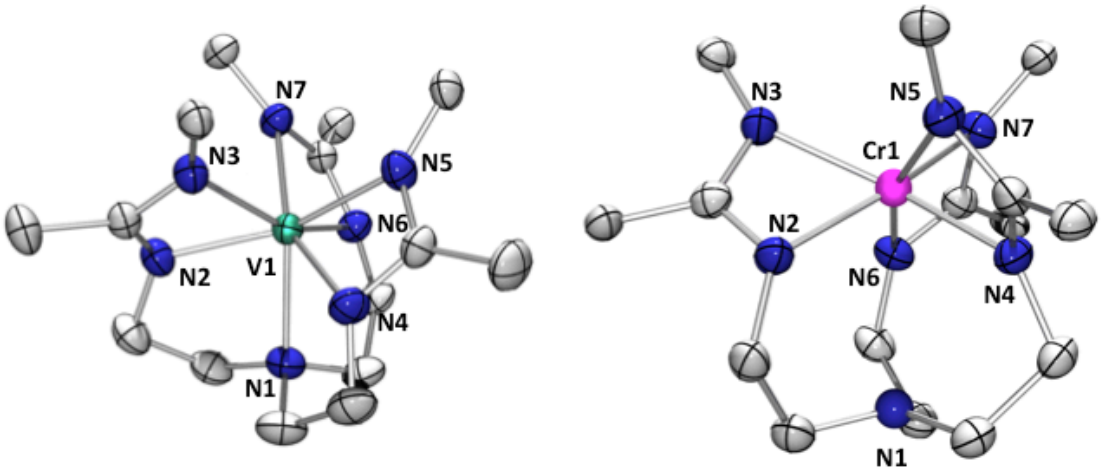

Figure 3.8. Solid-state structures of VL^{tBu} (left) and CrL^{Ph} (right) at 50% probability level. For clarity, hydrogens and organic substituents on the amidinate groups have been omitted. Selected bond distances (Å) and angles (°) for VL^{tBu}: V1-N1, 2.235(2); V1-N2, 2.062(2); V1-N3, 2.149(2); N2-V1-N4, 113.62(7); N3-V1-N5, 91.74(7); N2-C3-N3, 108.7(2). For CrL^{Ph}: Cr1-N1, 3.017; Cr1-N2, 2.036(2); Cr1-N3, 2.071(2); N2-Cr1-N4, 101.38(7); N3-Cr1-N5, 103.74; N2-C3-N3, 110.2(2).

Monometallic complexes of later metals can be prepared by the analogous reaction of the deprotonated tris-amidinate with the appropriate metal dihalide salt. Precise stoichiometry and slow addition of the metal salt is important in these reactions, to avoid irreversible addition of a second metal; thus, the less soluble metal dichlorides, rather than MBr_2 and $MCl_2(THF)_{1.5}$ salts, give best results. Reaction of the deprotonated ligands with $CoCl_2$ produces the lime-green and emerald-green products $K(THF)CoL^{Ph}$ (**3**) and $K(THF)CoL^{tBu}$ (**3a**), respectively. Their ^1H NMR spectra are paramagnetically

shifted, as expected for Co(II) ions, and consistent with solution-averaged C_{3V} symmetry, with eight and six peaks, respectively. Their solid state structures are shown in Figure 3.9. In both structures, the ligand is tetradentate, with the cobalt coordinated only to the apical amine and the bottom plane of nitrogen donors from the amidinates. The geometries at the cobalt centers are thus trigonal monopyrimidal, which is typical of Co(II) centers supported by related tris(amido)amine ligands.[42-44] The three remaining nitrogen donors coordinate to the potassium countercation. Rather than being chelated between the remaining three nitrogen donors of a single molecule, however, each cation is shared between the donors of three separate molecules, forming a continuous, two-dimensional network. In the structure of **3**, the THF coordinates to the potassium as well; in the structure we have obtained for **3a**, the THF is unbound and disordered with diethyl ether used in crystallization. Otherwise, there is little distinction between the two structures; the Co−N_{eq} bond distances are only slightly longer for **3a** (2.01 to 2.02 Å) than in **3** (1.96 to 1.98 Å).

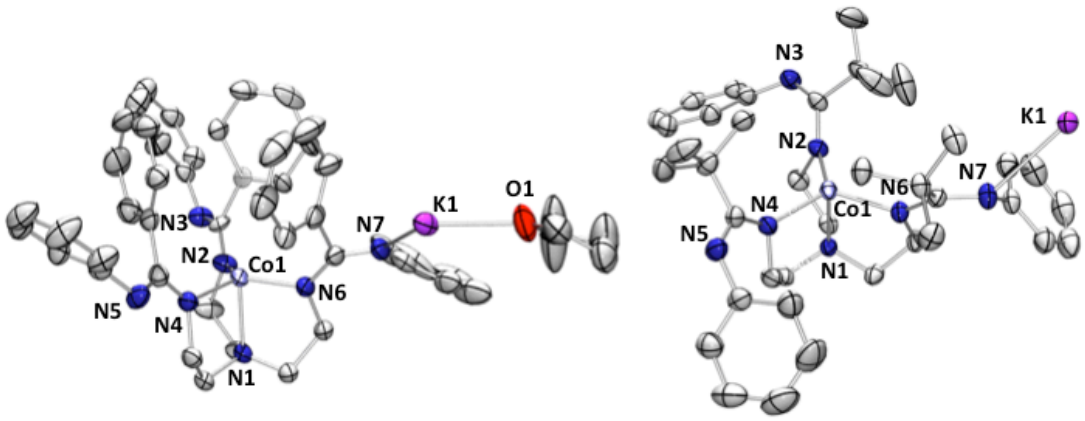

Figure 3.9. Solid-state structures of K(THF)CoL^{Ph} (**3,** left) and K(THF)CoL^{tBu} (**3a**, right) at 50% probability. Hydrogens and disordered atoms are omitted for clarity. Only the shortest K−N bond is shown. Selected bond distances (Å) and angles (°) for K(THF)CoL^{Ph}: Co1−N1, 2.108(2); Co1−N2, 1.958(2); Co1−N4, 1.978(2); Co1−N6, 1.983(2); K1−N7, 2.845(2); N2−Co1−N4, 117.12(9); N4−Co1−N6, 122.32(9);

N2−Co1−N6, 118.11(9); N1−Co1−N2, 85.28(8); N1−Co1−N4, 84.52(7); N1−Co1−N6 84.56(8). For K(THF)CoL^{tBu}: Co1−N1, 2.094(2); Co1−N2, 2.013(2); Co1−N4, 2.018(2); Co1−N6, 2.022(2); K−N5, 2.785(2); N2−Co1−N4, 118.89(9); N4−Co1−N6, 119.15(9); N2−Co1−N6, 119.99(9); N1−Co1−N2, 85.70(8); N1−Co1−N4, 85.11(9); N1−Co1−N6, 85.14(9).

Metallation of the deprotonated ligands with $FeCl_2$ yields bright-yellow monoiron compounds K(THF)FeL^{Ph}, **4**, and K(THF)FeL^{tBu}, **4a**. The NMR spectra are highly paramagnetically shifted and also consistent with solution C_{3V} symmetry. The solid-state structure of **4** was determined by X-ray crystallography (Figure 3.10) and is virtually identical to that of its cobalt analogue, with the only differences worth mentioning being the slightly different M-N distances (~0.04-0.05 Å longer for Fe than Co), consistent with the larger atomic radius of Fe than Co. The structure of **4a** was not determined crystallographically, but its NMR spectrum is very similar to the Co analogue, but more paramagnetically shifted, suggesting a similar coordination environment.

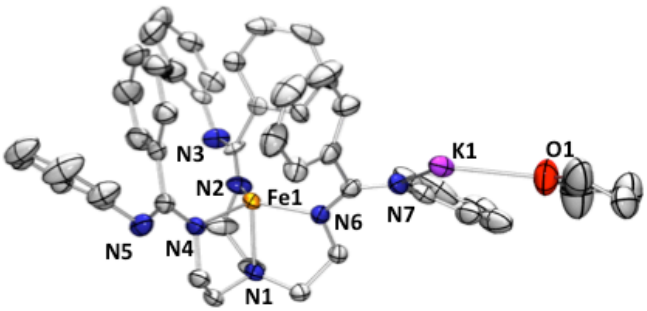

Figure 3.10. Solid-state structure of K(THF)FeL^{Ph}, **4**, at 50% probability. Hydrogens and disordered atoms are omitted for clarity. Only the shortest K−N bond is shown. Selected bond distances (Å) and angles (°): Fe1-N1, 2.158(2); Fe1-N2, 1.997(2); Fe1-N4, 2.017(2); Fe1-N6, 2.020(2); K1-N7, 2.835(2); N1-Fe1-N4, 116.24(8); N4-Fe1-N6, 117.73(8); N2-Fe1-N6, 117.73(8); N1-Fe1-N2, 83.97; N1-Fe1-N4, 83.21(7); N1-Fe1-N6, 8312(7).

3.3.3 Synthesis and Structural Characterization of a Dicobalt Tris-amidinate, Co_2L^{Ph}

The different coordination environments found for the early metals in (3+) oxidation states *versus* later metals in (2+) oxidation states is reflected in their ability to accept a second metal. Neutral bimetallics containing $[M_2]^{3+}$ cores could conceivably be obtained for the former by addition of a metal(0) reagent or a metal(II) with two equivalents of reductant; for the latter, the same reaction should involve addition of a metal(I) source or a metal(II) with one equivalent of reductant. Unfortunately, none of the neutral metal(III) compounds react with metal(0) sources such as $Ni(COD)_2$ (where COD is cyclooctadiene), $Fe(COT)_2$ (where COT is cyclooctatetraene), or $Cr(C_6H_6)_2$, even after extended heating. Nor are bimetallic products obtained from reaction with metal dihalides and reductants such as potassium graphite (KC_8), sodium naphthalenide, or Mg(0). No reaction was observed when the metal(III) species were combined with either the reductants or the metal salts separately, either. The stable chelation of the metal(III) ions in the hexa- and hepta-coordinate geometries apparently makes them essentially inert.

On the other hand, the three unchelated amidinate donors in the Fe(II) and Co(II) monometallics should be able to bind to a second metal center. Addition of a single equivalent of $CoCl_2$ or $CoBr_2$ to **3** in THF causes a color change to dark green and formation of a highly asymmetric, highly paramagnetic species with too many proton signals in the ^1H NMR spectrum to be consistent with a monomeric compound, even of low symmetry; we presume this to be a halide-bridged cluster of as-yet-unknown nuclearity, "$(ClCo_2L^{Ph})_n$" or "$(BrCo_2L^{Ph})_n$." On the other hand, the low-temperature addition of a cobalt dihalide, followed quickly by one equivalent of KC_8, causes a rapid change to brown and gives the homobimetallic dicobalt complex, Co_2L^{Ph}, **1**. We have

found that this product is produced more cleanly and reliably when using $CoBr_2$, rather than $CoCl_2$, as the source of the second cobalt atom. **1** can also be cleanly formed by direct reduction of the bromide cluster $(BrCo_2L^{Ph})_n$, although not the chloride cluster. The optimized synthesis, shown in Figure 3.11, involves addition of KC_8 to **3** in THF at -78 °C, followed by slow addition of $CoBr_2$ as a solution in THF. After slow warming to room temperature over 12 hours, the crude product can be obtained in upwards of 90% yield and is highly pure by ^{1}H NMR. Bulk crystallization is achieved by layering a THF solution with hexane and provides single crystals suitable for X-ray diffraction and further spectroscopic and magnetic characterization (*vide infra*).

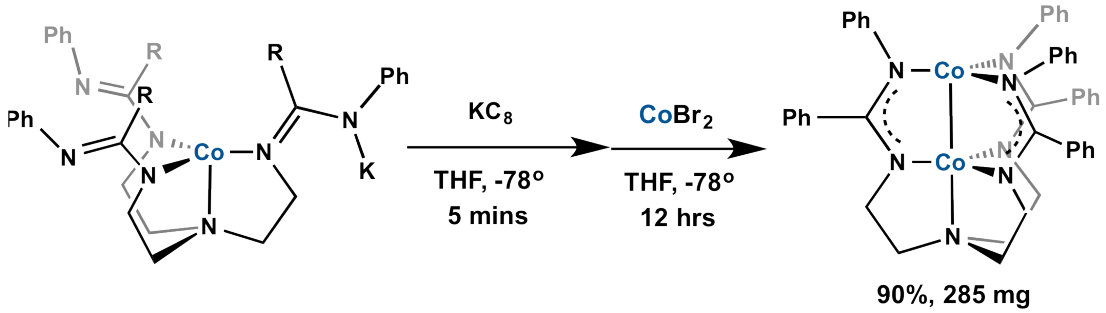

Figure 3.11. Synthesis of Co_2L^{Ph}, **1**.

The ^{1}H NMR spectrum of **1** shows only eight signals, consistent with C_{3V} symmetry in solution, and is highly paramagnetically shifted, with resonances spanning from 165 to -34 ppm, as shown in Figure 3.12. This range is similar to that of $Co_2(DPhF)_3$, in which the four protons were found to range from 175 to -50 ppm. Attempts to assign these resonances *via* 2D COSY were unsuccessful, as no cross-peaks were observed. However, the sharp resonances at -1.73 ppm and -34.4 ppm are assigned to the *para* protons on the two sets of phenyl rings based on their integration. Because of

their similarity to the phenyl resonances in $Co_2(DPhF)_3$, the sharp peak at 16.0 ppm and the broad peak at -34 ppm likely correspond to the *ortho* and *meta* protons on the N-substituted phenyl ring, although not necessarily in that order. The other resonances then must be assigned to the phenyl group on the bridgehead position of the amidinates and the ethyl backbone of the *tren* base. The downfield shifts of the peaks at 104 and 159 ppm are similar to the bridgehead-*H* of the formamidinates in $Co_2(DPhF)_3$, and on this basis we assign them to the *meta* and *ortho* protons of the bridgehead phenyl group.

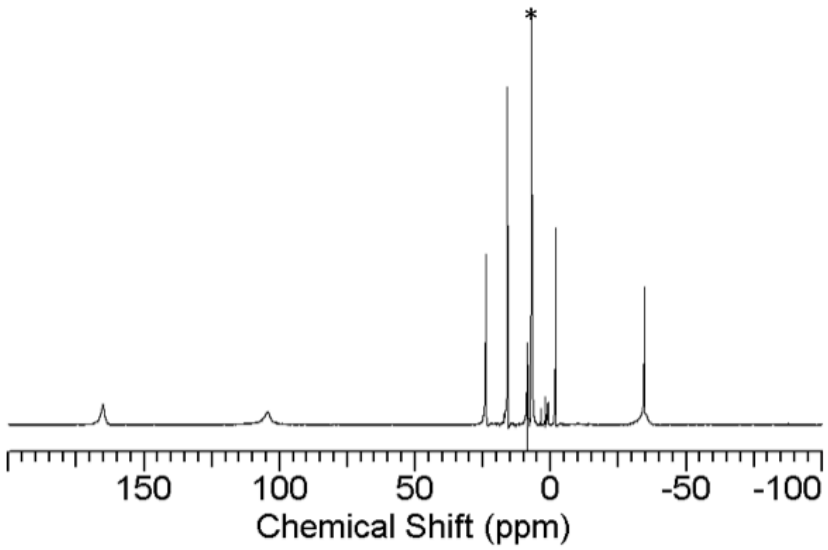

Figure 3.12. ^{1}H NMR spectrum of **2** (C_6D_6, 500 MHz). An asterisk denotes the residual solvent resonance.

The solid-state structure of Co_2L^{Ph} was determined by X-Ray diffraction, as shown in Figure 3.12. In contrast to $Co_2(DPhF)_3$, Co_2L^{Ph} crystallizes in the trigonal space group $R\text{-}3$, resulting in perfect molecular C_3 symmetry (crystallographic parameters are tabulated in Table 3.9). This is an interesting counterpoint to the deviations from trigonal symmetry observed for $Co_2(DPhF)_3$ and particularly the theoretically-optimized structures for that compound. Otherwise, the most notable difference between the

experimental structures of $Co_2(DPhF)_3$ and Co_2L^{Ph} is the Co−Co bond length. At 2.2944(7) Å it is nearly 0.1 Å shorter than the distance of 2.385(1) Å in $Co_2(DPhF)_3$.[40,41] This is somewhat surprising, since the additional axial donor in Co_2L^{Ph} would be expected to weaken the metal-metal interaction via the ligand's *trans* influence. For example, as discussed in Section 1.2.3, it is well-established that adding axial donors to dichromium tetracarboxylates significantly increases the Cr−Cr bond length.[45,46] Nevertheless, the Co-Co distance in Co_2L^{Ph} is not only significantly shorter than of $Co_2(DPhF)_3$, it is among the shortest distances in the literature. It is significantly shorter, for instance, than the tetragonal paddlewheel, $Co_2(DPhF)_4$ (2.37 Å),[47] which has a formal single bond. This is partly due to the steric presence from the phenyl group in the bridgehead position of the amidinates, which compresses the N-C-N angle of the amidinates and thereby forces the cobalt atoms closer together. For this reason, the better comparison is with the benzamidinate analogues, $Co_2(DPhBz)_3$ and $Co_2(DPhBZ)_4$, which have a similar bridgehead phenyl group: their Co-Co distances are 2.3201(9) and 2.302(1) Å for the trigonal and tetragonal compounds, respectively.[41,47] Since Co_2L^{Ph} has a shorter distance even than these, it is apparent that, at the very least, the presence of the apical amine does not significantly weaken the Co-Co bonding; rather, it retains the strong metal-metal bonding seen in the original trigonal lantern, within a perfectly trigonally symmetric structure (Figure 3.13).

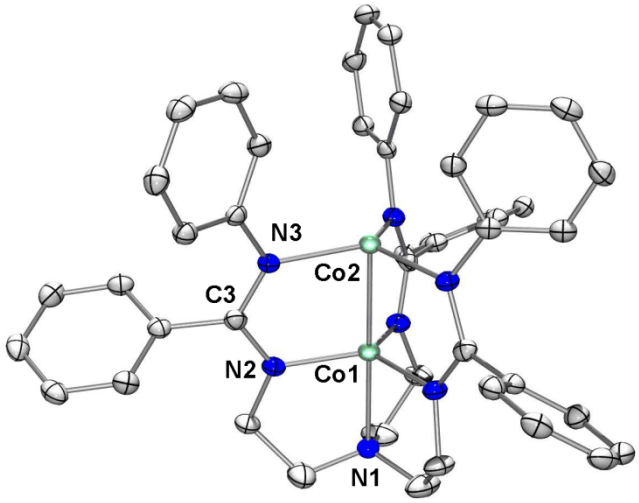

Figure 3.13. Solid-state structure of **1** at 50% probability level. Hydrogen atoms are omitted for clarity. Selected bond distances (Å): Co1−Co2 2.2944(7), Co1−N1 2.135(3), Co1−N2 1.923(2), Co2−N3 2.041(2); selected bond angles (°): N2−Co1−N2' 119.28(2), N3−Co2−N3' 119.18(2), N1−Co1−N2 85.11(5), N1−Co1−Co2 180.0, N2−Co1−Co2 94.90(5), N3−Co2−Co1 84.77(5); torsion (°): N2−Co1−Co2−N3 4.57(7).

While there is perfect, crystallographically-imposed symmetry around the M-M axis of Co_2L^{Ph}, there is significant asymmetry along the M-M axis. The two cobalt atoms are in different chemical environments, due to the presence of the axial donor and the different substituents on the two sets of amidinate donors. This is reflected in a few key structural features. The Co−N_{eq} bond distances are significantly shorter for Co1, which is bound to the axial amine donor, than for Co2. This could suggest more localized, Co(I)Co(II), valences, with the lower-valent, larger Co(I) center in the "top" site. In addition, there is a slight distortion towards pyramidal, rather than planar geometries: both cobalt atoms are displaced out of the planes defined by the equatorial nitrogen donors, away from the axial donor: Co2, in the top site, is displaced by 0.186 Å out of the plane, while Co1 is displaced by 0.164 Å. This is also manifested in the acute N3-Co2-Co1 angles of 84.77(5)° and obtuse Co2-Co1-N2 angles of 94.90(5). Interestingly, this

phenomenon was also observed in $Co_2(DPhF)_3$, where both metals are noticeably displaced in the same direction, but to a lesser extent. In that case, there are acute N-Co2-Co1 angles ranging from 88.19(2)° to 87.07(2)° and obtuse Co2-Co1-N angles of 90.06(2)° to 91.30(2)°. Since the metals in that compound are otherwise in identical environments, this seems to be a general phenomenon for the dicobalt compounds, rather than one induced by the asymmetric ligand. No such effect is observed in $Fe_2(DPhF)_3$, in which there is a C_2 symmetry axis making the iron centers equivalent and preventing such a distortion. No obvious electronic effect would explain this pyramidalization in the dicobalt complexes, but it could have an effect on the π and δ bonding by changing the overlap of the ligands with the d_{xy} and $d_{x^2-y^2}$ versus the d_{xz} and d_{yz} orbitals. Regardless of its origin, the effect appears to be present in both dicobalt complexes; thus, the strong metal-metal bonding originally seen in the simpler trigonal lantern framework is retained in the chelated dicobalt system.

3.3.4 Synthesis and Structural Characterization of a Heterobimetallic Tris-amidinate, $FeCoL^{Ph}$

The successful stepwise metallation strategy used to prepare the dicobalt complex can also be extended to the synthesis of a heterobimetallic iron-cobalt complex, $FeCoL^{Ph}$, **2**. Using an identical procedure but with $FeBr_2$ replacing $CoBr_2$ in the second step, **2** can be obtained as a red-purple solid in similarly good purity and yield (92%, 225 mg). It is indefinitely stable in the solid state but is extremely sensitive to adventitious O_2 in solution, and it also appears to slowly convert to the dicobalt complex, Co_2L^{Ph}, in solution, along with unidentified products (*vide infra*). The ^{1}H NMR spectrum for the

iron-cobalt species is very similar to that of the dicobalt (Figure 3.14) in showing eight protons with a similar pattern of paramagnetically shifted and broadened signals. In comparing the two bimetallics, the most shifted peaks are the two downfield resonances at 172.6 and 127.0 ppm. The fact that these two peaks are highly sensitive to the identity of the top metal center supports their assignment to the bridgehead phenyl group rather than the tren backbone.

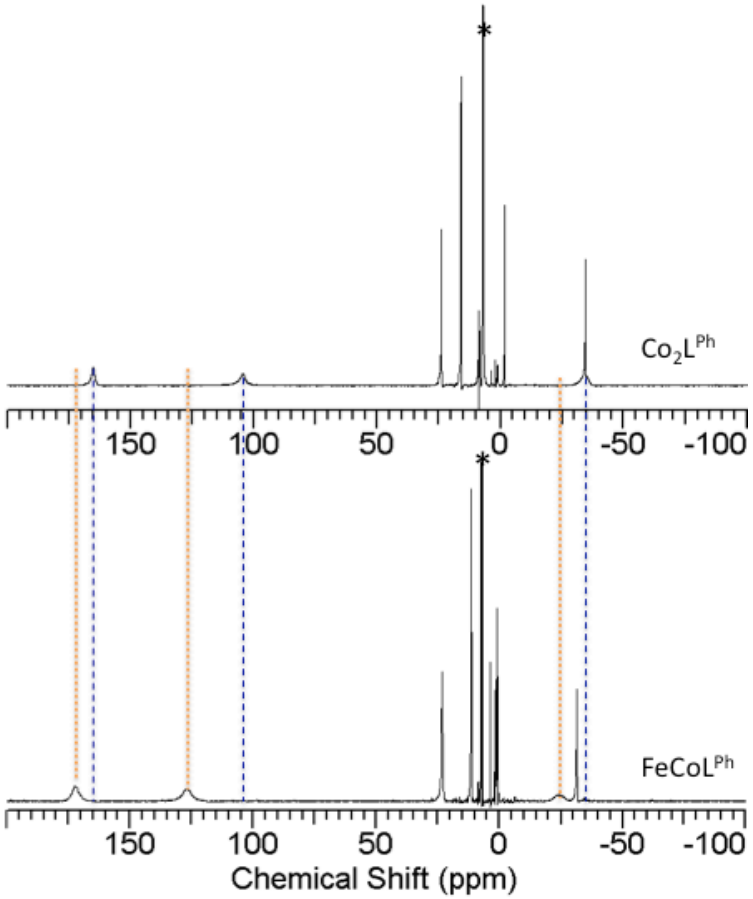

Figure 3.14. ^{1}H NMR (500 MHz, C_6D_6) spectra of **1** (top) and **2** (bottom). The residual solvent resonance is indicated by an asterisk. The lines distinguish the frequencies of the most shifted resonances for Co_2L^{Ph} (dashed blue line) and $FeCoL^{Ph}$ (dotted orange line).

$FeCoL^{Ph}$ crystallizes in the same space group, $R\bar{3}$, as **1**, with virtually identical

unit cell parameters. Moreover, their molecular structures, as revealed by X-ray diffraction studies, are remarkably similar. The perfect trigonal symmetry about the M-M axis is conserved. In addition, all the metal-ligand bond distances are within 0.022(3) Å, despite the difference of metal combinations. This confirms that the ligand is redox-innocent in this system and provides an ideal template to study the effects of metal identity on the metal-metal bonding. All the remaining structural differences can be attributed to the presence of iron or cobalt. Indeed, the only significant change occurs along the M-M axis, in which a shorter M-M bond is observed, along with a slightly shortened M-N distance. The change in the M−Co bond distance is dramatic, as it shortens from 2.2944(7) Å in Co_2L^{Ph} (M= Co) to 2.1846(4) Å in $FeCoL^{Ph}$ (M= Fe). The structure is shown in Figure 3.15.

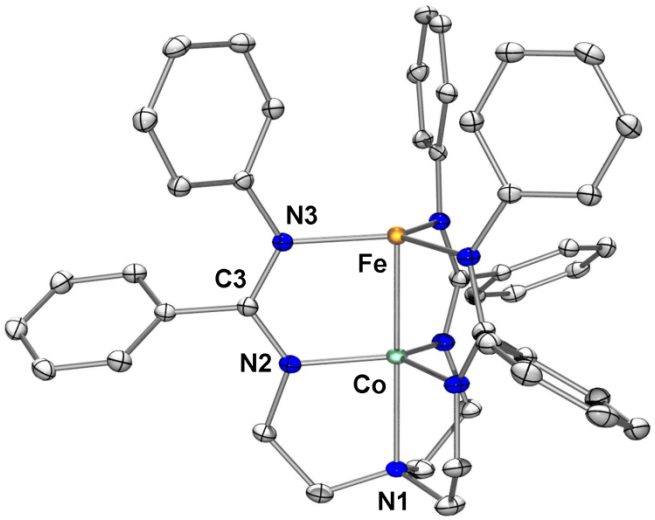

Figure 3.15. Solid-state structure of **2** at 50% probability. Hydrogen atoms are omitted for clarity. Selected bond distances (Å): Fe−Co 2.1846(4), Co−N2 1.927(1), Co−N1 2.116(2), Fe−N3 2.053(1); selected bond angles (°): N2−Co−N2' 119.644(6), N3−Fe−N3' 119.982(1), N1−Co−N2 86.56(3), N1−Co−Fe 180.0, N2−Co−Fe 93.44(3), N3−Fe−Co 89.21(3); torsion (°): N2−Co−Fe−N3 4.30(3).

The heterobimetallic nature of the iron-cobalt compound and the asymmetric

ligand framework implies that two isomers are possible for this combination of metals. For clarity, these heterobimetallic isomers will be denoted $FeCoL^{Ph}$ and $CoFeL^{Ph}$, with the former referring to the presence of iron in the "top" binding site and cobalt in the "bottom," and *vice versa* for the latter. Because refinement of conventional X-ray diffraction data cannot reliably distinguish metals with atomic numbers as similar as iron and cobalt, we turned to X-ray anomalous scattering techniques to assign the positions of the two metals. These methods have been widely used to identify metals within single crystals; in addition, they have been shown to be effective at quantifying the percentages of each metal in cases where their positions are mixed or disordered.[48,49]

Anomalous diffraction studies were carried out at the Advanced Photon Source at Argonne National Laboratory, in collaboration with Dr. Yu-Sheng Chen. Collection and refinement of the data were carried out by Dr. Victor G. Young and Laura Clouston. In these studies, several sets of X-ray diffraction data were collected on a single crystal of **2**, with the wavelength of the X-ray source tuned to cover a range of energies near the K-edge absorption energies of iron and cobalt. A final data set was collected at significantly higher energy. These studies exploit the fact that the anomalous dispersion contributions to the scattering factor of an atom change substantially when the energy of the X-ray source is close to that of the scattering atom's absorption edge energy. This results in an apparent decrease in electron density observed for the anomalous scatterer in the Fourier difference map. Since the edge energy is significantly different even between similar metals such as iron and cobalt, the positions of the two metals can be distinguished using this effect. We have determined the ratios of Fe/Co in the two metal sites by conducting

least-squares refinement of all the anomalous diffraction data collected at the different wavelengths simultaneously. This method varies from other literature reports that calculate Fourier difference maps (or apparent f') at each wavelength.[48] The current method has the benefit of reporting refined values with standard uncertainties and provides a straightforward scaling of the different anomalous data sets.

The least-squares refinement of the metal occupancies gives a precise structural formula of $(Fe_{0.94(1)}Co_{0.06(1)})(Co_{0.95(1)}Fe_{0.05(1)})L^{Ph}$ for **2**, wherein the cobalt remains largely in the "bottom" binding pocket, featuring the tren donor set, while the iron is primarily located in the "top" binding site, as expected given the synthetic protocol. There is an equal amount of iron and cobalt in the sample, within experimental error. These results are consistent with a formulation as 95% $FeCoL^{Ph}$ and 5% of its heterobimetallic isomer, $CoFeL^{Ph}$. Unfortunately, this cannot be distinguished from a four-component mixture of $FeCoL^{Ph}$, $CoFeL^{Ph}$, and the homobimetallics Co_2L^{Ph}, and Fe_2L^{Ph}. By taking the metal occupancies determined for the two binding sites and assuming purely statistical mixing, the percentages of each possible metal-metal pair would be 89.3% $FeCoL^{Ph}$, 5.7% Co_2L^{Ph}, 4.7% Fe_2L^{Ph}, and 0.3% $CoFeL^{Ph}$. Unfortunately, much higher data resolution would be needed in the crystal structure determination to fully model the precise formulation of this mixture. In any case, although a mixture of iron and cobalt is observed at both metal-binding sites, the dominant metal accounts for 95% of the occupancy at each site. This degree of selectivity is somewhat remarkable considering the similarity of the ligand donors and the known lability of high-spin metal centers. Even within the context of metal-metal bonded systems, these metals have been shown to be

quite labile, as demonstrated by the work of Betley and Eames, in which iron-cobalt heterometallics were prepared by simple substitution of cobalt dihalides into a preassembled triiron core.[36]

For simplicity, we have discussed the bond metrics of $FeCoL^{Ph}$ based on this structure determination as if it were the sole species present in the crystal; in reality, the composite nature introduces some uncertainties into these values. Nonetheless, these are expected to reflect the true bond metrics of the $FeCoL^{Ph}$ structure to a very good approximation. Not only is this clearly the predominant species within the crystal, but there are few significant structural differences even between $FeCoL^{Ph}$ and Co_2L^{Ph}, and fewer still would be expected between $FeCoL^{Ph}$ and $CoFeL^{Ph}$. A comparison of key structural parameters for Co_2L^{Ph}, $FeCoL^{Ph}$, and $Co_2(DPhF)_3$ is given in Table 3.1.

Table 3.1. Selected distances (Å) and angles (°) for **1** and **2**. The previously reported structure of $Co_2(DPhF)_3$ is shown for comparison.

distances, angles	$Co_2(DPhF)_3$, **1**[23]	Co_2L^{Ph}, **3**	bonds and angles	$FeCoL^{Ph}$, **4**[a]
Co−Co, Å	2.385(1)	2.2944(7)	Fe−Co, Å	2.1846(4)
$Co-N_{eq}$, Å	1.932(5)	1.923(2)	$Co-N_{eq}$, Å	1.927(1)
	1.955(5)			
	1.959(5)			
	1.957(5)	2.041(2)	$Fe-N_{eq}$, Å	2.053(1)
	1.978(5)			
	1.983(5)			
$Co-N_{ax}$, Å	−	2.135(3)	$Co-N_{ax}$, Å	2.116(2)
Co-out of N_3-plane, Å	0.090	0.164	Co-out of N_3-plane	0.115
	0.065	0.186	Fe-out of N_3-plane	0.028
$N_{eq}-Co-N_{eq}$, °	125.1(2)	119.28(2)	$N_{eq}-Co-N_{eq}$, °	119.644(6)
	119.2(2)			
	115.6(2)			
	120.1(2)	119.18(2)	$N_{eq}-Fe-N_{eq}$, °	119.982(1)
	114.8(2)			
	124.7(2)			
$N_{eq}-Co-Co$, °	88.19(2)	84.77(5)	$N_{eq}-Fe-Co$, °	89.21(3)
	88.24(2)			
	87.07(2)			
	90.06(2)	94.90(5)	$N_{eq}-Co-Fe$, °	93.44(3)
	90.32(2)			
	91.30(2)			

As mentioned previously, the major difference between the structures of $FeCoL^{Ph}$ and Co_2L^{Ph} is that the Fe-Co distance is more than 0.1 Å shorter, at 2.1846(4) Å *versus* 2.2944(7) Å. Correlated with the shorter M-M bond, the iron center is less displaced from the equatorial N_3-plane. This is clearly due to an electronic effect, since the covalent radius of iron is larger than cobalt and a larger distance would be expected in the absence of such an effect. An increase in M-M bonding is expected according to the MO model for bonding in trigonal lantern complexes, described in Chapter 2. In the case of $FeCoL^{Ph}$, there is one fewer M-M antibonding π^* electron than in the dicobalt complex, which should increase the formal M-M bond order by 0.5. The presence of iron-cobalt bonding at all is noteworthy, as such bonding is rarely observed with weak-field donor ligands. Yet the apparent strength of the bond is remarkable: it is the shortest Fe-Co bond known, by a significant margin, and it is by far the shortest such bond among dinuclear complexes or among molecules without a single-atom bridging ligand. Nearly all the structural examples of iron-cobalt bonds in the Crystallographic Structural Database are within carbonyl clusters, where the median Fe-Co bond distance is 2.55 Å.[50] Among these organometallic complexes, only a single molecule has Fe-Co distances approaching that of $FeCoL^{Ph}$: a trinuclear Fe_2Co core with a capping sulfide atom (Fe−Co = 2.225 and 2.296 Å).[51] Among complexes with weak-field ligands, only the heterotrimetallic iron-cobalt clusters very recently reported by Eames and Betley have Fe-Co distances indicative of substantial bonding. One of these shows a very short Fe-Co distance of 2.29 Å. However, as discussed in section 3.2.1, this bond was between two metal sites whose bond distance does not change regardless of the metals: the distances are 2.2955(8) Å for

$[Fe_2]^{5+}$, 2.2934(8) Å for $[FeCo]^{5+}$, and 2.2971(5) Å for $[Co_2]^{5+}$.[36,37] Between the metal sites in these clusters whose distances do depend on metal identity, the Fe-Co distances are far longer, between 2.51-2.52 Å.[36] In contrast to these examples, the Fe-Co bond in **2** is apparently much stronger, and its strength appears to be solely a result of the M-M interaction, uncomplicated by other structural or electronic factors.

3.3.5 Electronic Absorption Spectra of Co_2L^{Ph} and $FeCoL^{Ph}$

1 is an orange-brown color, similar to but distinct from the red-brown color of $Co_2(DPhF)_3$. **2** is a much darker red-purple color. Their Vis-NIR absorbance spectra are shown in Figure 3.16. Whereas $Co_2(DPhF)_3$ shows well-defined absorbances in the visible and a near-IR feature obscured by solvent artifacts, Co_2L^{Ph} has a much more amorphous spectrum, with several ill-defined shoulders overlapping with the low-energy tail of a strong UV absorption. Four features can be distinguished: two shoulders at 480 and 650 nm and two weak bands at 850 and 1160 nm (ε = 200, 150 M^{-1} cm^{-1}, respectively). $FeCoL^{Ph}$ has intense absorptions centered at 514 nm ($\varepsilon \sim 3{,}000$ M^{-1} cm^{-1}) and a weak band at 1050 nm (ε = 175 M^{-1} cm^{-1}). The visible-energy absorbances of $Co_2(DPhF)_3$ were tentatively assigned to transitions within the Co-Co bonding manifold. If the first two features in Co_2L^{Ph} are assumed to be analogous, their shift to higher energy would be consistent with greater orbital splitting due to the apparently stronger Co-Co bond. The greater intensity of these transitions could be attributed to the polarization of the Co-Co bond from the axial donor and inequivalent nitrogen donors. One explanation for the low extinction coefficients for the spin- and parity-allowed transitions in $Co_2(DPhF)_3$ is the Frank-Condon principle, according to which the change

in Co-Co bond distance upon excitation should cause poor overlap of vibrational wavefunctions. The asymmetry of Co_2L^{Ph} should result in more vibrational modes, which may mediate these transitions. The even greater intensity for the transitions in $FeCoL^{Ph}$ would be consistent with the even more polarized heterobimetallic complex. Alternatively, the more intense high-energy transitions may be interpreted as charge-transfer bands. In that case, the shift to higher energies for Co than Fe would be consistent with assignment as MLCT bands; however, this would be unusual for the strongly-donating amidinate ligands.

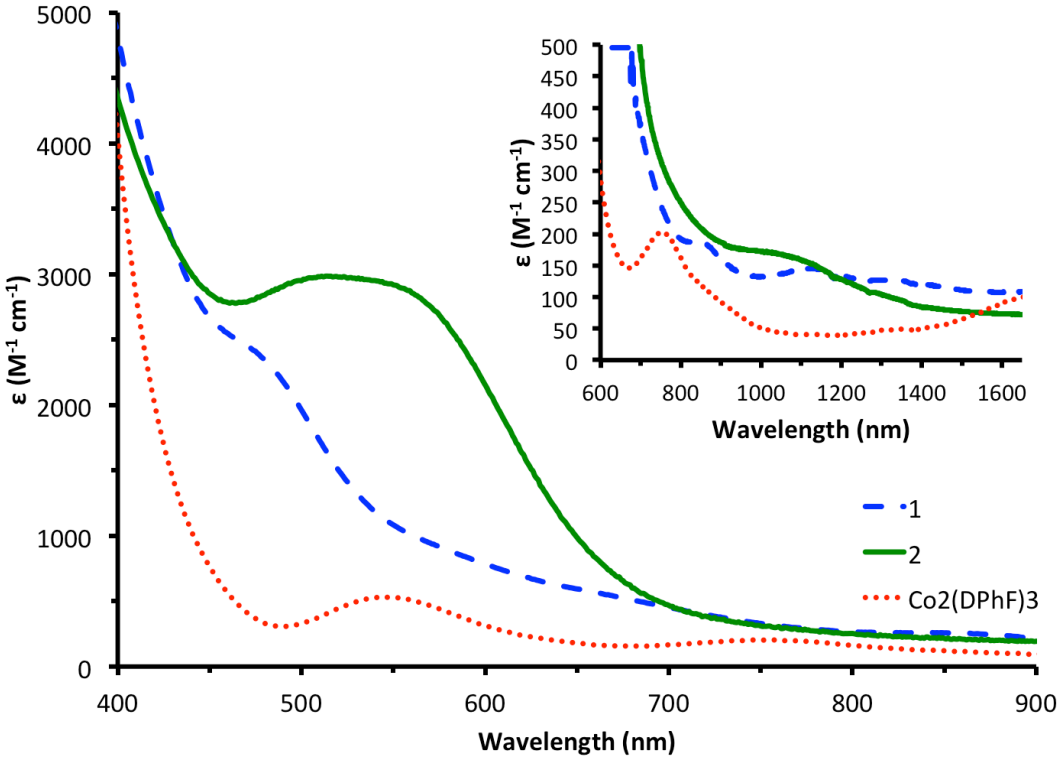

Figure 3.16. Vis-NIR spectra of dicobalt complexes **$Co_2(DPhF)_3$** (dotted red line), **1** (dashed blue line), and **2** (solid green line) in toluene at rt. Inset shows the NIR region. An asterisk marks the onset of imperfect background subtraction. See text for details.

3.3.6 Magnetic Measurements, EPR, and Mössbauer Spectroscopy

The variable temperature magnetic susceptibility measurements of Co_2L^{Ph}, shown in Figure 3.17, are consistent with a well-isolated sextet state similar to that observed for $Co_2(DPhF)_3$. From ~50 to 290 K, the effective magnetic moment, μ_{eff}, is essentially temperature independent at 6.39 μ_B. These plots are consistent with an energetically isolated sextet state, which has a spin-only value of 5.92 μ_B. Hence, the data can be fitted using a single spin $S = 5/2$ Hamiltonian. The deviation of the μ_{eff} from the spin-only value can be simulated by adopting an electronic g value different from $g = 2$; the best fit is obtained with $g_{5/2} = 2.16$. Because the presence of any magnetic impurities can obscure true *g*-values in these static susceptibility measurements, more reliable *g*-values are obtained from EPR spectroscopy (*vide infra*).

Below 50 K, the effective magnetic moment of **1** deviates from the high-temperature limit, possibly due to the combined effect of field saturation, zero-field splitting, and weak intermolecular interactions, which together can be simulated, as shown in the inset of Figure 3.17. The influence of weak intermolecular ferromagnetic interactions results in a slight rise in the μ_{eff} values around 15-20 K. At lower temperatures, zero-field splitting effects become more significant, resulting in the drop in μ_{eff} values. The best fits are obtained with zero-field splitting parameters $D_{5/2} = 9(\pm 2)$ cm^{-1}. The weak intermolecular interactions are to be expected, since the closest intermolecular M···M contacts are all greater than 8.5 Å.

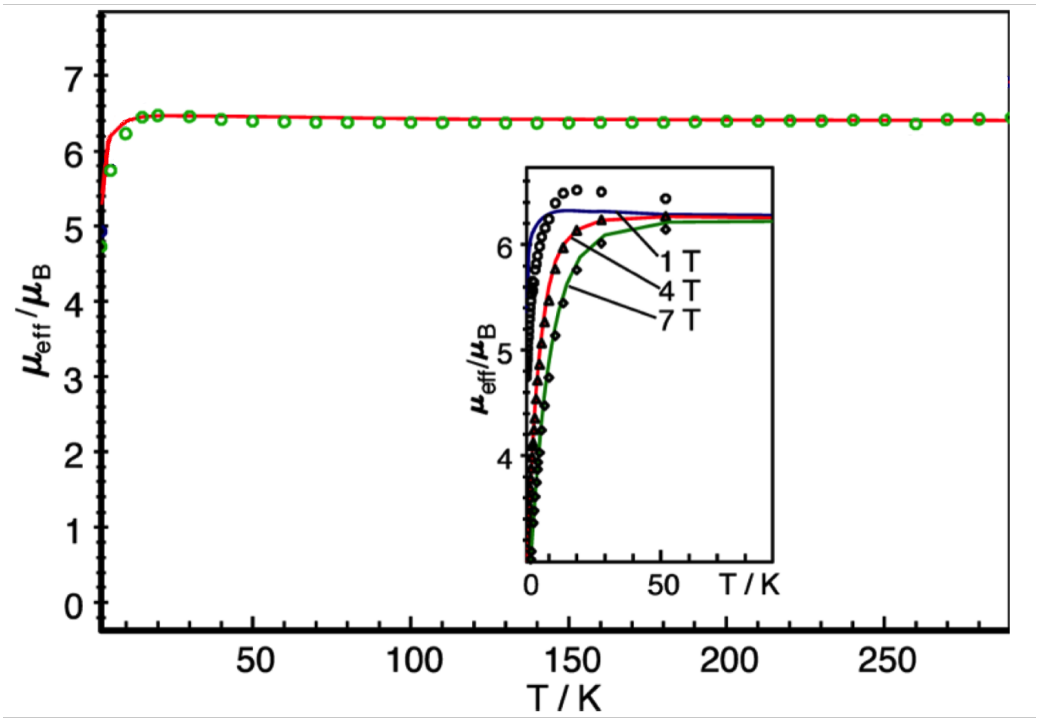

Figure 3.17. Temperature dependence of the effective magnetic moment, μ_{eff}, of **1** at 1 T, from 2 to 290 K. The solid lines represent the best fit. See text for simulation parameters. Inset: Low-temperature reduced magnetization plots and fits for **1** at 1, 4, and 7 T.

The EPR spectra of **1** has also been collected in frozen toluene at 20 K. As with its analogue, $Co_2(DPhF)_3$, it shows an axial derivative signal at an effective *g*-value around g_{eff} = 6 and 2, which are typical of transitions within the $m_s = \pm ½$ Kramers doublet of $S = 5/2$ systems with significant axial zero-field splitting (D >> hν at X-band, i.e. 0.3 cm^{-1}) and small-to-vanishing rhombicity, $E/D \approx 0$ (Figure 3.18). Under this condition, the ± 3/2 and ± 5/2 Kramers doublets are EPR-silent and the shape of the spectra is independent of the actual value of the zero-field splitting parameter *D*. The spectrum was simulated with the usual spin-Hamiltonian for the sextet spin state, and the axial zero-field splitting was fixed to correspond to the magnetic susceptibility measurements. (In the simulations, any value of $|D| > 2$ cm^{-1} was found to be consistent

with the experimental spectra.) The electronic g values were constrained to be axial, (g_1 = g_2), such that the effects of weak rhombic splitting could be assigned to finite values of E/D (see Figure caption 10). The average of the g-values obtained from the EPR fit is 2.2, which is reasonably close to the isotropic g-value of 2.16 found from the magnetic susceptibility fits and identical to the average of the g-values in the EPR spectrum of $Co_2(DPhF)_3$. Altogether, the experimental data support an electronic structure for Co_2L^{Ph} almost identical to that of $Co_2(DPhF)_3$. The greater number and intensity of absorptions in the absorption spectrum may suggest a more polarized M-M bond, but the magnetic measurements are virtually identical.

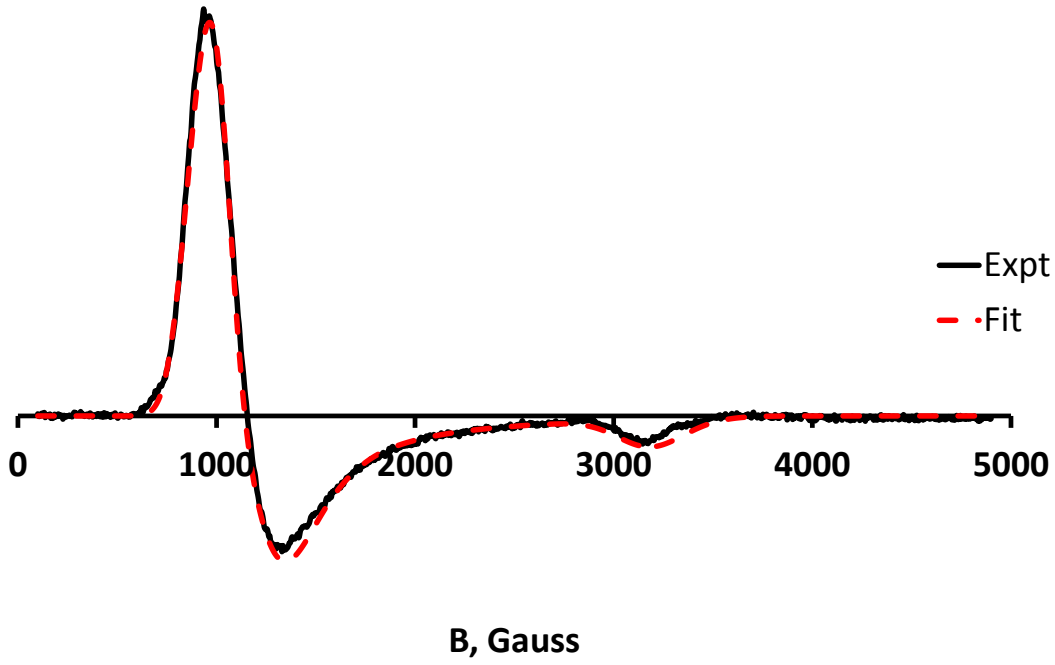

Figure 3.18. X-band EPR spectrum (dX″/dB) of **1** in toluene glass shown as solid black line (1.0 mM, 20.0 K, frequency = 9.646 GHz, modulation to 10 G, power = 2.01 mW). The spectrum was simulated (shown as dashed line) by adopting S = 5/2 with the following anisotropic values: g = (2.201, 2.201, 2.215); line widths W = (184.2, 184.2, 400); zero-field splitting parameters D = 2.80 cm^{-1}, E/D = 0.0366 (D value fixed).

Although the homobimetallic dicobalt complexes were expected to show similar electronic structures, the more interesting case was the heterobimetallic, **2**. The weak trigonal ligand field is identical to that in **1** and would similarly be expected to favor a high-spin state, but the different orbital energies for Fe and Co could engender a localization of the electron density and thus favor antiferromagnetic coupling. Consistent with the expected integer spin, **2** is EPR silent. The magnetic susceptibility data for **2** clearly show a temperature-independent magnetic moment of 6.89 m_B, which is qualitatively consistent with $S = 3$ (Figure 3.19). To model this spin within the constraints of the JulX program, we adopted two $S = 3/2$ spins, for formally high-spin Fe(I) and Co(II), with $J \geq +200$ cm^{-1}. The large J value renders the exited states at energies well above the ground state (>1200 cm^{-1}), so that thermal population of excited spin states is negligible, in accordance with the observation of an energetically isolated septet state. With respect to the magnetic data, this is thus indistinguishable from alternative descriptions of the molecule as a single $S = 3$ spin or as strongly-coupled high-spin Fe(II) ($S = 2$) and Co(I) ($S = 1$). The spin-Hamiltonian simulation yields a fitted g-value of 2.00 and an axial zero-field splitting parameter, $D = 6$ cm^{-1}. The noticeable rise in μ_{eff} between ~15-25 K was simulated by adopting a θ_W value of 3 K to account for weak intermolecular ferromagnetic coupling. Finally, the data was fitted assuming an S = 5/2 paramagnetic impurity of 11.5% in order to account for the observation of dicobalt Co_2L^{Ph} at this percentage in the NMR of the analyzed sample.

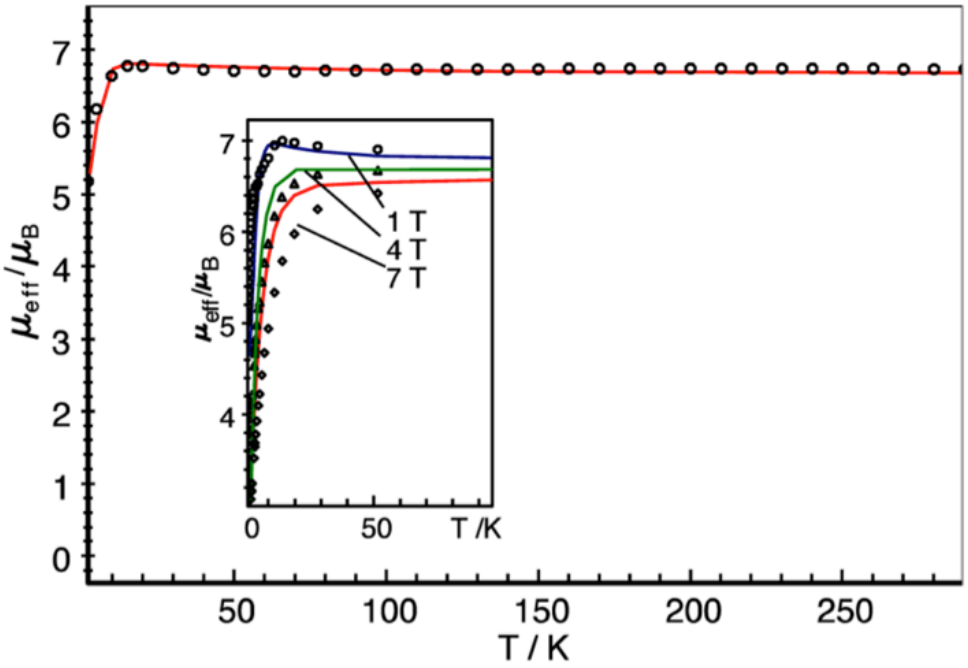

Figure 3.19. Temperature dependence of the effective magnetic moment, μ_{eff}, of **2** at 1 T, from 2 to 290 K. The solid lines represent the best fit for two strongly-ferromagnetically coupled $S = 1$ and $S = 3/2$ spins ($J \geq 200$ cm^{-1}, $g = 2.0$, $\chi_{TIP} = 1200 \times 10^{-6}$ emu, $D_3 = 6$ cm^{-1}, $\theta_W = 3$ K). Inset: Low-temperature reduced magnetization plots for FeCoL^{Ph} at 1, 4, and 7 T.

To our knowledge, this is a unique spin state for an Fe-Co bond; as mentioned above, virtually all known complexes with an Fe-Co distance less than 3.02 Å (the sum of covalent radii for high-spin Fe(II) and Co(II)) contain CO ligands, with most of the remainder bearing strong-field NO or Cp-type ligands, suggesting low-spin metal centers. The sole exceptions have well-characterized spins. Two have very long Fe-Co distances indicative of weak bonding: a Fe(III)Co(III)Fe(III) complex, with a Fe-Co distance of 2.870(1) Å,[52] was found to have an $S = 1$ ground state, and a salen-type Fe(II)-Co(II) complex has an $S = 3/2$ ground state, from weak antiferromagnetic coupling across an even longer M-M distance of 2.886(2) Å.[53] The others are the aforementioned $[Fe_2Co]^{7+}$ and $[FeCo_2]^{7+}$ clusters reported by Eames, Betley *et al.* The Fe-Co distances of ~2.5 Å in

these complexes indicate relatively strong bonding, but they were found to have intermediate- and low-spin $S = 1$ and $S = ½$ states for the $[Fe_2Co]^{7+}$ and $[FeCo_2]^{7+}$ complexes, respectively. Thus, in addition to having by far the shortest known Fe-Co distance, **2** also appears to possess the only known example of a high-spin Fe-Co bond. While it is possible that these two intriguing results are unrelated, both phenomena are likely the result of delocalization of the electrons between the iron and cobalt, which is enabled by the rigid ligand system and similar donor groups.

As a sensitive probe of the iron valence, and to compare it to the fully delocalized $Fe_2(DPhF)_3$, we examined **2** by Mössbauer spectroscopy, with measurements performed by the group of Eckhard Bill, at the Max Planck Institute for Chemical Energy Conversion. The zero-field spectrum at 80 K is shown in Figure 3.20. The spectra is broad and asymmetric, as observed for $Fe_2(DPhF)_3$ under the same conditions. In that case, the spectrum did not resolve unless the sample was cooled to 4.3 K under applied field. Unfortunately, **2** has not yet been examined under these conditions, although samples have been sent for analysis. The asymmetry in the Mössbauer doublet can be attributed to paramagnetic relaxation effects. Alternatively, they could be the result of a diiron impurity; although the shape of this signal appears identical in multiple batches of crystalline material appear, such an impurity cannot be ruled out, particularly in light of the metal-mixing observed in the anomalous scattering refinement (*vide supra*). Regardless of the origin of the asymmetry, the isomer shift obtained from a provisional line fit, $\delta = 0.65$ mm/s, is identical to that found for $Fe_2(DPhF)_3$, suggesting that the iron-cobalt complex is a fully delocalized Fe(1.5)Co(1.5) core. The quadrupole splitting, ΔE_Q

= 0.64 mm/s, is slightly larger than that of $Fe_2(DPhF)_3$ (ΔE_Q = 0.32 mm/s), reflecting the slightly larger electric field gradient upon substituting iron with cobalt.

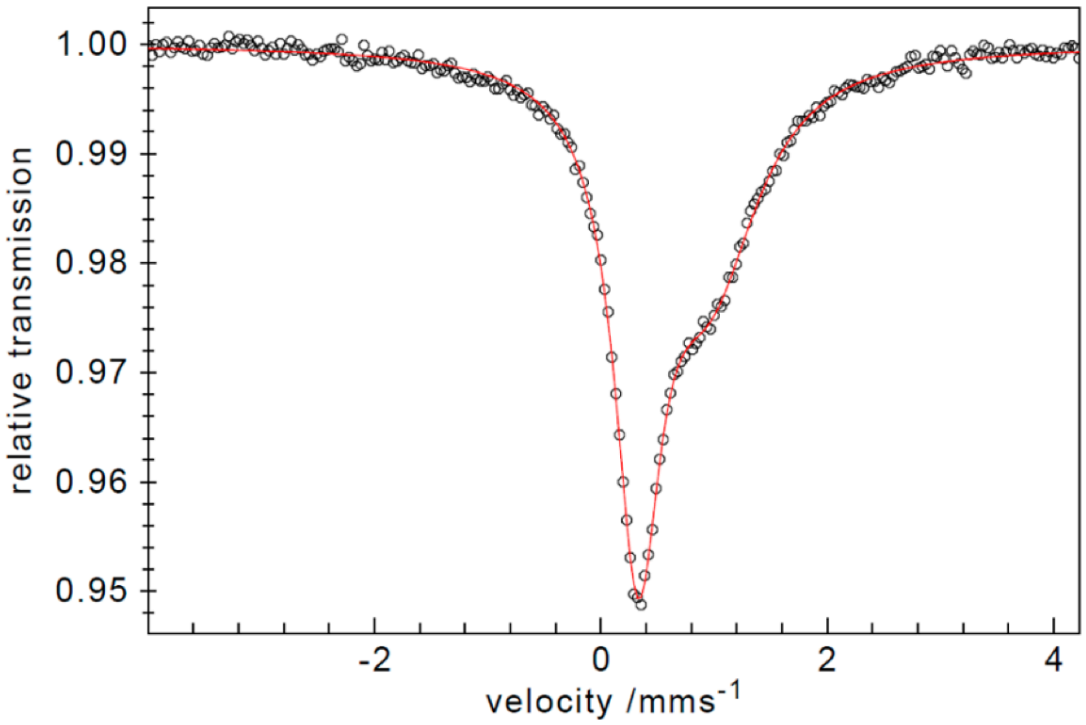

Figure 3.20. Zero-field Mössbauer spectrum of **2** at 80 K. The red solid line represents the best fit using two Lorentzian lines of equal intensity but different widths. Fitting parameters: δ = 0.65 mm/s, ΔE_Q = 0.64 mm/s, line width = 0.5 mm/s for the left line and 1.08 mm/s for the right one.

3.3.7 Theoretical Analysis of Co_2L^{Ph}

The electronic structure of **1** appears by all experimental measurements to be quite similar to that of $Co_2(DPhF)_3$. Nevertheless, we were interested in examining its electronic properties through multiconfigurational theoretical techniques. In addition to defining the bond order, these can help measure the extent of polarization in the Co-Co bond through properties such as the electron counts and spin densities of each metal. Understanding these features in the homobimetallic dicobalt complex, where they would

presumably be due to the asymmetric ligand system, provides a baseline with which to compare the polarization in heterobimetallic complexes like **2**. As with our investigation of the original trigonal lanterns, these theoretical studies were performed in collaboration with the group of Laura Gagliardi at the University of Minnesota and the Minnesota Supercomputing Institute.

The geometry of Co_2L^{Ph} was optimized by DFT methods for the doublet, quartet, and sextet spin states, based on an initial input from the experimental structure. These structures were then used for the multiconfigurational CASSCF/CASPT2 calculations. At all levels of theory, the sextet ^6A was found to be the ground spin state. The energies are shown in Table 3.2.

Table 3.2. Relative energies calculated for Co_2L^{Ph} at DFT, CASSCF, and CASPT2 levels of theory.

	doublet	quartet	**Sextet**
ΔE_{DFT}, eV (cm^{-1})	0.144 (1160)	0.191 (1540)	**0**
ΔE_{CASSCF}, eV (cm^{-1})	1.043 (8410)	0.885 (7140)	**0**
ΔE_{CASPT2}, eV (cm^{-1})	0.752 (6065)	0.614 (4950)	**0**

No symmetry constraints were used in these calculations; however, the geometry calculated for the sextet state reproduces the C_3 symmetry about the M-M axis. The Co-Co bond distance is calculated to be somewhat shorter than in the experimental structure (2.222 vs. 2.294 Å), as are the Co-N distances; underestimated bond distances are common with DFT methods. The other structural parameters are faithfully reproduced. Table 3.3 compares selected parameters for the experimental and calculated geometries.

Table 3.3. Selected structural features of Co_2L^{Ph}, determined experimentally and for the DFT-optimized septet state

Structure	Co_2L^{Ph}	Co_2L^{Ph} *PBE/def-TZVPP Sextet*
Co_1-Co_2, Å	2.2943(7)	2.222
Co_1-N_{ax}, Å	2.135(3)	2.230
Co_1-$N_{eq,}$ Å	1.923(2)	1.938, 1.939, 1.938
Co_2-N_{eq}, Å	2.041(2)	2.007, 2.007, 2.007
N-Co-N, °	119.28(2) 119.18(2)	119.0, 118.9, 118.8 119.7, 119.6, 119.4
N-Co-Co, °	94.89(5); 84.77(5)	96.1, 86.2
N-C-N, °	116.8	116.9

The CASSCF-derived molecular orbitals of **1** are more localized than those found for $Fe_2(DPhF)_3$ and $Co_2(DPhF)_3$. This was seen most dramatically in the attempts to define a set of active space orbitals for the calculations. The d_{xz} and d_{yz} orbitals would be expected to interact to form π-bonding and π*-antibonding orbitals, yet no such interactions were observed. Instead, two filled 3d orbitals are localized on the "top" Co atom, while the corresponding pair on the other cobalt are found at much lower energy, distributed among several orbitals with primarily ligand-based character. Even if they had delocalized, interacting character, these orbitals would represent a filled $\pi^4\pi^{*4}$ set with no net bonding interaction between them and no relevance to the molecular spin state. Therefore, their replacement with localized, non-bonding orbitals should not significantly affect the overall bonding. Because of this, the active space for the CAS calculations was truncated: the low-energy, filled d_{xz} and d_{yz} orbitals of Co1 were omitted from the

calculations, along with their four electrons, resulting in an active space of 11 electrons in 11 orbitals.

The molecular orbitals derived from these AS(11,11) calculations are shown in Figure 3.2.1, along with two representative molecular orbitals from the combination of the d_{xz} and d_{yz} orbitals of Co1 with the L^{Ph} π-system. Other than the unusual π-type orbitals, the MO manifold is qualitatively as expected. The lowest-energy configuration, $(3d_{Co1})^4(\sigma)^2(\sigma^*)^1(\delta)^2(\delta^*)^2$, gives a formal bond order of 0.5, from the $\sigma^2\sigma^{*1}$ pair, and five unpaired electrons in the σ*, δ, and δ* set, exactly as in $Co_2(DPhF)_3$. In addition to the localization of the π-type orbitals, however, there is evidence of some localization in the σ-bonding orbitals. This effect is more subtle, but possibly more important to the bonding. The σ- and σ*- orbitals are polarized, with the filled σ-orbital showing significantly more contribution from the "top" metal, Co2. The half-filled σ* is similarly weighted towards the "bottom" Co1. Unlike the localization of the π-type orbitals, this localization should have an effect on the charge and valence distribution between the Co ions, since the bonding and antibonding orbitals have unequal occupation. The calculated charge densities are only slightly different, at +1.10 for Co2 and +1.32 for Co1. This minor difference in charges likely underestimates the difference in oxidation states, however, since the charge at Co1 is somewhat attenuated by stronger donation from the extra amine and alkyl-substituted N_{eq} donors. The difference in oxidation states is better reflected in the spin densities, which are 2.04 for Co2 and 2.82 for Co1, suggesting that they may best be described as $S = 1$ Co(I) and $S = 3/2$ Co(II) centers. This would be consistent with the greater ability of the "bottom" pocket to stabilize the higher charge.

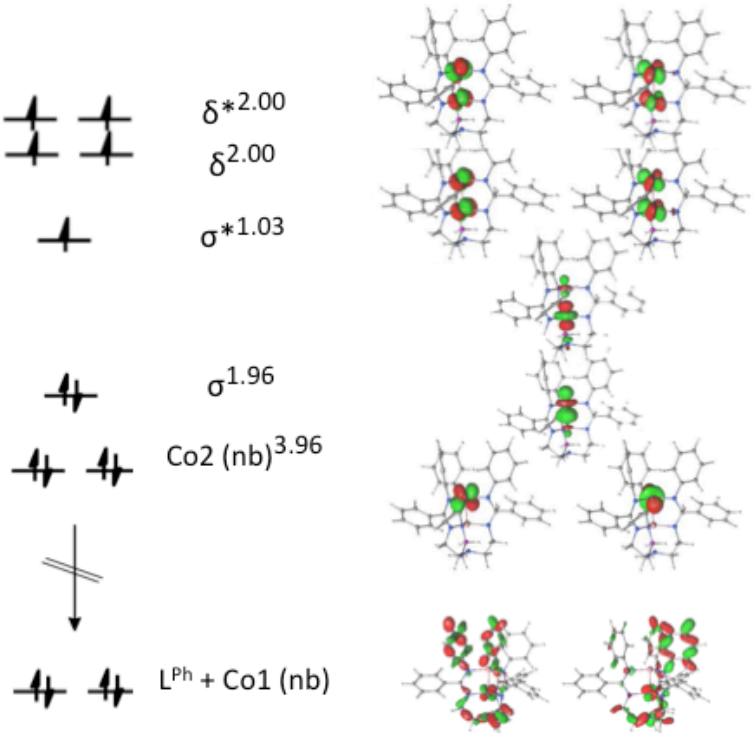

Figure 3.21. Molecular orbitals and occupation numbers for Co_2L^{Ph}, derived from CASSCF calculations with an active space of 11 valence electrons in 11 Co orbitals. Three additional orbitals containing primarily Co 4s and 4d character lie at higher energy and are not shown. Shown at bottom are representative molecular orbitals from the combination of the d_{xz} and d_{yz} orbitals of Co1 with the L^{Ph} π-system, which lie at much lower energy and were excluded from the calculation.

The lowest-energy configuration found in these AS(11,11) calculations represents 95% of the overall wavefunction, making the molecule essentially single-configurational. There are minor excitations into the σ* orbital that lower the bond order, but these are outweighed by excitations into the bonding combinations of fourth-shell orbitals, yielding overall occupancies of $(3d_{Co1})^{3.96}(\sigma)^{1.96}(\sigma^*)^{1.02}(\delta)^{2.00}(\delta^*)^{2.00}(4\sigma)^{0.04}(4\pi)^{0.04}$. This gives an EBO that is slightly higher than the FBO, at 0.51. This is a very different outcome than that of $Co_2(DPhF)_3$, which was highly multiconfigurational and which was found to have an EBO, at 1.14, far higher than the FBO. In that case, the multiconfigurational

wavefunction and higher EBO were the result of excitations out of the π* orbitals and into the δ orbitals. The single-configurational state calculated for Co_2L^{Ph} is likely due to the lack of these π* orbitals. It is still unclear whether this is an artifact of the calculations, which are highly dependent on the choice of an active space. We have attempted to recalculate the electronic structure of Co_2L^{Ph} using an active space of 15 electrons in 12 orbitals, in which the π-type orbitals were included. This indeed resulted in a much more multiconfigurational ground state, in which the lowest-energy configuration was only 27% of the total wavefunction, and in which delocalized π and π* orbitals were observed. However, these calculations also predicted substantial delocalization of the electron density from the half-filled δ and δ* orbitals onto the ligands, which is clearly not observed in the bond metrics of the experimental structure. We thus believe that the AS(11,11) calculations provide a more reliable overall description of the electronic structure; however, we suspect that the localization of the π and π* orbitals observed in these calculations may be due to an idiosyncrasy of the active space. Regardless, these orbitals would only affect the bonding through a second-order effect, *via* their role in higher-energy configurations. In a qualitative sense, the bonding is well-described by the lowest-energy configuration, which is nearly identical to that in $Co_2(DPhF)_3$, as expected.

3.3.8 Theoretical Analysis of $FeCoL^{Ph}$

There is much less precedent for iron-cobalt bonding within weak ligand fields, and we were very interested in the theoretical description of $FeCoL^{Ph}$. Gratifyingly, the

calculations for this molecule appear to be much more straightforward. The geometry of the full molecule was optimized at the DFT level in several possible spin states, from $S = 0$ to $S = 3$, as inputs for CASSCF and CASPT2 calculations. At all three levels of theory, the septet was confirmed as the ground spin state; the differences in energies are given in Table 3.4.

Table 3.4. Calculated relative energies (kcal/mol) of **2** for all possible spin states at DFT, CASSCF and CASPT2 levels of theory.

	DFT	CASSCF	CASPT2
Singlet	15.94	8.53	18.07
Triplet	7.09	10.86	13.99
Quintet	5.58	11.80	11.42
Septet	0	0	0

The septet structure agrees quite well with the experimental structure. The only significant difference with respect to experiment is a distortion from C_3 symmetry: for each metal, there are two smaller N_{eq}-M-N_{eq} angles between 110-115° and one much larger angle, at >130°. This is almost certainly a Jahn-Teller effect, which would be expected to remove degeneracy between the π* orbitals (*vide infra*). However, whereas a similar distortion was found to have a dramatic effect on the calculated M-M distance in the theoretical analysis of $Co_2(DPhF)_3$, it apparently has no significance to the Fe-Co bonding in $FeCoL^{Ph}$, as the calculated Fe-Co distance of 2.170 Å is within 0.015 Å of the trigonally-symmetric experimental structure. Structural parameters are tabulated in Table 3.5.

Table 3.5. Selected bond lengths (Å) and angles (°) for experimental and calculated $FeCoL^{Ph}$ structures

Structure	$FeCoL^{Ph}$	$FeCoL^{Ph}$ *PBE/def-TZVPP Septet*
Fe-Co, Å	2.1846(4)	2.170
Fe-N, Å	2.0528(9)	2.023, 2.040, 2.051
Co-N, Å	1.927(1)	1.939, 1.945, 1.959
N-Fe-N, °	119.982(1)	113.11, 115.34, 131.55
N-Co-N, °	119.643(6)	111.51, 114.20, 132.97
N-Fe-Co, °	89.20(3)	89.22, 88.75, 91.88
N-Co-Fe, °	93.44(3)	91.53, 94.37, 94.93
Fe-Co-N, °	180.0	177.45

CASSCF/CASPT2 calculations were performed using an active space of 14 electrons in 12 orbitals. The orbital manifold comprising the valence 3*d*-electrons is shown in Figure 3.22. The π and π* orbitals are conventional and delocalized, and no significant mixing with ligand orbitals is observed. However, the δ and δ* MOs are replaced by localized, nonbonding d_{xy} and d_{x2-y2} orbitals, likely because the energetic mismatch between iron and cobalt 3d-electrons is not overcome by any bonding interaction. The ground-state wavefunction is dominated by one main configuration (84.9%): $(\sigma)^2(\pi)^4(\pi^*)^3(\sigma^*)^1$(Co d_{xy})^1(Co d_{x2-y2})^1(Fe d_{xy})^1(Fe d_{x2-y2})^1. There is a pronounced difference in the occupation numbers of the two π* orbitals, with one essentially filled at 1.96 and the other half-filled at 1.02. This is attributable to the

aforementioned Jahn-Teller distortion from C_3 symmetry, which removes their degeneracy. The CAS calculations do not give orbital energies directly, but it is unlikely that this effect is energetically significant, as it can be overcome both by crystal packing forces and in solution to give the trigonal symmetry observed in the crystal structure and ^{1}H NMR spectra. Overall, the main configuration gives a formal bond order of 1, from the combination of two $(\sigma)^2(\sigma^*)^1$ and $(\pi)^2(\pi^*)^1$ half-bonds. The increase in bond order is consistent with the experimentally-observed decrease in M-M distance between the dicobalt and iron-cobalt complexes. The half-filled π* orbital also adds one unpaired electron to the five found in Co_2L^{Ph}, resulting in the septet spin state.

For the total ground-state wavefunction, the natural orbital occupation numbers are: $(\sigma)^{1.88}(\pi)^{3.92}(\pi^*)^{2.98}(\sigma^*)^{1.01}$(Co d_{xy})$^{1.04}$(Co d_{x2-y2})$^{1.03}$(Fe d_{xy})$^{1.00}$(Fe d_{x2-y2})$^{1.00}(4\sigma)^{0.11}(4\pi)^{0.03}$, in which the primary excitations are from the 3σ and 3π orbitals into the 4σ and 4π bonding orbitals. This gives an effective bond order of 0.975, essentially identical to the formal bond order.

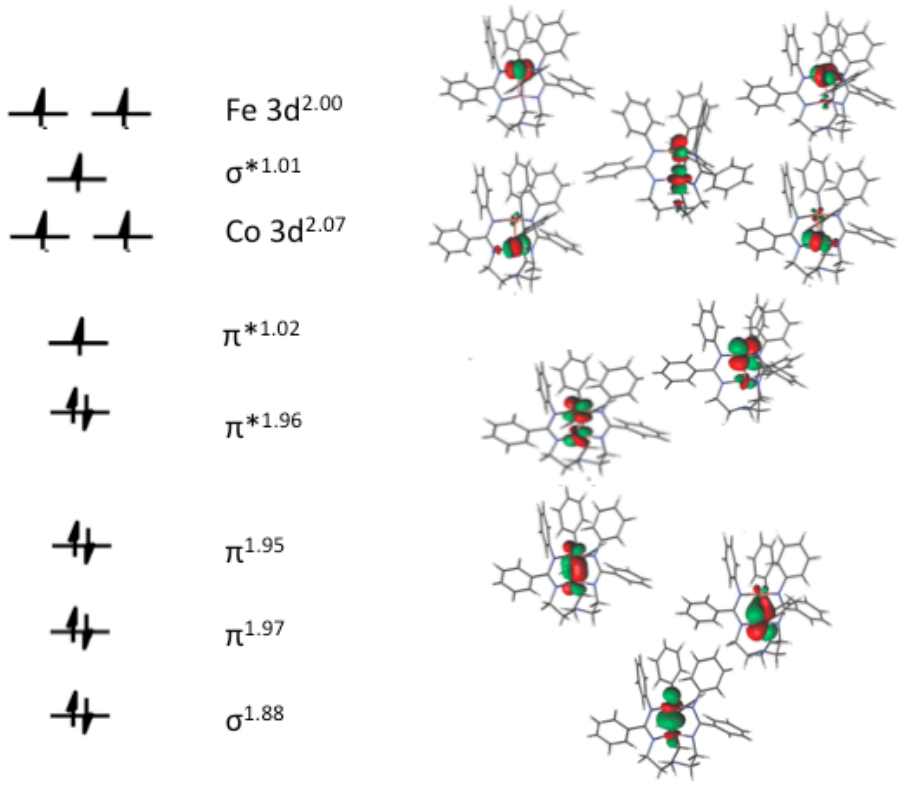

Figure 3.22. Qualitative MO diagram from CASSCF calculations on $FeCoL^{Ph}$. The leading configuration is shown schematically, along with the orbital occupancies from the overall wavefunction.

Inspection of the orbitals in Figure 3.22 reveals that σ and σ* orbitals appear polarized, as in Co_2L^{Ph}. The filled pair of π and π* orbitals are evenly distributed between both metals, but the other pair appears to be largely localized on the two metals. Interestingly, this means that both of the two half-bonding interactions are polarized, but in the opposite direction: in the $(\sigma)^2(\sigma^*)^1$ pair, the filled σ orbital is polarized towards Fe, while the half-filled σ* is polarized towards Co. In the $(\pi)^2(\pi^*)^1$, on the other hand, the filled π orbital is localized on Co while the half-filled π* is localized on Fe. The competing effects should largely cancel out, and, indeed, the d-electron counts calculated

for iron and cobalt are 6.62 and 7.38, respectively, giving oxidation states of $Fe^{+1.38}$ and $Co^{+1.62}$. Thus, the CAS calculations support a highly delocalized $Fe^{1.5}Co^{1.5}$ core, consistent with the conclusion from Mössbauer spectroscopy.

3.3.9 Bond Polarization Effects and Theoretical Comparison to $CoFeL^{Ph}$

Intriguingly, the calculations suggest that the two trigonal lanterns in the M_2L^{Ph} framework are polarized in opposite directions. Co_2L^{Ph} was found to have a more localized Co(I)Co(II) core, in which the more electron-rich center is Co(I), in the "top" position. On the other hand, $FeCoL^{Ph}$ was found to have delocalized, Fe(1.5)Co(1.5) valences, in which the more electron-rich center center is Co(1.5), in the "bottom" position. The reason for this difference is not entirely clear, but it seems to be a competition between polarization due to the ligand and polarization due to the metal position. The bottom binding site, with an extra donor and more strongly donating amidinate nitrogens, should clearly favor a higher positive charge than the top site, which has more electron-withdrawing phenyl substituents on its nitrogen donors. This difference in the binding sites probably favors polarization when the metals are identical, as in the dicobalt. When the top metal is iron, which is less able to stabilize a low-valent +1 oxidation state, this form of polarization is less favorable. This explanation would suggest that the other heterobimetallic isomer, $CoFeL^{Ph}$, should be more stable. To test this hypothesis, we have performed calculations on this hypothetical isomer in a manner entirely analogous to those for $FeCoL^{Ph}$. The geometry was optimized by DFT for all possible spin states, and these structures were used for CASSCF/CASPT2 calculations.

At all levels of theory, the septet was found to be the ground state. Since $CoFeL^{Ph}$ and $FeCoL^{Ph}$ are isomers, their energies can be compared directly. Table 3.6 gives the energies of the two septet states at DFT, CASSCF, and CASPT2 levels of theory, as well as the energies for the lower-spin states of $CoFeL^{Ph}$. Interestingly, while DFT predicts that $FeCoL^{Ph}$ is more stable by 2.5 kcal/mol, CASSCF and CASPT2 predict that $CoFeL^{Ph}$ is more stable.

Table 3.6. Calculated relative energies (kcal/mol) of $CoFeL^{Ph}$ for all possible spin states at DFT, CASSCF and CASPT2 levels of theory. Energies of $FeCoL^{Ph}$ (kcal/mol) are compared below, with values given relative to lowest $CoFeL^{Ph}$ state.

		DFT	CASSCF	CASPT2
$CoFeL^{Ph}$	Singlet	15.94	8.53	18.07
	Triplet	7.09	10.86	13.99
	Quintet	5.58	11.80	11.42
	Septet	0	0	0
$FeCoL^{Ph}$	Septet	-2.51	0.690	1.757

The structural parameters calculated for the CoFe septet geometry are essentially identical to those of $FeCoL^{Ph}$ except for the Co-Fe distance and the M-N_{ax} distance. Important parameters are given in Table 3.7. At 2.148 Å, the M-M distance in $CoFeL^{Ph}$ is calculated to be even shorter than the 2.170 Å calculated for $FeCoL^{Ph}$. The M-N_{ax} distance is calculated to be slightly longer, 2.213 Å for Fe-N in $CoFeL^{Ph}$ vs. 2.170 Å for Co-N in $FeCoL^{Ph}$.

Table 3.7. Selected bond lengths (Å) and angles (°) for calculated $CoFeL^{Ph}$ and $FeCoL^{Ph}$ structures. The labeling scheme is shown at the left.

	Structure	$CoFeL^{Ph}$ *PBE/def-TZVPP* *Septet*	$FeCoL^{Ph}$ *PBE/def-TZVPP* *Septet*
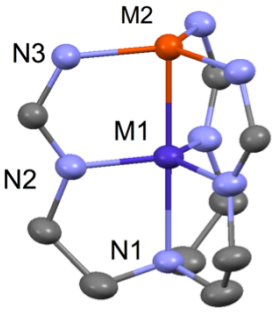	M1-M2, Å	2.148	2.170
	M1-N1, Å	2.213	2.170
	M1-N2, Å	1.967, 1.968, 1.972	1.939, 1.945, 1.959
	M2-N3, Å	2.022, 2.026, 2.024	2.023, 2.040, 2.051
	N2-M1-N2', °	114.04, 115.04, 128.68	113.11, 115.34, 131.55
	N3-M2-N3', °	111.14, 112.18, 136.31	111.51, 114.20, 132.97
	N3-M2-M1, °	86.90, 89.15, 89.41	89.22, 88.75, 91.88
	N2-M1-M2, °	94.67, 95.16, 95.19	91.53, 94.37, 94.93
	Fe-Co-N, °	179.78	177.45

The molecular orbitals found by CASSCF calculations are shown in Figure 3.23. Interestingly, while many features are similar to the MO manifold found for $FeCoL^{Ph}$, there are also large differences. One major difference is that both π* orbitals are half-filled and presumably degenerate. Compensating for the one fewer electron in the π* manifold, one of the nonbonding Co d orbitals from the d_{xy}, $d_{x^2-y^2}$ set is filled and presumably at much lower energy. Because one electron moves from an Fe-Co antibonding orbital to a nonbonding orbital, the formal bond order increases from 1 to 1.5. The overall orbital occupancies are $(\text{Co 3d})^{1.99}(\sigma)^{1.92}(\pi)^{3.86}(\pi^*)^{2.12}(\sigma^*)^{1.02}(\text{Co 3d})^{1.01}(\text{Fe 3d})^{2.01}(4\sigma)^{0.05}(4\pi)^{0.02}$. The EBO calculated from this is 1.355. This large EBO is somewhat surprising, since it is

significantly larger than the EBO of 0.975 calculated for $FeCoL^{Ph}$, yet the bond distance is predicted to be less than 0.03 Å shorter. The larger EBO may in fact be more consistent with the very short Fe-Co distances calculated for both structures: for instance, they are both significantly shorter than the Fe-Fe distance of 2.23 Å in $Fe_2(DPhF)_3$, for which an EBO of 1.15 was calculated.

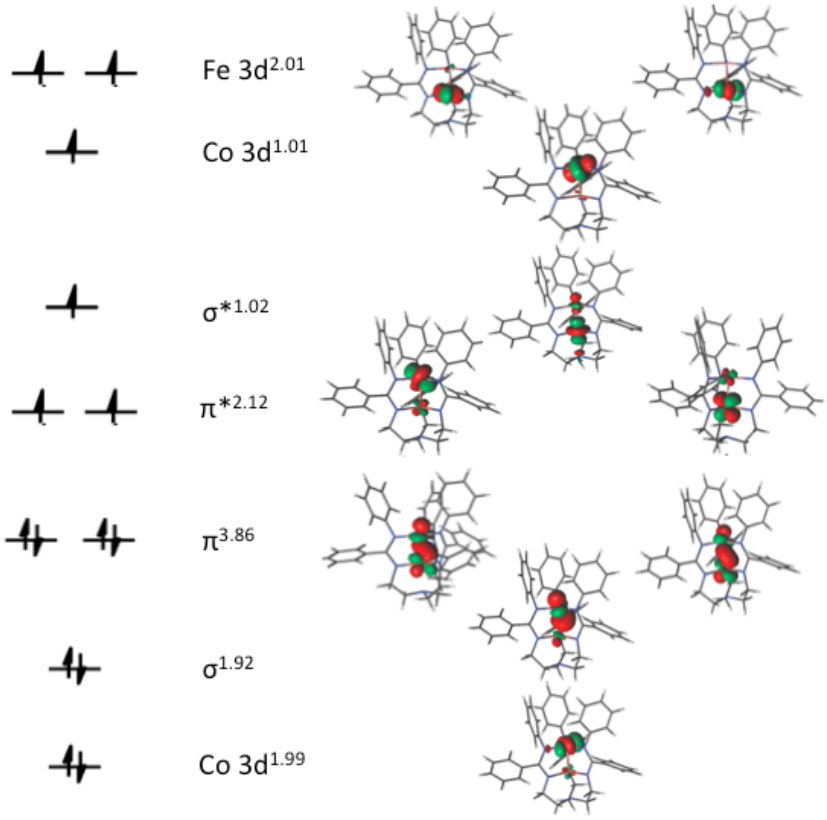

Figure 3.23. Qualitative MO diagram from CASSCF calculations on $CoFeL^{Ph}$. The leading configuration is shown schematically, along with the orbital occupancies from the overall wavefunction.

Finally, the direction of bond polarization in $CoFeL^{Ph}$ should be reversed from that in $FeCoL^{Ph}$, and this was predicted to lead to a more localized distribution of valences, closer to Co(I)Fe(II). The calculations support this assignment: the Mulliken charge density calculated for Fe (+1.42) is higher than for Co (+1.03), despite the

stronger donors around Fe. A better measure of the oxidation states in this high-spin complex is the calculated Mulliken spin density, which is 2.1 for Co and 3.77 for Fe, close to what would be expected for high-spin $S = 1$ Co(I) and $S = 2$ Fe(II) centers. These calculations support the idea that the ligand induces polarization towards $M^{I}M^{II}$ valences, with the top binding site favoring the M(I) oxidation state. The delocalized $M^{1.5}M^{1.5}$ valences in **2** are due to the inability of Fe to stabilize a full (+1) oxidation state; when the more electronegative Co is in the top position, in both Co_2L^{Ph} and $CoFeL^{Ph}$, the valences are indeed more localized.

3.3.10 Attempted Synthesis of $CoFeL^{Ph}$

It would seem that the simple stepwise metallation strategy used in the synthesis of $FeCoL^{Ph}$ should also be extensible to the synthesis of $CoFeL^{Ph}$. However, the analogous reaction, involving reduction of $K(THF)FeL^{Ph}$ with KC_8 and then addition of $CoBr_2$ gives very inconsistent results. Two species are observed by ^1H NMR, which appear to be $FeCoL^{Ph}$ and Co_2L^{Ph}. The relative yields of these species are highly variable. Most often, they are obtained as mixtures; however, in various reactions, each has been isolated as essentially the sole product. Representative spectra are shown in Figure 3.24 for the different product distributions obtained under essentially identical reaction conditions.

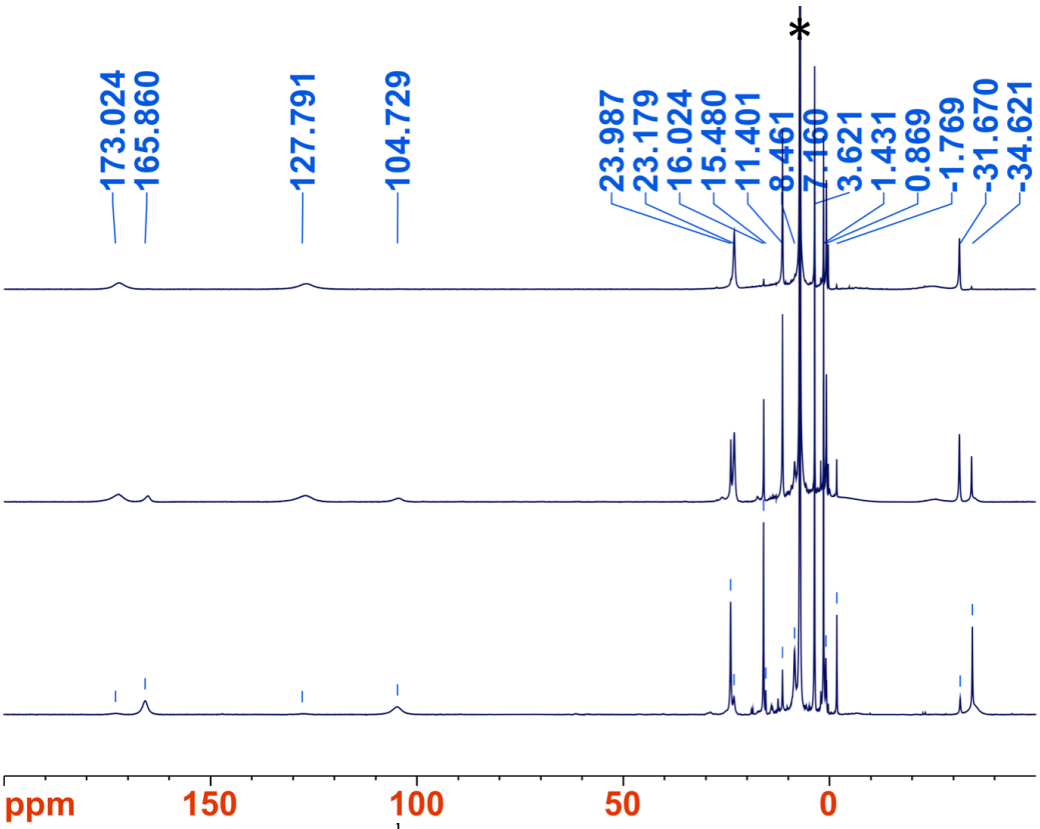

Figure 3.24. Representative crude ^{1}H NMR spectra (500 MHz, C_6D_6) from attempted syntheses of $CoFeL^{Ph}$, showing the variability in product distributions. The products are $FeCoL^{Ph}$ (top), Co_2L^{Ph} (bottom) or, more often, a mixture (middle). For all three spectra shown, the reaction involved addition of KC_8 to a THF solution of **4** at -78°, followed after 5 minutes by dropwise addition of $CoBr_2$ as a solution in THF. The reaction mixture was stirred at -78° for 30 minutes, then raised to room temperature and stirred an additional 12 hours before filtration and removal of solvent *in vacuo*. The ratios of $FeCoL^{Ph}$:Co_2L^{Ph}, determined by the ratios of the peaks at 11.4:16.0 ppm are: > 15:1 (top), 3:1 (middle), and < 1:6 (bottom).

In cases where a single major product was observed, the products have been analyzed by a number of spectroscopies. Initial Mössbauer studies showed mixtures of $FeCoL^{Ph}$ and another iron-containing product, with a slightly higher isomer shift of 0.93 mm s^{-1} and a much higher quadrupole splitting of 2.5 mm s^{-1} (Figure 3.25). Since its intensity varied with the distribution of the products observed by NMR, it was assumed to be $CoFeL^{Ph}$; we figured that this isomer might have an NMR spectrum coincidentally

similar to Co_2L^{Ph}, and that this was the other species observed in these reactions. However, subsequent studies showed that the second species observed by NMR is in fact the dicobalt, **1**. When isolated cleanly, it has UV-Vis-NIR and EPR spectra identical to Co_2L^{Ph}. The latter, in particular, is definitive evidence for its identity as Co_2L^{Ph}, since $CoFeL^{Ph}$ must be integer-spin and should not be EPR-active. In fact, when they are isolated cleanly, both the $FeCoL^{Ph}$ and Co_2L^{Ph} produced by these reactions have identical absorption spectra to samples of **2** and **1**, respectively produced via the metallation of $K(THF)CoL^{Ph}$ (Figure 3.26). The second signal in the initial Mössbauer spectra must therefore have been due to an impurity. Its Mössbauer parameters are similar to those of iron(II)-containing species with similar ligand systems produced in our lab, and we suspect that it is either the product of oxidative decomposition or incomplete reduction to the Co(I)Fe(II) product. This is not entirely surprising, since the crude products from reactions that produce substantial amounts of Co_2L^{Ph} are in general less pure (c.f. the baselines of the bottom two spectra in Figure 3.24, vs. the baseline in the top spectrum) as necessitated by the limiting amount of cobalt in these reactions.

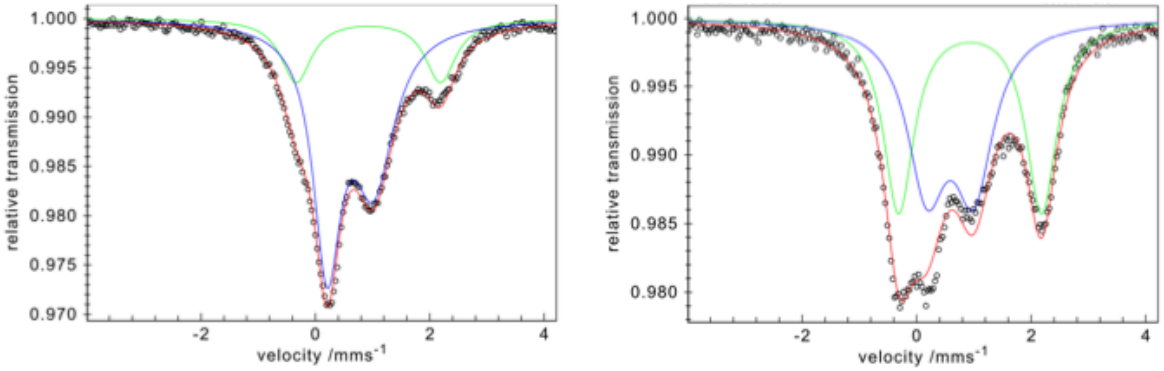

Figure 3.25. Mössbauer spectra observed for crude products in early attempts to produce $CoFeL^{Ph}$. Provisional line fits find two species, with fitting parameters δ 0.61 mm/s, ΔE_q 0.82 mm/s (blue line) and δ 0.93 mm/s, ΔE_q 2.51 mm/s (green line).

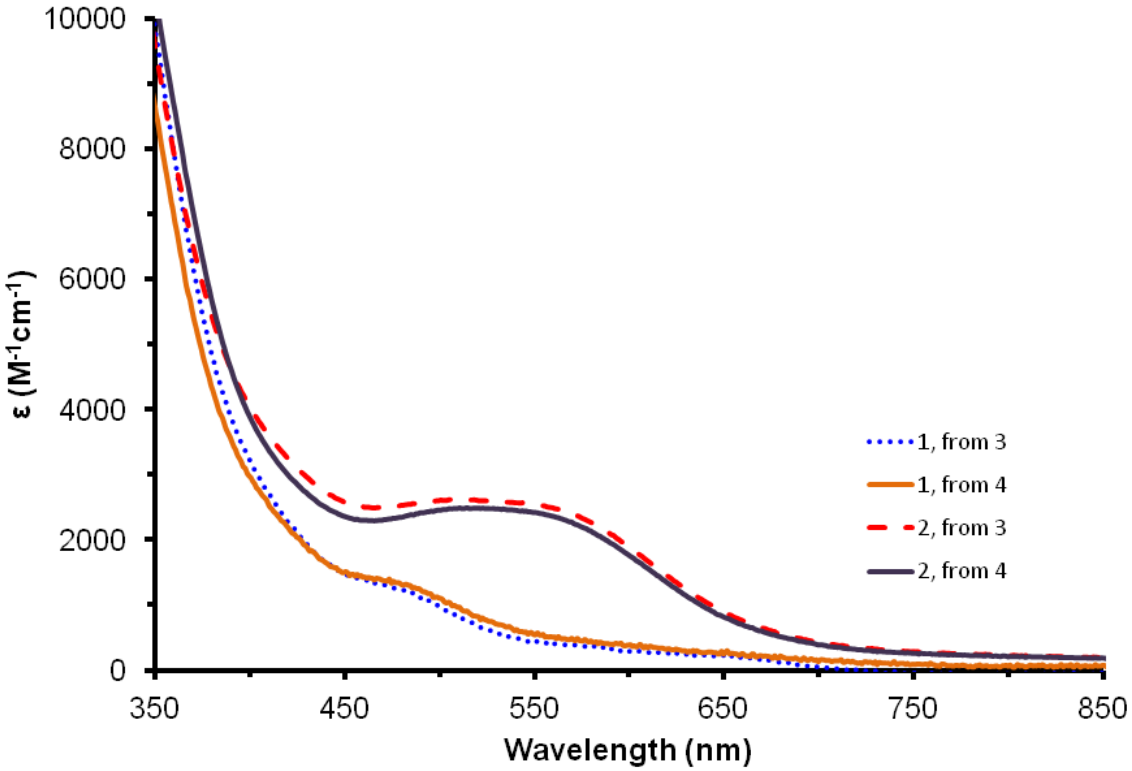

Figure 3.26. UV-Vis absorption spectra (THF, 0.04 – 0.14 mM) for samples of **1** and **2** produced by different reactions. The dashed red and dotted blue lines represent authentic samples of **1** and **2** produced by reduction of **3** and addition of $CoBr_2$ or $FeBr_2$, respectively. The solid purple line represents **2** isolated from the reduction of **4** and addition of $CoBr_2$. The solid orange line represents **1** isolated from a different reaction using the same procedure.

With the two products assigned as $FeCoL^{Ph}$ and Co_2L^{Ph}, we sought to develop methods to control their distribution, hoping that this would inform the synthesis of new bimetallic species. Variation of the reaction conditions and synthetic protocol for the reaction of $K(THF)FeL^{Ph}$ with KC_8 and $CoBr_2$ does not result in any products other than $FeCoL^{Ph}$ or Co_2L^{Ph}. Only the distribution of these products varies, typically within the range 2:1-5:1 $FeCoL^{Ph}$: Co_2L^{Ph}. These distributions cannot reliably be controlled by factors such as concentration, temperature, or reaction scale (most reactions were run at a 75 mg scale, *ca*. 2 mM in THF). Variation of the reaction time does not produce a significant difference in product distribution, either; nor does the order of addition for

the KC_8 and $CoBr_2$ reactants. Use of a different solvent was problematic, as the reactants are insoluble in less polar solvents than THF, while more polar solvents are either unstable to KC_8 or have melting points too high to be used at -78 °C. The heterogeneous reaction of the undissolved reactants in toluene gives no products; presumably, the KC_8 simply reduces the $CoBr_2$ to Co metal before it can react with the mono-iron.

Use of the weaker reductants Mg(0), Na/Hg, or $CoCp^*_2$, does not produce reduced products, giving instead the metal(II) clusters "$(BrFeCoL^{Ph})_n$" and "$(BrCo_2L^{Ph})_n$." The stronger reductant sodium naphthalenide gives $FeCoL^{Ph}$ and Co_2L^{Ph} in variable amounts, with product ratios ranging between 3:1-7:1 $FeCoL^{Ph}$:Co_2L^{Ph}. However, variation of the cobalt dihalide source has a strong and predictable effect on the product distribution. Specifically, use of CoI_2 instead of $CoBr_2$ leads reliably to $FeCoL^{Ph}$ as essentially the sole product, with ratios typically between 10:1 and 20:1 FeCo:CoCo, as measured by ^{1}H NMR integration. Use of $CoCl_2(THF)_{1.5}$ instead gives Co_2L^{Ph} as the sole product; the reaction is cleanest when the dichloride salt is added 15-30 mins before KC_8. Finally, addition of 1 equivalent of the Co(I) source $CoCl(PPh_3)_3$ to $K(THF)FeL^{Ph}$ results in clean and exclusive formation of $FeCoL^{Ph}$ after washing away the product PPh_3, indicating that rearrangement of the isomers occurs even without an external reductant. These results are summarized in Figure 3.27.

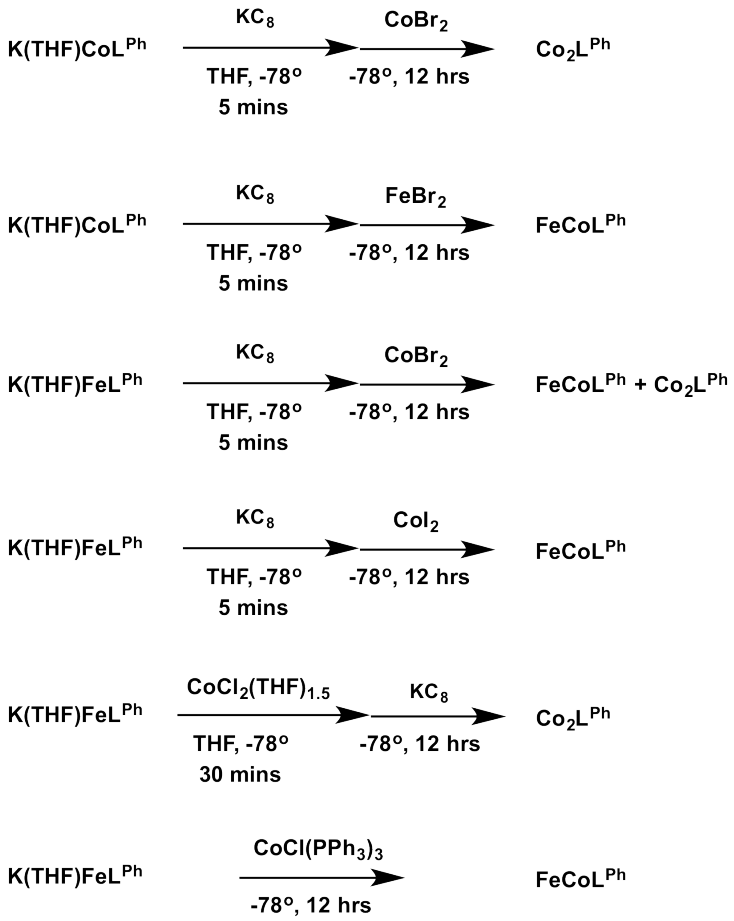

Figure 3.27. Summary of reaction conditions and outcomes in synthesis of **1** and **2**.

The fact that the same heterobimetallic complex is observed regardless of synthetic procedure strongly implies that the preference for iron to bind in the top position and cobalt in the bottom is driven by thermodynamics. This is unfortunate, in one sense, as we had envisioned the stepwise metallation procedure leading to a variety of heterobimetallic systems, assuming that the metal positions could be kinetically controlled, with selectivity imparted by the synthetic route. Thermodynamic control over the selectivity implies that far fewer metal combinations are achievable in this system. It is also worth noting that the CASSCF and CASPT2 calculations predict that $CoFeL^{Ph}$

is the thermodynamically-preferred isomer, which is contrary to the experimental results; however, the opposite prediction was made by DFT, and, moreover, the predicted energy difference between the isomers was less than 2.5 kcal/mol at all levels of theory, which is within the error of most calculations. In this sense, the observed thermodynamic preference is informative: even such a small difference in energy can lead to the observed selectivity. This suggests that the metals are quite labile, even within the context of a metal-metal bonding framework.

The lability of the metals in these systems is also demonstrated in the observation that $FeCoL^{Ph}$ slowly converts to Co_2L^{Ph} over time when kept in solution. This conversion appears too slow to be the source of the large dicobalt byproduct formed in many of the synthetic routes described above. However, it occurs at a rate significant enough to be an issue in crystallization. With the optimized synthetic procedure, $FeCoL^{Ph}$ can be isolated quite cleanly after filtration of the crude reaction mixture to remove graphite, removal of volatiles, and extraction into toluene to remove KBr. The $FeCoL^{Ph}$ produced by this method is quite pure, obtained in good yield, and essentially free of Co_2L^{Ph} as a byproduct, as observed by ^{1}H NMR (Figure 3.28, top). However, crystallization of this crude material consistently results in the formation of Co_2L^{Ph}, as measured by ^{1}H NMR (Figure 3.28, bottom). As an additional measure of the iron and cobalt content in **2**, a sample of bulk crystalline material was analyzed by inductively-coupled plasma optical emission spectroscopy (ICP-OES). This technique revealed Fe and Co percentages of 44.5% and 55.5%, respectively. Integration of the NMR spectrum for this same batch of crystals gave percentages of 12.5% Co_2L^{Ph} and 87.5% $FeCoL^{Ph}$, based on the relative

integrations of the peaks at 16.0 and 11.4 ppm. This corresponds to an iron content of 44% and a cobalt content of 56%, in excellent agreement with the ICP-OES results. This result appears to validate the use of ^{1}H NMR to quantify the relative amounts of **1** and **2**.

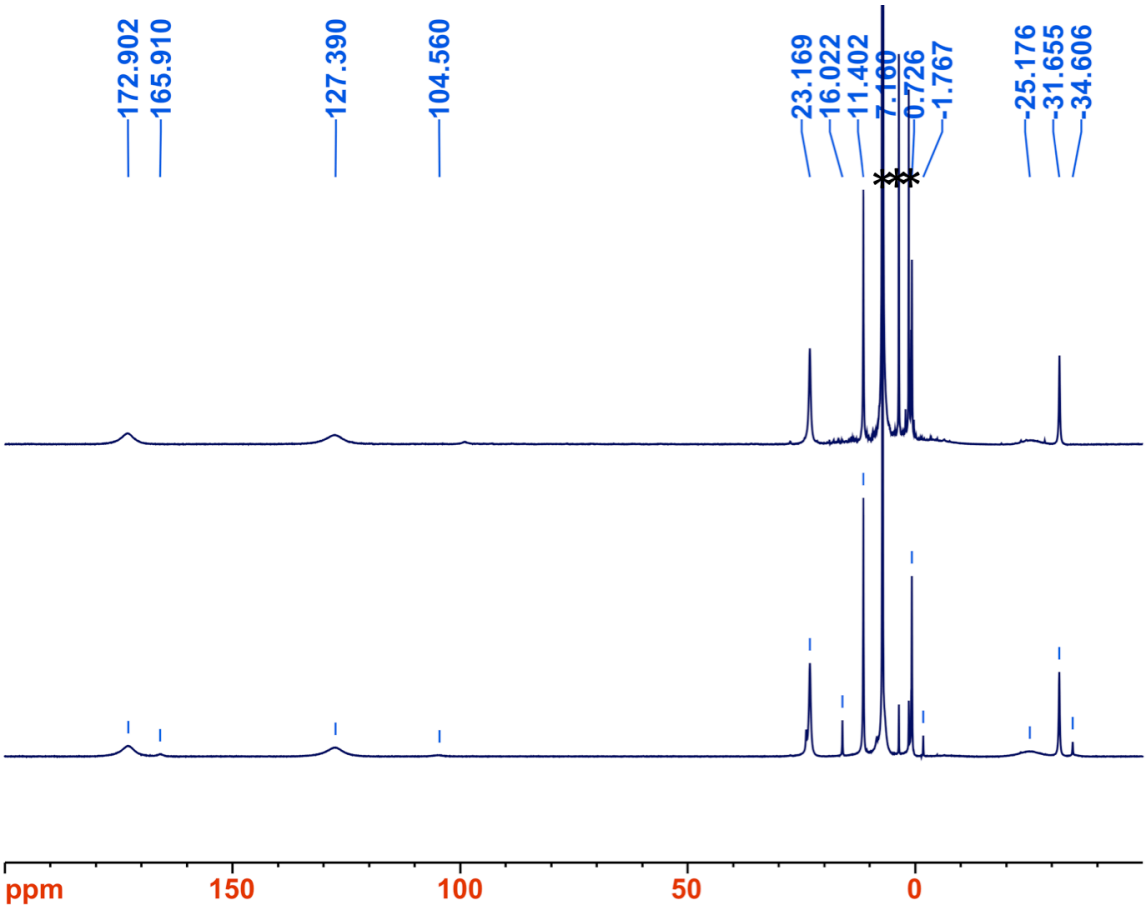

Figure 3.28. ^{1}H NMR comparison (500 MHz, C_6D_6) of crude (top) and crystallized (bottom) samples from the same batch of **2**, showing partial conversion to **1**. Residual solvent peaks are marked with an asterisk.

This conversion to Co_2L^{Ph} can apparently only be mitigated by increasing the rate of crystallization as much as possible. The best results are obtained by layering near-saturated THF solutions with hexane; use of pentane, which is less dense and diffuses more slowly into THF, results in more Co_2L^{Ph}, as does crystallization *via* vapor diffusion.

No other products are observed in the crystals, and after crystallization is essentially complete, the supernatant is consistently a yellow-brown mixture of unidentified and asymmetric-looking paramagnetic products. We have found that the diiron homobimetallic, Fe_2L^{Ph}, is entirely unstable with this ligand system (*vide infra*). One plausible explanation for the conversion to Co_2L^{Ph} is thus that the high-spin metal ions in $FeCoL^{Ph}$ are quite labile, and that the complex is therefore in equilibrium with the homobimetallics, Co_2L^{Ph} and Fe_2L^{Ph}; since the latter species is unstable, its conversion to other, as-yet-unidentified products drives the equilibrium away from the heterobimetallic species. This rearrangement is somewhat remarkable, in that it requires cleavage, at minimum, of three Fe-N bonds and four Co-N bonds, in addition to the Fe-Co bond. However, similar rearrangements were observed by Betley and Eames in the preparation of their $[Fe_2Co]^{7+}$ and $[FeCo_2]^{7+}$ clusters from the $[Fe_3]^{7+}$ homotrimetallic.[36] In that case, the rearrangement took place upon reaction with excess $CoCl_2$ and was presumed to proceed through halide-bridged intermediates; in this case, the rearrangement apparently occurs through direct reaction of the bimetallics themselves. The $^{Ph}L^{(3-)}$ ligand has proven flexible enough to bridge between the bimetallic units in dimerized, tetranuclear oxo structures (*vide infra*), and it is plausible that this rearrangement proceeds through similar intermediates.

3.3.11 Attempted Synthesis of Other Bimetallics

We have also attempted to extend the stepwise metallation procedure to the synthesis of new bimetallic pairs, without much success. Although the mono-cobalt

precursor **3** metallates cleanly with iron and cobalt to form **1** and **2**, attempts to use this monometallic to prepare other Co-containing bimetallics have been largely unsuccessful. Analogous reactions with manganese reagents produced an intractable mixture of paramagnetic products, which we have been unable to characterize. Reaction of **3** with KC_8 and nickel dihalides gives only the reduced mono-cobalt dianion, $Co^{I}(L^{Ph})^{2-}$, which is an intermediate in the synthesis of **1** and **2**, characterized by its bright yellow color and its paramagnetic, C_{3V}-symmetric ^{1}H NMR spectrum. This is not particularly surprising, as the "$NiCoL^{Ph}$" target would be expected to have one more M-M antibonding electron than Co_2L^{Ph} and thus no M-M bond. A similar prediction would hold for "$CuCoL^{Ph}$," but, interestingly, **3** reacts rapidly with CuBr in THF. The NMR spectrum of the yellow product shows two asymmetric species with a similar pattern and only slightly different shifts. These can be easily separated, as one is insoluble in toluene or benzene. This insoluble species was crystallized from THF and Et_2O; its solid state structure is plagued by disordered solvent and low-quality data, but the molecular structure is nevertheless quite evident from the refinement, shown in Figure 3.29. The Co binds in the bottom pocket in the usual κ^4 trigonal pyramidal geometry**,** but the Cu atom resides in the top binding site in an unexpected linear, two-coordinate geometry. It is coordinated by only two of the amidinates and has a long Cu-Co distance of 2.590(2) Å that is unlikely to correspond to a significant bonding interaction. The third amidinate has rotated and is bound end-on to a dangling, dinuclear unit of heavy atoms that are assigned as CuBr. This assignment appears valid based on both the thermal ellipsoids and the bond metrics: The Cu2-N7 distance of 1.892(1) Å for the dangling copper is nearly identical to the Cu1-

N3 and Cu-N5 distances of 1.878(1) and 1.901(1) Å for the chelated copper atom. Likewise, the N7-Cu2-Br1 angle of 173.2(4)° is consistent is similar to the N3-Cu1-N5 angle of 171.0(5)° for the chelated copper. The linearity of the chelated copper atom is suggestive of a two-coordinate, d^{10} Cu(I) ion, in which little to no significant delocalization occurs between the Cu and Co.

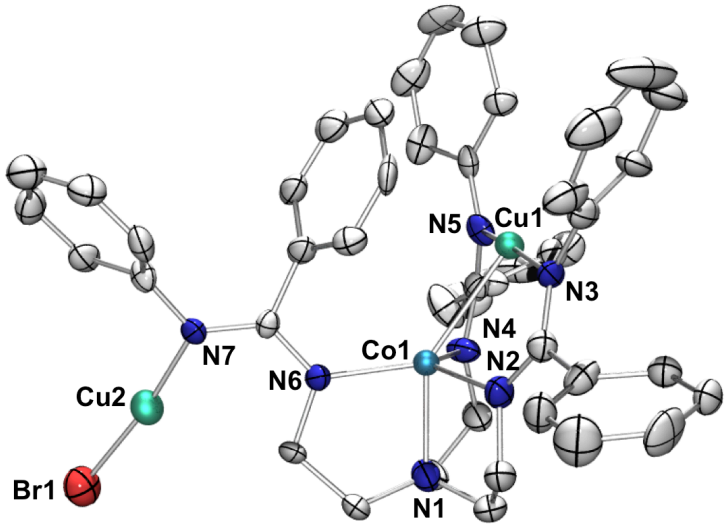

Figure 3.29. Molecular structure of $CuCoL^{Ph}$•CuBr at 50% probability level. For clarity, hydrogen atoms and disordered THF solvent have been omitted. Selected bond distances (Å) and angles (°): Co1-Cu1, 2.590(2); Co1-N1, 2.103(1); Co1-N2, 1.993(1); Co-N4, 1.953(1); Co-N6, 1.963(1); Cu1-N3, 1.901(1), Cu-N5, 1.878(1); Cu2-N7, 1.892(1); Cu2-Br1, 2.213(3); N1-Co1-Cu1, 144.0(3); N3-Cu1-N5, 171.0(5); N7-Cu2-Br1, 173.2(4).

This "$CuCoL^{Ph}$•CuBr," THF-soluble species could be separated from the other product observed in the crude mixture by extraction into toluene. The similarity of the NMR spectra for both species suggests similar structures, and we suspected that this second species was the "$CuCoL^{Ph}$•$K(THF)_x^+$" cation, in which potassium replaces the dangling CuBr. This species can be produced essentially quantitatively by the reaction of **3** with $Cu(MeCN)_4$•PF_6 instead of CuBr, which seems to validate the hypothesis. Its ^{1}H

NMR spectrum is shown in Figure 3.30: 18 resonances are clearly visible, consistent with solution-averaged C_{2V} symmetry, in which one arm is distinct and the other two are equivalent, making the *tren* backbone diastereotopic. This is clearly supports the solid-state structure and shows that its asymmetry is retained in solution.

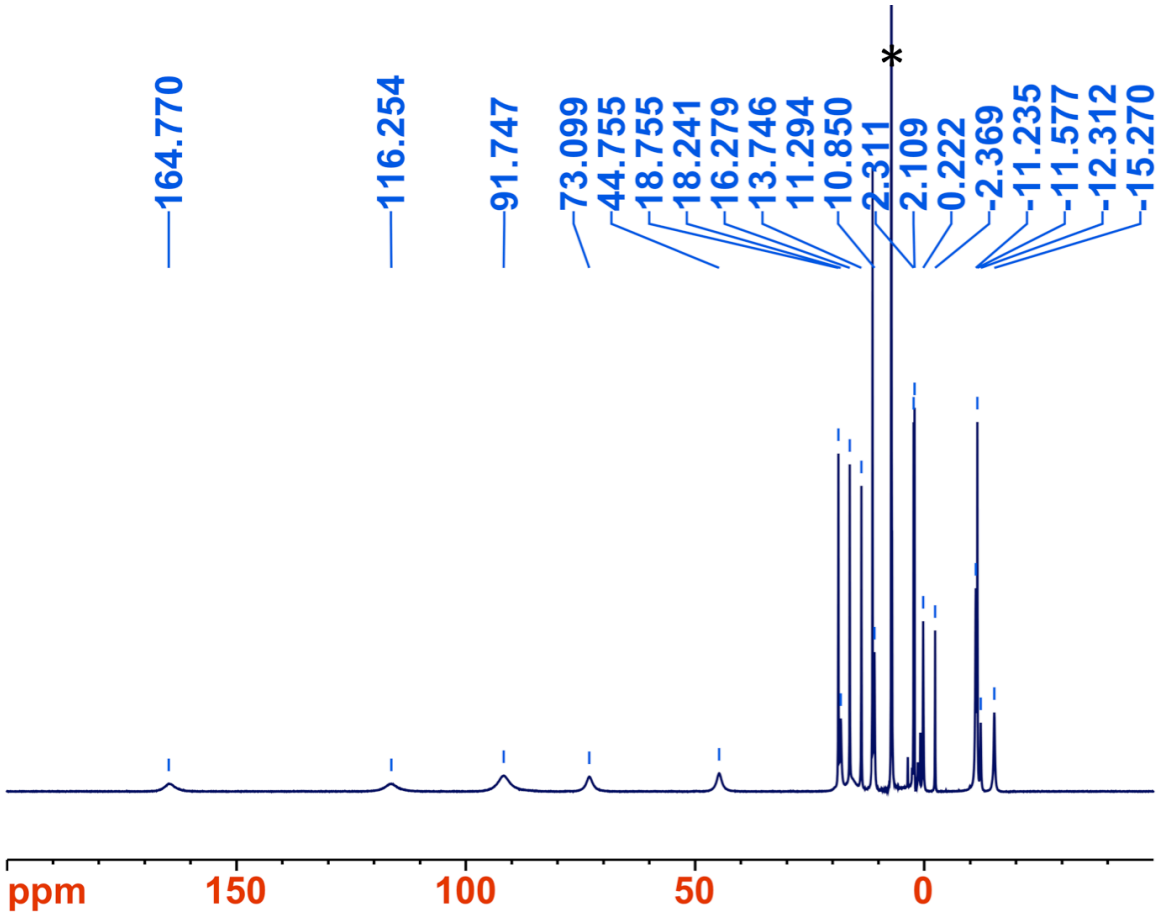

Figure 3.30. ^{1}H NMR spectrum of "CuCoLPh•KPF_6" (500 MHz, C_6D_6). The residual solvent signal is marked with an asterisk.

This species was also examined by EPR spectroscopy (Figure 3.31). It shows an axial signal with g_{eff} values of ~4.3 and 2, consistent with an S = 3/2 overall spin. The complex is thus "high-spin," but the spin appears to be entirely localized on Co, based on the 8-line signal observed for the low-g resonance. This is consistent with hyperfine

coupling to the $I = 7/2$ ^{59}Co nucleus. No coupling is observed to the $I = 3/2$ ^{63}Cu nucleus. Thus the molecule appears to have fully localized Cu(I)Cu(II) oxidation states, in which the spin resides solely on the high-spin, $S = 3/2$, Co(II), rather than the d^{10} Cu(I) center. The axial signal further suggests that the Co ion, despite the bent N_{ax}-Co_1-Cu_1 angle of 144°, does not perturb the electronic environment of Co enough to cause even a rhombic distortion.

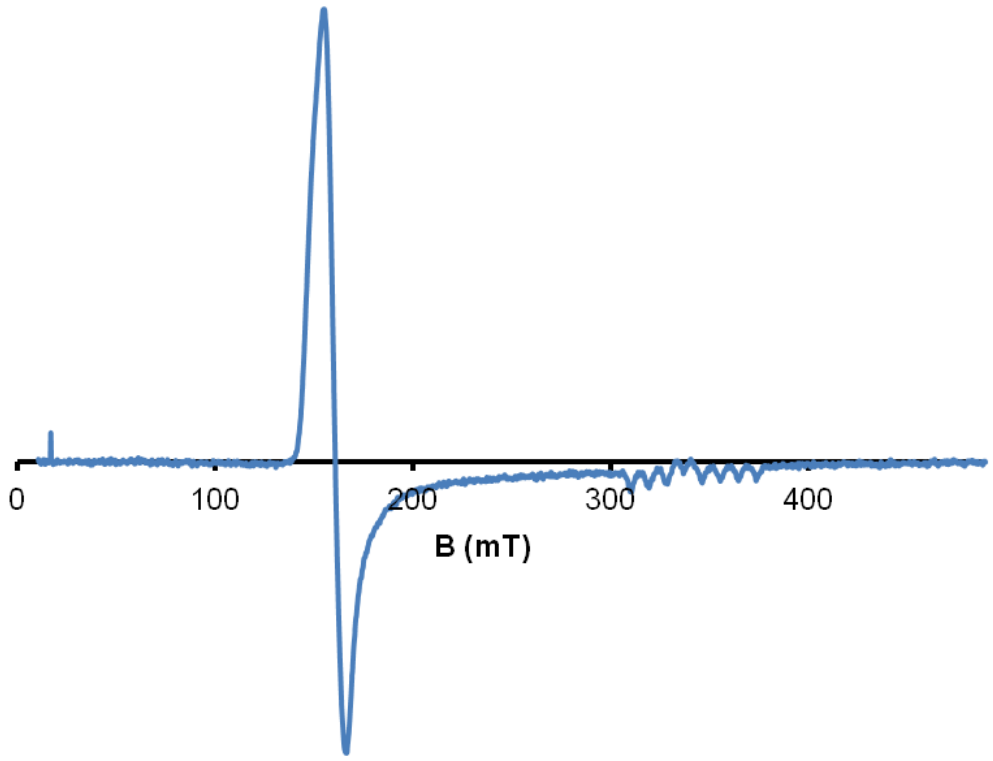

Figure 3.31. X-band EPR spectrum (dX″/dB) of "CuCoLPh•K(THF)$_n$" in toluene glass (1.0 mM, 20.0L, frequency = 9.646 GHz, modulation to 1.0 G, power = 20.0 mM. Residual signal from within the instrument cavity causes the slight irregularity in the low-*g* resonance.

A yellow copper-iron product with a very similar pattern of resonances in its NMR spectrum can also be prepared by addition of Cu(MeCN)$_4$•PF$_6$ to mono-iron **4**. The C_{2V} symmetry of the complex suggests a similar two-coordinate copper center, and no

significant Cu-Fe interaction is expected. For both Cu(I)Co(II) and Cu(I)Fe(II) cores, the d^{17} and d^{16} electron counts should not yield net bonding within the trigonal lantern MO manifold; there would be too many electrons filling antibonding orbitals. Attempts were made to prepare more electron-deficient complexes using Cu(II) reagents: a potential d^{15} electron configuration in a "$Cu^{II}Fe^{II}L^{Ph+}$" cation or halide complex, for instance, would be formally isoelectronic with Co_2L^{Ph}. However, the results suggest that the Cu(II) ion simply oxidizes the Fe(II) or Co(II) monometallics. Addition of Cu(II) sources to **4** gives the characteristic deep purple color and paramagnetic NMR spectrum of $Fe^{III}L^{Ph}$. The analogous $Co^{III}L^{Ph}$ monometallic is unstable, and addition of Cu(II) precursors to **3** gives only the characteristic paramagnetic decomposition products. For this reason, the copper complexes were not pursued further.

Attempts to synthesize other iron-containing bimetallics from **4** have been unsuccessful. We have found no promising routes to the diiron complex Fe_2L^{Ph}; it appears unstable when accessed via reduction of the mono-iron(II) complex and addition of an iron dihalide, with the product mixture showing too many peaks (by ^{1}H NMR) to be consistent with even a C_1-symmetric bimetallic product. Similar results are obtained from reduction of the diiron halide cluster "$(XFe_2L^{Ph})_n$," which we have been unable to crystallographically characterize but which shows a consistent, highly asymmetric, highly paramagnetic ^{1}H NMR spectrum. We have also attempted, without success, reactions of the $Fe^{III}L^{Ph}$ monometallic complex with iron(0) sources $Fe_{(s)}$, $Fe^0(COT)_2$, (where COT = cyclooctatetraene), or combinations of iron(II) reagents and reductant. Finally, "comproportionation" reactions were attempted where $K(THF)FeL^{Ph}$ was reacted with

combinations of Fe^{II} and Fe^{0} sources in an attempt to install an Fe^{I}. Adding $FeBr_2/Fe_{(s)}$ or $FeBr_2/Fe(COT)_2$, however, yields only a mixture of the cluster "$(BrFe_2L^{Ph})_n$" and monometallic $K(THF)FeL^{Ph}$. Considering that the metals in the iron-cobalt heterobimetallics are quite labile, and their synthesis is apparently thermodynamically controlled, it is possible that, even if it can be formed transiently, the diiron compound is simply less stable than some other, as-yet uncharacterized product or mixture of products.

On the other hand, reactions to form the heterobimetallic $NiFeL^{Ph}$ are more promising. The reaction of $K(THF)FeL^{Ph}$ with KC_8 and NiI_2 is inconsistent, but some reactions form a new orange-brown product with a C_{3V} NMR spectrum very similar to that of **1** and **2** (Figure 3.32). This reaction only proceeded successfully with NiI_2 as a reagent: use of $NiBr_2$ or $NiCl_2$ give only the $Fe^{I}L^{(Ph)2-}$ dianion or decomposition products. Even the reaction with NiI_2 is inconsistent, often only giving low conversion and primarily $Fe^{I}L^{(Ph)2-}$. A more reliable route to this complex was found to be the "comproportionation" reaction of $K(THF)FeL^{Ph}$ with one half equivalent each of $NiBr_2$ and $Ni(COD)_2$ (where COD = cyclooctadiene). This reaction is extremely slow, however, taking up to one week for substantial conversion. With this slow timescale, oxidative decomposition is competitive with product formation. A much faster, and therefore much cleaner, conversion was achieved by adding one equivalent of the crown ether 18-crown-6 to these reaction mixtures. This presumably binds to the potassium in $K(THF)FeL^{Ph}$ and thereby promotes the addition of Ni. With the added crown ether, the reaction is essentially complete within 12-36 hours and gives $NiFeL^{Ph}$ as an light orange-brown product quite cleanly. The diagnostic downfield shifts in the ^1H NMR spectrum at δ 169

and 103 ppm are very similar to those of **1** (δ 165.3 and 104.5), as is the orange-brown color of the compound. This is intriguing, as the 15-electron bimetallics are formally isoelectronic. Unfortunately, while the COD byproduct can be easily removed by washing with hexane, the crown-ether-KBr adduct is not easily removed. This has hindered our attempts to crystallize $NiFeL^{Ph}$, and as a result, only its oxidized decomposition product has thus far been crystallographically characterized (*vide infra*).

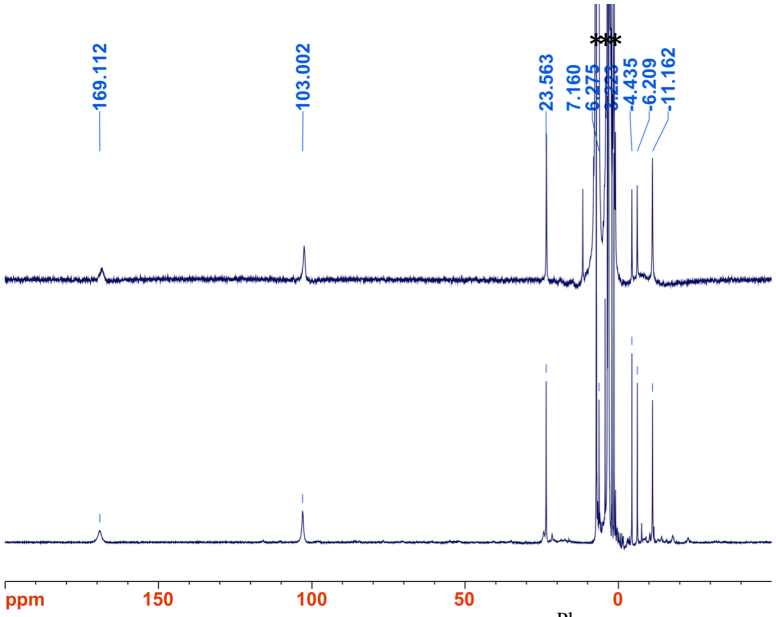

Figure 3.32. ^{1}H NMR spectra (500 MHz, C_6D_6) of $NiFeL^{Ph}$ produced by either addition of NiI_2 to reduced **4** (top) or addition of ½ equivalent each of $NiBr_2$ and $Ni(COD)_2$ to **4** (bottom).

3.3.12 Oxidized Cluster Complexes

As with the original trigonal lanterns, Co_2L^{Ph} and $FeCoL^{Ph}$ are extremely sensitive to reaction with adventitious oxygen, as are the other bimetallic species we have attempted to prepare. This has led to the characterization of a number of heteronuclear oxo complexes in our attempts to crystallize the bimetallic compounds. For the most part, these oxo species are analogous to the homonuclear tetrairon oxo, $[Fe_2(DPhF)_3]_2O$: they

are tetranuclear compounds in which two bimetallic units have combined to form a distorted tetrahedron around a central, μ^4-bridging oxo atom. This implies one-electron oxidation of each bimetallic unit. These compounds are structurally quite similar and crystallize in nearly identical unit cells within the monoclinic space group $C_{2/c}$. Crystallographic parameters are given in Table 3.8. The structure $(MnFeL^{Ph})_2O$ was determined by another member of our lab and is included for the sake of comparison. The structure $(FeCoL^{Ph})O$ was obtained from the reaction of $K(THF)CoL^{Ph}$ with $FeBr_2$ and KC_8 and "$(CoFeL^{Ph})O$" was obtained from the reaction of $K(THF)FeL^{Ph}$ with $CoBr_2$ and KC_8. Aside from a difference in non-coordinated solvent, these structures are identical, within error, providing further evidence that these reactions in fact produce the same isomer.

Table 3.8. Crystallographic details for heterobimetallic $M_2M'_2L^{Ph}_2$ μ^4-O structures. For $(FeCoL^{Ph})_2O$ •THF, data was collected only for unit cell determination (N/D = not determined).

	$(MnFeL^{Ph})_2O$• C_6H_6	**$(FeCoL^{Ph})_2O$• C_6H_6**	**$(FeCoL^{Ph})_2O$• THF**	**"$(CoFeL^{Ph})_2O$"• THF**	**$(NiFeL^{Ph})_2O$• THF**
space group	C2/c	C2/c	N/D	C2/c	C2/c
a (Å)	16.383(1)	16.2414(8)	16.61	16.569(2)	16.627(3)
b (Å)	21.345(2)	21.304(1)	20.79	20.757(2)	20.674(3)
c (Å)	23.885(2)	23.814(1)	23.87	23.815(3)	23.881(4)
α (deg)	90.00	90.00	90.00	90.00	90.00
β (deg)	90.927(1)	90.975(1)	93.5	93.466(1)	93.513(2)
γ (deg)	90.00	90.00	90.00	90.00	90.00
R_1, wR_2	0.0543, 0.1285	0.0424, 0.1024	N/D	0.0455, 0.1190	0.0614, 0.1625

Because the tris-amidinate ligand is asymmetric, the core structure of these oxo complexes is more complex than for the diiron compound with simple bridging ligands.

Two perspectives of this core structure are shown in Figure 3.8, for the $[FeCoL^{Ph}]_2O$ (left) and $[NiFeL^{Ph}]_2O$ structures (right). There is a C_2 rotation axis through the oxygen atom, making the ligands and two bimetallic units equivalent. The bimetallic units are largely intact, as there is one shorter and one longer M1-M2 distance ca. 2.8 Å and 3.2 Å in each complex. The M1-M1' and M2'-M2' distances are ca. 3.4 and 3.65 Å between the metals in and out of the *tren* pocket, respectively. As was the case with $[Fe_2(DPhF)_3]_2O$, two of the bridging amidinates remain bridging the original bimetallic unit, while the third rearranges to bridge to the other M2. The top metal, M2, is therefore in a distorted tetrahedral environment (not accounting for M-M interactions) defined by the three distal amidinate N3 donors and the oxo ligand; the bottom metal, M1, is in a distorted trigonal bipyramidal geometry with the amidinate N2 donors in the equatorial positions and the oxo ligand and amine N1 of the *tren* base as the axial ligands. Important structural parameters are given in Table 3.8.

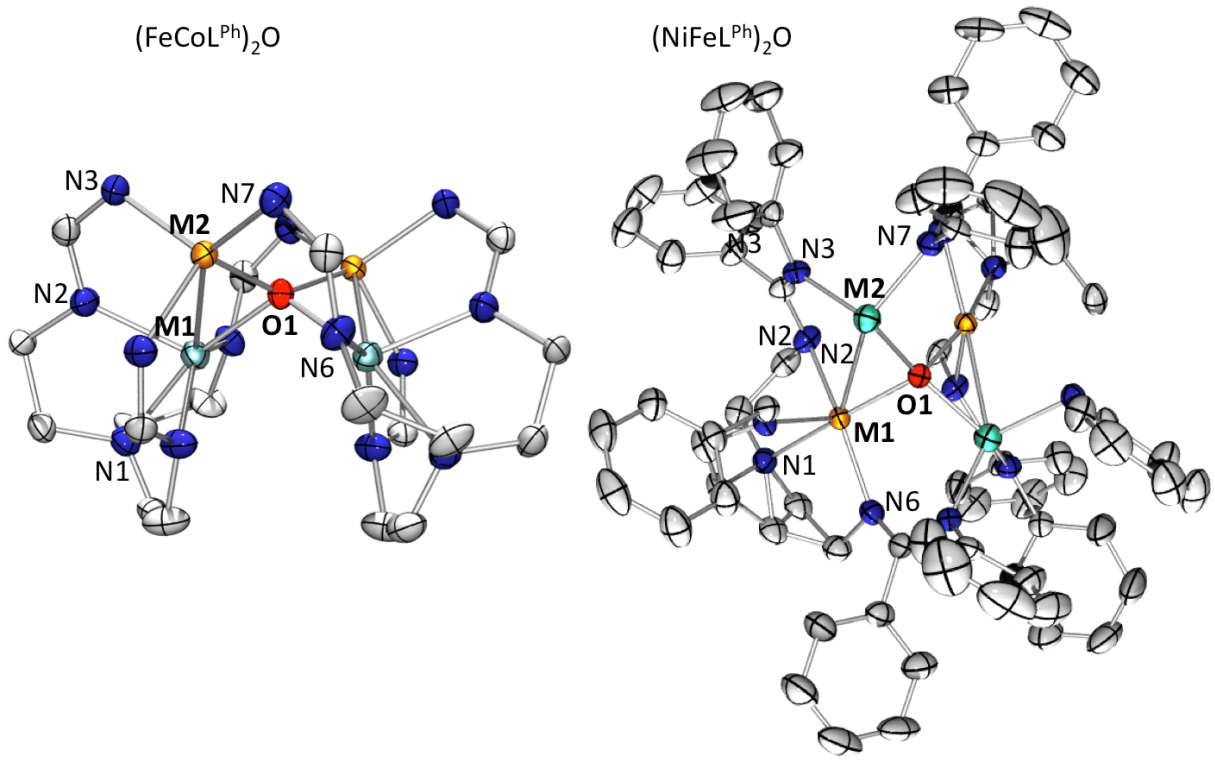

Figure 3.33. M_4O core structure of $(CoFeL^{Ph})_2O$ (left) and full structure of $(NiFeL^{Ph})_2O$ (right) at 50% probability. Solvent atoms, hydrogens, and disordered positions have been omitted. Important structural parameters are given in Table 3.9.

Table 3.9. Selected bond distances (Å) in oxo complexes described in this work. Numbering scheme is shown in Figure 3.33

	M1-M2	**M1-O1**	**M2-O1**	**M1-N1**	**M1-N2**	**M1-N6**	**M2-N3**	**M2-N7**
$(MnFeL^{Ph})_2O$	2.8845(6)	2.024 (1)	1.993(8)	2.180(3)	2.282(2) 2.187(2)	2.147(2)	2.112(2) 2.123(2)	2.090(2)
$(FeCoL^{Ph})_2O$	2.7817(4)	2.009(1)	1.929(1)	2.238(2)	2.106(2) 2.117(2)	2.124(2)	2.037(1) 2.054(2)	2.031(2)
$(CoFeL^{Ph})_2O$	2.7784(5)	2.005(2)	1.922(1)	2.226(2)	2.101(2) 2.120(2)	2.123(2)	2.032(2) 2.048(2)	2.026(2)
$(NiFeL^{Ph})_2O$	2.7806(8)	2.011(2)	1.935(1)	2.119(3)	2.117(3) 2.127(3)	2.116(3)	2.052(3) 2.064(3)	2.047(3)

The structural parameters are fairly similar for all of the oxo complexes. The largest difference is between the M1-M2 distance of the iron-manganese complex and the

other structures, but the M1-M2 distances of the iron-cobalt and iron-nickel structures are essentially identical. It is tempting to draw comparisons between the manganese-iron and nickel-iron structures: as assigned, they have the same basal iron center but should have their M-M bonds polarized in opposite directions. However, these X-ray diffraction methods are unable to assign the metal positions; the assignment is made solely on the basis of synthetic approach, and, as demonstrated with the iron-cobalt bimetallics, there is no reason to believe that the metals do not rearrange during synthesis or during their oxidation to form these clusters. Nor are there clear trends among the metal-ligand distances that would suggest one assignment or another. The M2-N and M2-O distances for the manganese-iron complex, for instance, are significantly larger than the same distances in the other clusters, which might suggest that M2 is the larger Mn(II) ion. However, the M1-N2, M1-N2', and M1-O distances of this complex are also significantly larger than for the other complexes. The M2-L distances for the nickel-iron complex are somewhat larger than for the iron-cobalt complex, while its M1-L distances are somewhat shorter. This might reflect the larger Fe ion in the top position and smaller Ni in the bottom. However, without additional supporting data, such assignments are clearly without basis.

The ^{1}H NMR spectra of the oxo compounds are highly paramagnetic and appear to be of little use in structural assignment, other than confirming that the highly asymmetric molecular geometries seen in the solid-state structures are retained in solution. However, the situation is more complex when examined more closely. The crystallographically-observed asymmetry includes not only the three inequivalent ligand

arms but also the associated diastereotopism in the *tren* backbone. A highly asymmetric spectrum is thus to be expected for each oxo structure. However, the actual spectra show so many discrete resonances that even the asymmetric solid-state structure is unable to account for them. Since there is a C_2 symmetry axis observed in the crystal structure, the two ligands are identical. There are 42 protons in the ligand, and if the phenyl groups are free to rotate, as expected, there are only 30 unique protons in each structure. There are in fact far too many unique resonances in each spectrum to account for even this large number. One plausible explanation would be that each heterobimetallic oxo product actually contains a mixture of different metal distributions; this could be a combination of heterobimetallic isomers or it could be a mixture of the heterobimetallic oxo species with the homobimetallic oxos. We can rule out the latter by comparing the spectra of $(FeCoL^{Ph})_2O$ to that of the homobimetallic dicobalt oxo product. Surprisingly, we have not obtained X-ray quality crystals for this product. Unlike the oxo complexes of the heterobimetallics, which crystallize readily as large blocks, the blue product of Co_2L^{Ph} oxidation is fairly insoluble and tends to give polycrystalline films rather than slowly growing single crystals. The ^1H NMR spectrum observed for this polycrystalline material is shown in Figure 3.34. The intensities of the signals are weak due to the low solubility, but the pattern is much more well-defined than for the heterobimetallic species. 30 signals can be discerned, consistent with the number expected for the C_2-symmetric $(M_2LPh)_2O$ geometry. Since the spectrum for the homobimetallic complex is much simpler than the heterobimetallics, and since they do not have frequencies in common, we tentatively conclude that the highly asymmetric spectra observed for the

heterobimetallic oxo complexes reflect a mixture of different heterobimetallic isomers. This conclusion is supported by the lack of clear trends in the bond distances observed for the various solid-state structures. However, we acknowledge that this conclusion rests on a number of assumptions, chiefly that the oxidized dicobalt compound is structurally and compositionally similar to the heterobimetallic oxo compounds. More detailed characterization of these compounds is needed in order to make more informed conclusions. We have not extensively pursued this chemistry, as the metal-metal interactions in these complexes are not expected to show significant bonding.

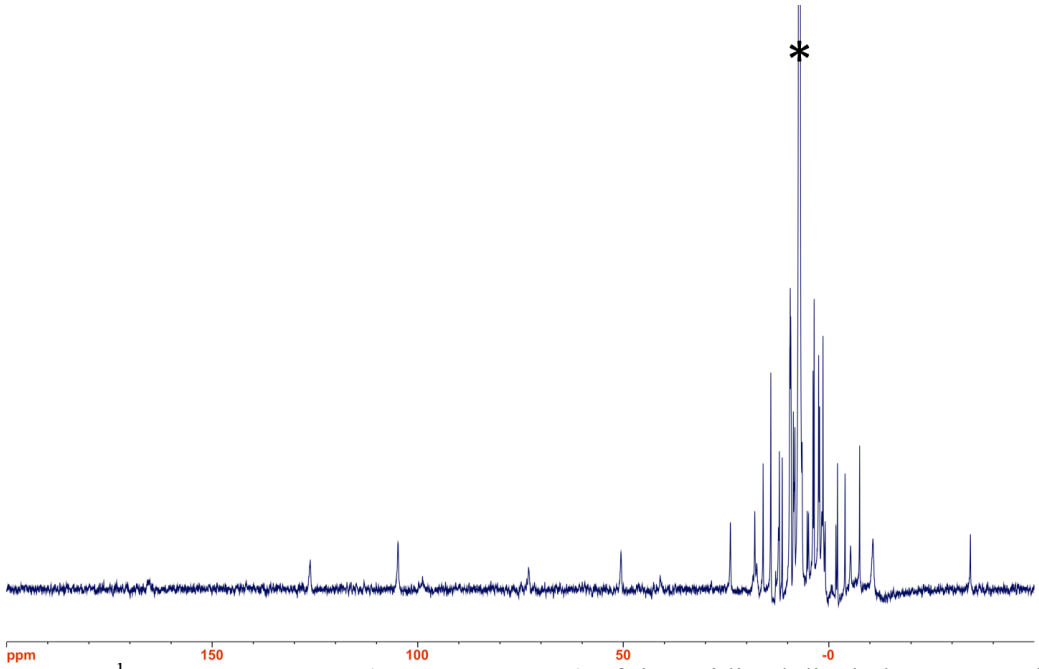

Figure 3.34. ^{1}H NMR spectrum (500 MHz, C_6D_6) of the oxidized dicobalt compound. Residual solvent peak is marked with an asterisk.

3.4 Conclusions

Since their initial report, the trigonal lantern bimetallics have been intriguing because of their short metal-metal bond distances, unusual high-spin electronic configurations, and mixed valency. Using a new tris(amidinato)amine ligand, this

motif has been extended to two new complexes: a dicobalt homobimetallic (**1**) and a rare, mixed iron-cobalt complex (**2**). X-ray anomalous scattering techniques have been used to definitively assign the metal positions in the heterobimetallic. While there is some mixing of the metals between the two sites, the iron-cobalt isomer $FeCoL^{Ph}$ is the major component. **1** and **2** are entirely isostructural, with the only structural differences along the M-M axis. Thus the differences between them can be attributed entirely to the differences in their M-M interactions. This is most apparent in the Fe-Co separation in **2**, which, at 2.18 Å, is much closer than even the short Co-Co distance of 2.29 Å in **1**. This is the shortest Fe-Co distance known, by a significant margin.

Thus the strong bonding engendered by the trigonal lantern motif appears to be quite general, accommodating axial donor groups and even extending to bonds between different metals. In addition, the high-spin configuration is retained in the heterobimetallic complex, making **2** the only known example of a high-spin Fe-Co bond and a very rare example of ferromagnetic coupling within a heterobimetallic complex. The low-coordinate, weak-field ligand motif thus appears to be an excellent way to enforce strong bonding between first-row transition metals. The weak orbital splitting leads to a high-spin electronic configuration that causes minimal occupation of the M-M antibonding orbitals. This is essentially the same as was found for the original trigonal lanterns, $Fe_2(DPhF)_3$ and $Co_2(DPhF)_3$, and the spins of **1** and $Co_2(DPhF)_3$ are essentially identical by EPR and magnetic measurements. There are some key differences revealed by theoretical analysis, however. The calculations suggest that the chelated complexes **1** and **2**, and the hypothetical complex $CoFeL^{Ph}$, are essentially single-configurational. The

reason for this is unknown, but its effect is to make the effective bond orders (EBOs) essentially equivalent to the formal bond order (FBO), unlike in $Fe_2(DPhF)_3$, where the EBO is significantly lower than the FBO, and in $Co_2(DPhF)_3$, where the EBO was found to be significantly higher. More interestingly, analysis of the d-electron populations and spin densities suggest that the homobimetallic complex **1** is actually more polarized than the heterobimetallic **2**, at least in terms of oxidation states. The σ-bonding orbitals are polarized in both complexes, placing more electron density on the "top" metal. In **2**, however, the additional π-bonding interaction is polarized in the opposite direction, cancelling this effect and leading to a delocalized Fe(1.5)Co(1.5) core, which is supported experimentally by Mössbauer spectroscopy. We attribute the polarization in the case of **1** to the asymmetry of the metal binding sites, in which the more weakly π-donating nitrogens at the "top" site induce a lower valence, Co(I), while the stronger donors in the "bottom" induce a higher valence, Co(II). In **2**, the delocalization is likely a result of the less-electronegative Fe being unable to support a (+1) oxidation state with this donor set. This is supported by the prediction from theory that the hypothetical $CoFeL^{Ph}$ isomer, in which Co is in the "top" site, has a more polarized Co(I)Fe(II) core.

We have attempted to synthesize this isomer and a variety of other bimetallics within this framework; unfortunately, most of these do not appear to be accessible with this ligand set. Attempts to synthesize the other iron-cobalt isomer, $CoFeL^{Ph}$, give only **2** instead. This suggests that the high-spin metals are quite labile, as seen with similar iron-cobalt heterobimetallics.[36] Attempts to synthesize other heterobimetallics have been even less successful, apparently due to the instability of the products towards either cluster

formation, oxidative decomposition, or other unknown pathways. As a result of the flexibility of the ligand and the lability of the metals, the metal combinations that are accessible and their positions within the asymmetric ligand appear to be thermodynamically controlled. This is unfortunate, since it appears to prevent the controlled, stepwise metallation strategy we envisioned for these systems. However, it is also informative: even within chelating ligand frameworks and apparently similar donor sets, the synthesis of these bimetallics is more akin to self-assembly than controlled metallation. A more rigid, perhaps macrocyclic, ligand framework might limit molecular rearrangement and enable a more controlled metallation strategy. Alternatively, judicious choice of donors may allow access to metal pairs that have proven unfavorable with this ligand system. Others in our group have been pursuing diiron, dicobalt, and iron-cobalt complexes with ligands that have analogous trigonal, trianionic donor sets but which have a greater disparity in charges between the two planes of donors.[54] The characterization of these complexes is not yet complete, but they will provide an interesting comparison with the trigonal lantern species described here.

3.5 Experimental Procedures

3.5.1 Synthetic Considerations

Unless otherwise stated, all manipulations were performed under a dinitrogen atmosphere in a VAC Atmosphere glovebox. Standard solvents were deoxygenated by sparging with dinitrogen and dried by passing through activated alumina columns of a SG Water solvent purification system. Benzylpotassium[39] and KC_8[40] were prepared according to literature methods. Deuterated solvents were purchased from Cambridge Isotope Laboratories, Inc., degassed via freeze-pump-thaw cycles, dried over activated alumina, and stored over activated 4 Å molecular sieves. All other reagents were purchased from Aldrich or Strem and used without further purification. Elemental analyses were performed by Complete Analysis Laboratories, Inc. (Parsippany, NJ).

Synthesis of tris(2-benzamidoethyl)amine. Tris(2-aminoethyl)amine (or tren) (3.2 mL, 21.4 mmol) and NEt_3 (10.3 mL, 73.8 mmol) were combined in a 250 mL RB flask with THF (100 mL) and cooled to 0 °C under ambient atmosphere. Benzoyl chloride (7.8 mL, 67.1 mmol, diluted in 10 mL THF) was added dropwise, forming a white precipitate. After warming to rt overnight, the precipitate was filtered, then dissolved in $CHCl_3$, washed 4x with distilled water and once with brine, then dried with anhydrous $MgSO_4$. After filtering to collect the supernatant and removing the solvent under vacuum, the resulting pale yellow solid was stirred with diethyl ether and filtered to give a fine white powder (7.7 g, 85% yield). ^{1}H NMR (300 MHz, $CDCl_3$): δ 7.60 (dd, J = 7.2 Hz & 1.2 Hz, 6H), 7.29 (tt, J = 7.5 & 1.2 Hz, 3H), 7.27 (br, 3H), 7.06 (t, J = 8.1 Hz, 6H), 3.55

(quart, J = 5.4 Hz, 6H), 2.72 (t, J = 5.7 Hz, 6H). ESI-TOF-MS (MeOH) *m/z*: $[M + H]^+$ calc'd for $C_{27}H_{31}O_3N_4$, 459.24; found: 459.28, 481.27 $[M + Na^+]$, 497.27 $[M + K^+]$, 497.27 $[2M + H^+]$, 917.58 $[2M + Na^+]$ 939.57.

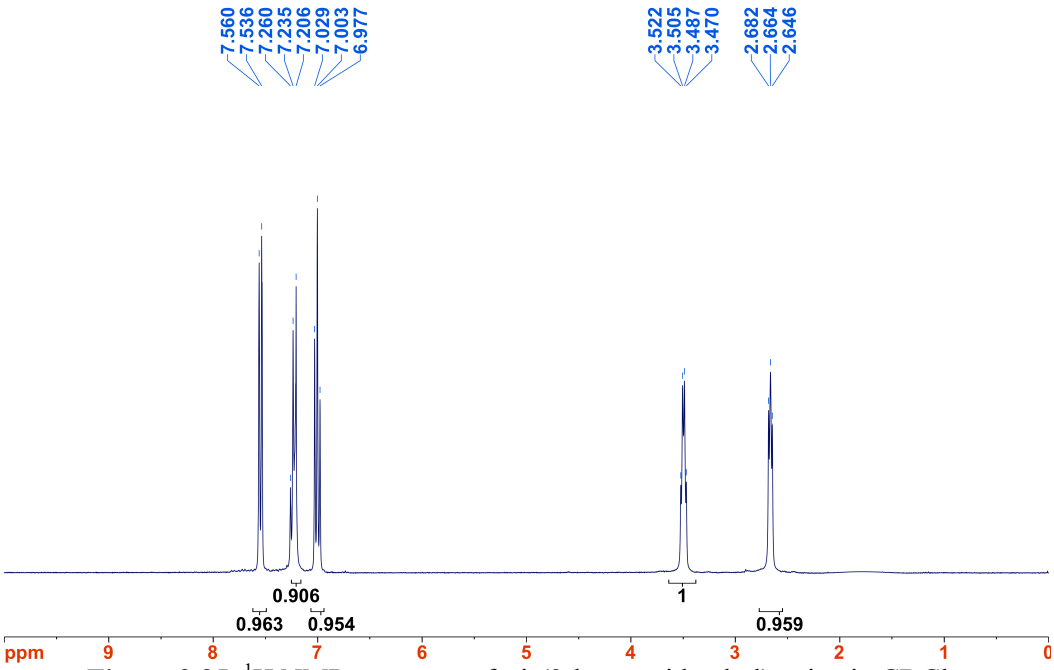

Figure 3.35. ^{1}H NMR spectrum of tris(2-benzamidoethyl)amine in $CDCl_3$.

Synthesis of tris(2-benzimidoylchloroethyl)amine hydrochloride. Tris(2-benzamidoethyl)amine (7.6 g, 16.6 mmol) was dissolved in CH_2Cl_2 (50 mL) in a 100 mL thick-walled flask. Phosphorous pentachloride (11.8 g, 56.7 mmol) was added, the flask was sealed with a Teflon stopper, and the mixture was refluxed at 50 °C. After 24 h, the volatiles were removed under vacuum. The resulting white residue was washed with toluene (100 mL) and filtered, giving a fine white powder (8.4 g, 85% yield). ^{1}H NMR (300 MHz, $CDCl_3$): δ 12.66 (br, 1H), 7.93 (d, J = 7.5 Hz, 6H), 7.44 (t, J = 7.5 Hz, 3H), 7.27 (t, J = 7.8 Hz, 6H), 4.34 (t, J = 4.8 Hz, 6H), 3.86 (quart, J = 3.9 Hz, 6H).

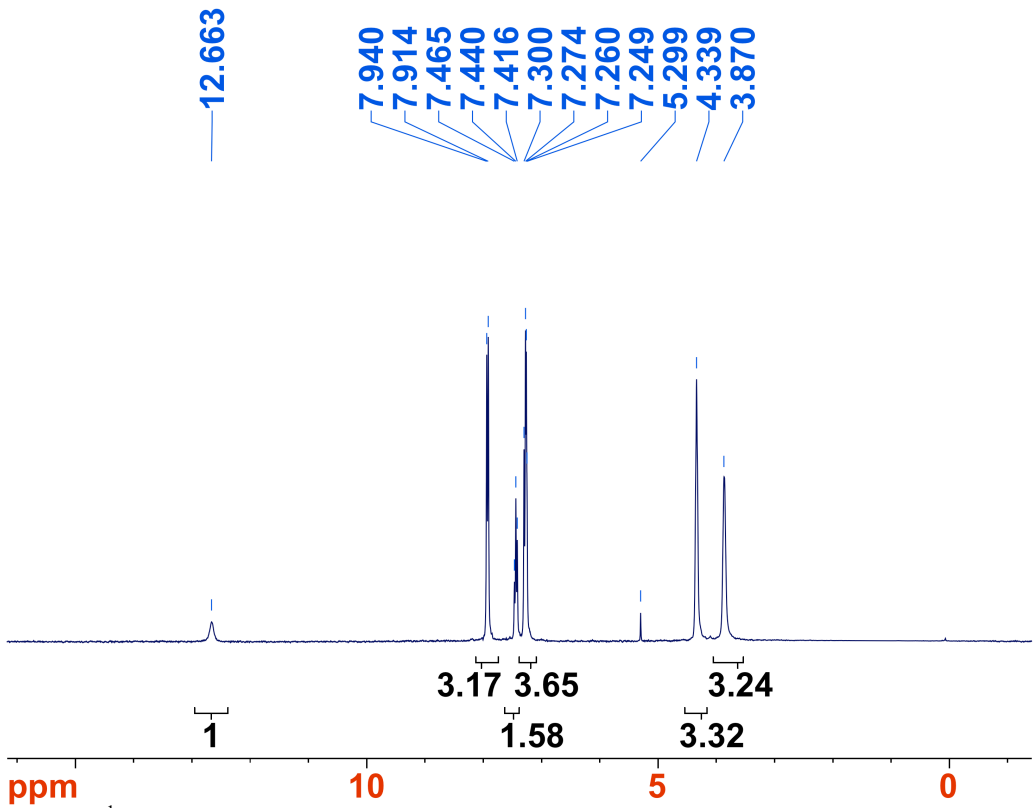

Figure 3.36. ^{1}H NMR spectrum of tris(2-benzimidoylchloroethyl)amine hydrochloride in $CDCl_3$.

Synthesis of tris(2-(N-phenylbenzamidinyl)ethyl)amine ($H_3\mathbf{L}^{Ph}$). Aniline (5.3 g, 57 mmol) was dissolved in CH_2Cl_2 and cooled to −78 °C. A suspension of tris(2-benzimidoylchloroethyl)amine hydrochloride (5.24 g, 9.53 mmol) in CH_2Cl_2 was added dropwise, and the reaction was allowed to slowly warm to rt overnight. The resulting suspension was filtered, giving a fine, white powder, which was washed with CH_3CN (50 mL). After dissolving the powder in water, NaOH (17 mL, 0.1 mol) was added, causing a large amount of white precipitate to form. The precipitate was dissolved in $CHCl_3$, washed three times with water and once with brine, then dried with anhydrous $MgSO_4$. The solvent was removed under vacuum, and the resulting yellow oil was recrystallized from diethyl ether to give a white solid. The solids were dried overnight under vacuum at 60 ^{o}C, and finally re-washed with Et_2O to yield a white powder (5.5 g, 80% yield). ^{1}H

NMR (500 MHz, CD_3CN): δ 7.22 (t, bridgehead *para*-C-*H*, 3H), 7.12 (m, aryl,12H), 6.99 (t, bridgehead *meta*-C-*H*, 6H), 6.73 (t, apical *para*-C-*H*, 3H), 6.52 (d, apical *ortho*-C-*H*, 6H), 5.53 (br, N-*H*, 3H), 3.56 (br, CH_2, 6H), 2.99 (br, CH_2, 6H). ESI-MS-TOF *m/z*: $[M + H]^+$ calc'd for $C_{45}H_{46}N_7$, 684.3815; found 684.3806. Anal. Calc'd. for $C_{45}H_{45}N_7$: C, 79.03; H, 6.63; N, 14.34. Found C 78.92; H 6.53; N 14.26.

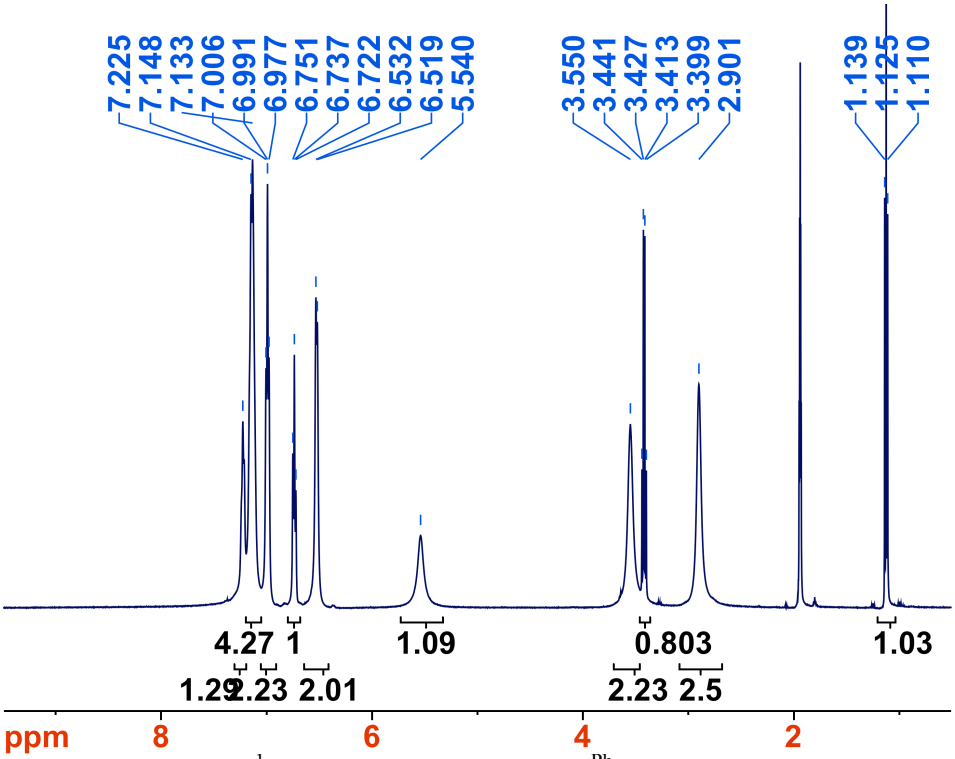

Figure 3.37. ^1H NMR spectrum of $H_3L^{Ph}(Et_2O)_{0.5}$ in CD_3CN.

Synthesis of tris(2-pivalamidoethyl)amine. This compound was synthesized in a manner entirely analogous to that of *tris(2-benzamidoethyl)amine,* above, starting from tren (3.1 mL, 20 mmol) and pivaloyl chloride (7.6 mL, 62 mmol). Yield: 6.08 g (76%). ^1H NMR (500 MHz, $CDCl_3$): δ 6.175 (br. s, 3H, N*H*), 3.289 (dd, *J* = 6.25 & 12.25 Hz, NH-CH_2, 12H), 2.606 (t, *J* = 6 Hz, NH-CH_2-CH_2, 12H), 1.194 (s, C(CH_3)$_3$, 27H). ESI-MS-TOF *m/z*: $[M + H]^+$ calc'd for $C_{21}H_{43}N_4O_3$, 399.3335; found: 399.3491.

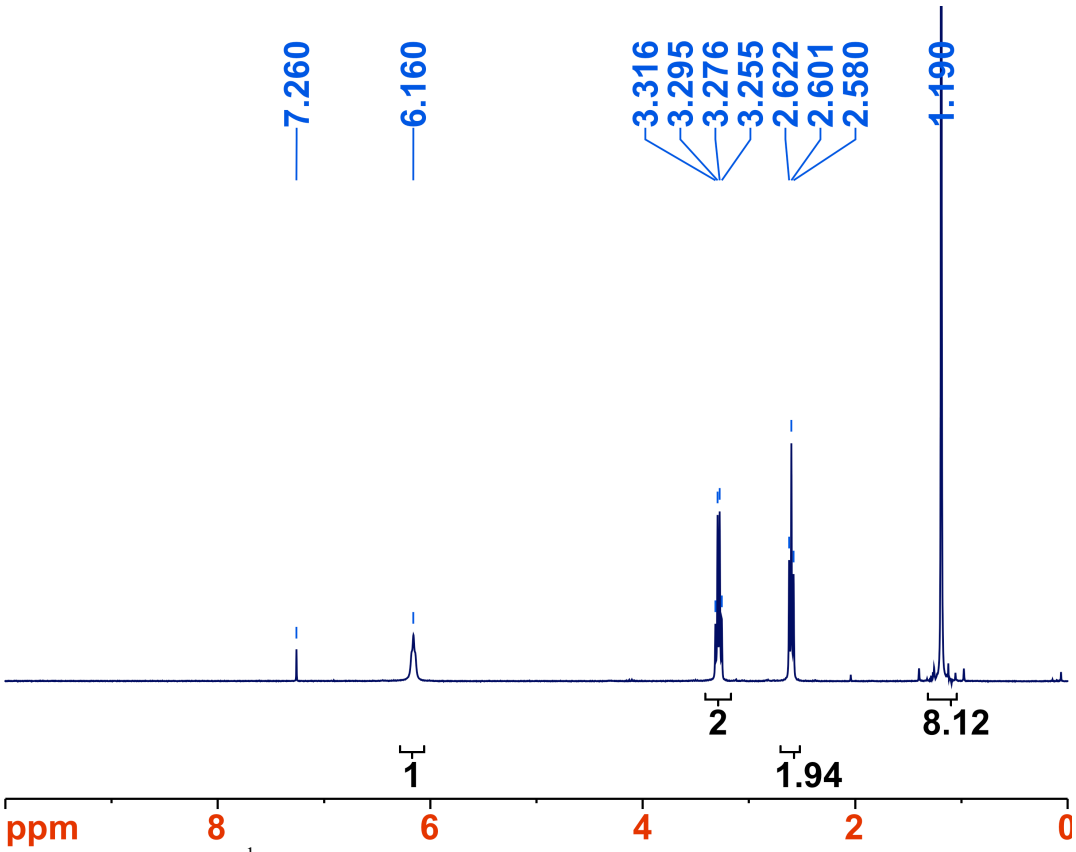

Figure 3.38. ^{1}H NMR spectrum of tris(2-pivaloamidoethyl)amine in $CDCl_3$.

Synthesis of tris(2-pivalimidoylchloroethyl)amine hydrochloride. This compound was synthesized in a manner entirely analogous to that of *tris(2-benzimidoylchloroethyl)amine,* starting from the tris-amide, above, (5.813 g, 14.6 mmol) and phosphorous pentachloride (9.56 g, 46 mmol). Yield: 6.19 g (86%). ^{1}H NMR (500 MHz, $CDCl_3$): δ 12.978 (s, N-*H*$^{+}$, 1H), 4.025 (t, *J* = 6 Hz, CH_2-C*H*$_2$-N-H^{+}, 6H), 3.555 (dd, *J* = 5.5 Hz & 4.5 Hz, C*H*$_2$-CH_2-N-H^{+}, 6H), 1.227 (s, $C(CH_3)_3$, 27H).

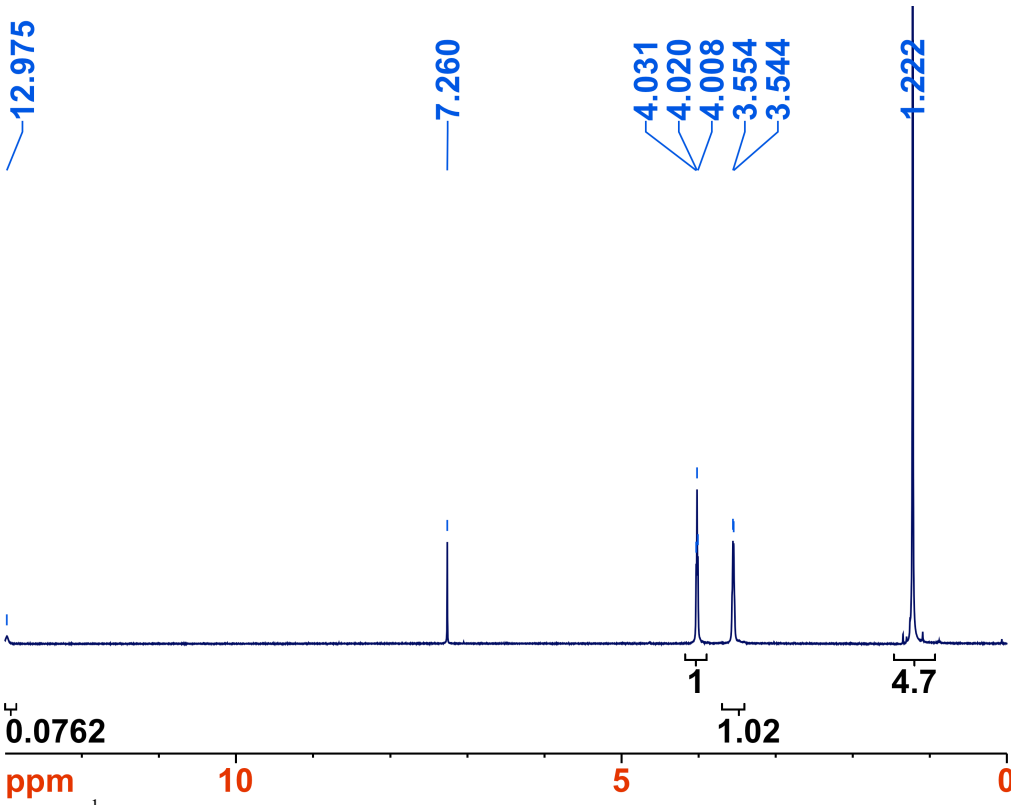

Figure 3.39. ^{1}H NMR spectrum of tris(2-pivalimidoylchloroethyl)amine hydrochloride in $CDCl_3$.

Synthesis of tris(2-(N-phenylpivalamidinyl)ethyl)amine ($H_3\mathbf{L}^{\mathbf{tBu}}$). This compound was synthesized in a manner entirely analogous to that of H_3L^{Ph} above, starting from the tris-imidoyl chloride HCl salt, above, (6.19 g, 12.6 mmol) and aniline (4.004 g, 4.3 mmol). Yield: 6.2g (80%). ^{1}H NMR (500 MHz, CD_3CN): δ 7.13 (t, J = 8 Hz, *meta*-C-*H*, 6H), 6.80 (t, J = 7 Hz, *para*-C-*H*, 3H), 6.64 (d, J = 7.5 Hz, *ortho*-C-*H*, 6H), 4.90 (br, N*H*, 3H), 2.59 (br, CH_2, 6H), 2.08 (br, CH_2, 6H), 1.16 (s, C(CH_3)$_3$, 27H). ESI-MS-TOF *m/z*: [M + H]$^+$ calc'd for $C_{39}H_{58}N_7$, 624.4754; found: 624.4848.

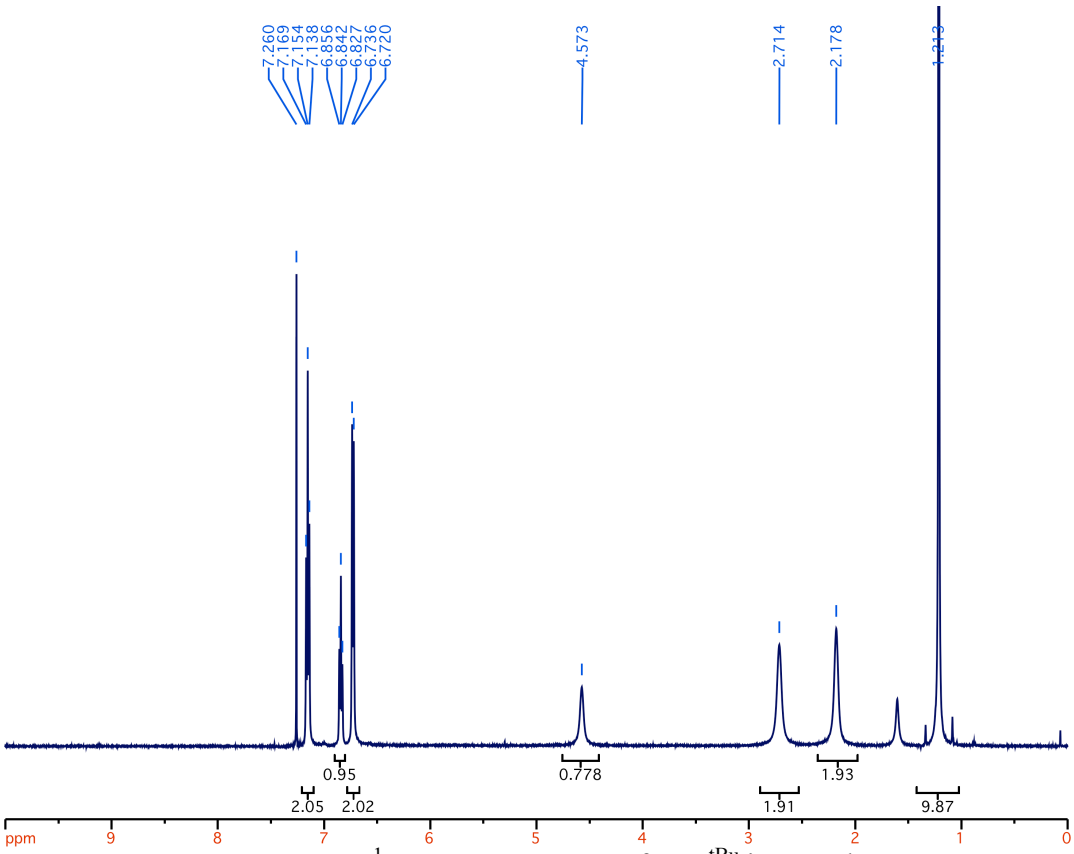

Figure 3.40. ^{1}H NMR spectrum of H_3L^{tBu} in $CDCl_3$.

Synthesis of K(THF)[CoL^{Ph}] (**2**). H_3L^{Ph} (1.499 g, 2.2 mmol) was dissolved in THF (180 mL) and cooled to −78 °C. Benzylpotassium (895 mg, 6.87 mmol, in 10 ml THF) was added dropwise over 5 minutes, during which time the solution turned bright yellow. The solution was stirred for 15 minutes at −78 °C. $CoCl_2$ (286 mg, 2.2 mmol) was then added. The resulting cloudy green solution was allowed to slowly warm to rt overnight. After 12 h, the mixture was filtered through Celite, and the solvent was removed under vacuum. The solid was washed with toluene (15 mL) and pentane (5 mL), and then dried under vacuum, yielding a bright, lime-green powder (1.60 g, 90% yield). ^{1}H NMR (500 MHz, CD_3CN): δ 70.2 (br, 6H), 59 (br, 6H), 15.2 (s, 6H), 13.3 (br, 6H), 4.36 (s, 6H), 0.41 (s,

3H), −1.86 (s, 3H) −3.76 (s, 6H). UV-vis (THF): λ_{max}, nm (ε, $M^{-1}cm^{-1}$): 275 (30,900), 355 (20,350), 598 (80), 618 (80), 780 (12). Anal. Calc'd. for $C_{45}H_{42}N_7CoK(OC_4H_8)$: C, 69.16; H, 5.92; N, 11.52. Found C, 69.22; H, 6.00; N, 11.61.

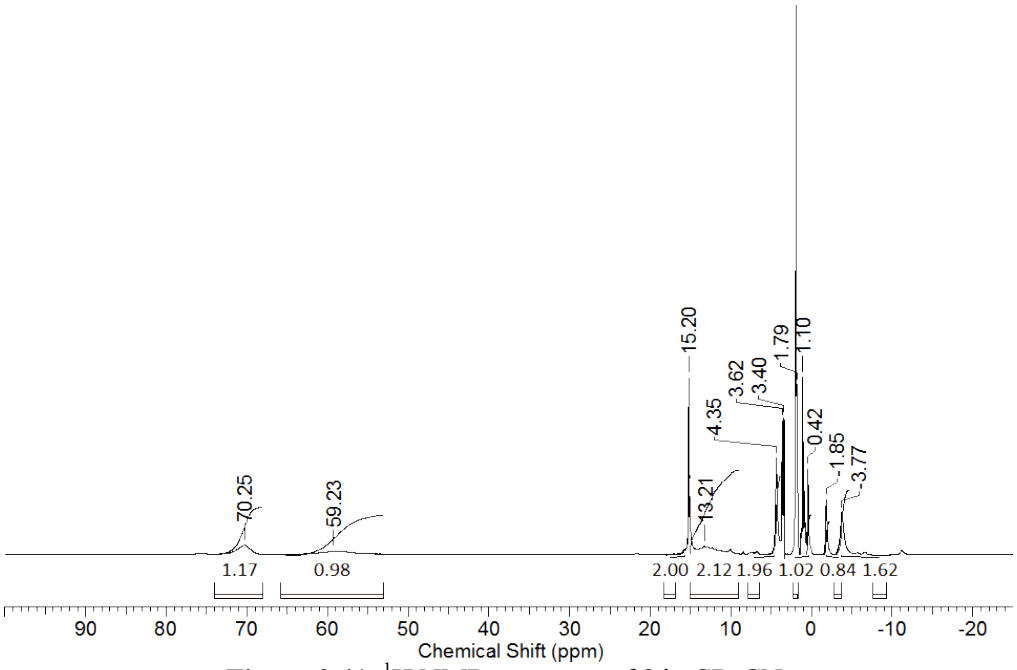

Figure 3.41. ^{1}H NMR spectrum of **3** in CD_3CN.

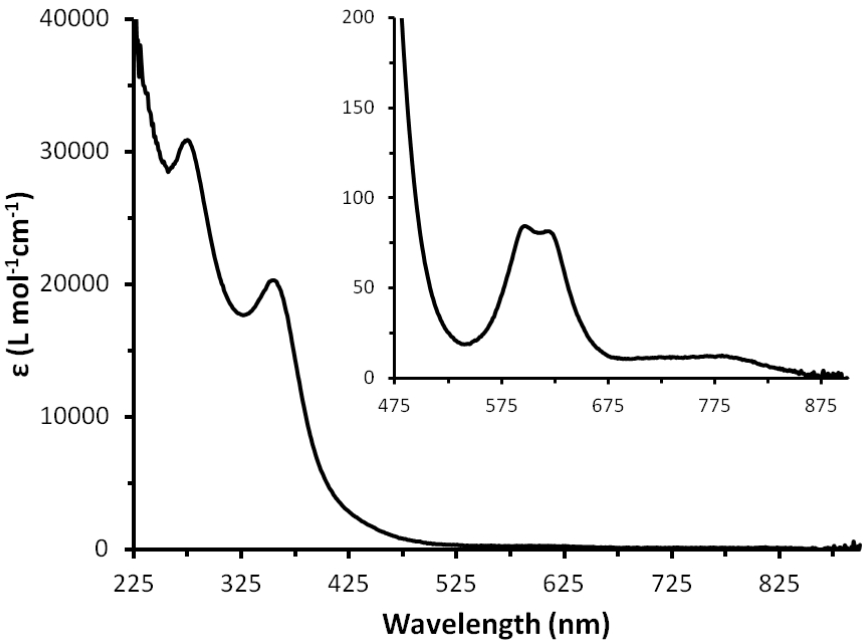

Figure 3.42 UV-Vis absorption spectrum of **3** (THF). Inset: Expansion of visible region.

Synthesis of K(THF)[CoL^{tBu}]. This compound was synthesized in a manner entirely analogous to that of K(THF) CoL^{Ph} (**2**), above, using H_3L^{tBu} (751 mg, 1.2 mmol), benzylpotassium (475 mg, 3.65 mmol) and $CoCl_2(THF)_{1.5}$ (287 mg, 1.2 mmol). Yield: 812 mg (85%).. Yield: 812 mg (85%). ^{1}H NMR (500 MHz, CD_3CN): δ 140.9 (br, 6H), 62.8 (br, 6H), 16.0 (br, 27H), 8.02 (s, 6H), 3.11 (s, THF, 1.3H), 2.74 (s, 6H), 1.17 (s, THF, 1.3H) −19.1 (s, 3H). Anal. Calc'd. for $C_{39}H_{54}N_7CoK(OC_4H_8)$: C, 65.29; H, 7.90; N, 12.39. Found C, 65.21; H, 7.96; N, 12.36.

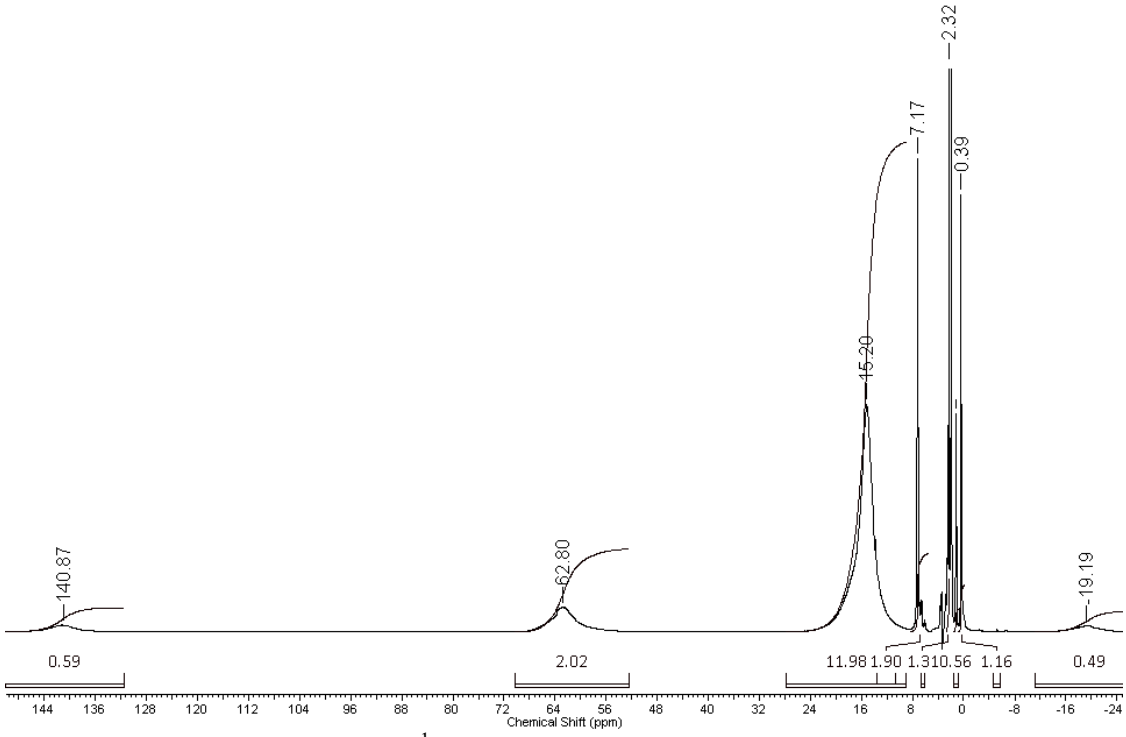

Figure 3.43. ^{1}H NMR spectrum of **3a** in CD_3CN.

Synthesis of K(THF)[FeL^{Ph}] (**3**). This compound was synthesized in a manner entirely analogous to that of K(THF)CoL^{Ph} (**2**), above, using $H_3L^{Ph}(Et_2O)_{0.4}$ (0.751 g, 1.1 mmol), benzylpotassium (445 mg, 3.43 mmol) and $FeCl_2(THF)_{1.5}$ (139 mg, 1.1 mmol). Yield:

725 g (77%). ^{1}H NMR (500 MHz, THF-d_8): δ 150 (br, 6H), 39 (br, 6H), 16.9 (s, 6H), 15.6 (s, 6H), 9.88 (s, 6H), 1.13 (s, 3H), -3.5 (s, 3H) -11.1 (s, 6H). Anal. Calc'd. for $C_{45}H_{42}N_7FeK(OC_4H_8)$: C, 69.41; H, 5.94; N, 11.56. Found C, 69.43; H, 5.86; N, 11.41.

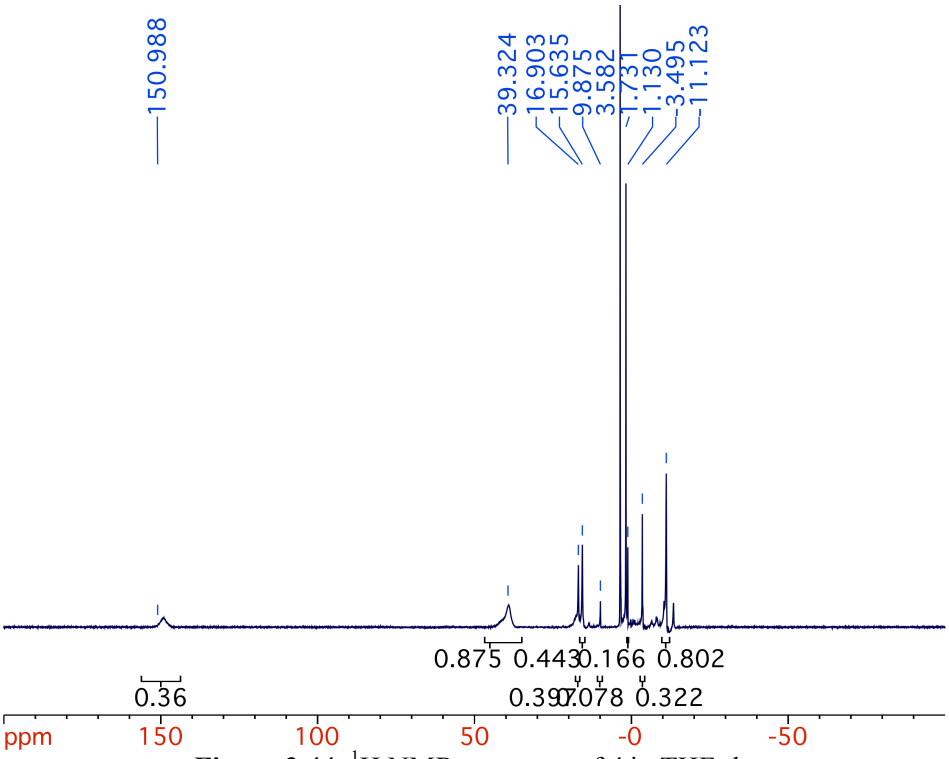

Figure 3.44. ^{1}H NMR spectrum of **4** in THF-d_8.

Synthesis of K(THF)[FeL^{tBu}] (**4a**). This compound was synthesized in a manner entirely analogous to that of K(CoL^{Ph}K) (**3**), above, using H_3L^{tBu} (1.37 mg, 2.2 mmol), benzylpotassium (290 mg, 2.2 mmol) and $FeCl_2(THF)_{1.5}$ (277 mg, 2.2 mmol). Yield: 1.37 g (85%). ^{1}H NMR (500 MHz, CD_3CN): δ 234 (br, 6H), 66 (br, 6H), 53.4 (br, 27H), 6.23 (s, 6H), 3.64 (s, THF, 1.3H), 2.57 (s, 3H), 1.80 (s, THF, 1.3H) 1.15 (s, 6H), -6.28 (s, 6H).

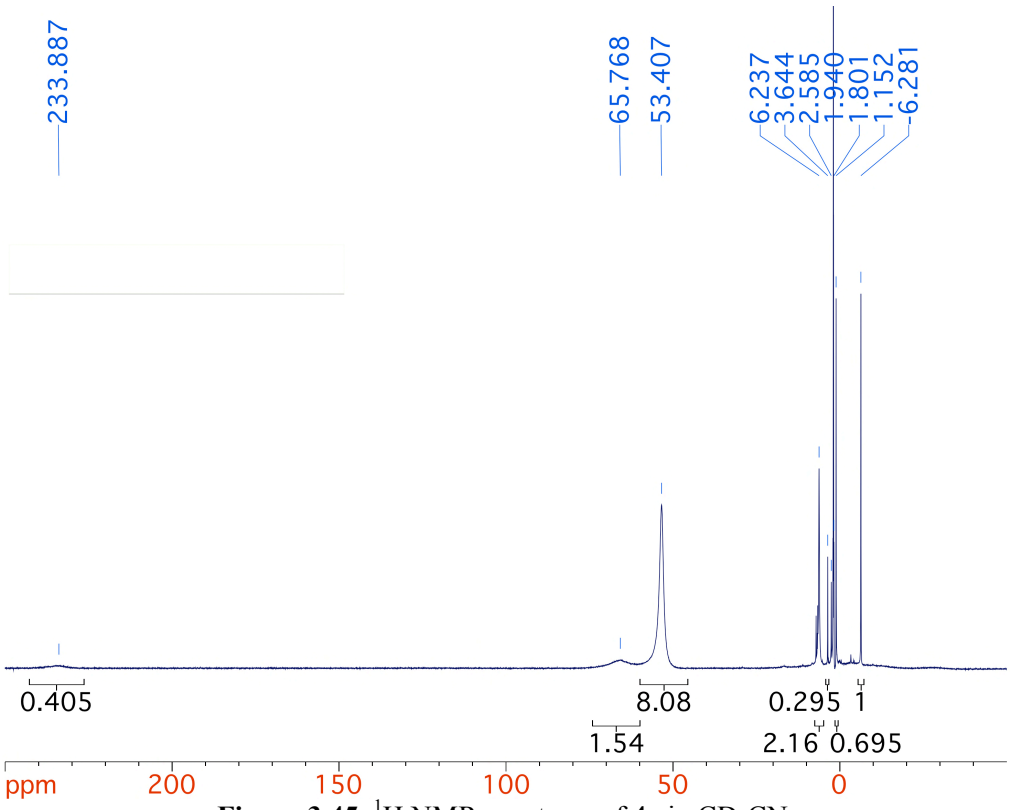

Figure 3.45. ^{1}H NMR spectrum of **4a** in CD_3CN.

Synthesis of Co_2L^{Ph} (**1**). K(THF)[CoL^{Ph}] (325 mg, 0.382 mmol) was dissolved in THF (120 mL) and cooled to −78 °C. Potassium graphite (54 mg, 0.399 mmol) was added as a slurry in THF (3 mL), causing the reaction mixture to turn dark yellow. After stirring for 5 min, $CoBr_2$ (85 mg, 0.39 mmol) was added dropwise as a solution in THF. The mixture was allowed to slowly warm to rt overnight. After 24 h, it was filtered to remove graphite, giving a dark brown filtrate, which was pumped down under vacuum, taken up in toluene, filtered through Celite, and dried to give a brown solid (285 mg, 90% yield). ^{1}H NMR (500 MHz, THF-d_8): δ 158.7 (br, 6H), 104.6 (br, 6H), 24.2 (s, 6H), 16.5 (s, 6H), 10.4 (br s, 6H), −0.09 (s, 3H), −37.1 (s, 3H), −39.05 (br, 6H). ^{1}H NMR (500 MHz, C_6D_6): δ 165.3 (br, 6H), 104.5 (br, 6H), 23.9 (s, 6H), 16.0 (s, 6H), 8.66 (br, 6H), −1.73 (s, 3H), −34.4 (s, 3H), −35.1 (br, 6H). Vis-NIR (THF): λ_{max}, nm (ε, $M^{-1}cm^{-1}$): 480 sh (2200), 650

sh (430), 850 (150), 1140 (120), 1340 sh (105). Anal. Calc'd. for $C_{45}H_{42}N_7Co_2$: C, 67.67; H, 5.30; N, 12.28. Found C 67.58; H 5.24; N 12.17.

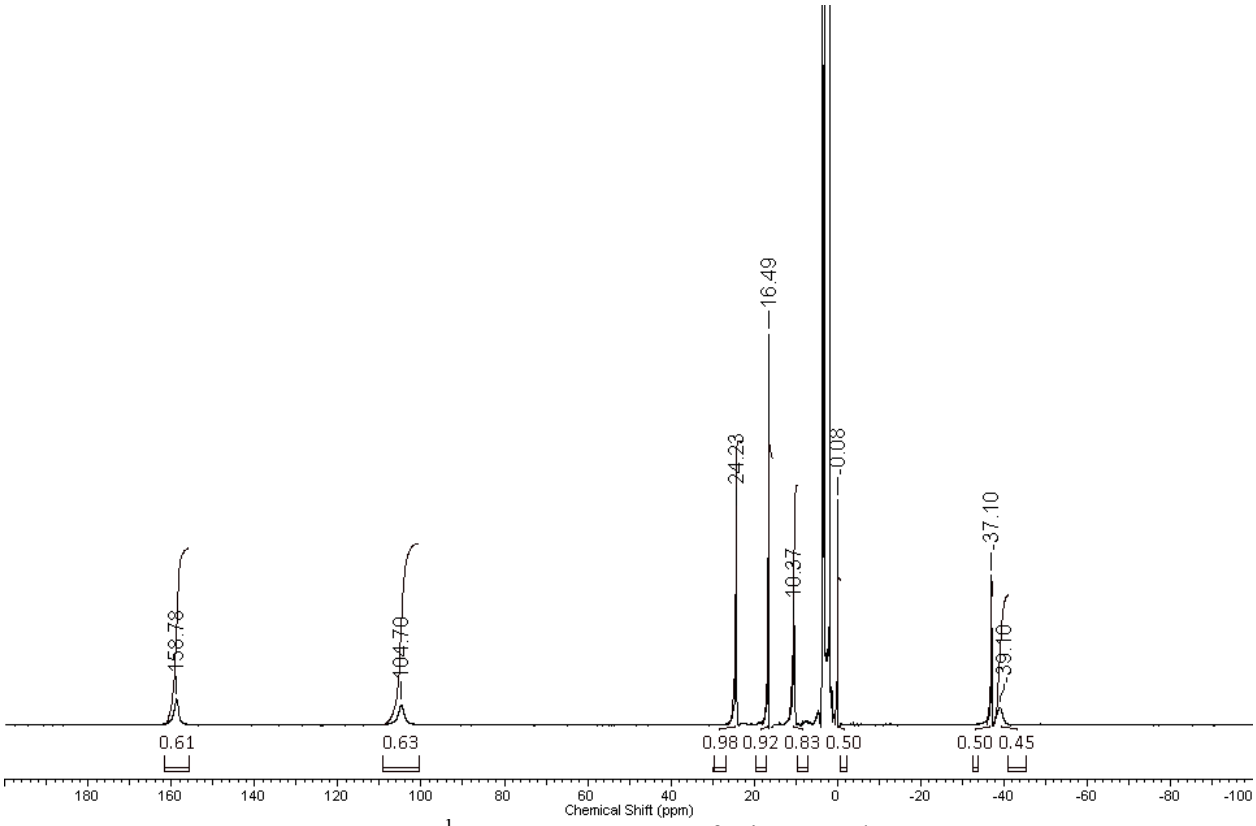

Figure 3.46. ^{1}H NMR spectrum of **1** in THF-d_8.

Synthesis of FeCoL^{Ph} (**2**). K(THF)[CoL^{Ph}] (260 mg, 0.306 mmol) was dissolved in THF (100 mL) and cooled to −78 °C. Potassium graphite (45.2 mg, 0.334 mmol) was added as a slurry in THF (3 mL), causing the reaction mixture to turn dark yellow. After stirring for 5 min, $FeBr_2$ (72.0 mg, 0.334 mmol) was added dropwise as a solution in THF. The mixture was allowed to slowly warm to rt overnight. After 12 h, it was filtered to remove graphite, giving a dark purple filtrate, which was pumped down under vacuum, taken up in toluene, filtered through Celite, and dried under vacuum to give a purple powder (225 mg, 92% yield). ^{1}H NMR (500 MHz, C_6D_6): δ 172.6 (br, 6H), 127.0 (br, 6H), 23.13 (s,

6H), 11.40 (s, 6H), 6.94 (br s, 6H), 0.78 (s, 3H), 24.1 (s, 3H), −31.5 (br, 6H). Vis-NIR (THF): λ_{max}, nm (ε, $M^{-1}cm^{-1}$): 514 (3000), 1050 (175). Anal. Calc'd. for $C_{45}H_{42}N_7CoFe$: C, 67.93; H, 5.32; N, 12.32. Found C 67.86; H 5.28; N 12.23.

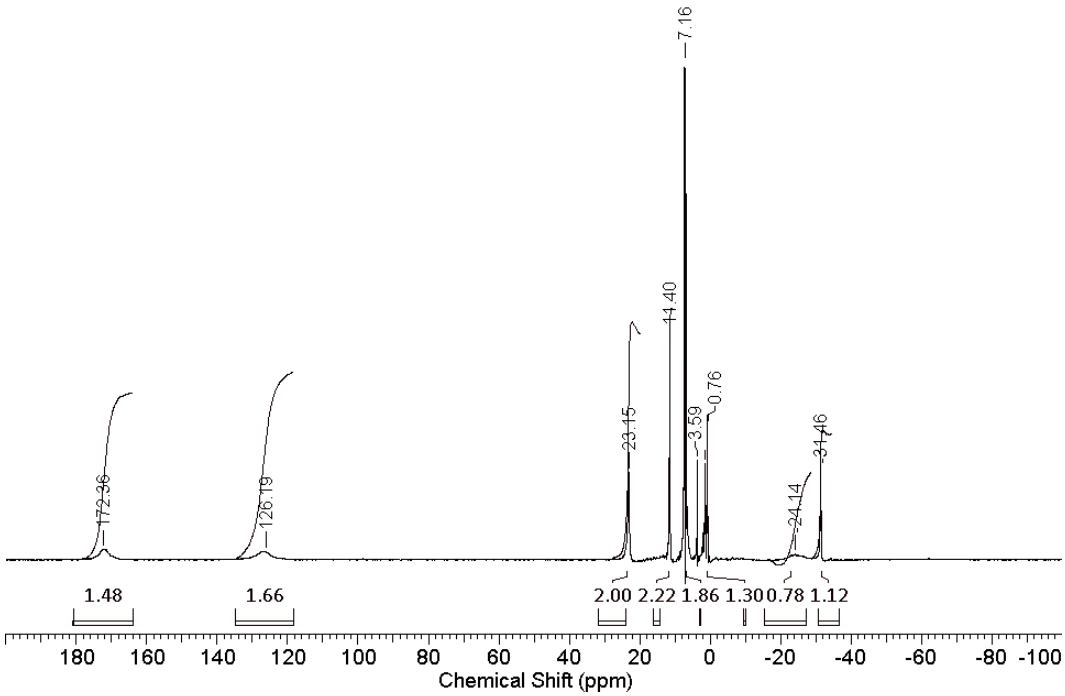

Figure 3.47. ^{1}H NMR spectrum of **2** in C_6D_6.

3.4.2 X-Ray Crystallographic Data Collection and Refinement of the Structures

Single crystals of K(THF)[CoL^{Ph}] (**3**), K[CoL^{tBu}] (**3a**), K(THF)[FeL^{Ph}] (**4**), Co_2L^{Ph} (**1**), and $FeCoL^{Ph}$ (**2**) were grown by vapor diffusion of Et_2O or pentane into concentrated THF solutions of **3**, **3a**, **4**, **1**, and **2** at rt, respectively. Green blocks of **3** (0.60 x 0.30 x 0.20 mm^3) and **3a** (0.50 x 0.38 x 0.18 mm^3), a yellow block of **4** (0.30 x 0.30 x 0.20 mm^3), a brown block of **1** (0.5 x 0.5 x 0.4 mm^3), and a red plate of **2** (0.36 x 0.20 x 0.06 mm^3) were placed on the tip of a glass capillary and mounted on a Bruker APEX-2 Platform CCD diffractometer for data collection at 173(2) K. The data collection was carried out using Mo-Kα radiation (graphite monochromator). The data intensity was corrected

for absorption and decay (SADABS). Final cell constants were obtained from least squares fits of all measured reflections. The structure was solved using SHELXS-97 and refined using SHELXL-97. A direct-methods solution was calculated which provided most non-hydrogen atoms from the E-map. Full-matrix least squares / difference Fourier cycles were performed to locate the remaining non-hydrogen atoms. All non-hydrogen atoms were refined with anisotropic displacement parameters. Hydrogen atoms were placed ~~i~~deally and refined as riding atoms with relative isotropic displacement parameters. For **3a**, the PLATON program, SQUEEZE function, was used to remove disordered solvent comprising two molecules of THF/Et_2O per asymmetric unit.[41] A total of 672 electrons were removed in a total volume of 2976 $Å^3$ per unit cell, equally distributed between two positions at (0, 0, 0) and (0.3, 0.3, 0.5) in the asymmetric unit. The number of electrons is consistent with removal of 12 ether and 4 THF molecules per unit cell, which is consistent with the 3:1 ratio observed by ^1H NMR spectroscopy. Crystallographic data for these complexes are summarized in Table 3.9. Crystallographic data for the tetranuclear oxo complexes are given in Table 3.10; these were grown from vapor diffusion of pentane into concentrated THF or benzene solutions of the bimetallic complexes. They crystallized as large blocks, and the data collection and refinement was performed exactly as for the other species.

Table 3.10. Crystallographic details for K(THF)[CoL^{Ph}], K[CoL^{tBu}, Co_2L^{Ph}, and $FeCoL^{Ph}$.

	Co_2L^{Ph}, 1	**$FeCoL^{Ph}$, 2**	**K(THF)[CoL^{Ph}], 3**	**K(THF)[FeL^{Ph}], 4**	**K[CoL^{tBu}], 3a**
chemical formula	$C_{45}H_{42}N_7Co_2$	$C_{45}H_{42}N_7CoFe$	$C_{49}H_{50}CoKON_7$	$C_{49}H_{50}CoKON_7$	$C_{39}H_{54}N_7CoK$
formula weight	798.72	795.64	850.99	847.91	718.92

crystal system	trigonal	trigonal	monoclinic	monoclinic	orthorhombic
space group	R_{-3}	R_{-3}	$P2_1/c$	$P2_1/c$	P_{bca}
a (Å)	14.937(1)	14.956(2)	11.3407(5)	11.3407(5)	20.568(2)
b (Å)	14.937(1)	14.956(2)	21.550(1)	21.550(1)	19.149(2)
c (Å)	29.199(2)	29.250(4)	17.9220(8)	17.9220(8)	24.290(2)
α (deg)	90	90	90	90	90
β (deg)	90	90	92.494(1)	92.494(1)	90
γ (deg)	120	120	90	90	90
V (Å^3)	5641.8(6)	5666(1)	4375(9)	4376(3)	9567(2)
Z	6	6	4	4	8
D_{calcd} (g cm^{-3})	1.411	1.399	1.292	1.287	0.998
l (Å), μ (mm^{-1})	0.71073, 0.925	0.71073, 0.866	0.71073, 0.53	0.71073, 0.485	0.71073, 0.475
T (K)	173(2)	173(2)	173(2)	173(2)	173(2)
θ range (deg)	1.72 to 28.24	1.72 to 27.50	2.29 to 26.47	1.80 to 27.45	1.68 to 27.59
reflns collected	21580	13888	49826	49755	92104
unique reflns	3083	2900	10090	9987	11058
data/restraint/ parameters	3083 / 0 / 163	2900 / 0 / 163	10090 / 92 / 714	9987 / 73 / 694	11058 / 0 / 439
R_1, wR_2 ($I >$ 2σ(I))	0.0378, 0.0952	0.0380, 0.0834	0.0446, 0.1083	0.0439, 0.1143	0.0554, 0.1264

3.5.3 Anomalous Diffraction Data Collection and Refinement of Fe/Co Occupancies in ***2***

A single crystal of **2** was mounted on a glass fiber and cooled to 100K using an Oxford Instruments Cryojet cryostat. The Bruker D8 diffractometer, integrated with an APEX-II CCD detector, was modified for synchrotron use at the ChemMatCARS 15-ID-B beam line at the Advanced Photon Source (Argonne National Laboratory). Diffraction data were collected at seven different energies with 0.3 s frames while manually attenuating

the beam to minimize overages of individual pixels. The scan at 30.0 keV (λ=0.41328 Å), which is energetically well above the atomic absorption energies, gave a least-squares refinement of all model positional- and displacement parameters to 0.5 Å resolution. To determine the compositions of Fe/Co at the two independent metal sites, a total of six anomalous diffraction data sets were collected near the absorption K-edges of Fe and Co (3 each): one preceding the Fe K-edge at 7.062 keV (1.7557 Å); one at the Fe K-edge 7.112 keV (λ=1.743 Å); one following the Fe K-edge at 7.162 keV (1.7311 Å); one preceding the Co K-edge at 7.659 keV (1.6188 Å); one at the Co K-edge at 7.709 keV (λ=1.6083 Å); and one following the Co K-edge at 7.759 (1.5979 Å). The anomalous diffraction can readily distinguish Fe/Co compositions at the two metal sites because of the expected differences in the $\Delta f'$ and $\Delta f''$ values for these two elements, as shown in Figure 3. Basically, $\Delta f'$ and $\Delta f''$ values of an element change dramatically near the element's absorption edge, but, for other element(s), they remain relatively constant. Each of these six anomalous diffraction data sets thus provides a different view of the electrons present at both sites. All six data sets were collectively used in a least-squares refinement to determine the Fe/Co occupancies at the two metal sites. GSAS-II was employed for these least-squares refinements because it allows multiple diffraction data sets as an input with subsequent refinement using a common crystallographic model.[42] The 30 keV data was refined using a structural model of **4** that had been determined at 173 K (see above). The converged positional- and displacement parameters were than frozen, so that only the Fe/Co occupancies of the two independent sites could be refined simultaneously using the six anomalous diffraction data sets. The refinement results

shows slightly mixed occupancies of the metal elements at both sites with significantly higher percentages of Fe at the top site (Fe 94(1)%, Co 6(1)%) and Co at the bottom site (Co 95(1)%, Fe 5(1)%). Hence, the precise structural formula of **2** is $(Fe_{0.94(1)}Co_{0.06(1)})(Co_{0.95(1)}Fe_{0.05(1)})L^{Ph}$, in which the total iron and cobalt content is equivalent, within error. Crystallographic details are: empirical formula, $C_{45}H_{42}N_7Co_{1.01}Fe_{0.99}$; fw, 795.64; trigonal; *R*-3; *a,b* = 14.9093(6) Å, *c* = 29.191(1) Å; α,β = 90°, γ = 120°; *V*, 5619.4(4) Å^3; *Z*, 6; D_{calcd}, 1.410 g/cm^3; μ, 0.205 mm^{-1}; λ, 0.41328 Å; *T*, 100(2) K; *q*, 1.86-20.30°; reflns collected, 45843; unique reflns, 6123; data/restraint/parameters, 6123/0/163; R_1,wR_2 ($I > 2\sigma(I)$): 0.0376, 0.00881.

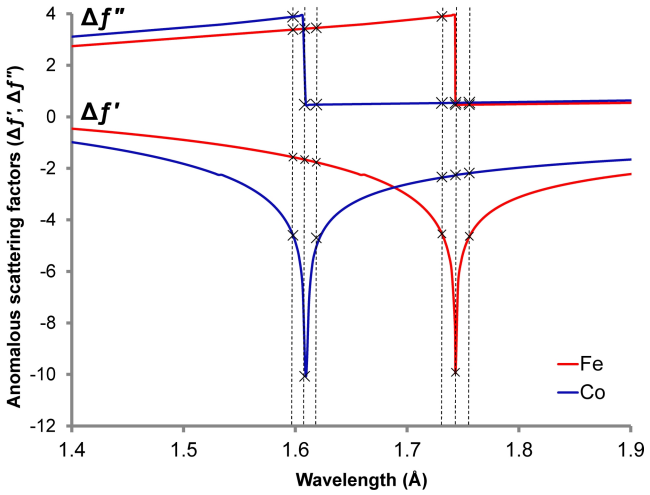

Figure 3.48. The anomalous dispersion corrections to normal scattering factors, including the real ($\Delta f'$) and imaginary ($\Delta f''$) components, for Fe (red) and Co (blue) as a function of wavelength (Å). The six dotted lines are the experimental wavelengths for the anomalous experiments, which were selected to span the Fe and Co absorption edge energies. The cross marks (×) indicate the Fe and Co anomalous scattering factor values used in the least-squares refinement to determine the metal occupancies.

3.5.4 Physical Measurements

NMR spectra were collected on a Varian Inova 500 MHz spectrophotometer. Visible and near-infrared absorption data were collected on a Cary-14 spectrophotometer. UV-wavelength absorption spectra were collected on a Cary 300 Bio UV-Visible spectrophotometer. Perpendicular-mode X-band EPR spectra were recorded on a Bruker EPP 300 spectrometer equipped with an Oxford ESR 910 liquid helium cryostat and an Oxford temperature controller. X-band EPR spectra were simulated using the ESIM program written by Eckhard Bill. Mössbauer data were recorded on an alternating constant acceleration spectrometer. The minimum experimental line width was 0.24 mm s^{-1} (full width at half-height). The ^{57}Co/Rh source (1.8 GBq) was positioned at rt inside the gap of the magnet system at a zero-field position. Isomer shifts are quoted relative to iron metal at 300 K.

Magnetic susceptibility data were measured from powder samples of solid material in the temperature range 2 - 300 K by using a SQUID susceptometer with a field of 1.0 T (MPMS-7, Quantum Design, calibrated with standard palladium reference sample, error <2%). Multiple-field variable-temperature magnetization measurements were done at 1 T, 4 T, and 7 T also in the range 2 to 300 K with the magnetization equidistantly sampled on a 1/T temperature scale. The experimental data were corrected for underlying diamagnetism by use of tabulated Pascal's constants ($\chi_{dia} < 0$).[43,44] The susceptibility and magnetization data were simulated with the program julX for exchange coupled systems.[45] The simulations are based on the usual spin-Hamiltonian operator for mononuclear complexes with spin $S = 5/2$ and $S = 3$:

$$\hat{H} = g\beta\hat{\vec{S}}\cdot\vec{B} + D[\hat{S}_z^{\,2} - 1/3S(S+1) + E/D(\hat{S}_x^{\,2} - \hat{S}_y^{\,2})]$$

where g is the average electronic g value, and D and E/D are the axial zero-field splitting and rhombicity parameters. Magnetic moments are calculated after diagonalization of the Hamiltonian from the eigenfunctions using the Hellman-Feyman theorem. Powder summations were done by using a 16-point Lebedev grid. Because the program is not equipped for individual spins larger than 5/2, we reproduced the septet ground state of **4** by adopting two individual spins $S_1 = S_2 = 3/2$ with a hypothetical and arbitrarily chosen large, positive exchange coupling constant, $J = +200$ cm^{-1}. This approach is physically equivalent to a simulation with an isolated total spin $S = 3$ for the bimetallic, because the resulting septet ground state is energetically well isolated by an energy gap ΔE of 1200 cm^{-1} or more from the other calculated total spin manifolds ($\Delta E/k$ >1700 K), such that Boltzmann population of other manifolds is negligible up to ambient temperature (300 K).

3.5.5 Computational Methods

DFT Calculations. The bimetallic complexes were studied using density functional theory (DFT) and the complete active space self-consistent field (CASSCF) method,[55] followed by a multiconfigurational second-order perturbation theory (CASPT2) method.[56] Previous studies on similar systems have demonstrated that this approach is successful in predicting accurate results for ground and electronically excited states of bimetallic systems.[57-60] Gas-phase geometry optimizations were performed for the

various possible spin states at the DFT level of theory with the use of the Perdew−Burke−Ernzerhof (PBE) exchange-correlation functional.[61] within the TURBOMOLE 6.1 program package.[62] For C and H atoms, the double-ζ quality basis set def-SV(P) was used, whereas the triple-ζ quality basis set def-TZVP was employed for N and additional polarized functions where introduced by using def-TZVPP for Fe and Co. The DFT calculations were performed with the broken symmetry option (unrestricted calculations) and the resolution-of-the-identity (RI) approximation for several spin states.[63]

CASSCF/CASPT2 Calculations. All CASSCF/CASPT2 calculations were performed with the MOLCAS-7.4 package[64] using the DFT-optimized structure. The relativistic all-electron ANO-RCC basis sets[65,66] were used for all elements. In all of these calculations, the ANO-RCC-VDZP basis set was used for Fe, Co, and N while the ANO-RCC-MB basis set was used for C and H. Scalar relativistic effects were included by using the Douglas−Kroll−Hess Hamiltonian.[67] The two-electron integral evaluation was simplified by employing the Cholesky decomposition technique.[68,69] In order to avoid intruder states, an imaginary level shift of 0.2 au was used in the CASPT2 calculations.[70] For Co_2L^{Ph}, a truncated valence shell comprising 11 d-electrons in 11 orbitals was used as the active space; this omits the $3d_{x^2-y^2}$ and $3d_{xy}$ orbitals on Co1 and their four electrons, for reasons described in the text, but adds three orbitals from the fourth shell, to account for correlation effects. For $FeCoL^{Ph}$ and $CoFeL^{Ph}$, an active space comprising 14 d-electrons in 12 orbitals (14,12) was used, including all 3d orbitals and two from the fourth Co shell.

Chapter 4

Synthesis and Hydride-Transfer Reactivity of Palladium Complexes with Ligands Containing Organic Hydride Donors

4.1 Overview

A new ligand system containing a redox-active phenanthridinium group tethered to a phosphine donor has been developed. This system positions organic hydride donors in close proximity to a metal center, in order to promote bifunctional reactivity, in which the metal and ligand work cooperatively to activate and reduce substrates. This ligand can be synthesized in a reduced, hydride-bearing, "loaded," form or an oxidized, "unloaded," form, and these forms can be interconverted by reactions with known hydride donors and acceptors. The bis-phosphine palladium dichloride complexes of these ligands have been synthesized and characterized, and these can be readily interconverted between loaded and unloaded forms. Low-coordinate palladium bis-phosphine complexes have also been synthesized that show intriguing interconversion between metal-bound and ligand-bound hydrides. Although these dynamics are not yet fully characterized, the ligands appear to stabilize both a low-coordinate Pd(0) complex and the products of its reaction with H_2. These preliminary results represent a promising beginning in the development of bifunctional catalysts based on simple, modular ligands containing organic hydride donors.

4.2 Introduction

Many renewable, abundant small molecules, such as N_2 and CO_2, require reduction by several electrons to form useful chemical commodities such as NH_3 and CH_3OH. In these transformations, the more electrons that can be delivered simultaneously, the more efficient the reactions become, avoiding the thermodynamic

cost and potential side-reactions of high-energy intermediates. However, delivering multiple electrons simultaneously can challenging, even when more than one metal is used (*vide supra*). Even more challenges are encountered in the simultaneous transfer of the multiple protons that are needed to balance the charge, especially with the low-valent transition metal clusters are not often acid-stable.

In Nature, although multi-electron reactions are often *mediated* by transition metal clusters, the electrons and protons are typically *stored* together in the form of weak chemical bonds in organic heterocycles. The most prominent of these heterocycles is the coenzyme dihydronicotinamide adenine dinucleotide, or NADH, in which two electrons and a proton are stored in the form of an organic hydride, and its oxidized counterpart, nicotinamide adenine dinucleotide, or NAD^+. These two forms of the coenzyme can be efficiently interconverted through oxidation or reduction, which can be coupled to redox reactions of a variety of substrates.[1,2] The two forms of the coenzyme are shown in Figure 4.1.

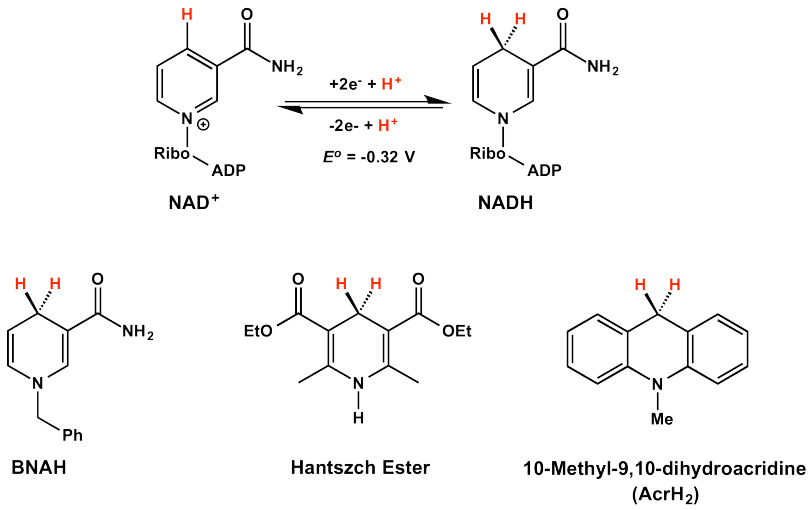

Figure 4.1 Structures of NAD^+/NADH and selected synthetic analogues. Ribo = ribose; ADP = adenine diphosphate. Reduction potential is for aqueous solution, pH 7, referenced to NHE. Bottom: synthetic analogues of NADH.[3,4]

In water, the NADH/NAD^+ redox couple is relatively negative, E^o = -0.32 V *vs* NHE, making NADH somewhat strongly reducing.[3] Thus, synthetic derivatives of NADH, such as 1-benzyl-1,4-dihydronicotinamide (BNAH) and the Hantzsch ester (diethyl-1,4-dihydro-2,6-dimethyl-3,5-pyridinedicarboxylate), and other molecules with N-substituted pyridinium rings, have been investigated as reducing agents in organic chemistry.[5] However, the substrate scope of BNAH and its analogues has mostly been limited to the reduction of activated, electron-deficient substrates, such as electron-poor olefins and requires heating, due to kinetic and thermodynamic constraints. Photoactivation of the hydride donors was found to promote these reactions: the pyridinium groups are UV chromophores and can be photoexcited directly or using a photosensitizer such as $Ru(bpy)_3^{2+}$ (bpy = 2,2'-bipyridine) to generate much more reactive excited states.[6] However, the excited pyridinium groups are prone to radical side-reactions, including radical one-electron transfer reactions and dimerization through C-C coupling at the hydridic *para*-position.[7] The Hantzsch ester has found more utility as a transfer-hydrogenation reagent in the reduction of activated C=C, C=N, and C=O bonds, especially when coupled with a Lewis acid catalyst, but it suffers from being an expensive stoichiometric reagent, as effective methods for its regeneration are not well developed.[5]

Creative solutions to the issues of selectivity, substrate scope, and regeneration may be found through cooperative interactions between the hydride donors and transition metal centers. In Nature, NADH and its analogues often work in concert with metals to achieve selective and efficient redox reactions. For instance, even in reactions that

involve direct transfer of a hydride from NADH to substrate, as in alcohol dehydrogenase and related dehydrogenases, the substrate is polarized and activated by binding to a metal center.[1,8] In synthetic systems, appending NADH analogues in close proximity to a metal center has been shown to be an effective method for increasing the efficiency of hydride transfer. For example, the reduction of flavin by BNAH was shown to occur 175 time faster when the BNAH group was covalently linked to a Lewis-acidic zinc ion that promotes the binding of flavin.[9] More significantly, from the standpoint of small molecule reduction, Tanaka and coworkers have reported the electrocatalytic reduction of acetone to isopropanol using the ruthenium complex $Ru(bpy)_2(pbn)^{2+}$. This complex is an analogue of the $Ru(bpy)_3^{2+}$ photosensitizers used to promote the *intermolecular* reactions of NADH analogues, but it incorporates an NADH-like ligand, 2-(2-pyridyl)-benzo[*b*]-1,5-naphthyridine, or pbn.[10] This complex can be reduced electrochemically or photochemically to a hydride-bound pbnHH form (pbnHH = 1,5-dihydro-2-[2-pyridyl]-benzo[*b*]-1,5-naphthyridine). It is this organic hydride, positioned in the secondary coordination sphere of the ruthenium, that serves as the key intermediate in the reduction.[11,12] Similarly, Colbran and coworkers have cleverly incorporated a Hantzsch ester into the secondary coordination sphere of a rhodium diimine complex, $[Cp^*Rh^{III}(NN)Cl]^+$, that is commonly used to electrochemically catalyze the reduction of NAD^+ to NADH (where Cp* is pentamethylcyclopentadiene and NN is a diimine ligand).[13] This complex was shown to be active toward the transfer hydrogenation of imines, using formate as the reducing agent. These examples are shown in Figure 4.2.

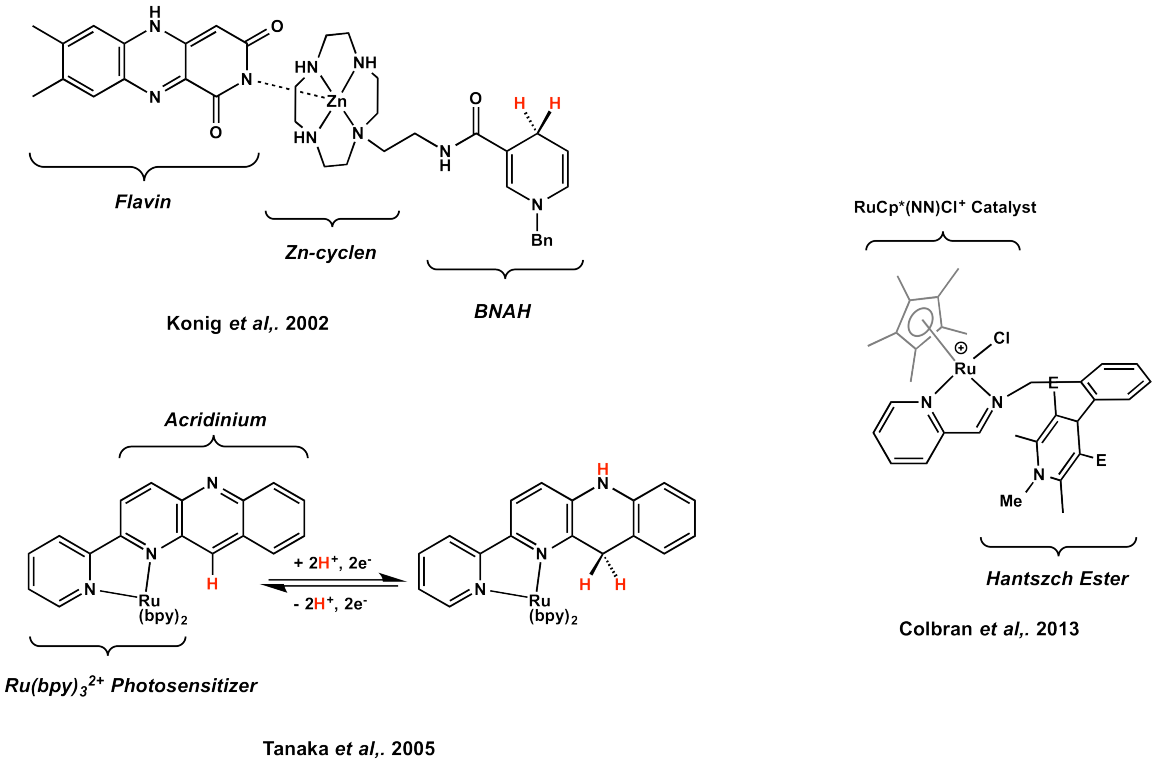

Figure 4.2 Examples of metal-ligand cooperativity with NADH-like functional groups.[9,10,13]

Thus far, most such reports have focused on additions of a single equivalent of hydride to unsaturated substrates. Reduction of industrially-important small molecules such as CO_2 and N_2, however, will require multiple hydride equivalents to give products such as methanol and ammonia. We envisioned that, by incorporating more than one organic hydride donor in the secondary coordination sphere of a metal, the total number of reductive equivalents that can be delivered simultaneously could be easily varied. Accordingly, we have designed platforms that combine multiple NADH-like pyridinium groups within a single ligand scaffold. In previous work performed in our group, three BNA^+ groups were tethered to a tripodal *tren* base.[14] This produced a ligand with three hydride donors in the secondary coordination sphere of a metal-binding site. As shown in

Figure 4.3, this ligand, which is synthesized in the "unloaded" $H_3(NA)_3$tren form, can be reduced, using $Na_2S_2O_4$ (sodium dithionite) in a biphasic mixture of toluene and basic water, to give the "loaded" $H_3(NAH)_3$tren form; it can also be "unloaded" by reaction with the hydride acceptor CPh_3BF_4. The coordination complexes of this ligand with zinc and cobalt were also demonstrated, and the crystal structure of the former clearly showed the three organic hydrides in the secondary coordination sphere of the zinc ion. This platform is poised to deliver multiple hydrides to metal-bound substrates and thus appears to be a promising delivery system for multiple equivalents of protons and electrons.

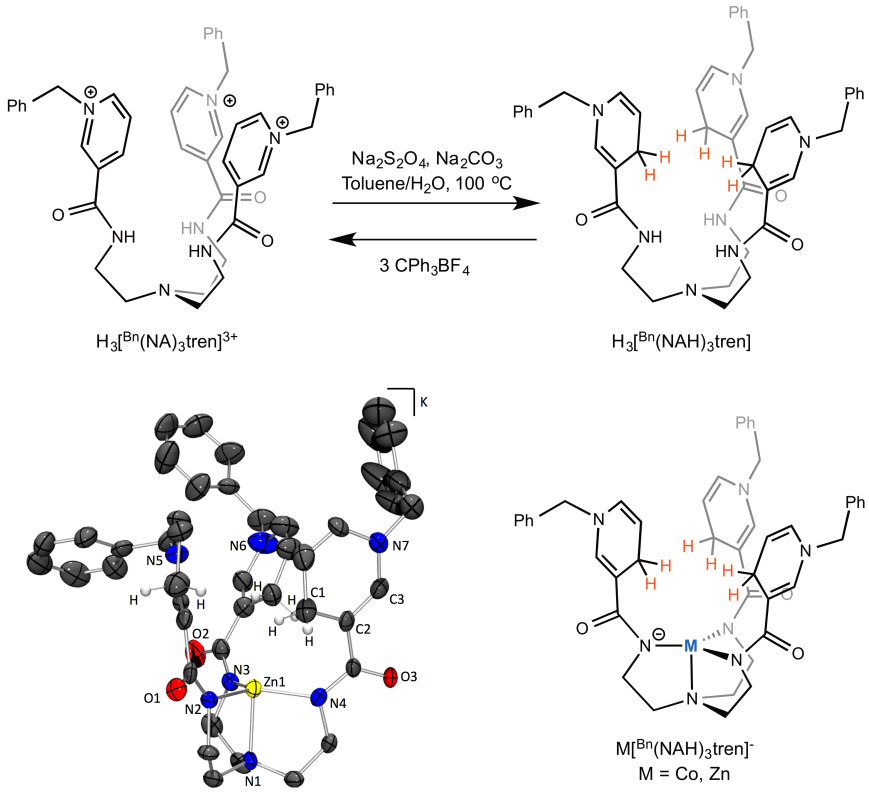

Figure 4.3 $^{Bn}(NAH)_3$tren platform combining multiple BNAH groups within a single chelating ligand. Top: demonstrated loading and unloading of ligand platform. Bottom: Metal complexes synthesized within this framework.

However, there are several aspects of these ligands that could be modified to

create more convenient catalysts. Chief among these is to use a neutral ligand donor set, to impart stability of the complexes to acid and/or water. The trianionic *tren* base used in the $M[^{Bn}(NAH)_3tren]^-$ system is highly basic and demetallates when exposed to protons or other strong Lewis acids. This is particularly disadvantageous, considering that most small-molecule substrates require addition of protons, to balance the negative charge buildup associated with hydride transfer. In addition, many hydride acceptors themselves can be quite Lewis acidic and might potentially react with the amides. Another consideration was to select a pyridinium-derived organic hydride donor that could be reduced selectively and easily but would still be sufficiently hydridic to effect hydride transfer to substrates. BNAH groups are powerful donors, but selectively loading them with hydrides is typically accomplished only through reaction with aqueous dithionite. Common hydride sources such as $LiAlH_4$, $NaBH_4$, and NaH are either too powerfully reducing, and thus cause overreduction to the saturated heterocycle, or are unselective, giving mixtures of the 1,2-, 1,4-, and 1,6-dihydropyridines instead of the desired 1,4-dihydropyridine. A final consideration, although far less important than the first two, was to simplify the system by using the N-alkyl substituent on the pyridinium ring as a tether to the ligand donor group. This substituent is necessary to create the positive charge on the pyridinium group and activate the ring to accept a hydride, but it is an extra appendage that may cause issues with crystallization and adds an extra step in the synthesis. As the link between the pyridinium and the ligand, however, it becomes an integral part of the ligand design.

The new, bifunctional ligand we have designed is shown in Figure 4.4. A

phenanthridinium, or benzo(c)quinoline, heterocycle serves as the hydride donor. This is connected to a phosphine donor *via* an ethyl linker. The phenanthridinium moiety was chosen because it can be easily and selectively loaded with simple borohydrides, yet is a relatively strong hydride donor, slightly less reducing than BNAH but more so than the Hantzsch ester.[5,15,16] The selectivity is a result of the asymmetry of the fused ring system, which prevents hydride loading at the *para*- and one of the two *ortho*-positions on the pyridinium ring, leaving the second *ortho*-carbon as the only hydride-accepting position. A phosphine was chosen as the donor group because of its soft, neutral character, which leads to a preference for binding metals over protons, and because there is a rich chemical literature with these donors. Finally, a monodentate ligand was chosen for simplicity, ease of synthesis, and flexibility. We have preliminarily abbreviated this ligand pedipp$^+$ and pedippH, for the unloaded and loaded forms of 2-*p*henanthridinium-*e*thyl*dip*henyl*p*hosphine, but will refer to it in the following discussion as L^+ and LH for simplicity.

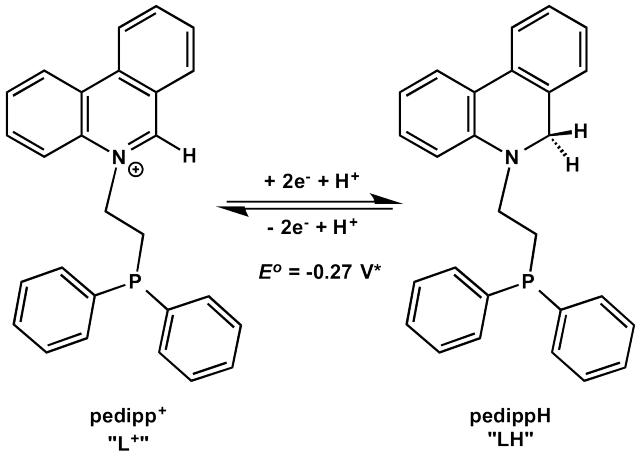

Figure 4.4 "Unloaded" and "loaded" forms of the bifunctional phenanthridinium-phosphine ligand described in this study. *Reduction potential calculated from thermodynamic data for methyl-substituted phenanthridinium in 4:1 ^{i}PrOH:H_2O.

We have begun exploring the coordination chemistry of this ligand only recently, focusing on bis-phosphine complexes of palladium. The characterization of the molecules described herein is thus quite preliminary, and we have not extensively explored their substrate scope. Nevertheless, even in this early work, we have found encouraging results. Notably, the ligands, and their palladium(II) compounds, can be cleanly synthesized in both "loaded" and "unloaded" forms; these forms are stable to acid and can be interconverted by reaction with organic hydride acceptors. Moreover, although these results are not fully understood, we have observed that reduced, low-coordinate palladium compounds with these ligands can undergo intriguing exchange of hydrides between the metal and ligands. In these cases, the ligands appear to act cooperatively with the metals to stabilize both a low-coordinate palladium(0) compound and the products of its reaction with H_2. These results appear to be a promising start for achieving metal-ligand cooperativity using hydride-donating ligands.

4.3 Results and Discussion

4.3.1 Synthesis of Phenanthridinium-Containing Phosphine Ligands

The reduced ligand can be made in a simple three-step procedure as shown in Figure 4.5. First, phenanthridine is heated in neat 1,2-dibromoethane, according to a previously-reported procedure, to produce the bromoethyl phenanthridinium salt, 5-(2-bromoethyl)-phenanthridinium bromide (BrEtPhenBr).[17] This produces the alkylated phenanthridinium group, in which the alkyl linker contains a halide leaving group. We envisioned that substitution of the bromide by a phosphide nucleophile would generate the unloaded ligand. However, the carbon *ortho* to the nitrogen on the phenanthridinium is highly electrophilic and susceptible to attack by by nucleophiles. To prevent competitive substitution at this position, the phenanthridinium is reduced with sodium borohydride in 2:1 methanol:H_2O to give 5(2-bromoethyl)-5,6-dihydrophenanthridine (BrEtPhenH), according to an adaptation of a literature precedent for related phenanthridinium groups.[18] This serves a dual role of loading the hydride onto the phenanthridinium and protecting the *ortho*-carbon by masking its electrophilicity. Finally, the phosphine group is introduced by reaction of BrEtPhenH with $KPPh_2$ in THF at -78 °C. After a slight workup, the reduced phosphine ligand can be obtained as a white powder on a multi-gram scale and in good yield (79% in three-steps).

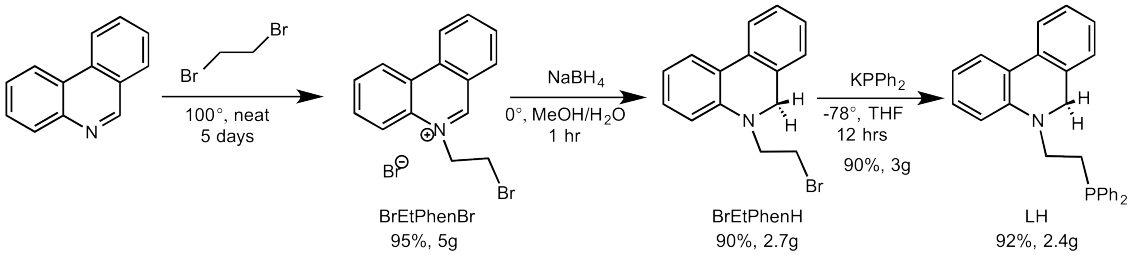

Figure 4.5 Synthesis of the loaded phosphine ligand, LH.

The ^{1}H NMR spectrum of LH is clean after workup and shows the expected three resonances for the PPh_2 group, two for the ethyl linker, and nine peaks for the phenanthridine ring system. Crucially, the resonance for the hydridic *ortho*-hydrogens is shifted far upfield and out of the aromatic region, to 3.85 ppm, and integrates to 2 H. The ^{31}P NMR spectrum has only one peak, at -21.4 ppm. The protonated ligand is the major ionic species observed in the ESI-MS spectrum, with the only other ions corresponding to the phosphine oxide and unloaded ligand; each of these is at less than 5% the intensity of the major ion.

The ligand can also be unloaded to form the oxidized tetrafluoroborate salt $L^{+}BF_4^{-}$ by simple hydride transfer to triphenylcarbenium (trityl) BF_4 at room temperature, as shown in Figure 4.6. This reaction is surprisingly slow, taking two days for substantial conversion (~70%), but the unloaded ligand precipitates out of the THF solution as a clean, white, microcrystalline solid.

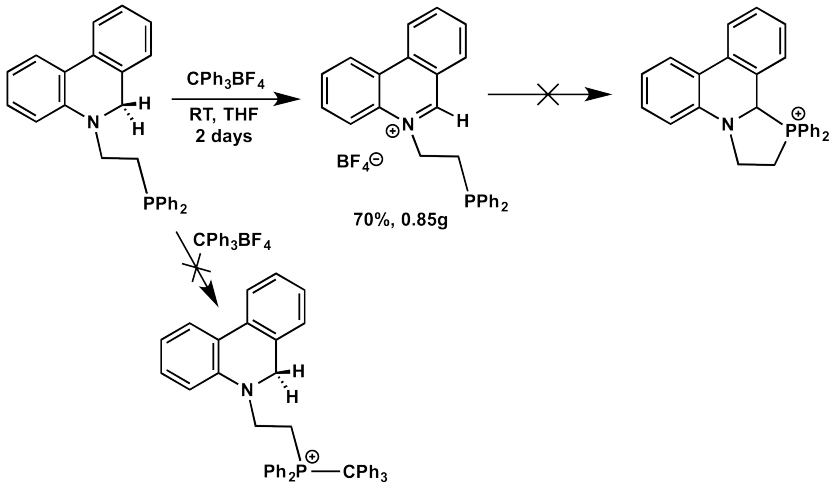

Figure 4.6 Synthesis of unloaded $L^{+}BF_4^{-}$ through hydride transfer.

This was gratifying, since the presence of the nucleophilic phosphine donor could

potentially have complicated the unloading process in two different ways, also shown in Figure 4.6. First, it could react with the strongly electrophilic trityl cation to irreversibly alkylate the phosphine. This is not observed in the product; moreover, the leftover reaction mixture shows only starting material and the byproduct $HCPh_3$, suggesting a very clean reaction that could potentially give higher yields with prolonged stirring. In addition, it was not clear that the electrophilic phenanthridinium moiety would be stable to the free phosphine. Notably, similar phenanthridinium complexes that contain dangling aminoethyl groups, instead of the phosphinoethyl moiety here, were reported to form five-membered heterocycles in which the amine attacks the *ortho*-carbon.[17-19] However, the ^{1}H NMR spectrum of the unloaded ligand is quite similar to that of the bromoethyl phenanthridinium precursor, except for the addition of the resonances due to the diphenylphosphine unit. The diaryl substituents on the phosphine are probably key to preventing these side-reactions, as they both reduce the nucleophilicity of the phosphine and provide some steric hindrance. It is possible that, if more basic dialkylphosphine variants of this ligand are developed, they will need to use bulkier substituents to hinder the more nucleophilic phosphine from either of these reactions.

The ^{1}H NMR spectra for LH and $L^+BF_4^-$ are compared in Figure 4.7. The spectra are quite distinct. The most diagnostic resonance is that for the hydridic protons on the *ortho*-carbon. In L^+, this resonance shifts far downfield, to 9.66 ppm, consistent with its position next to the cationic nitrogen; its integration is for 1 H, consistent with unloading. The other aromatic peaks also shift downfield, indicating that the charge is delocalized throughout the tricyclic ring system. Only one of the two peaks from the ethyl backbone

is significantly shifted in L^+, consistent with a position next to the cationic nitrogen. Finally, the resonances from the PPh_2 group are essentially unchanged, supporting the assertion that the phosphine does not significantly interact with the phenanthridinium group. Likewise, the ^{31}P resonances are only slightly different, at -21.4 ppm for LH in C_6D_6 and -19.1 ppm for LBF_4 in CD_3CN, a minor difference that might be attributed to the difference in solvent. ^1H NMR is therefore quite diagnostic in distinguishing the oxidation state of the phenanthridinium moiety, especially the resonances for the phenanthridinium protons, whereas ^{31}P is not particularly helpful.

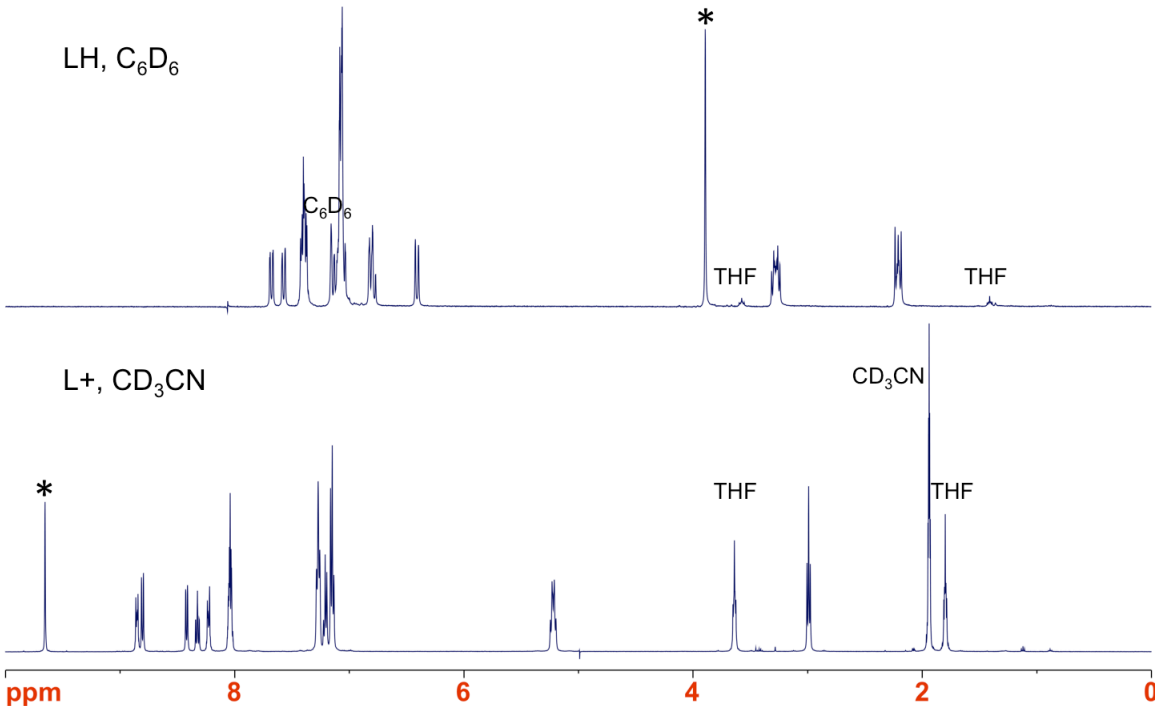

Figure 4.7 ^1H NMR spectra for LH (top, C_6D_6, 500 MHz) and LBF_4 (bottom, CD_3CN, 500 MHz). An asterisk marks the resonance for the hydridic H in each spectrum.

4.3.2 Substrate Scope and Thermodynamics of Hydride Transfer

The thermodynamic driving force for hydride transfer determines the scope of the substrates that can be reduced or oxidized by this ligand. This value is typically quantified as the "hydricity" of a hydride donor, $\Delta G°_{H^-}$, defined as the free energy for the heterolytic dissociation of a reduced organic hydride donor (D-H) into the free donor (D^+) and hydride ion (H^-), Eqn 4.1

$$\Delta G°_{H^-} = \Delta G°(D^+) + \Delta G°(H^-) - \Delta G°(D\text{-}H) \qquad \text{(Eqn 4.1)}$$

This value provides a scale with which to compare various hydride donors. The larger the value of $\Delta G°_{H^-}$, the stronger the D-H bond: thus, a small value indicates that a reduced molecule will be a good hydride donor and that its oxidized form will be a poor acceptor. Likewise, a large value will correspond to a poor donor and strong acceptor. The hydricity values of a few hydride donors have been experimentally measured in absolute terms,[20] which allows the assignment of others' based on comparison of their hydride transfer equilibria. One study of note, by Kreevoy *et al.*, has measured the equilibrium constants for reactions of phenanthridinium complexes with a few known donors and acceptors, including BNAH.[15] Since the hydricity of BNAH has subsequently been determined,[20] these equilibrium constants can be converted to hydricities; such a calculation gives values for $\Delta G°_{H^-}$ for these phenanthridinium groups in the range 63-67 kcal/mol. These are moderate values for a hydride donor, higher than the value of 59 kcal/mol for BNA^+ but less than the value of 72 kcal/mol for 1-methylacridinium, which has a tricyclic ring system isomeric with that of phenanthridinium and is generally considered a weak-to-moderate donor.[16] The values also do not vary substantially when

the substituents on the phenanthridinium nitrogen were varied from methyl to benzyl to *para*-cyano-benzyl and *para*-trifluoromethyl-benzyl. Thus, the introduction of the diphenylphosphine moiety should not dramatically affect the hydricity. A comparison of these values is given in Figure 4.8.

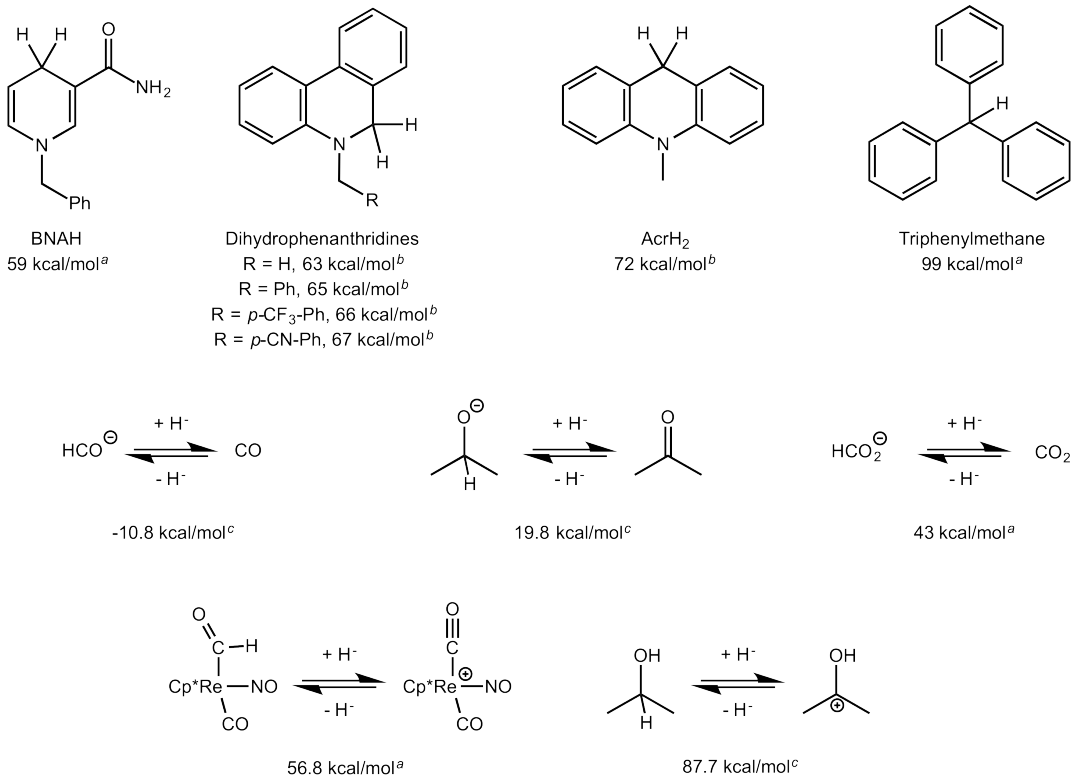

Figure 4.8 Hydricity values of some organic hydride donors (top row) and small molecule reactions of interest (middle and bottom rows). *a:* value determined experimentally in absolute terms. [20,21] *b:* value calculated from experimentally-measured equilibrium constant for reaction with reference compound of known hydricity.[15] *c:* value determined using DFT calculations.[22]

These values are useful because they determine the range of substrates that can be reduced by the loaded phenanthridinium group. The hydricities of some interesting small molecule reductions are given in the lower two rows of Figure 4.8. The values in the middle rows do not appear promising for the reduction of small molecules with this ligand. The $\Delta G°_{H^-}$ for HCO_2^-, for instance, is 43 kcal/mol, making its formation from

CO_2 unfavorable by approximately 20 kcal/mol. Thus, if the reaction were solely between the reduced ligand, LH, and either CO_2, CO, acetone, or a wide variety of other substrates, it would be highly disfavored. More promising outcomes are suggested by the thermodynamic data in the bottom row of Figure 4.8. These show the hydricities for two of these small molecules, CO and acetone, when they are instead pre-activated by binding to a transition metal or a proton. In this case, hydride transfer becomes much more favorable: the difference between hydride transfer to free CO *vs.* a rhenium-bound carbonyl, for instance, is nearly 70 kcal/mol! Likewise, protonation of acetone makes it a much better hydride acceptor ($\Delta G°_{H^-}$ = 87.7 kcal/mol), to the point where it can be reduced even by the weakly-donating (pbnHH) ligand in Tanaka's complex, $Ru(bpy)_2(pbn)^{2+}$, which has a calculated $\Delta G°_{H^-}$ of 88.7 kcal/mol.[22] The 1 kcal/mol difference between these values is within the error of the DFT calculations from which they were derived. This contrast highlights the utility of combining the hydride-donor ligands with a metal center, so that the two can work cooperatively to activate and reduce the substrate. It also emphasizes the need for acid-stable catalysts, as transfer of a hydride *and* a proton is usually far more favorable than hydride transfer alone.

The ethyldiphenylphosphine substituent on the phenanthridinium group of L^+ probably places its hydricity in between those of the methyl- and benzyl-substituted phenanthridinium compounds, around 64 kcal/mol. We have not undertaken an independent measurement of this value. Such an analysis has proven difficult, as the loaded and unloaded forms of the ligand have different charges that impart very different solubilities, precluding equilibrium measurements. We have nevertheless studied the

reaction of the ligand with BNAH and 1-methylacridinium. The results are entirely as expected. The reaction of BNAH with unloaded L^+ in MeCN causes formation of BNA^+ and precipitation of LH essentially quantitatively; likewise, reaction of acridinium with LH in THF causes quantitative precipitation of L+. The reverse of these reactions does not proceed to any observable extent. These results are consistent with a hydricity of LH/L^+ around ~64 kcal/mol and suggest that it is a hydride donor of moderate strength.

4.3.3 Palladium Dichloride Complexes with L^+ and LH

Due to the rich literature precedent for the chemistry of Group 10 metals with phosphine ligands, we chose to begin our studies by synthesizing bis-phosphine dihalide complexes with nickel and palladium. Palladium complexes proved the most convenient; nickel dihalide complexes were plagued by low solubility when the ligands were in the unloaded form, and the complexes with loaded ligand had paramagnetically broadened NMR spectra that would complicate spectroscopic monitoring of reactions. On the other hand, the reaction of $PdCl_2(PhCN)_2$ with two equivalents of LH proceeds quite cleanly in THF to give *trans*-$PdCl_2(LH)_2$, **1**, in good yield and high purity. The ^1H NMR spectrum is consistent with solution-averaged D_{2h} symmetry, indicating that the ligands are equivalent on the NMR timescale. The resonances for the phenanthridinium group are only slightly shifted compared to the spectrum of the free ligand, and, most importantly, the hydride resonance at 4.23 ppm is intact. The diphenylphosphine peaks, however, shift farther downfield, as expected from coordination to the palladium. Similarly, the ^{31}P NMR signal shifts from -21.4 to 13.9 ppm, consistent with coordination to the metal

X-ray quality crystals of **1** were grown by vapor diffusion of hexane into a concentrated benzene solution. **1**$(C_6H_6)_2$ crystallizes in the triclinic space group P-1, with only one molecule per unit cell, thereby imposing inversion symmetry about palladium. The structure is shown in Figure 4.9. The phosphines are mutually *trans*, as expected, with Pd-P distances of 2.3205(5) Å and Pd-Cl distances of 2.3163(5) Å. The Pd center is nearly perfectly square planar, with P1-Pd1-Cl1 angles of 90.33(2)° and P1-Pd1-Cl1A angles of 89.67°.

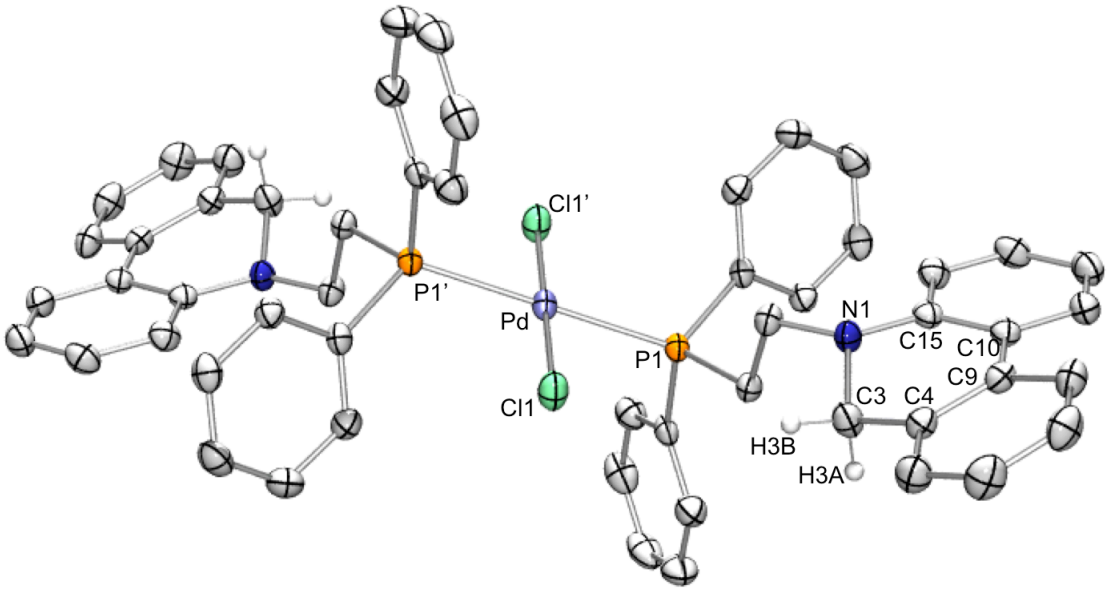

Figure 4.9 Solid-state molecular structure of **1**, at 50% probability level. For clarity, solvent molecules and hydrogen atoms not placed from the difference map have been omitted. Selected bond distances (Å) and angles (°): Pd-Cl1, 2.3163(5); Pd-P1, 2.3205(5); N1-C3, 1.460; C3-C4, 1.501(6), C3-H3A, 1.02(2); C3-H3B, 0.097; Cl1-Pd-P1, 90.33(2); Cl1A-Pd1-P1, 89.67, N1-C3-C4, 110.8(2); N1-C15-C-10, 117.9(2).

The structural metrics clearly demonstrate the effect of the hydride loading on the phenanthridine group. The planarity of the aromatic ring system is broken: the six-membered ring containing the nitrogen, N1, and the *ortho*-carbon, C3, is puckered into a pseudo-chair conformation to accommodate the tetrahedral geometry of the hydride-bearing C3. This causes a distortion of the other two rings in the "biphenyl" backbone,

giving a C4-C9-C10-C15 torsion angle of 18.51° between these rings. The reflection data and refinement are both of high quality (R_{int} = 0.0293; R_1 = 0.0314), which allowed placement and refinement of the hydrides from the Fourier difference map. The hydrides are distinct, with one axial C-H and one equatorial C-H in the pseudo-chair conformation of the ring. The equatorial C3-H3B distance is slightly shorter, at 0.097(2) Å than the axial C3-H3A distance of 1.02(2) Å. These values are longer than the standard values for an aromatic C-H bond (0.95 Å) and, compared to a standard methylene C-H distance (0.98 Å), one is slightly shorter and one is larger. However, these values cannot be accurately refined from X-ray diffraction methods, since the hydrogens do not have core electrons.

The synthesis of the unloaded palladium complex $PdCl_2(L^+BF_4^-)_2$ (**2**) is analogous to that of **1** but is run in CD_3CN instead of THF, due to the insolubility of the $L^+BF_4^-$ ligand and the product **2** in THF. The product is also bright yellow and shows a very similar ^{1}H NMR spectrum to that of the free unloaded ligand, except that the resonances due to the -PPh_2 unit are shifted downfield. The ^{31}P spectrum shows a single major peak, a singlet at 15.64 ppm, as well as a minor resonance at 27.6 ppm, corresponding to another species also observed in the ^{1}H NMR spectra. We have been unable to isolate **2** separately from this species, despite all attempts to wash or crystallize it, and it is observed regardless of synthetic method, *i.e.*, whether **2** is formed from metallation of $L^+BF_4^-$ or from unloading of **1**, or other related interconversions. Its pattern in the ^{1}H NMR spectrum mostly overlaps with that of **2**, except for a downfield shift for the hydride signal and one of the protons from the ethyl linker. Its ^{31}P shift is similar to those

of low-coordinate Pd complexes we have prepared with this ligand (*vide infra*), and we suspect it may be due to decoordination of a chloride ligand and/or substitution of CD_3CN in solution. The ^1H spectra of **1** and **2** are compared in Figure 4.10.

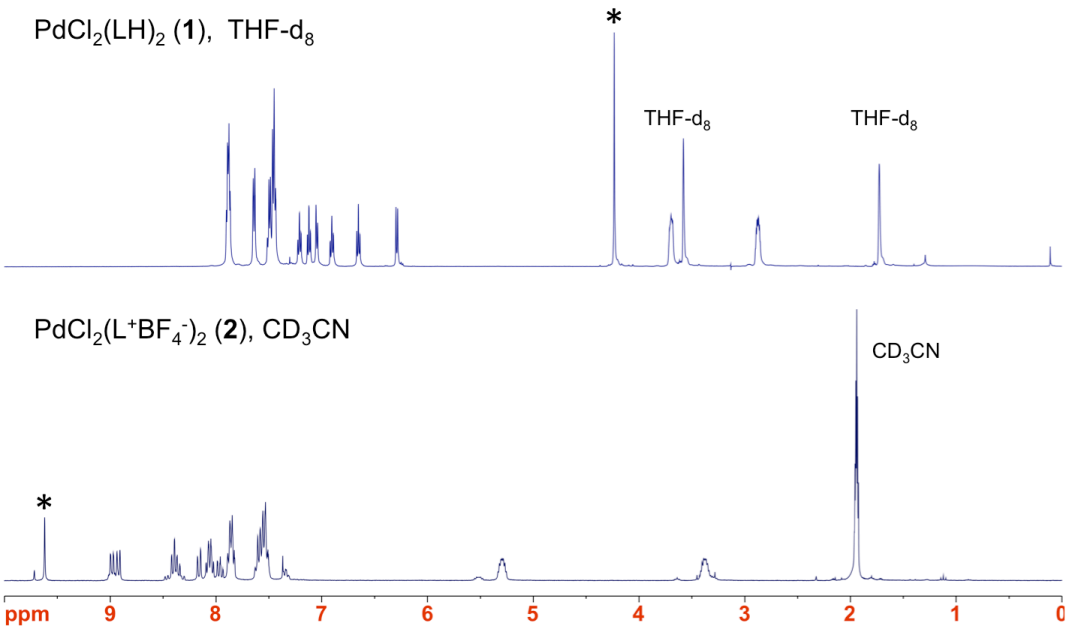

Figure 4.10 ^1H NMR spectra of **1** (top, 500 MHz, THF-d_8) and **2** (bottom, 500 MHz, CD_3CN). The hydride resonance is marked with an asterisk.

UV-Vis spectroscopy has generally been quite useful in monitoring reactions of NADH and its analogues. LH is colorless and L^+ is yellow, but both **1** and **2** are bright yellow, and their spectra overlap extensively, as shown in Figure 4.11. This makes absorption spectroscopy less informative in determining the oxidation state of the ligand over the course of a reaction. The ^{31}P NMR shifts are also quite similar, at *ca.* 14 ppm for **1** and 15.6 for **2**. ^1H NMR spectroscopy is thus the most diagnostic spectroscopic technique for distinguishing the loaded and unloaded species. The major advantage of UV-Vis and ^{31}P techniques over ^1H NMR spectroscopy is that they do not require

deuterated solvents, allowing reaction progress to be monitored easily *in situ*. However, since **1** and **2** are not soluble in the same solvents, the products of loading and unloading reactions tend to precipitate from the reaction mixture. This complicates kinetic analysis and titration measurements, but it aids in the isolation of products. Our study of these reactions has thus focused less on the reaction dynamics and more on product analysis, for which ^{1}H NMR spectroscopy is well-suited.

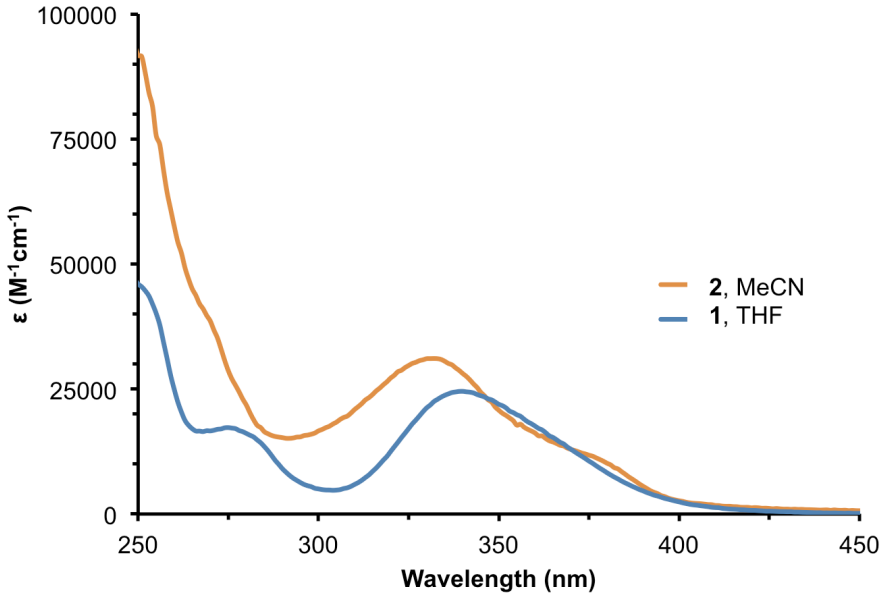

Figure 4.11 UV absorption spectra of **1** (THF, 41 μM, blue) and **2** (MeCN, 4.9 μM, orange).

*4.3.4 Hydride-Transfer and Small-Molecule Reactivity of **1** and **2***

1 and **2** can be readily interconverted by reaction with known hydride donors and acceptors. **1**, for instance, reacts with the acceptors 10-methylacridinium iodide and trityl tetrafluoroborate to generate **2**. The latter reaction proceeds smoothly in THF, causing precipitation of **2**; this precipitate is quite clean, as shown in Figure 4.12, overlaid with the spectrum of independently-prepared **2**. Also shown is the product left over from the remaining THF solution; this contains only the $HCPh_3$ byproduct and a slight amount of **2**

that did not precipitate.

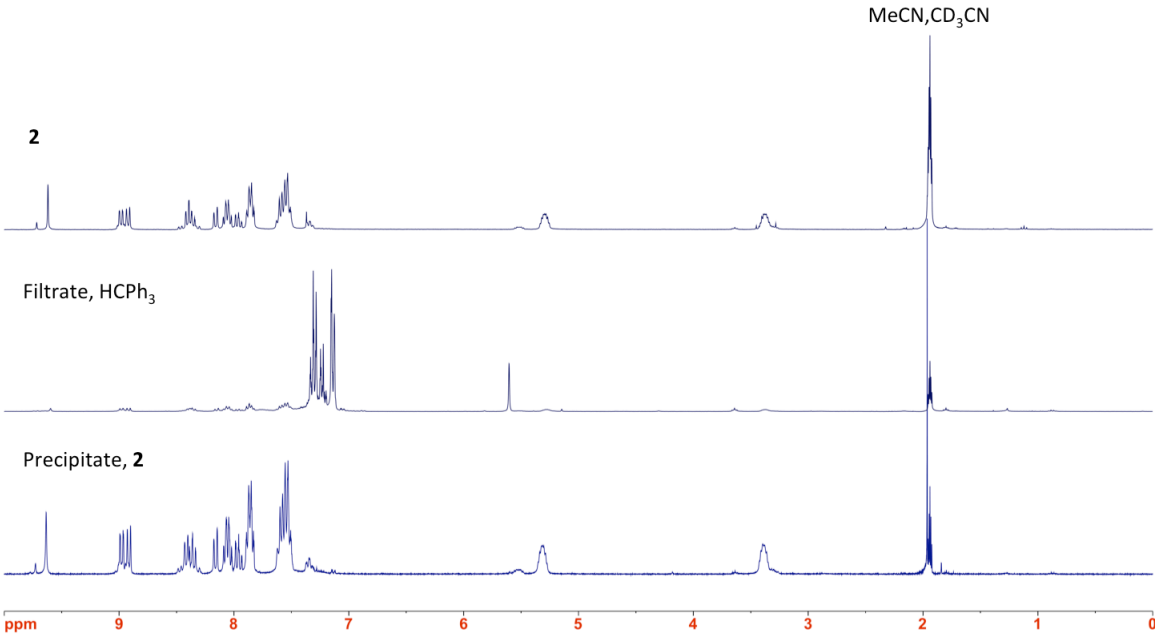

Figure 4.12 Overlay of ^{1}H NMR spectra (500 MHz, CD_3CN) for **2** (top) and products from reaction of **1** with CPh_3BF_4.

Use of 10-methylacridinium iodide as an acceptor proceeds similarly, but in that case the precipitate contains both **2•I$_2$** and 10-methyl-9,10-dihydroacridine. The acridine byproduct can be removed by washing with benzene, leaving **2•I$_2$**. The NMR spectra of **2** and **2•I$_2$** are essentially identical, indicating that the iodides remain outer-sphere anions. These reactions demonstrate that the hydride transfer reactions are not complicated by the presence of the metal. The transfer of hydrides from the ligands in these cases is not particularly groundbreaking, but it already represents progress beyond what was achieved with the earlier M[(^{Bn}NAH)$_3$tren]$^-$ system, which was stymied by demetallation processes competitive with the unloading reactions. It is not clear whether the metal plays a role in these reactions or if it is merely a spectator. It is obviously not necessary for the hydride transfer, since the same reactions proceed with the free ligand, but it is potentially of note

that these reactions appear to proceed much more quickly for **1** than for the free ligand. This is particularly apparent in the reaction with trityl cation, which is essentially complete after 45 minutes, compared to the free ligand, which is not fully unloaded even after two days.

Our attempts to extend the chemistry of **1** and **2** beyond these simple hydride transfers have thus far been limited to only a few substrates. **1** does not react with CO_2, or a mixture of CO_2 and H_2, even with extended heating or UV-wavelength irradiation. Nor does it react with the potential oxo-transfer reagents N_2O and pyridine-N-oxide, or the unsaturated C=O bond in benzaldehyde. This is not particularly surprising: these reactions are thermodynamically uphill in the absence of protons. Protonation of the reactants or intermediates might also lower the activation barrier to hydride transfer. Yet the solubility of **1** has limited the reaction conditions to the aprotic solvents benzene and THF. We have therefore attempted to promote these reactions by adding an acid source: in most studies, this was the conjugate acid of Hünig's base, $[HNEt^{i}Pr_2]Cl$, which was chosen because its weak acidity and steric hindrance should minimize potential side reactions. Gratifyingly, **1** and **2** are both stable to this acid source. This validates the original reasoning for selecting neutral phosphines as the donor set for this system. However, the addition of this acid does not promote the reaction of **1** with CO_2, CO_2/H_2 mixtures, N_2O, or benzaldehyde. One limitation of this system is that $[HNEtiPr_2]Cl$ is insoluble in benzene and only moderately soluble in THF, the two reaction solvents we have studied. This limits the amount of excess acid that could be used in these reactions. It is possible that larger excesses of acid would promote the protonation of substrates and

help drive the reactions. This might be achieved by using the more soluble triflate or $B^{Ar}F$ salts of the acids.

We were also interested in loading reactions that would generate **1** from **2**. The two hydrides in **1** could obviously be supplied by two hydride donors, or they could be formed from other combinations of two protons and four electrons. We were particularly interested in using H_2, with its two electrons and two protons, as a reductant. The additional two electrons could be supplied by an external reductant; alternatively, two equivalents of H_2 could be combined with two equivalents of base to generate **1** and two protonated bases. This latter reaction seemed particularly appealing, as these protons could potentially later be transferred from the base to substrates in an atom-economical process. However, the reaction of **2** with H_2 and Hünig's base resulted in only decomposition; this was found to result from reaction of the amine with **2** in the absence of H_2. Although we have not characterized this decomposition product, it is presumably due to attack by the amine at the electrophilic *ortho*-carbon of the phenanthridinium group. This position is known to be quite susceptible to nucleophiles, but it is disappointing to see its reaction even with the sterically hindered, weakly nucleophilic NEt^iPr_2. In our attempts to load hydrides onto **2** using H_2 and two equivalents of the reductant Cp_2Co, the reactions with the reductant occurred rapidly, before H_2 could be added. The reductions appear metal-centered rather than ligand-centered and appear to involve loss of Cp_2CoCl to generate a Pd(0) bis-phosphine complex. We have synthesized this complex and studied its reactivity with H_2, but this route is not the preferred method for its synthesis, as discussed in section 4.3.5.

We have only just begun exploring the redox chemistry of **1** and **2**. While they show little reactivity with the substrates we have targeted, there is a wealth of potential targets left to explore. The clean hydride transfer reactions with known acceptors are promising. However, thus far the reactivity of the palladium dichloride complexes does not seem to differ substantially from that of conventional organic hydride donors. The reactions with other hydride donors and acceptors appear to be somewhat faster than the reaction of the free ligand with the same substrates, but even if so, this would be a quantitative difference that would require more rigorous kinetic monitoring. Otherwise, there is little reason to believe that the metal is playing a role in the chemistry of these complexes.

4.3.5 Synthesis of Weakly-Coordinated Palladium Complexes

We imagined that one way to involve the metal in cooperative interactions with the ligand would be to open up coordination sites at palladium by using lower coordination numbers or more labile ligands. The coordinatively unsaturated metal should promote the binding and activation of substrates. Because the unloaded ligands already contain noncoordinating BF_4 anions, a simple method to lower the coordination number was to replace the chloride ligands in **1** and **2** with two more non-coordinating BF_4 ions. We therefore investigated the reaction of two phosphine ligands with $Pd(MeCN)_4(BF_4)_2$, to generate low-coordinate, bis-phosphine bis-acetonitrile complexes. $Pd(MeCN)_4(BF_4)_2$ reacts with two equivalents of $L^+BF_4^-$ to generate the bright yellow palladium bis-phosphine tetracation, $Pd(MeCN)_2(L^+)_2(BF_4)_4$, (**3**). The ^1H NMR spectrum

of **3** is quite similar to that of **2**, but its ^{31}P signal is shifted downfield, to 26.05 ppm.

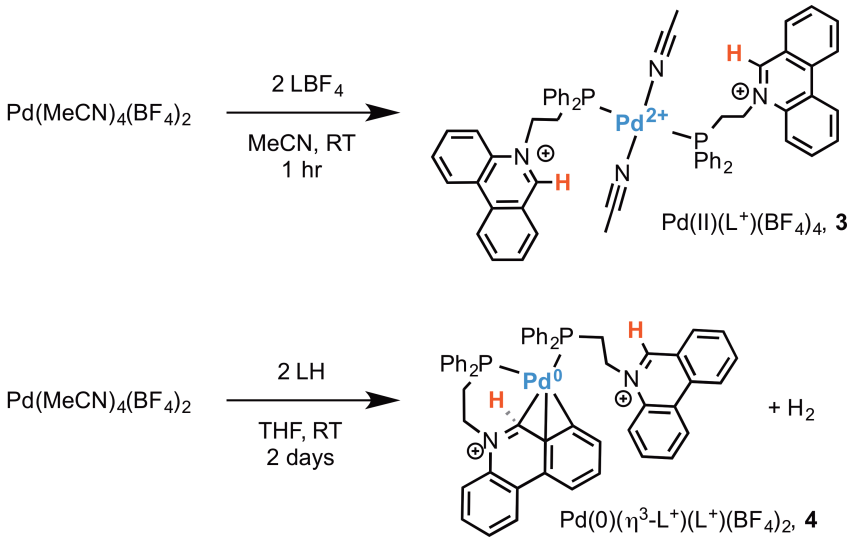

Figure 4.13 Synthesis of weakly-coordinated palladium compounds.

Interestingly, while the reaction to form **3** is clean and straightforward, the analogous reaction of $Pd(MeCN)_4(BF_4)_2$ with two equivalents of LH is not. The ligand and palladium reagents are not soluble in the same solvents, and the reaction outcome is different when run in THF or acetonitrile. In THF, the reaction mixture immediately turns bright orange, then red, and precipitates out a bright orange solid over the course of a few days. The remaining red filtrate shows a mixture of a large number of very broad, ill-defined peaks in the ^{1}H NMR spectrum, inconsistent with a single species. However, the THF-soluble fraction does not make up a large amount of the total product. The bulk of the product, isolated upon filtration and washing with copious THF, is an acetonitrile-soluble orange powder with an apparently clean, but somewhat unexpected, NMR spectrum (Figure 4.14).

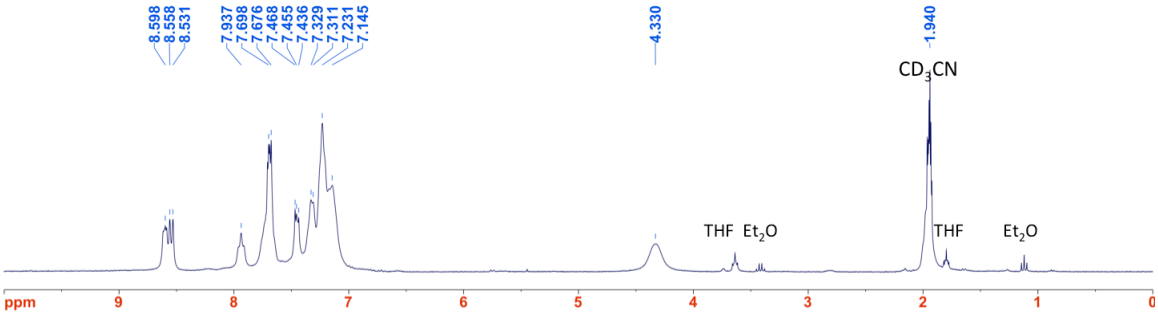

Figure 4.14 ^{1}H NMR spectrum of **4** (500 MHz, CD_3CN).

The ^{31}P spectrum shows a single peak, centered at 15.4 ppm, that is extremely broad and poorly resolved. The ^{1}H spectrum is slightly more informative; it is similarly broad but interpretable, as there is only one set of resonances for the ethyl backbone, suggesting a single, symmetric structure. The broadened peaks in the NMR spectra suggest that this species is likely a mixture of isomers equilibrating on the NMR timescale. Curiously, there is no peak that would obviously correspond to the hydride ligand. The aryl resonances are all downfield of 7 ppm, however, characteristic of unloaded, rather than loaded, ligands. Loss of two hydrides from the ligands would be an overall four-electron process. If, as we suspected, they were lost as H_2, then the remaining two electrons must have been transferred to some other unit, with the metal being the most likely recipient. This would make the product a Pd(0) compound with two unloaded ligands. Indeed, reduction of the unloaded Pd(II) compound **3** with two equivalents of Cp_2Co yielded the same species; likewise, the oxidation of this new species with two equivalents of Cp_2FeBF_4 gave **3** quite cleanly. These results strongly suggested its formulation as $Pd^0(L^+)_2(BF_4^-)_2$, **4**. However, given its unusual NMR spectrum, its structure was not clear; notably, despite being apparently clean by ^{1}H and

^{31}P NMR, ESI-MS analysis showed a number of species, most prominently the Pd(0) monophosphine. Thus, the structure of this compound was not known until X-ray quality crystals were grown from MeCN/Et_2O. The molecular structure determined from these crystals is shown in Figure 4.15.

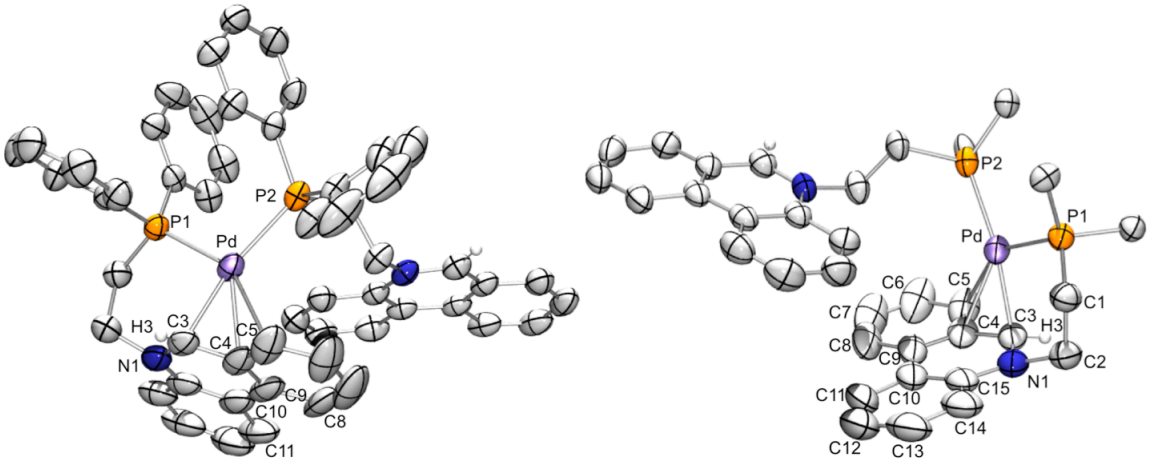

Figure 4.15 Two views of the solid state molecular structure of **4** at 50% probability level. BF_4 anions and hydrogen atoms, other than those placed from the Fourier difference map, have been omitted. For the view at right, phenyl groups have been omitted. Selected bond distances (Å) and angles (°): Pd-P1, 2.2966(7); Pd-P2, 2.3585(8); Pd-C3, 2.161(3); Pd-C4, 2.291(3); Pd-C5, 2.493(3); C3-C4, 1.438(5); N1-C3, 1.371(4); C3-H3, 0.91(3); P1-Pd-P2, 104.40(3); P1-Pd-C3, 87.32; P2-Pd-C5, 105.84; N1-C3-C4, 120.0(3); H3-C3-C4, 119(2); C8-C9-C10-C11, 3.8.

The actual molecular structure is asymmetric, with one phenanthridinium group dangling freely and the other coordinated in an unusual η^3 fashion to the Pd center through the *ortho*-carbon, C3, and its two neighboring carbons. There are two outer-sphere BF_4^- anions balancing the charge. The complex could thus be formulated as either $Pd^0(L^+)_2$ or $Pd^{II}(L^+)(L^-)$, with one noninnocent, formally two-electron-reduced ligand. Both phenanthridinium groups are planar, suggesting the former assignment is more valid, as two-electron reduction of the ring system would break its aromaticity. The planarity is indicated by torsion angle for the biphenylene backbone, C8-C9-C10-C11, is

3.8 for the phenanthridinium bound to Pd and 3.5 for the free phenanthridinium. The planarity of the ligands is also consistent with the phenanthridinium groups being unloaded, which was confirmed by placing the *ortho*-hydrogen atoms from the difference map. The C-H distance for the hydride bound to Pd, C3-H3 is 0.91(3) Å, contracted by nearly 0.1 Å compared to the hydridic C-H distances in **1**.

The coordination of the Lewis-acidic phenanthridinium to the palladium center helps to explain the thermal stability of **4,** which is unusual for a palladium(0) bis-phosphine compound without strongly-donating or bulky ligands. Most such 14-electron complexes are unstable with respect to loss of the phosphines and formation of palladium black.[23,24] The stability of **4** is obviously advantageous, but if the Pd-C bonds are not labile, this interaction would defeat the purpose of having moved to a low-coordinate palladium center. Fortunately, the simplicity of the NMR spectra suggests that the arms are equivalent on the NMR timescale and are presumably rapidly exchanging, implying that the Pd-C bonds are easily broken in solution. The breadth of the peaks in both the ^{1}H and ^{31}P NMR spectra indicates that this conversion is occurring on the NMR timescale. This is supported by variable-temperature (VT) NMR data: as the temperature is lowered, the already-broad peaks broaden even further. Unfortunately, the CD_3CN solvent does not allow cooling below 238 K. While the ^{1}H spectra broaden substantially at this temperature, they do not resolve into the spectra for their component species. The broadened peaks are actually even less structurally informative than the higher-temperature resonances. The ^{31}P VT spectrum is more informative and is shown in Figure 4.16. The broad peak observed at ~14 ppm at 298 K decoalesces into two peaks as the

temperature is lowered. The peaks do not fully resolve at 238 K, but they are clearly approaching values of ~19 and ~10 ppm.

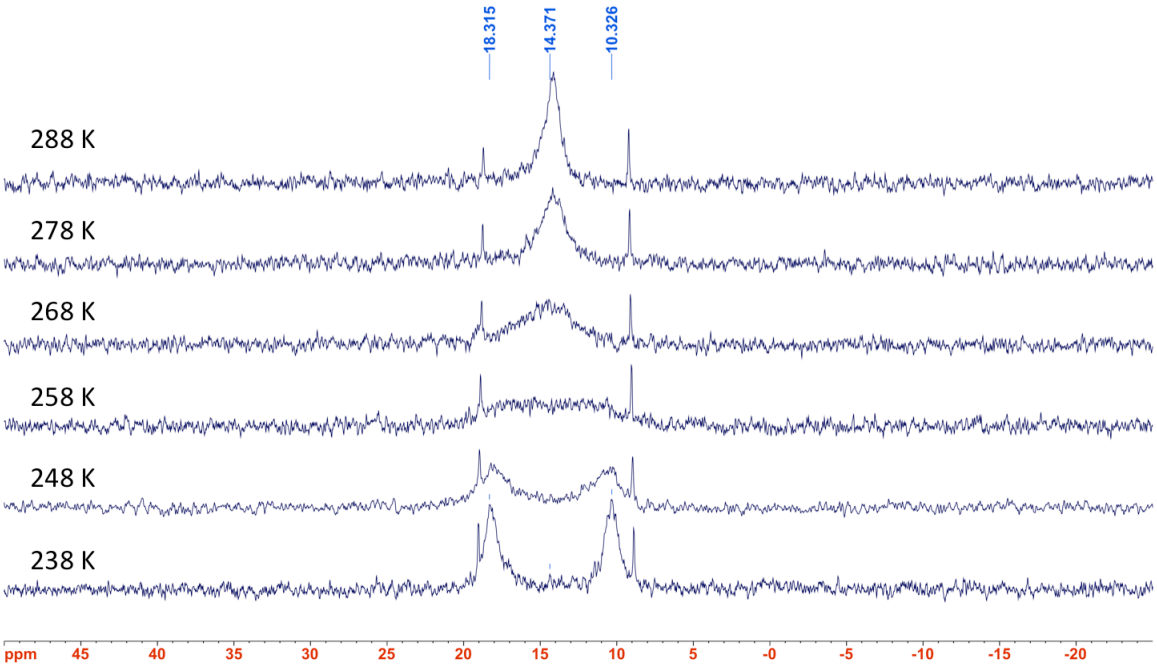

Figure 4.16 ^{1}H-decoupled ^{31}P VT-NMR spectrum of **4** (CD_3CN, 202 MHz).

The rate constant for two exchanging nuclei at their decoalescence temperature is approximated by Eqn. 4.2.[25]

$$k = \frac{\pi \Delta\nu}{\sqrt{2}} \qquad \text{Eqn 4.2}$$

Given the peak separation (Δν) of around 1600 Hz for **4**, the rate constant for exchange of the two phosphines is approximately 3.5×10^3 s^{-1} at the decoalescence temperature of ~260 K. Thus, the exchange is quite rapid, and the palladium is not strongly coordinated by the phenanthridinium. The observation of only two phosphorous signals at low temperature is consistent with the molecular structure observed in the

crystal. The downfield resonance around ~19 ppm is somewhat similar to the value of 26 ppm for the phosphines in **3** and is assigned to the dangling phosphine ligand. The more upfield resonance is therefore assigned to the cyclometallated phosphine and is consistent with greater electron density in this ligand due to back-donation from the electron-rich palladium. There is an impurity in this sample that has two doublets, with shifts of 18.7 and 9.22 ppm, very similar to the decoalesced resonances of **4**. These peaks appear prominent because they are much sharper than those of **4**; they are actually less than 5% of the sample by integration. Their similarity to the peaks of **4** and their much smaller linewidths suggest they are a non-fluctional compound that has a similar set of η^3 and dangling phenanthridinium groups. The possible identity of this species is discussed below.

The loss of H_2 from the ligands to form **4** must involve the metal in some role, presumably through the intermediacy of a metal-hydride. The ease with which the phenanthridinium can coordinate to the Pd center to create a six-membered palladacycle indicates that the organic hydrides of the reduced ligands should be accessible for direct reaction of the C-H bond with the metal. One plausible pathway for H_2 loss would therefore be sequential hydride transfer from both ligands to form a Pd-dihydride intermediate. This could then lose H_2 to form the Pd^0 in a conventional reductive elimination reaction. Another possible mechanism involves hydride transfer from only one ligand, followed by a heterolytic reaction between the metal-bound hydride and the remaining organic hydride. Since palladium hydrides can be quite acidic,[26] this would be essentially a deprotonation of the metal-bound hydride by the organic hydride, leaving

the two electrons on Pd. These alternatives are shown in Figure 4.17.

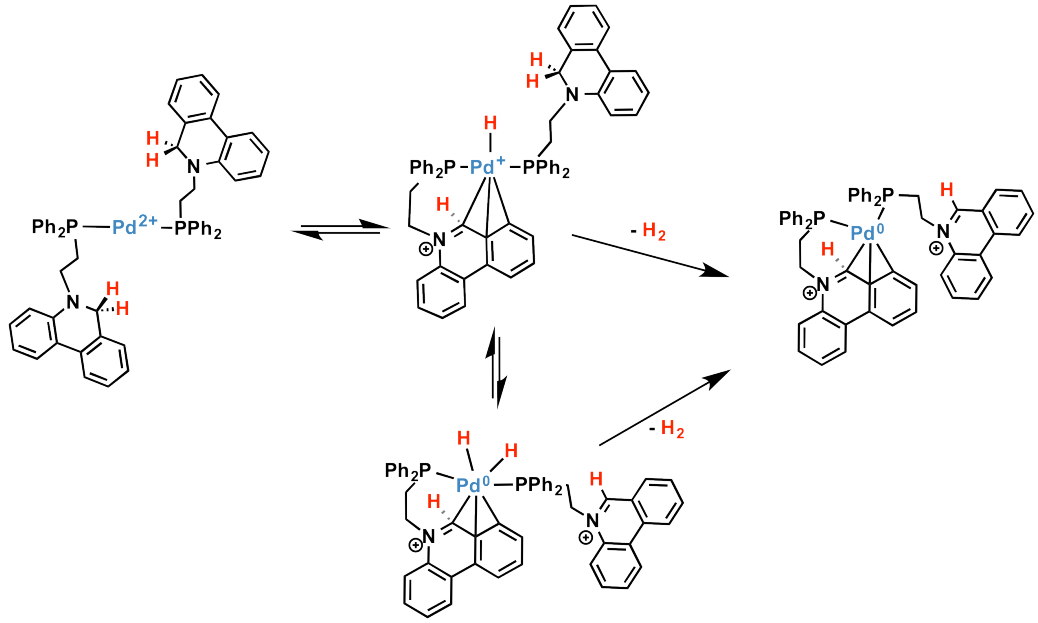

Figure 4.17. Two possible pathways for the formation of **4**.

Whichever pathway is operative, the loss of H_2 should occur through a metal-bound hydride, suggesting some interactions between the metal and ligand. By the principle of microscopic reversibility, the reverse reaction, addition of H_2 to load the ligands, should also occur *via* metal-ligand cooperativity. **4** does indeed react with an atmosphere of H_2, although the reaction is very slow, taking 7-10 days for full conversion. The ^{31}P NMR spectrum shows two species in a 3:2 ratio. The major species has a single peak at 19.2 ppm, while the minor species has two peaks: one at 8.9 ppm and another, with a shift of 18.3 ppm at room temperature and 19.2 at 238 K (Figure 4.18). This minor species appears to be the same one observed as an impurity in the VT-NMR sample of **4**.

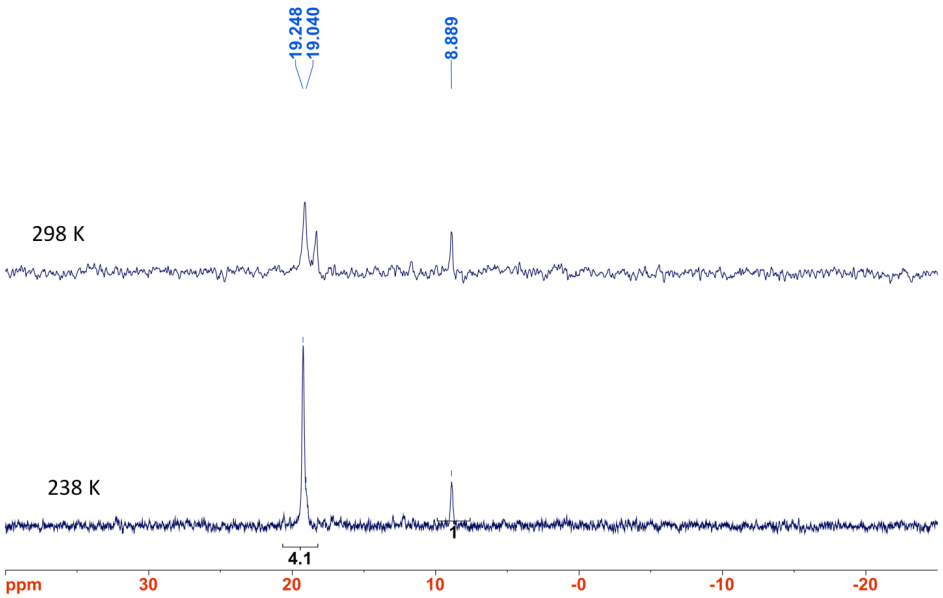

Figure 4.18 ^{31}P NMR spectra at room temperature (top) and 238 K (bottom) for the products of reaction of **4** with H_2.

Based on the assignments made for **4**, the ^{31}P spectrum indicates that the major species has two free phenanthridine groups while the minor species has one free and one bound η^3 to the palladium. This is supported by the proton spectrum of the product, which is interesting but difficult to interpret, due to the number of resonances. As with the spectrum of **4**, it is quite broad at room temperature. Cooling the sample to 238 K resolves the resonances somewhat; although there is still substantial overlap, there does appear to be a major and minor species, in a roughly 3:2 ratio. Most importantly, the major species has a symmetric spectrum, consistent with both phenanthridinium groups being loaded. The phenanthridine resonances in the major species are all upfield of 8 ppm, and the hydride resonance is clearly observed at 4.14 ppm. In addition to the hydride signal, there are the expected 10 resonances in the aryl region, for the phenanthridine and PPh_2 protons, and two signals for the ethyl linker. These data, as well

as the single downfield peak observed by ^{31}P NMR spectroscopy, are all consistent with a low-coordinate, structurally symmetric species with two loaded ligands uncoordinated to palladium, *i.e.* $Pd(LH)_2(BF_4)_2$. We denote this species **4**·H_2.

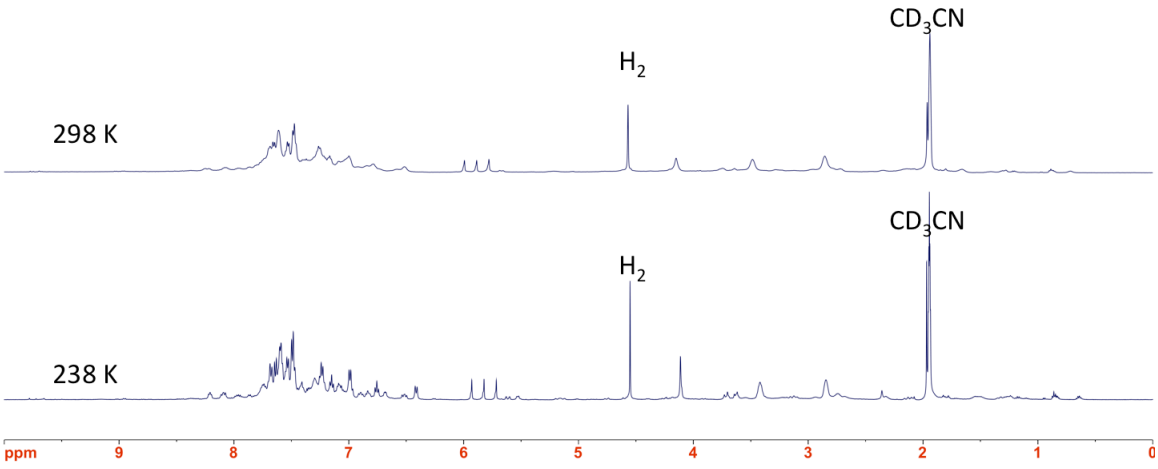

Figure 4.19 ^{1}H NMR spectra at room temperature (top) and 238 K (bottom) for the products of reaction of **4** with H_2.

Interpretation of the other peaks in the proton NMR spectrum is less straightforward. The simplest interpretation of the second pair of resonances in the ^{31}P spectrum is of a species with one free phenanthridine and one η^3-bound to the palladium, very likely the same species observed in the sample of **4** used for ^{31}P VT-NMR. The ^{1}H spectrum appears to support the interpretation of one of the ligands being cyclometalated, as there are several resonances corresponding to the ethyl linker, consistent with the asymmetric structure and associated diastereotopism. One possibility for the identity of this species, considering the proposed mechanisms for H_2 loss in the formation of **4**, is that it is a C-H activated palladium complex, *i.e.* $Pd(H)(LH)(\eta^3\text{-}L)^{2+}$. This species could be in equilibrium with the major species, **4**•$\mathbf{H_2}$, and an equilibrium on the NMR timescale might explain the broad resonances observed at room temperature for both species.

The spectrum of **4•H$_2$** would not otherwise be broadened at room temperature, as it is structurally symmetric and should not have a self-exchange interaction like that in **4**.

The presence of some peaks downfield of 8 ppm is characteristic of an unloaded phenanthridinium group, partially supporting this formulation. However, the most diagnostic signals for the unloaded phenanthridinium, the singlet at ~9.5 ppm and the two doublets around ~9.0 ppm, are absent in this spectrum. The former is the hydridic *ortho*-proton; the doublets correspond to its two nearest neighbors on the phenanthridine ring, based on assignment from the COSY spectrum of L^+ (4.26). These peaks do not change much in the spectra of **2** and **3** but are also notably absent in the spectrum of **4**, suggesting that they may simply be shifted upfield due to coordination to Pd. When the sweep width of the ^{1}H spectra is increased, a signal can be observed far upfield, at -14 ppm, supporting the assignment of this second species as a palladium-hydride. The signal is very broad at 298 K but resolves into a triplet at 238 K (Figure 4.20), consistent with equivalent coupling to the two phosphine ligands; the coupling constant at 238 K is small, $J_{H,P}$ = 8.0 Hz, suggesting a *cis*-orientation with respect to both phosphines. This would be consistent with either a hydride or *trans*-dihydride. The signal integrates to 1 H with respect to the minor species in the spectrum, suggesting a mono-hydride. In addition, the shift of -14 ppm is consistent with other mono-hydride complexes of palladium, rather than a dihydride or polynuclear bridging hydride, both of which tend to have more upfield shifts.[26] Thus, we tentatively assign the second species in the spectrum to the C-H activated palladium mono-hydride, $Pd(H)(LH)(\eta^3\text{-}L)^{2+}$, which is isomeric with **4•H$_2$** and is therefore denoted **4•H$_2$'**.

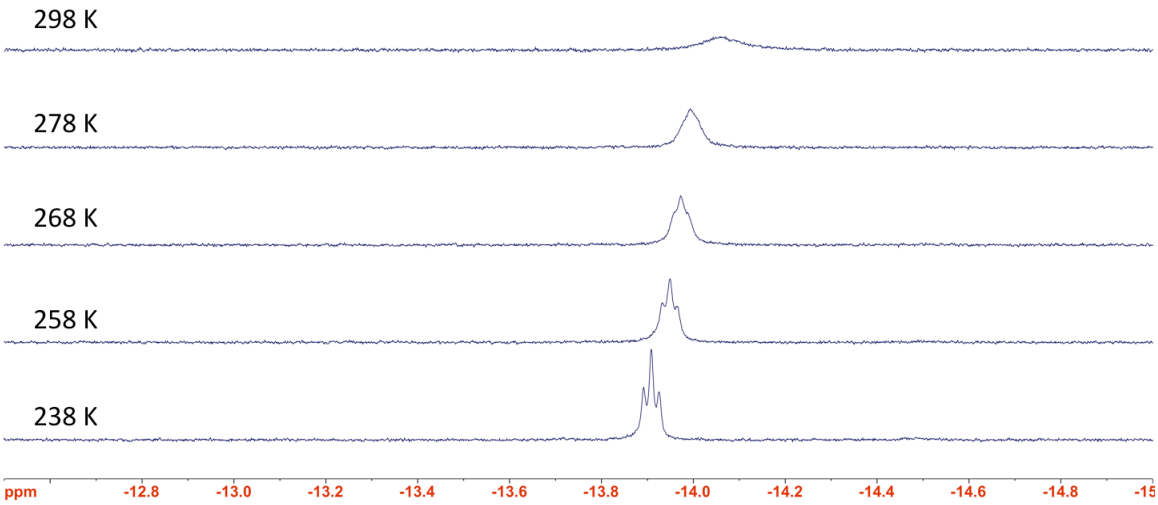

Figure 4.20 Temperature Dependence of the Palladium-Hydride Signal Observed in the ^{1}H NMR Spectrum (500 MHz, CD_3CN) of the Reaction of **4** with H_2.

The data thus suggest, very preliminarily, the possibility that **4** reacts directly with H_2 to load a hydride equivalent onto each ligand. Moreover, there is some evidence for interconversion between this species and a C-H activated isomer. These species are the only two observed by ^{31}P NMR, and after approximately one week, their appearance and integration do not change noticeably, suggesting that they have reached equilibrium. Low-coordinate palladium hydride and dihydride complexes are rarely observed or isolated from reactions of Pd(0) complexes with H_2.[24] This is not for lack of interest; these reactions are quite relevant to heterogeneous hydrogenation on palladium surfaces, and as a result, they have been extensively studied in frozen matrices.[27-29] Rather, low-coordinate, mononuclear phosphine and related complexes of palladium simply tend to be both unreactive towards direct activation of H_2[24,30,31] and tend to decompose under hydrogenation conditions unless the ligands are very donating or bulky.[24,32,33] More often, palladium hydrides are generated from Pd(0) through addition of acids or oxidative

addition of other X-H bonds, generating more stable $L_2Pd(H)(X)$ compounds (X = C, N, O, S).[26] Notably, active Pd(0)-based hydrogenation catalysts have recently been developed, but these appear to appear to operate in cooperation with substrates pre-coordinated to the Pd center, *via* heterolytic activation of H_2.[34,35] In the conversion of **4** to **4•H₂** and **4•H₂'**, the initial coordination of the redox-active phenanthridinium may play a similar role in promoting heterolytic activation of H_2. In addition, as no palladium black is formed and only two products are observed by ^{31}P NMR despite the very long reaction time, the products appear to be thermally stable. The coordination of the phenanthridinium group to the palladium center in the **4•H₂'** isomer may play a key role in stabilizing the low-coordinate products. However, these conclusions are only very provisional, and significantly more detailed characterizations of both proposed products must be performed before they can be made with confidence.

One practical limitation in the formation of **4•H₂** and **4•H₂'** *via* this method is the very long reaction time and small scales on which **4•H₂** and **4•H₂'** are prepared. Thus far, these additions have been run only on NMR scales in deuterated solvents. Larger-scale additions of H_2 are possible, of course, and would allow higher pressures of H_2, which might speed the reaction, but these have not yet been attempted. Interestingly, another route to **4•H₂'** appears to be the simple reaction of two equivalents of LH with $Pd(MeCN)_4(BF_4)_2$ in acetonitrile or acetone. This is the same reaction that, when run in THF, gives **4** as an orange precipitate; in these more polar solvents, however, the crude reaction product shows a variable mixture of **4** and **4•H₂'** by ^{1}H and ^{31}P NMR spectroscopy. Very little **4•H₂** is seen in these reaction products, suggesting that the

equilibrium constant for its formation is small and requires added H_2 to produce it in appreciable quantity. In fact, the observation of **4** and **4•H₂'** together in solution suggests that all three species are in equilibrium: in polar solvents and without added H_2, **4** and **4•H₂'** appear to predominate. In less polar THF, however, **4** is insoluble and some combination of its precipitation from THF and loss of H_2 drives the equilibrium towards **4**. Finally, under an atmosphere of H_2, **4•H₂** becomes the major species.

Of course, it must be reiterated that the characterization of these species has thus far been wholly inadequate to make strong conclusions. In particular, the ill-defined spectra of **4•H₂** and **4•H₂'** raise the questions of product purity and decomposition reactions. We have not been able to isolate or crystallographically characterize either **4•H₂** or **4•H₂'**. All attempts to crystallize these compounds have thus far given only crystals of **4**. As an indirect means to test the formulation of **4•H₂'** as containing loaded hydride donors, we have investigated its reaction with various substrates. Surprisingly, this has shown **4•H₂/4•H₂'** to be an extremely versatile platform, capable of cleanly forming several previously-characterized species. More specifically, starting from unpurified **4•H₂'** and various reagents, we have been able to prepare **1**, **2**, **3**, and **4**. The routes to these species are shown in Figure 4.21. It has already been mentioned that **4** forms readily from **4•H₂'** upon simple precipitation from THF; it can also be prepared very cleanly through crystallization from acetonitrile/Et_2O mixtures. More significantly, **4•H₂'** can be cleanly unloaded in reactions with hydride acceptors, forming the unloaded complexes **2** and **3**. When CPh_3BF_4 is used, the non-coordinating BF_4 anions leave the product as low-coordinate complex **3**. When 1-methylacridinium iodide is used, the

iodide anions apparently coordinate to Pd, forming the diiodide complex, **2•I$_2$**. No leftover **4** is observed in the products, as shown in Figure 4.22. Interestingly, in reactions with the acid source [HNEtiPr$_2$]Cl, **4•H$_2$'** simply abstracts the chloride anions, precipitating out as the loaded dichloride complex **1** and leaving the acid, [HNEt^{i}Pr$_2$]BF$_4$, in solution.

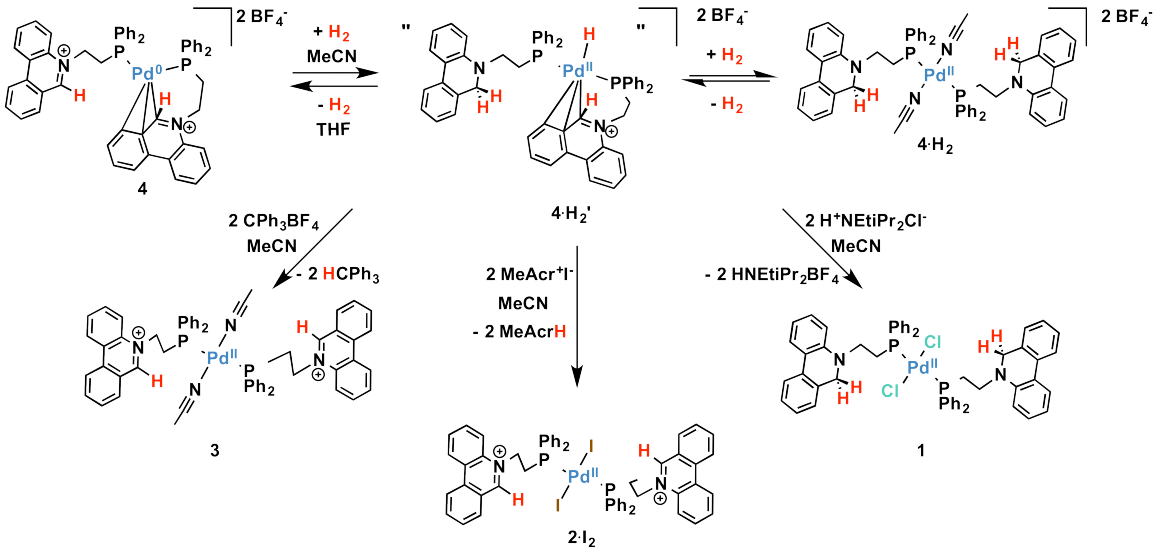

Figure 4.21 Routes to well-defined palladium species **1**, **2**, **3**, and **4** from **4•H$_2$'**.

The ^{1}H spectra of the products, as isolated, are shown in Figure 4.22. All of these products are quite clean. This appears to validate, at least, the formulation of **4•H$_2$/4•H$_2$'** as a reduced palladium bis-phosphine system that does not appear to undergo decomposition or irreversible side-reactions. While this does not provide insight into the actual structure of the complex(es), it suggests that whatever fluxional and dynamic interconversions are occurring in solution, they are all reversible processes. Thus, despite the poorly characterized nature of **4•H$_2$** and **4•H$_2$'**, they react to form well-characterized products. It is particularly notable that, whereas **4** starts out as a palladium(0) species with two oxidized ligands, after reaction with H$_2$, it can be trapped as **1**, in which the

palladium is clearly in the (2+) oxidation state and the ligands are loaded. This clearly demonstrates cooperativity between the ligands and the metal, as H_2 and two electrons from the metal are converted into two hydrides on the ligand, an overall four-electron process. The hydride-donating capability of the ligands is also retained in this system, as demonstrated by the transfer to acridinium and trityl cation.

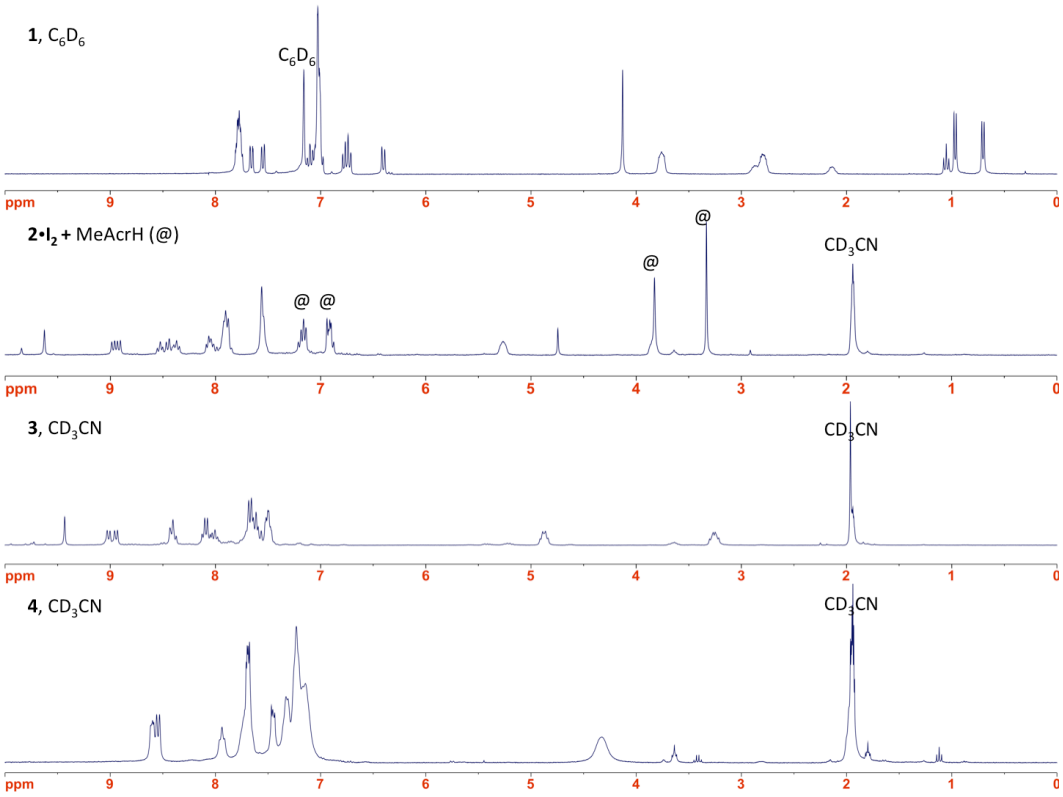

Figure 4.22 Products from reactions of **4•H$_2$'**. See text and Figure 4.21 for reactions. For reaction forming **2•I$_2$**, the byproduct 9,10-dihydro-10-methylacridinium was not removed; the peaks for this byproduct are labeled with "@" symbols.

4.4 Conclusions and Future Work

A new ligand system has been developed that ties a phenanthridinium moiety to a neutral phosphine donor. This provides a bifunctional platform that positions an organic hydride donor of moderate strength within the secondary coordination sphere of a metal center. The ligand can be synthesized simply, cleanly, and in good yield in both loaded and unloaded forms, and these are easily interconverted through reaction with known hydride donors and acceptors. The coordination chemistry of these ligands has been explored using palladium. The palladium dichloride compounds are stable to the weak acid $[HEt^{i}Pr_2]Cl$ and can mediate clean hydride transfer to known acceptors. This addresses an issue found with earlier designs that used anionic donor sets. Thus far, however, the observed reactivity of these palladium dichloride bis-phosphine complexes has not been extended beyond these simple hydride transfers. The known chemistry of hydride transfer reactions is extensive, and there are reactions with numerous substrates that could be explored. However, the role of the palladium center in mediating these reactions is unclear. Qualitative observations suggest that the rates of the hydride transfer reactions are faster for the metal complexes than the free ligand, but this remains to be measured quantitatively. Moreover, we have yet to find a practical source of hydrides for this system; the palladium complexes are currently loaded by reactions with other hydride sources, borohydrides and BNAH, that would themselves react with the substrates we have studied.

In an attempt to encourage metal-ligand cooperativity and facilitate substrate activation, low-coordinate palladium bis-phosphine complexes have also been

synthesized. A stable palladium(0) compound with two unloaded ligands has been structurally characterized, revealing an unusual asymmetric geometry. In this structure, one ligand coordinates in an η^3-fashion to Pd, through the hydride-bearing *ortho*-carbon, suggesting that close interactions between the ligand and metal can occur within these low-coordinate systems. The dynamic NMR behavior observed for the ligand resonances indicates that these interactions are weak and exchange rapidly in solution. The Pd(0) compound forms from reaction of a palladium(II) precursor with two loaded ligands; this reaction presumably involves loss of H_2 *via* C-H activation of one or both of the ligands, as the oxidation of the ligands is coupled to reduction of the metal center. The reverse reaction has also been demonstrated: the Pd(0) compound reacts with H_2 to form a Pd(II) compound with reduced ligands. This suggests an intriguing interconversion between metal-bound and ligand-bound hydrides. We have begun to characterize the dynamics of this process, but the reactions and data remain quite preliminary. Some of the best evidence for the interconversion remains indirect, in that the reduced species can be converted to other, better-characterized species, through hydride transfer or halide abstraction. These transformations are all quite clean, indicating that, whatever the dynamics of H_2 activation and intramolecular hydride transfer, the products do not irreversible decompose, and the species remain competent for intermolecular hydride transfer. Characterization of the species formed in this process and their interconversion is currently underway. These studies should provide valuable insight into the chemistry of palladium hydrides and the reaction of H_2 at Pd(0). This is a subject of great relevance to heterogeneous catalysis but one for which experimental data are currently limited.

The apparently facile interconversion between the hydride-containing species **4•H_2/4•H_2'** and the Pd(0) species **4** suggests a shallow potential energy surface for H_2 uptake and release that may be useful in catalysis. We have begun to explore the hydrogenation chemistry of these species. The stoichiometric reactions of **4•H_2'** with a number of potential substrates is not encouraging. However, the *catalytic* reaction of **4** (5-10 mol %) with diphenylacetylene under an atmosphere of H_2 is promising; product analysis by GC-MS indicates nearly quantitative conversion to the *cis*- and *trans*-alkene product isomers and negligible over-reduction to the alkane. However, given the complexity of the system and the preliminary nature of the data, this reaction requires much more study before any firm statements can be made regarding these early results.

Overall, these results represent a promising start to the development of bifunctional catalysts based on simple, modular ligands containing organic hydride donors. There is much work left to be done in the near future, particularly in the screening of substrates for reactivity and in the characterization of the Pd species involved in these reactions. This characterization should help direct the further development of this system, ideally allowing the extension of this chemistry to the activation of more difficult small-molecule substrates and the development of analogues using other metals. Necessary changes might include variation of the organic hydride donor or the substituents on phosphorous. The modularity of this ligand design should allow such alterations to be made quite easily. The versatile coordination chemistry of the neutral phosphine donors should also aid in the extension to other metals. Low-coordinate palladium species in general tend to be unstable, and reduced palladium

hydrides in particular are notoriously difficult intermediates to characterize. Other noble metals, especially ruthenium and rhodium, appear far more amenable to this type of chemistry and could be explored. Alternatively, the extension of this chemistry to first-row metal systems would be quite interesting.

4.5 Experimental Procedures

4.5.1 General Considerations

Unless otherwise stated, all operations were performed in a VAC Atmosphere double-dry box under an atmosphere of purified nitrogen or using high vacuum standard Schlenk techniques under a nitrogen atmosphere. Anhydrous *n*-Hexane, pentane, toluene, tetrahydrofuran, diethyl ether, acetonitrile and benzene were purchased from Aldrich and dried on an SG Waters solvent purification system. C_6D_6, CD_3CN, and d_8-THF were purchased from Cambridge Isotope Laboratory, degassed and stored over 4 Å molecular sieves. Celite, alumina, and 4 Å molecular sieves were activated under vacuum for four days at 350ºC. All other chemical were used as received. ^{1}H NMR spectra were recorded on Varian VI-300 300 MHz or VI-500 NMR spectrometers. ^{31}P NMR spectra were recorded on Varian VI-300 or VXR-300 300 MHz NMR spectrometers. Variable-temperature ^{1}H and ^{31}P NMR spectra were recorded on a Bruker AV-500 500 MHz spectrometer. ^{1}H NMR resonances were referenced to residual solvent peaks. ^{31}P NMR resonances were referenced to external samples of 85% H_3PO_4. Elemental analyses were performed by Complete Analysis Laboratories, Inc. (Parsippany, NJ). UV-Visible wavelength absorption spectra were collected on a Cary 300 Bio UV-Visible

spectrophotometer.

4.5.2 Synthetic Procedures

Synthesis of 5-(2-Bromoethyl)-phenanthridinium bromide (BrEtPhenBr)

The synthesis of this compound was performed according to the procedure reported by Parenty *et al.*[17] The product (5 g, 95%) was recovered as a beige powder after washing with ethyl acetate. ^{1}H NMR (D_2O, 500 MHz): δ 9.83 (s, 1H), 8.66 (d, 1H, J = 8.2 Hz), 8.57 (d, 1H, J =8.4 Hz), 8.38 (d, 1H, J = 8.0 Hz), 8.29 (d, 1H, J = 8.7 Hz), 8.18 (t, 1H, J = 8.0 Hz), 8.00 (t, 1H, J = 8.0 Hz), 7.92 (m, 2H), 5.400 (t, 2H, J = 5.7 Hz), 4.09 (t, 2H, J = 5.7 Hz).

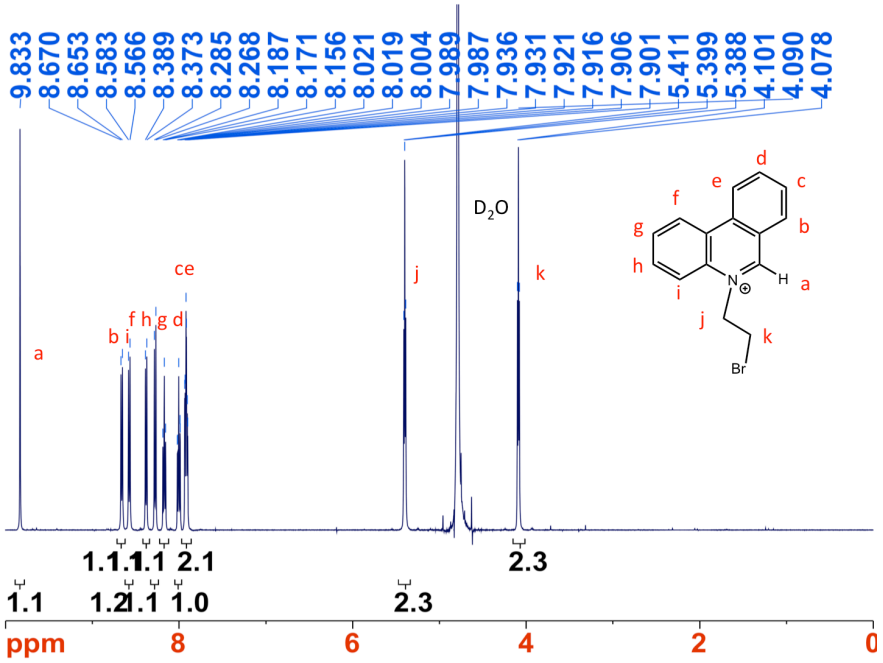

Figure 4.23 ^{1}H NMR Spectrum (D_2O, 500 MHz) of BrEtPhenBr

Synthesis of 5-(2-Bromoethyl)-5,6-dihydrophenanthridine (BrEtPhenH)

The synthesis of this compound was adapted from a procedure reported by Kreevoy *et*

al.[15] A round bottom flask was charged with 200 mL of 2:1 methanol:H_2O that had been thoroughly sparged with dinitrogen, into which was dissolved BrEtPhenBr (3.93 g, 10.7 mmol). The dull yellow solution was cooled to 0 °C, and sodium borohydride (512 mg, 13.5 mmol) was slowly syringed in as a solution in degassed H_2O. The reaction solution immediately bubbled vigorously, turned pink, and gave a copious white precipitate. This mixture was allowed to stir for one hour, then stirring was stopped and H_2O (200mL) was added *via* cannula to aid in crystallization. The mixture was left to crystallize for one hour. The supernatant was then removed *via* cannula and methanol was added, heated to 40 °C, then filtered and washed with copious degassed water. The white solid was collected; the filtrate was set to crystallize and was filtered after one week. The two crops were combined and dried, giving 2.77 g total 5-bromoethyl dihydrophenanthridine as a beige, fibrous solid (90%). ^{1}H NMR ($CDCl_3$, 500 MHz): δ 7.76 (d, 1H, J = 7.6 Hz), 7.71 (d, 1H, J = 7.6 Hz), 7.34 (t, 1H, J = 7.6 Hz), 7.25 (m, 2H), 7.13 (d, 1H, J = 7.6 Hz), 6.89 (t, 1H, J = 7.6 Hz), 6.76 (d, 1H, J = 8.0 Hz), 4.40 (s, 2H), 3.77 (t, 2H, J = 7.4 Hz), 3.57 (t, 2H, J = 7.4 Hz).

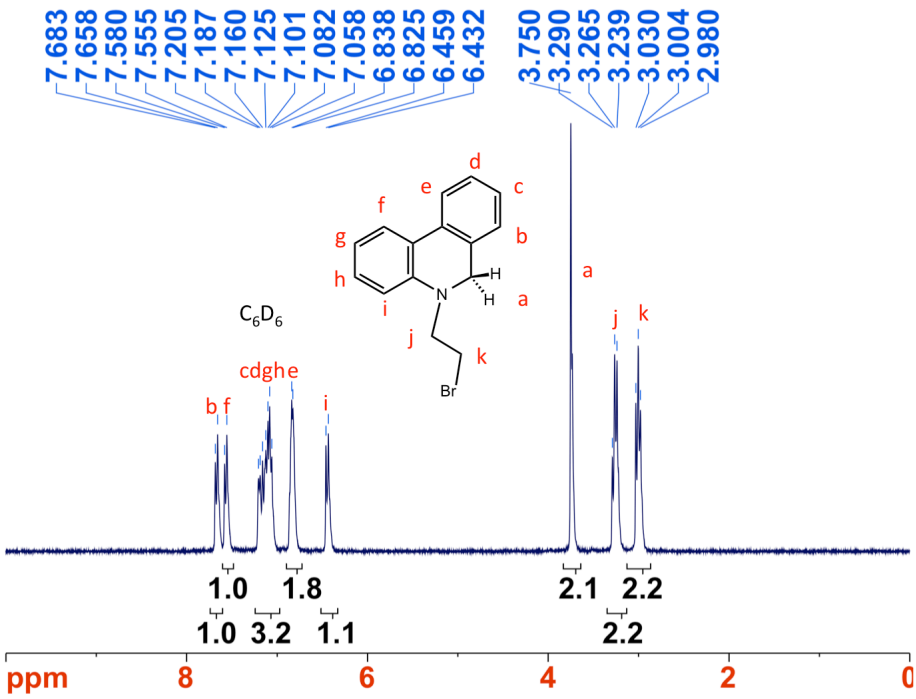

Figure 4.24 ^{1}H NMR Spectrum (C_6D_6, 500 MHz) of BrEtPhenH

Synthesis of 5-(2-Diphenylphosphinoethyl)-5,6-dihydrophenanthridine (LH)

A round bottom flask was charged with 1.86 g (6.44 mmol) of BrEtPhenH and 100 mL THF and cooled to -78 °C. A solution of potassium diphenylphosphide (13.0 mL, 0.5 M, 6.5 mmol) was syringed in dropwise, causing the solution to turn bright yellow, then orange. The reaction mixture was left to slowly warm to rt over 12 hours, after which time the mixture was slightly cloudy. It was filtered through a pad of celite, then dried under vacuum. The resulting orange residue was rinsed with methanol (20 mL), causing it to turn colorless. The solid was then filtered and washed with acetonitrile (30 mL), then dried, giving LH as a flaky white powder (2.34 g, 92%). ^{1}H NMR (C_6D_6, 500 MHz): δ 7.67 (d, 2H, J = 7.6 Hz), 7.57 (d, 2H, J = 7.6 Hz), 7.40 (m, 8H), 7.15 (t, 2H, J = 8.0 Hz), 7.07 (m, 16H), 6.8 (m, 4H), 6.42 (d, 1H, J = 8.0 Hz), 4.40 (s, 2H), 3.77 (dd, 4H, J =

8.0 Hz, J = 5.0 Hz), 2.21 (t, 4H, J = 8.0 Hz). $^{31}P(^{1}H)$ NMR (C_6D_6, 121 MHz): δ -21.40.

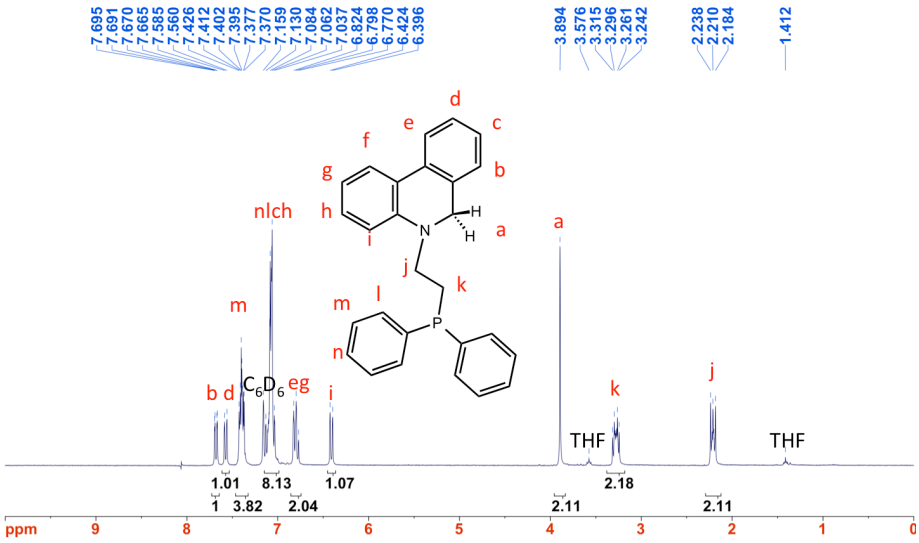

Figure 4.25 ^{1}H NMR Spectrum (C_6D_6, 500 MHz) of LH

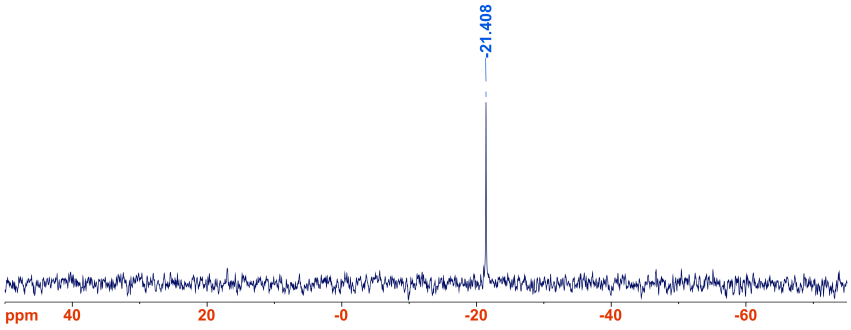

Figure 4.26 ^{31}P NMR Spectrum (C_6D_6, 121 MHz) of LH

Synthesis of 5-(2-Diphenylphosphinoethyl)-phenanthridinium tetrafluoroborate (LBF_4)

A round bottom flask was charged with 1 g (2.54 mmol) of LH and 75 mL THF at room temperature. Triphenylcarbenium tetrafluoroborate was added to the flask, causing the solution to turn a peach color within 5 minutes and cloudy within 15 minutes. The cloudy mixture was stirred for one week. During that time, any precipitate that formed was recovered by filtration. After each filtration, the precipitate was washed with copious THF and the filtrate was returned to stirring. The precipitates were combined and dried to

give 0.85g (70%) of $L^{+}BF4^{-}$ as a white solid. ^{1}H NMR (500 MHz, CD_3CN, δ, ppm from TMS): 9.656 (s, 1H), 8.54 (m, 1H) 8.805 (d, 1H, J = 8.5 Hz) 8.420 (d, 1H, J = 8 Hz), 8.334 (dt, 1H, J = 8.5 Hz, J = 1 Hz), 8.227 (m,), 8.040 (m, 3H), 7.272 (t, 4H, J = 7 Hz), 7.211 (t, 2H, J = 7.5 Hz), 7.149 (t, 4H, J = 7.5 Hz), 5.221 (dd, 2H, J = 7.3 Hz, J = 10 Hz), 2.991 (t, 2H, J = 7.3 Hz). ^{31}P NMR: (121 MHz, CD_3CN): -19.233 ppm.

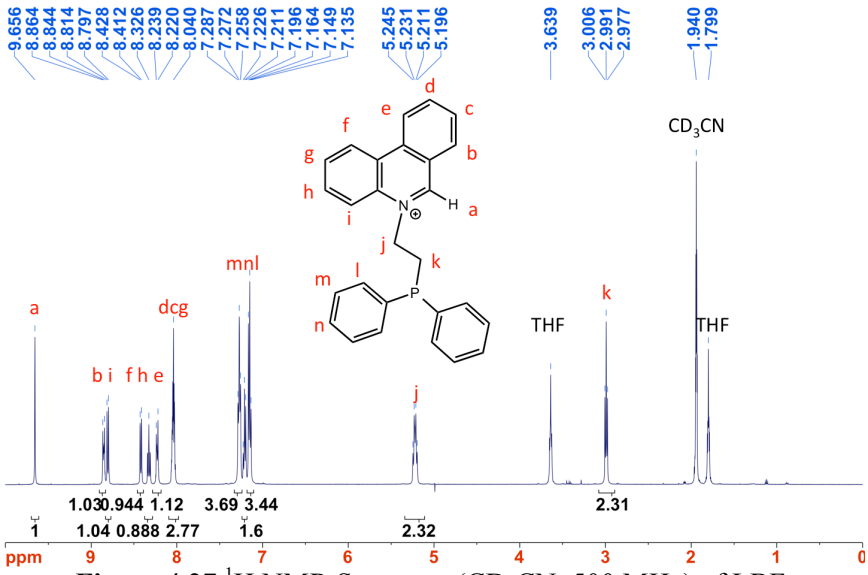

Figure 4.27 ^{1}H NMR Spectrum (CD_3CN, 500 MHz) of LBF_4

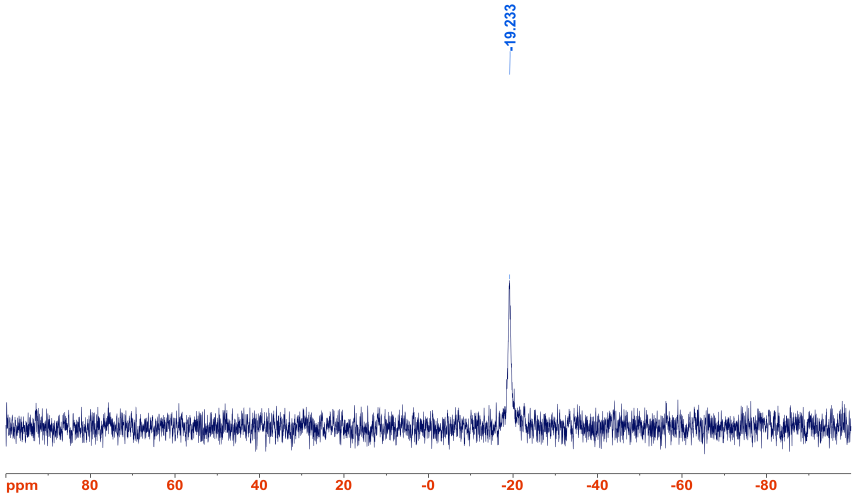

Figure 4.28 ^{31}P NMR Spectrum (CD_3CN, 121 MHz) of LBF_4

*Synthesis of $PdCl_2(LH)_2$, **1***

To a solution of LH (99 mg, 0.25 mmol) in THF (5 mL) was added $PdCl_2(MeCN)_2$ (32.6 mg, 12.6 mmol), causing the solution to turn light yellow-orange. The solution was diluted to 20 mL and stirred for 12 hours, then dried under vacuum. The resulting yellow solid was taken back up in THF (5 mL) to remove a black solid, then layered with pentane and set at -35 °C to crystallize for one week. The resulting crystalline precipitate was collected to give a **1** as a light yellow solid. Yield: 110 mg (90.5%). ^{1}H NMR (500 MHz, THF-d_8, δ, ppm from TMS): 7.89 (dd, 4 H, *J* = 6.8 Hz *J* = 5.4 Hz), 7.64 (d, 2 H, *J* = 7.8 Hz) 7.5 (t, 2H, *J* = 7.8 Hz) 7.43 (t, 4 H, *J* = 7.8 Hz), 7.22 (t, 2H, *J* = 7.4 Hz), 7.12 (t, 2 H, *J* = 7.4 Hz), 7.05 (d, 2H, *J* = 7 Hz), 6.91 (t, 2H, J = 8.4 Hz), 6.65 (t, 2H, J = 7 Hz), 6.29 (d, 2H, *J* = 8.1 Hz), 4.234 (s, 4H), 3.69 (m, 4H), 2.87 (m, 4H). ^{31}P NMR: (121 MHz, THF-d_8): 13.90 ppm. UV-Vis (THF, 0.041 mM): λ_{max}, nm (ε, $M^{-1}cm^{-1}$) = 248 (90,000), 270 (sh, 38,000), 332 (35,000), 380 (sh, 10,000). Calcd for $C_{54}H_{48}Cl_2N_2P_2Pd$: C, 67.26; H, 5.02; N, 2.91. Found: C, 67.23; H, 5.11; N, 2.90.

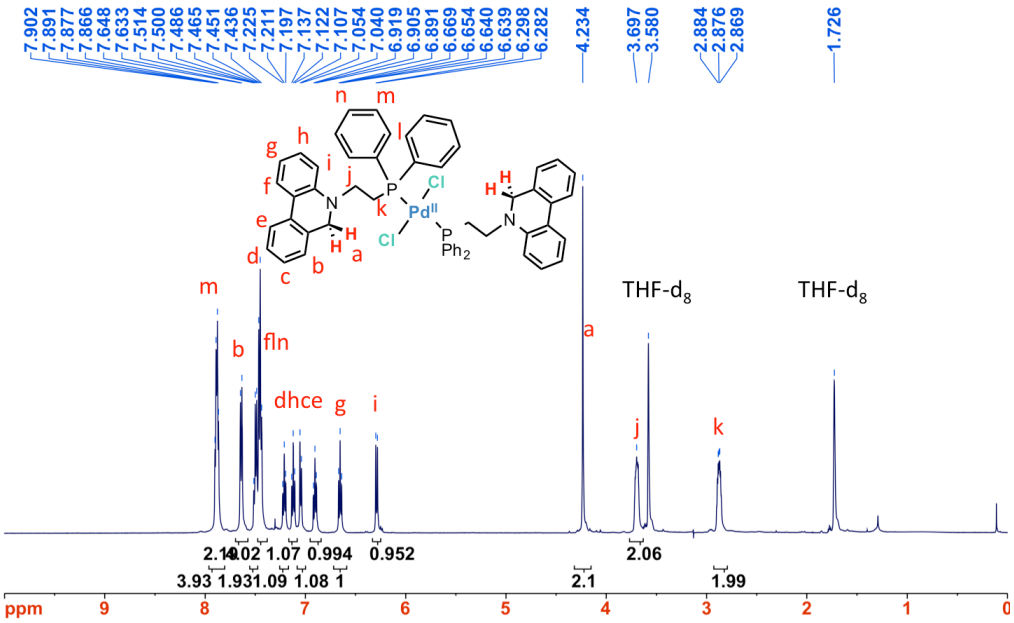

Figure 4.29 ^{1}H NMR Spectrum (THF-d_8, 500 MHz) of **1.**

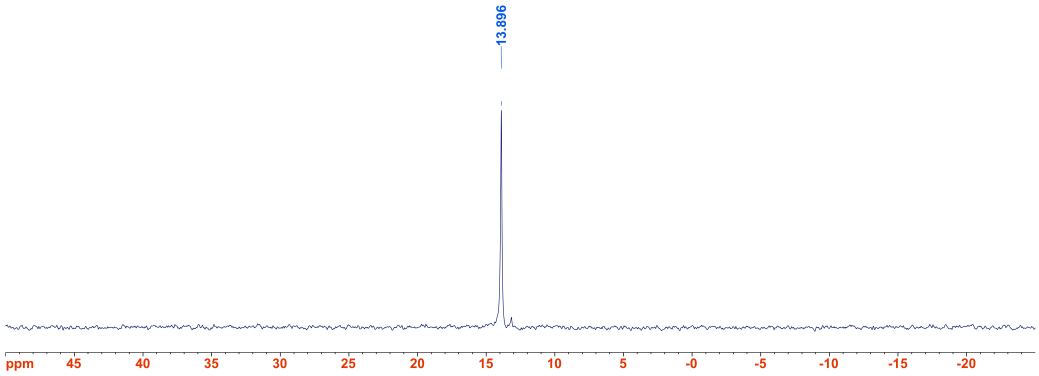

Figure 4.30 ^{31}P NMR Spectrum (THF-d_8, 121 MHz) of **1.**

*Synthesis of $PdCl_2(LBF_4)_2$, **2***

To a solution of LBF_4 (37.8 mg, 0.079 mmol) in MeCN (5 mL) was added $PdCl_2(MeCN)_2$, causing the solution to turn from dull to bright yellow. The solution was stirred for four hours, then dried under vacuum to give **2** as a goldenrod-colored solid. Yield: 41.3 mg (45%). ^{1}H NMR (500 MHz, CD_3CN, δ, ppm from TMS): 9.62 (s, 2 H),

8.99 (d, 2 H, J = 7.8 Hz) 8.92 (d, 2H, J = 7.8 Hz) 8.39 (m, 4 H), 8.16 (d, 2H, J = 7.4 Hz), 8.06 (m, 4 H), 7.86 (dd, 8H, J = 7 Hz, J = 6.5), 7.53 (m, 12H), 7.34 (t, 2H, J = 7 Hz), 5.30 (m, 4H), 3.78 (m, 4H), 3.69 (m, 4H). ^{31}P NMR: (121 MHz, CD_3CN): 15.64 ppm. UV-Vis (MeCN, 4.9 μM): λ_{max}, nm (ε, $M^{-1}cm^{-1}$) = 245 (52,000), 255 (sh, 52,000), 274 (19,000), 340 (27,000).

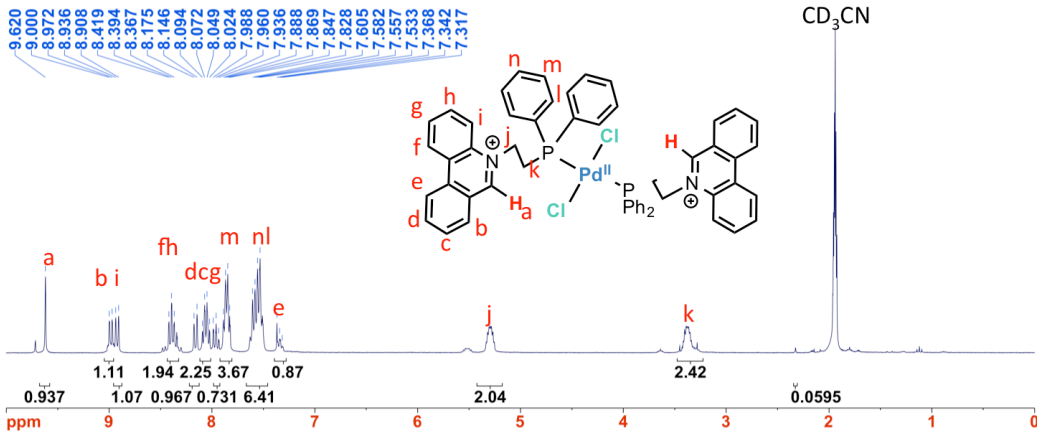

Figure 4.31 ^{1}H NMR Spectrum (CD_3CN, 500 MHz) of **2**

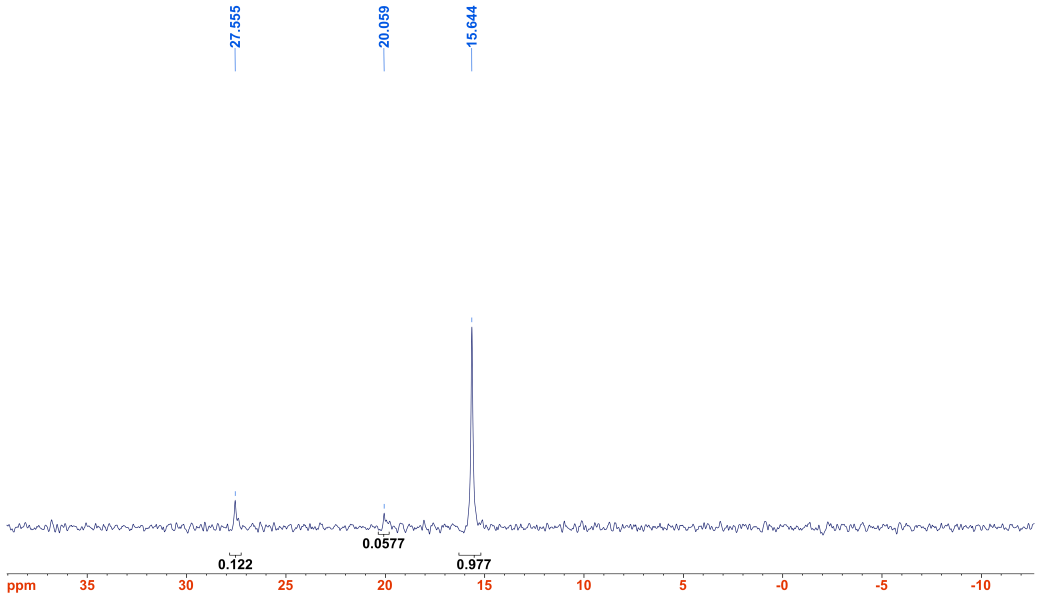

Figure 4.32 ^{31}P NMR Spectrum (CD_3CN, 121 MHz) of **2.**

*Synthesis of $Pd(MeCN)_2(L)_2(BF_4)_4$, **3***

To a solution of LBF_4 (150 mg, 0.31 mmol) in MeCN (5 mL) was added $Pd(MeCN)_4(BF_4)_2$ (70 mg, 0.16 mmol), leaving the solution a pale yellow color. The solution was stirred for 24 hours, then dried under vacuum, washed with THF, and filtered, to give **3** as a pale yellow solid (114 mg, 55%). ^{1}H NMR (500 MHz, CD_3CN, δ, ppm from TMS): 9.44 (s, 2 H), 9.01 (d, 2 H, J = 7.8 Hz) 8.94 (d, 2H, J = 7.8 Hz) 8.4 (m, 4 H), 8.16 (d, 2H, J = 7.4 Hz), 8.1 (m, 4 H), 8.0 (t, 2H, J = 7 Hz), 7.6 (m, 12H), 7.58 (d, 2H, J = 7 Hz), 7.5 (m, 4H), 4.88 (m, 4H), 3.26 (m, 4H). ^{31}P NMR: (121 MHz, CD_3CN): 26.1 ppm.

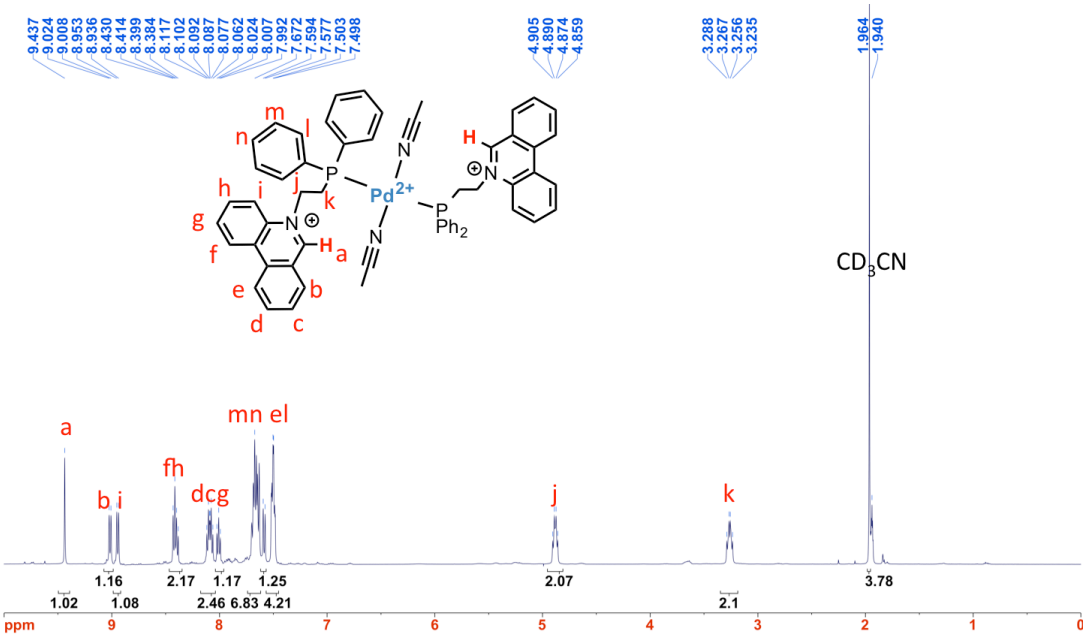

Figure 4.33 ^{1}H NMR Spectrum (CD_3CN, 500 MHz) of **3.**

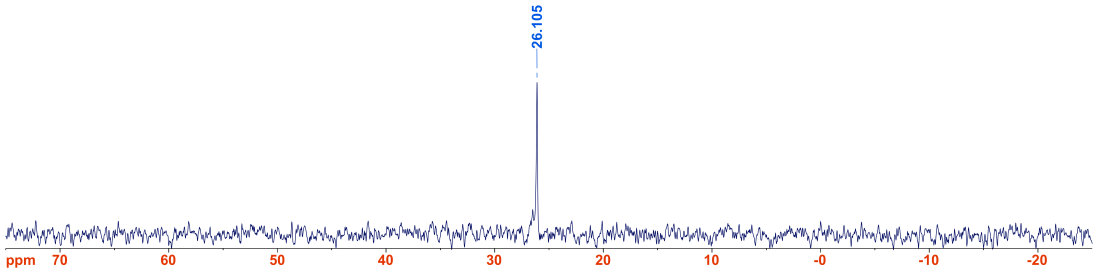

Figure 4.34 ^{31}P NMR Spectrum (CD_3CN, 121 MHz) of **3.**

*Synthesis of **4***

To a solution of LH (99.5 mg, 0.253 mmol) in THF (5 mL) was added $Pd(MeCN)_4(BF_4)_2$, causing the solution to turn from colorless to bright orange and gradually red, with a bright orange precipitate. The solution was stirred for one week, during which time any solid that formed was periodically filtered and washed with THF. The filtrates were returned to stirring. The precipitates were combined, washed with THF, and dried, giving 86 mg of **4** (64%) as a bright orange solid. ^{1}H NMR (500 MHz, CD_3CN, δ, ppm from TMS): 8.6 (m, 2 H), 8.54 (d, 2 H, J = 8 Hz) 7.93 (br t, 2H, J = 6 Hz) 7.68 (m, 8 H), 7.46 (m, 4 H), 7.33 (br d, 4 H, J = 4 Hz), 7.23 (br m, 12H), 4.33 (br s, 4 H), 1.94 (br s, 4H). ^{31}P NMR: (121 MHz, CD_3CN): 15.4 ppm.

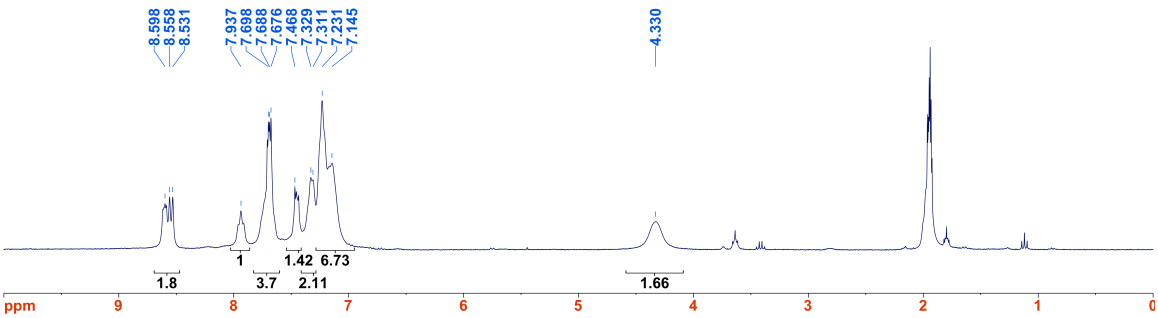

Figure 4.35 ^{1}H NMR Spectrum (CD_3CN, 500 MHz) of **4.**

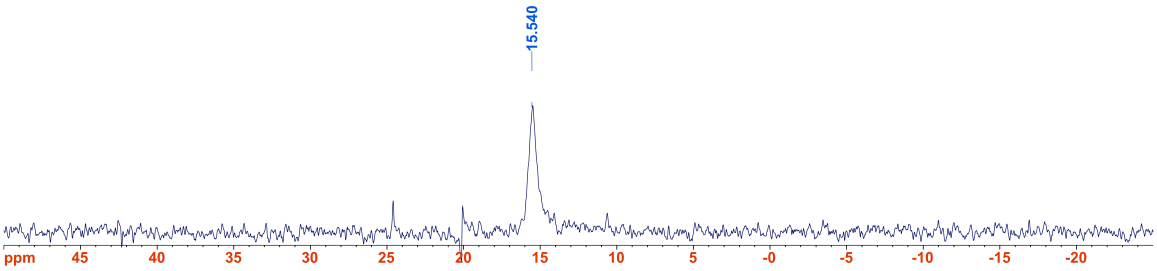

Figure 4.36 ^{31}P NMR Spectrum (CD_3CN, 121 MHz) of **4.**

*Synthesis of **4/4•H$_2$'***

To a suspension of LH (50 mg, 0.013 mmol) in MeCN (15 mL) was added $Pd(MeCN)_4(BF_4)_2$ (28 mg, 0.006 mmol), causing the solution to immediately turn bright orange, then red. The solution was stirred for 24 hours; the solvent was then removed under vacuum, and the product was washed with THF and filtered, leaving 40 mg of **4/4•H$_2$'** (63%) as a red/brown solid. ^{1}H NMR (300 MHz, CD_3CN, δ, ppm from TMS): 8.98 (m), 8.58 (m) 8.2-6.8 (broad, overlapping resonances) 5.91 (t, J = 53 Hz), 4.81 (br s), 4.56 (br s), 4.35 (br s), 2.81 (br d). ^{31}P NMR: (121 MHz, CD_3CN): 19.95, 19.5, 15.4, 10.50 ppm.

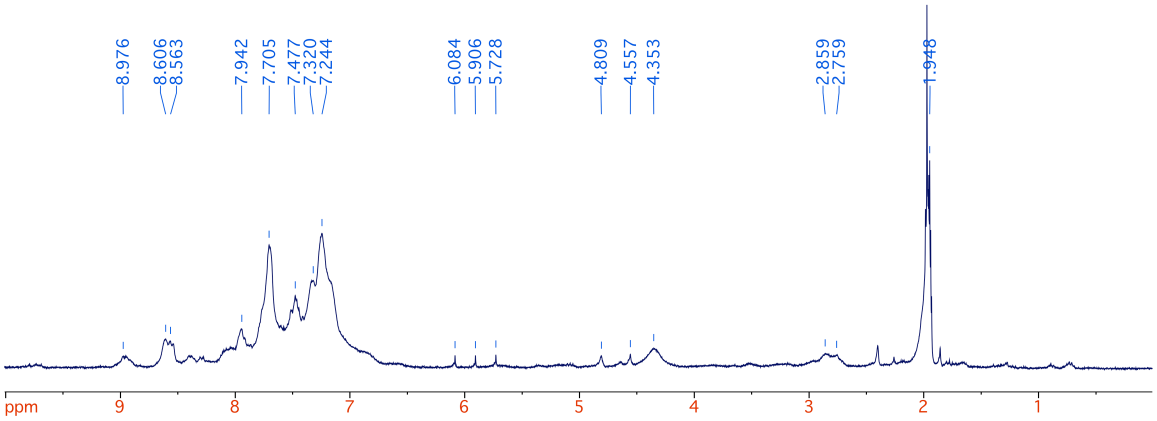

Figure 4.37 ^{1}H NMR Spectrum (CD_3CN, 500 MHz) of ***4/4•H$_2$'.***

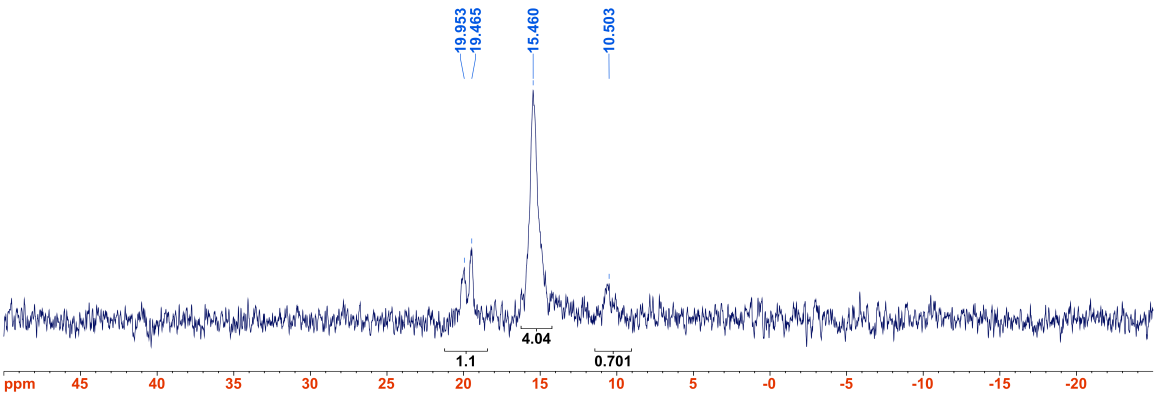

Figure 4.38 ^{31}P NMR Spectrum (CD_3CN, 121 MHz) of ***4/4•H₂'.***

4.5.3 X-Ray Crystallographic Data Collection and Refinement of the Structures

Single crystals of **1** and **2** were grown from vapor diffusion of hexane into a concentrated solution of benzene for **1** and from vapor diffusion of Et_2O into concentrated solution of acetonitrile for **2**. A yellow block of **1** (0.25 x 0.25 x 0.10 mm^3) and an orange block of **4** (0.40 x 0.30 x 0.20 mm^3) were placed on the tip of a glass capillary and mounted on a Bruker APEX Platform CCD diffractometer for data collection at 173(2) K.[36] The data collection was carried out using Mo-Kα radiation (graphite monochromator). The data intensity was corrected for absorption and decay (SADABS).[37] Final cell constants were obtained from least squares fits of all measured reflections after integration (SAINT).[38] The structures were solved using SHELXS-97 and refined using SHELXL-97.[39] Direct-methods solutions were calculated which provided most non-hydrogen atoms from the E-map. Full-matrix least squares / difference Fourier cycles were performed to locate the remaining non-hydrogen atoms. All non-hydrogen atoms were refined with anisotropic displacement parameters. Hydrogen atoms were placed in ideally and refined as riding atoms with relative

isotropic displacement parameters, except those in hydridic positions, which were placed from the difference map and refined independently. Crystallographic data are summarized in Table 4.1

Table 4.1 Crystallographic and Refinement Details for Complexes **1** and **4**.

	$PdCl_2(LH)_2$, **1**	$Pd(LBF_4)_2$, **4**
chemical formula	$C_{54}H_{48}N_2P_2PdCl_2\ 2(C_6H_6)$	$C_{54}H_{46}N_2P_2PdB_2F_8$
formula weight	1120.40	1064.89
crystal system	Triclinic	monoclinic
space group	*P-1*	$P2_1/c$
a (Å)	8.4615(4)	21.856(1)
b (Å)	12.4786(6)	12.5965(8)
c (Å)	13.8728(6)	17.236(1)
α (deg)	70.28	90
β (deg)	82.956(1)	97.623(1)
γ (deg)	89.958(1)	90
V (Å^3)	1367.2(1)	4702(5)
Z	1	4
D_{calcd} (g cm^{-3})	1.361	1.504
λ (Å), μ (mm^{-1})	0.71073, 0.539	0.71073, 0.535
T (K)	173(2)	173(2)
Θ range (deg)	1.57 to 27.51	1.87 to 27.49
reflns collected	15891	53277
unique reflns	6177	10775
data/restraint/ parameters	6177 / 0 / 339	10775 / 65 / 751
R_1, wR_2 ($I > 2\sigma(I)$)	0.0314, 0.0698	0.0399, 0.0895

Bibliography

Chapter 1 References

(1) Shima, S.; Ermler, U. Structure and Function of [Fe]-Hydrogenase and its Iron-Guanylylpyridinol (FeGP) Cofactor. *Eur. J. Inorg. Chem.* **2010**, *2011*, 963–972.

(2) Artero, V.; Fontecave, M. Some general principles for designing electrocatalysts with hydrogenase activity. *Coord. Chem. Rev.* **2005**, *249*, 1518–1535.

(3) Fontecilla-Camps, J. C.; Volbeda, A.; Cavazza, C.; Nicolet, Y. Structure/Function Relationships of [NiFe]- and [FeFe]-Hydrogenases. *Chem. Rev.* **2007**, *107*, 4273–4303.

(4) *International Energy Outlook*; US Department of Energy: Washington, DC, 2011.

(5) *Annual Energy Outlook*; US Department of Energy: Washington, DC, 2013.

(6) *IPCC, 2007: Climate Change 2007: Synthesis Report. Contribution of Working Groups I, II and III to the Fourth Assessment Report of the Intergovernmental Panel on Climate Change*; Pachauri, R. K.; Reisinger, A., Eds. IPCC: Geneva, Switzerland, 2007.

(7) Santer, B. D.; Wigley, T. M. L.; Taylor, K. E. The Reproducibility of Observational Estimates of Surface and Atmospheric Temperature Change. *Science* **2011**, *334*, 1232–1233.

(8) Wigley, T. M. L.; Richels, R.; Edmonds, J. A. Economic and environmental choices in the stabilization of atmospheric CO2 concentrations. *Nature* **1996**, *379*, 240–243.

(9) Hoffert, M. I.; Caldeira, K.; Jain, A. K.; Haites, E. F.; Harvey, L. D. D.; Potter, S. D.; Schlesinger, M. E.; Schneider, S. H.; Watts, R. G.; Wigley, T. M. L.; Wuebbles, D. J. Energy implications of future stabilization of atmospheric CO2 content. *Nature* **1998**, *395*, 881–884.

(10) Lewis, N. S.; Nocera, D. G. Powering the planet: Chemical challenges in solar energy utilization. Proc. Natl. Acad. Sci. **2006**, 1–7.

(11) Nocera, D. G. "Fast food" energy. *Energy Environ. Sci.* **2010**, *3*, 993-994.

(12) Field, L. D. Nitrogen activation: An iron step towards N2 fixation. *Nature Chem.* **2010**, *2*, 520–521.

(13) Erisman, J. W.; Sutton, M. A.; Galloway, J.; Klimont, Z.; Winiwarter, W. How a century of ammonia synthesis changed the world. *Nature Geoscience* **2008**, *1*, 636–639.

(14) Smil, V. Nitrogen and Food Production: Proteins for Human Diets. *AMBIO: A Journal of the Human Environment* **2002**, *31*, 126–131.

(15) Hazari, N. Homogeneous iron complexes for the conversion of dinitrogen into ammonia and hydrazine. *Chem. Soc. Rev.* **2010**, *39*, 4044–4056.

(16) Yandulov, D. V.; Schrock, R. R. Catalytic reduction of dinitrogen to ammonia at a single molybdenum center. *Science* **2003**, *301*, 76–78.

(17) Arashiba, K.; Miyake, Y.; Nishibayashi, Y. A molybdenum complex bearing PNP-type pincer ligands leads to the catalytic reduction of dinitrogen into ammonia. *Nature Chem.* **2011**, *3*, 120–125.

(18) Benson, E. E.; Kubiak, C. P.; Sathrum, A. J.; Smieja, J. M. Electrocatalytic and homogeneous approaches to conversion of CO2 to liquid fuels. Chem. Soc. Rev. **2008**, *38*, 89-99.

(19) Shilov, A. E. Catalytic reduction of molecular nitrogen in solutions. *Russian Chem. Bull., Int. Ed.* **2003**, *52*, 2555–2462.

(20) Benson, E. E.; Kubiak, C. P.; Sathrum, A. J.; Smieja, J. M. Electrocatalytic and homogeneous approaches to conversion of CO2 to liquid fuels. *Chem. Soc. Rev.* **2009**, *38*, 89–99.

(21) Ferreira, K. N.; Iverson, T. M.; Maghlaoui, K.; Barber, J.; Iwata, S. Architecture of the Photosynthetic Oxygen-Evolving Center. *Science* **2004**, *303*, 1831–1838.

(22) Sproviero, E. M.; Gascón, J. A.; McEvoy, J. P.; Brudvig, G. W.; Batista, V. S. A Model of the Oxygen-Evolving Center of Photosystem II Predicted by Structural Refinement Based on EXAFS Simulations. *J. Am. Chem. Soc.* **2008**, *130*, 6728–6730.

(23) Blackburn, N. J.; Barr, M. E.; Woodruff, W. H.; van der Ooost, J.; de Vries, S. Metal-Metal Bonding in Biology: EXAFS Evidence for a 2.5 Å Copper-Copper Bond in the CuA Center of Cytochrome Oxidase. *Biochemistry* **1994**, *33*, 10401–10407.

(24) Blackman, A.; Tolman, W. Copper-Dioxygen and Copper-Oxo Species Relevant to Copper Oxygenases and Oxidases. In *Structure and Bonding*; Meunier, B., Ed. Structure and Bonding; Springer Berlin Heidelberg: Berlin, Heidelberg, 2000; Vol. 97, pp. 179–211–211.

(25) Solomon, E. I.; Randall, D. W.; Glaser, T. Electronic structures of active sites in electron transfer metalloproteins: contributions to reactivity. *Coord. Chem. Rev.* **2000**, *200-202*, 595–632.

(26) McCollum, D. G.; Bosnich, B. Cooperative bimetallic reactivity. *Inorg. Chim.*

Acta **1998**, *270*, 13–19.

(27) Bosnich, B. Cooperative Bimetallic Redox Reactivity. *Inorg. Chem.* **1999**, *38*, 2554–2562.

(28) Incarvito, C.; Rheingold, A. L.; Gavrilova, A. L.; Qin, C. J.; Bosnich, B. Bimetallic Reactivity. One-site Addition Two-metal Oxidation Reactions Using a Di-Co(II) Complex of a Binucleating Ligand with 5- and 6-Coordinate Sites. *Inorg. Chem.* **2001**, *40*, 4101–4108.

(29) Gavrilova, A. L.; Qin, C. J.; Sommer, R. D.; Rheingold, A. L.; Bosnich, B. Bimetallic Reactivity. One-Site Addition Two-Metal Oxidation Reaction of Dioxygen with a Bimetallic Dicobalt(II) Complex Bearing Five- and Six-Coordinate Sites. *J. Am. Chem. Soc.* **2002**, *124*, 1714–1722.

(30) Incarvito, C.; Lam, M.; Rhatigan, B.; Rheingold, A. L.; Qin, C. J.; Gavrilova, A. L.; Bosnich, B. Bimetallic reactivity. Preparations, properties and structures of complexes formed by unsymmetrical binucleating ligands bearing 4- and 6-coordinate sites supported by alkoxide bridges. *J. Chem. Soc., Dalton Trans.* **2001**, 3478–3488.

(31) Bertrand, J. A.; Cotton, F. A.; Dollase, W. A. The Crystal Structure of Cesium Dodecachlorotrirhenate-(III), a Compound with a New Type of Metal Atom Cluster. *Inorg. Chem.* **1963**, *2*, 1166–1171.

(32) Cotton, F. A.; Curtis, N. F.; Harris, C. B.; Johnson, B. F. G.; Lippard, S. J.; Mague, J. T.; Robinson, W. R.; Wood, J. S. Mononuclear and Polynuclear Chemistry of Rhenium (III): Its Pronounced Homophilicity. *Science* **1964**, *145*, 1305–1307.

(33) Cotton, F. A.; Murillo, C. A.; Walton, R. A. Multiple bonds between metal atoms. Springer US: New York, 2005; pp. 1–21.

(34) Brosset, C. Crystal Structure of some Alkali Tungsten Chlorides. *Nature* **1935**, *135*, 874–874.

(35) Cotton, F. A.; Murillo, C. A.; Walton, R. A. Introduction and Survey. In *Multiple Bonds Between Metal Atoms*; Cotton, F. A.; Murillo, C. A.; Walton, R. A., Eds. Springer US: New York, 2005; pp. 1–21.

(36) Cotton, F. A. Metal-Metal Bonding in [Re2X8]2- Ions and Other Metal Atom Clusters. *Inorg. Chem.* **1965**, *4*, 334–336.

(37) Chisholm, M. H.; Hollandsworth, C. B. X3M≡MX3 Compounds of Molybdenum and Tungsten. In *Multiple Bonds Between Metal Atoms*; Cotton, F. A.; Murillo, C. A.; Walton, R. A., Eds. Springer US: New York, 2005; pp. 203–250.

(38) Nippe, M.; Goodman, S. M.; Fry, C. G.; Berry, J. F. Chemically Reversible Four-Electron Oxidation and Reduction Utilizing Two Inorganic Functional Groups. *J. Am. Chem. Soc.* **2011**, *133*, 2856–2859.

(39) Laplaza, C. E.; Cummins, C. C. Dinitrogen Cleavage by a Three-Coordinate Molybdenum (III) Complex. *Science* **1995**, *268*, 861–863.

(40) Hebden, T. J.; Schrock, R. R.; Takase, M. K.; Müller, P. Cleavage of dinitrogen to yield a (t-BuPOCOP)molybdenum(iv) nitride. *Chem. Commun.* **2012**, *48*, 1851.

(41) Doyle, M. P.; Duffy, R.; Ratnikov, M.; Zhou, L. Catalytic Carbene Insertion into C−H Bonds. *Chem. Rev.* **2010**, *110*, 704–724.

(42) Doyle, M. P.; Forbes, D. C. Recent Advances in Asymmetric Catalytic Metal Carbene Transformations. *Chem. Rev.* **1998**, *98*, 911–936.

(43) Timmons, D. J.; Doyle, M. P. Chiral Dirhodium(II) Catalysts and Their Applications. In *Multiple Bonds Between Metal Atoms*; Cotton, F. A.; Murillo, C. A.; Walton, R. A., Eds. Springer US: New York, 2005; pp. 591–632.

(44) Doyle, M. P.; Ren, T. The influence of ligands on dirhodium(II) on reactivity and selectivity in metal carbene reactions. *Progress in Inorganic Chemistry* **2001**, *49*, 113–168.

(45) Nakamura, E.; Yoshikai, N.; Yamanaka, M. Mechanism of C−H Bond Activation/C−C Bond Formation Reaction between Diazo Compound and Alkane Catalyzed by Dirhodium Tetracarboxylate. *J. Am. Chem. Soc.* **2002**, *124*, 7181–7192.

(46) Berry, J. F. The role of three-center/four-electron bonds in superelectrophilic dirhodium carbene and nitrene catalytic intermediates. *Dalton Trans.* **2011**, *41*, 700.

(47) Lloret, J.; Carbó, J. J.; Bo, C.; Lledós, A.; Pérez-Prieto, J. Influence of the Nature of the Ligand on Dirhodium(II) Carbene Species: A Theoretical Analysis. *Organometallics* **2008**, *27*, 2873–2876.

(48) Pap, J. S.; DeBeer George, S.; Berry, J. F. Delocalized Metal-Metal and Metal-Ligand Multiple Bonding in a Linear Ru-Ru-N Unit: Elongation of a Traditionally Short Ru-N Bond. *Angew. Chem. Int. Ed.* **2008**, *47*, 10102–10105.

(49) Musch Long, A. K.; Yu, R. P.; Timmer, G. H.; Berry, J. F. Aryl C−H Bond Amination by an Electrophilic Diruthenium Nitride. *J. Am. Chem. Soc.* **2010**, *132*, 12228–12230.

(50) Corcos, A. R.; Long, A. K. M.; Guzei, I. A.; Berry, J. F. A Synthetic Cycle for

Nitrogen Atom Transfer Featuring a Diruthenium Nitride Intermediate. *Eur. J. Inorg. Chem.* **2013**, *2013*, 3808–3811.

(51) Dulebohn, J. I.; Ward, D. L.; Nocera, D. G. Synthetic design of a multielectron series of homologous dirhodium fluorophosphines possessing an emissive dσ* excited state. *J. Am. Chem. Soc.* **1990**, *112*, 2969–2977.

(52) Kadis, J.; Shin, Y.-G. K.; Dulebohn, J. I.; Ward, D. L.; Nocera, D. G. Molecular Structures and Photophysical Properties of Dirhodium Fluorophosphine Complexes. *Inorg. Chem.* **1996**, *35*, 811–817.

(53) Heyduk, A. F.; Macintosh, A. M.; Nocera, D. G. Four-Electron Photochemistry of Dirhodium Fluorophosphine Compounds. *J. Am. Chem. Soc.* **1999**, *121*, 5023–5032.

(54) Heyduk, A. F.; Nocera, D. G. Hydrogen Produced from Hydrohalic Acid Solutions by a Two-Electron Mixed-Valence Photocatalyst. *Science* **2001**, *293*, 1639–1641.

(55) Cotton, F. A. Chromium Compounds. In *Multiple Bonds Between Metal Atoms*; Cotton, F. A.; Murillo, C. A.; Walton, R. A., Eds. Springer US: New York, 2005; pp. 35–68.

(56) Hall, M. B. Problems in the theoretical description of metal-metal multiple bonds or how I learned to hate the electron correlation problem. *Polyhedron* **1987**, *6*, 679–684.

(57) Cotton, F. A.; Hillard, E. A.; Murillo, C. A.; Zhou, H.-C. After 155 Years, A Crystalline Chromium Carboxylate with a Supershort Cr−Cr Bond. *J. Am. Chem. Soc.* **2000**, *122*, 416–417.

(58) Cotton, F. A.; Feng, X. Density Functional Theory Study of Transition-Metal Compounds Containing Metal−Metal Bonds. 1. Molecular Structures of Dinuclear Compounds by Complete Geometry Optimization. *J. Am. Chem. Soc.* **1997**, *119*, 7514–7520.

(59) Andersson, K.; Bauschlicher, C. W., Jr.; Persson, B. J.; Roos, B. O. The structure of dichromium tetraformate. *Chem. Phys. Lett.* **1996**, *257*, 238–248.

(60) Schultz, N. E.; Zhao, Y.; Truhlar, D. G. Databases for Transition Element Bonding: Metal−Metal Bond Energies and Bond Lengths and Their Use To Test Hybrid, Hybrid Meta, and Meta Density Functionals and Generalized Gradient Approximations. *J. Phys. Chem. A* **2005**, *109*, 4388–4403.

(61) Barden, C. J.; Rienstra-Kiracofe, J. C.; Schaefer, H. F. Homonuclear 3d transition-metal diatomics: A systematic density functional theory study. *J.*

Chem. Phys. **2000**, *113*, 690–700.

(62) Nguyen, T.; Sutton, A. D.; Brynda, M.; Fettinger, J. C.; Long, G. J.; Power, P. P. Synthesis of a Stable Compound with Fivefold Bonding Between Two Chromium(I) Centers. *Science* **2005**, *310*, 844–847.

(63) Brynda, M.; Gagliardi, L.; Widmark, P.-O.; Power, P. P.; Roos, B. O. A Quantum Chemical Study of the Quintuple Bond between Two Chromium Centers in [PhCrCrPh]:trans-Bent versus Linear Geometry. *Angew. Chem. Int. Ed.* **2006**, *45*, 3804–3807.

(64) Kreisel, K. A.; Yap, G. P. A.; Dmitrenko, O.; Landis, C. R.; Theopold, K. H. The Shortest Metal−Metal Bond Yet: Molecular and Electronic Structure of a Dinuclear Chromium Diazadiene Complex. *J. Am. Chem. Soc.* **2007**, *129*, 14162–14163.

(65) Noor, A.; Wagner, F. R.; Kempe, R. Metal-Metal Distances at the Limit: A Coordination Compound with an Ultrashort Chromium-Chromium Bond. *Angew. Chem. Int. Ed.* **2008**, *47*, 7246–7249.

(66) Hsu, C.-W.; Yu, J.-S. K.; Yen, C.-H.; Lee, G.-H.; Wang, Y.; Tsai, Y.-C. Quintuply-Bonded Dichromium(I) Complexes Featuring Metal-Metal Bond Lengths of 1.74 Å. *Angew. Chem. Int. Ed.* **2008**, *47*, 9933–9936.

(67) Tsai, Y.-C.; Hsu, C.-W.; Yu, J.-S. K.; Lee, G.-H.; Wang, Y.; Kuo, T.-S. Remarkably Short Metal-Metal Bonds: A Lantern-Type Quintuply Bonded Dichromium(I) Complex. *Angew. Chem. Int. Ed.* **2008**, *47*, 7250–7253.

(68) Noor, A.; Glatz, G.; Müller, R.; Kaupp, M.; Demeshko, S.; Kempe, R. Metal-Metal Distances at the Limit: Cr-Cr 1.73 Å - the Importance of the Ligand and its Fine Tuning. *Z. Anorg. Allg. Chem.* **2009**, *635*, 1149–1152.

(69) Bondybey, V. E.; English, J. H. Electronic structure and vibrational frequency of Cr2. *Chem. Phys. Lett.* **1983**, *94*, 443–447.

(70) Murillo, C. A. Iron, Cobalt and Iridium Compounds. In *Multiple Bonds Between Metal Atoms*; Cotton, F. A.; Murillo, C. A.; Walton, R. A., Eds. Springer US: New York, 2005; pp. 447–464.

(71) Cotton, F. A.; Daniels, L. M.; Murillo, C. A. Divalent iron formamidinato complexes: a highly distorted dinuclear compound. *Inorg. Chim. Acta* **1994**, *224*, 5–9.

(72) Cotton, F. A.; Daniels, L. M.; Feng, X.; Maloney, D. J.; Matonic, J. H.; Murilio, C. A. The use of CoCl2(amidine)2 compounds in the synthesis of tetragonal lantern dicobalt compounds: synthesis, structures and theoretical studies of Co2(DPhF)4 and the oxidized species [Co2(DPhBz)4]+ (DPhF = N,N′-

diphenylformamidinate, DPhBz = N,N′-diphenylbenzamidinate). *Inorg. Chim. Acta* **1997**, *256*, 291–301.

(73) Nguyen, T.; Merrill, W. A.; Ni, C.; Lei, H.; Fettinger, J. C.; Ellis, B. D.; Long, G. J.; Brynda, M.; Power, P. P. Synthesis and Characterization of the Metal(I) Dimers [Ar′MMAr′]: Comparisons with Quintuple-Bonded [Ar′CrCrAr′]. *Angew. Chem. Int. Ed.* **2008**, *47*, 9115–9117.

(74) Klose, A.; Solari, E.; Floriani, C.; Chiesi-Villa, A.; Rizzoli, C.; Re, N. Magnetic Properties Diagnostic for the Existence of Iron(II)-Iron(II) Bonds in Dinuclear Complexes Which Derive from Stepwise Insertion Reactions on Unsupported Iron-Aryl Bonds. *J. Am. Chem. Soc.* **1994**, *116*, 9123–9135.

(75) Fout, A. R.; Basuli, F.; Fan, H.; Tomaszewski, J.; Huffman, J. C.; Baik, M.-H.; Mindiola, D. J. A Co2N2 Diamond-Core Resting State of Cobalt(I): A Three-Coordinate CoI Synthon Invoking an Unusual Pincer-Type Rearrangement. *Angew. Chem. Int. Ed.* **2006**, *45*, 3291–3295.

(76) Fohlmeister, L.; Liu, S.; Schulten, C.; Moubaraki, B.; Stasch, A.; Cashion, J. D.; Murray, K. S.; Gagliardi, L.; Jones, C. Low-Coordinate Iron(I) and Manganese(I) Dimers: Kinetic Stabilization of an Exceptionally Short Fe-Fe Multiple Bond. *Angew. Chem. Int. Ed.* **2012**, *51*, 8294–8298.

(77) Jones, C.; Schulten, C.; Rose, R. P.; Stasch, A.; Aldridge, S.; Woodul, W. D.; Murray, K. S.; Moubaraki, B.; Brynda, M.; La Macchia, G.; Gagliardi, L. Amidinato- and Guanidinato-Cobalt(I) Complexes: Characterization of Exceptionally Short Co-Co Interactions. *Angew. Chem. Int. Ed.* **2009**, *48*, 7406–7410.

(78) Timmer, G. H.; Berry, J. F. Jahn-Teller distortion, ferromagnetic coupling, and electron delocalization in a high-spin Fe-Fe bonded dimer. *Comptes Rendus - Chimie* **2011**, *15*, 192–201.

(79) Cotton, F. A.; Daniels, L. M.; Maloney, D. J.; Matonic, J. H.; Murillo, C. A. Dicobalt trigonal lanterns: Compounds containing the Co2(3+) core Co2 RC(NPh)(2) (3) (R=H, C6H5) and an oxidized compound {Co2HC(NPh)(2) (3)(CH3CN)(2)}PF6 .3. *Inorg. Chim. Acta* **1997**, *256*, 283–289.

(80) Cotton, F. A.; Daniels, L. M.; Falvello, L. R.; Murillo, C. A. A new class of dinuclear compounds: The synthesis and x-ray structural characterization of tris([mu]-diphenyl-formamidinato) diiron. *Inorg. Chim. Acta* **1994**, *219*, 7–10.

(81) Cotton, F. A.; Daniels, L. M.; Maloney, D. J.; Murillo, C. A. Tri-bridged amidinato compounds of dicobalt 1: Co2[PhNC(R)NPh]3 with R = H and C6H5. *Inorg. Chim. Acta* **1996**, *249*, 9–11.

(82) Cotton, F. A.; Daniels, L. M.; Falvello, L. R.; Matonic, J. H.; Murillo, C. A.

Trigonal-lantern dinuclear compounds of diiron(I,II): The synthesis and characterization of two highly paramagnetic Fe2(amidinato)3 species with short metal-metal bonds. *Inorg. Chim. Acta* **1997**, *256*, 269–275.

(83) Cotton, F. A.; Feng, X.; Murillo, C. A. Electronic structure of dinuclear trigonal-lantern amidinato compounds of iron and cobalt. *Inorg. Chim. Acta* **1997**, *256*, 303–308.

(84) Girerd, J.-J.; Journeaux, Y. Molecular Magnetism in Bioinorganic Chemistry. In *Physical Methods in Bioinorganic Chemistry: Spectroscopy and Magnetism*; Que, L. J., Ed. University Science Books: Sausalito, CA, 2000; pp. 321–374.

(85) Blondin, G.; Girerd, J.-J. Interplay of electron exchange and electron transfer in metal polynuclear complexes in proteins or chemical models. *Chem. Rev.* **1990**, *90*, 1359–1376.

(86) Beinert, H.; Holm, R. H.; Münck, E. Iron-Sulfur Clusters: Nature's Modular, Multipurpose Structures. *Science* **1997**, *277*, 653–659.

(87) Achim, C.; Golinelli, M.-P.; Bominaar, E. L.; Meyer, J.; Münck, E. Mössbauer Study of Cys56Ser Mutant 2Fe Ferredoxin from Clostridium Pasteurianum: Evidence for Double Exchange in an [Fe 2S 2] +Cluster. *J. Am. Chem. Soc.* **1996**, *118*, 8168–8169.

(88) Gamelin, D. R.; Bominaar, E. L.; Kirk, M. L.; Wieghardt, K.; Solomon, E. I. Excited-state contributions to ground-state properties of mixed-valence dimers: Spectral and electronic-structural studies of [Fe-2(OH)(3)(tmtacn)(2)](2+) related to the [Fe2S2](+) active sites of plant-type ferredoxins. *J. Am. Chem. Soc.* **1996**, *118*, 8085–8097.

(89) Ding, X.-Q.; Bominaar, E. L.; Bill, E.; Winkler, H.; Trautwein, A. X.; Drüeke, S.; Chaudhuri, P.; Wieghardt, K. Mössbauer and electron paramagnetic resonance study of the double-exchange and Heisenberg-exchange interactions in a novel binuclear Fe(II/III) delocalized-valence compound. *J. Chem. Phys.* **1990**, *92*, 178–186.

(90) Lee, D.; Krebs, C.; Huynh, B. H.; Hendrich, M. P.; Lippard, S. J. Valence-Delocalized Diiron(II,III) Cores Supported by Carboxylate-Only Bridging Ligands. *J. Am. Chem. Soc.* **2000**, *122*, 5000–5001.

(91) Hagadorn, J. R.; Que, L.; Tolman, W. B.; Prisecaru, I.; Münck, E. Conformational Tuning of Valence Delocalization in Carboxylate-Rich Diiron Complexes. *J. Am. Chem. Soc.* **1999**, *121*, 9760–9761.

(92) Noodleman, L.; Peng, C. Y.; Case, D. A.; Mouesca, J. M. Orbital interactions, electron delocalization and spin coupling in iron-sulfur clusters. *Coord. Chem.*

Rev. **1995**, *144*, 199–244.

(93) Angaridis, P. Ruthenium Compounds. In *Multiple Bonds Between Metal Atoms*; Cotton, F. A.; Murillo, C. A.; Walton, R. A., Eds. Springer US: New York, 2005; pp. 377–430–430.

(94) Eames, E. V.; Harris, T. D.; Betley, T. A. Modulation of magnetic behavior via ligand-field effects in the trigonal clusters (PhL)Fe3L*3 (L* = thf, py, PMe2Ph). *Chem. Sci.* **2012**, *3*, 407.

Chapter 2 References

(1) Cotton, F. A.; Daniels, L. M.; Falvello, L. R.; Murillo, C. A. A new class of dinuclear compounds: The synthesis and x-ray structural characterization of tris([mu]-diphenyl-formamidinato) diiron. *Inorg. Chim. Acta* **1994**, *219*, 7–10.

(2) Cotton, F. A.; Daniels, L. M.; Maloney, D. J.; Murillo, C. A. Tri-bridged amidinato compounds of dicobalt 1: Co2[PhNC(R)NPh]3 with R = H and C6H5. *Inorg. Chim. Acta* **1996**, *249*, 9–11.

(3) Cotton, F. A.; Daniels, L. M.; Falvello, L. R.; Matonic, J. H.; Murillo, C. A. Trigonal-lantern dinuclear compounds of diiron(I,II): The synthesis and characterization of two highly paramagnetic Fe2(amidinato)3 species with short metal-metal bonds. *Inorg. Chim. Acta* **1997**, *256*, 269–275.

(4) Cotton, F. A.; Daniels, L. M.; Maloney, D. J.; Matonic, J. H.; Murillo, C. A. Dicobalt trigonal lanterns: Compounds containing the Co2(3+) core Co2RC(NPh)(2) (R=H, C6H5) and an oxidized compound [Co2HC(NPh)(2)(3)(CH3CN)(2)]PF6. *Inorg. Chim. Acta* **1997**, *256*, 283–289.

(5) Cotton, F. A.; Daniels, L. M.; Maloney, D. J.; Murillo, C. A. Transition metal complexes with amidinato ligands: the ubiquitous tris-chelated structural motif. *Inorg. Chim. Acta* **1996**, *242*, 31–42.

(6) Fohlmeister, L.; Liu, S.; Schulten, C.; Moubaraki, B.; Stasch, A.; Cashion, J. D.; Murray, K. S.; Gagliardi, L.; Jones, C. Low-Coordinate Iron(I) and Manganese(I) Dimers: Kinetic Stabilization of an Exceptionally Short Fe-Fe Multiple Bond. *Angew. Chem. Int. Ed.* **2012**, *51*, 8294–8298.

(7) Cotton, F. A.; Daniels, L. M.; Feng, X.; Maloney, D. J.; Matonic, J. H.; Murilio, C. A. The use of CoCl2(amidine)2 compounds in the synthesis of tetragonal lantern dicobalt compounds: synthesis, structures and theoretical studies of Co2(DPhF)4 and the oxidized species [Co2(DPhBz)4]+ (DPhF = N,N′-diphenylformamidinate, DPhBz = N,N′-diphenylbenzamidinate). *Inorg. Chim. Acta* **1997**, *256*, 291–301.

(8) Jones, C.; Schulten, C.; Rose, R. P.; Stasch, A.; Aldridge, S.; Woodul, W. D.; Murray, K. S.; Moubaraki, B.; Brynda, M.; La Macchia, G.; Gagliardi, L. Amidinato- and Guanidinato-Cobalt(I) Complexes: Characterization of Exceptionally Short Co-Co Interactions. *Angew. Chem. Int. Ed.* **2009**, *48*, 7406–7410.

(9) Cotton, F. A.; Feng, X.; Murillo, C. A. Electronic structure of dinuclear trigonal-lantern amidinato compounds of iron and cobalt. *Inorg. Chim. Acta* **1997**, *256*, 303–308.

(10) Murillo, C. A. Iron, Cobalt and Iridium Compounds. In *Multiple Bonds Between Metal Atoms*; Cotton, F. A.; Murillo, C. A.; Walton, R. A., Eds. Springer US: New York, 2005; pp. 447–464.

(11) Gamelin, D. R.; Bominaar, E. L.; Kirk, M. L.; Wieghardt, K.; Solomon, E. I. Excited-state contributions to ground-state properties of mixed-valence dimers: Spectral and electronic-structural studies of [Fe-2(OH)(3)(tmtacn)(2)](2+) related to the [Fe2S2](+) active sites of plant-type ferredoxins. *J. Am. Chem. Soc.* **1996**, *118*, 8085–8097.

(12) Timmer, G. H.; Berry, J. F. Jahn-Teller distortion, ferromagnetic coupling, and electron delocalization in a high-spin Fe-Fe bonded dimer. *Comptes Rendus - Chimie* **2011**, *15*, 192–201.

(13) Girerd, J.-J.; Journeaux, Y. Molecular Magnetism in Bioinorganic Chemistry. In *Physical Methods in Bioinorganic Chemistry: Spectroscopy and Magnetism*; Que, L. J., Ed. University Science Books: Sausalito, CA, 2000; pp. 321–374.

(14) Blondin, G.; Girerd, J.-J. Interplay of electron exchange and electron transfer in metal polynuclear complexes in proteins or chemical models. *Chem. Rev.* **1990**, *90*, 1359–1376.

(15) Achim, C.; Golinelli, M.-P.; Bominaar, E. L.; Meyer, J.; Münck, E. Mössbauer Study of Cys56Ser Mutant 2Fe Ferredoxin from Clostridium Pasteurianum: Evidence for Double Exchange in an [Fe2S2]+ Cluster. *J. Am. Chem. Soc.* **1996**, *118*, 8168–8169.

(16) Angaridis, P. Ruthenium Compounds. In *Multiple Bonds Between Metal Atoms*; Cotton, F. A.; Murillo, C. A.; Walton, R. A., Eds. Springer US: New York, 2005; pp. 377–430.

(17) Eames, E. V.; Harris, T. D.; Betley, T. A. Modulation of magnetic behavior via ligand-field effects in the trigonal clusters (PhL)Fe3L*3 (L* = thf, py, PMe2Ph). *Chem. Sci.* **2012**, *3*, 407.

(18) Tsai, Y.-C.; Hsu, C.-W.; Yu, J.-S. K.; Lee, G.-H.; Wang, Y.; Kuo, T.-S. Remarkably Short Metal-Metal Bonds: A Lantern-Type Quintuply Bonded Dichromium(I) Complex. *Angew. Chem. Int. Ed.* **2008**, *47*, 7250–7253.

(19) Cotton, F. A.; Daniels, L. M.; Falvello, L. R.; Matonic, J. H.; Murillo, C. A.; Wang, X.; Zhou, H. Transition metal (Mn, Co) and zinc formamidinate compounds having the basic beryllium acetate structure, and unique isomeric iron compounds. *Inorg. Chim. Acta* **1997**, *266*, 91–102.

(20) Cotton, F. A.; Daniels, L. M.; Murillo, C. A. Divalent iron formamidinato complexes: a highly distorted dinuclear compound. *Inorg. Chim. Acta* **1994**, *224*,

5–9.

(21) Cotton, F. A.; Daniels, L. M.; Matonic, J. H.; Murillo, C. A. Highly distorted diiron(II, II) complexes containing four amidinate ligands. A long and short metal-metal distance. *Inorg. Chim. Acta* **1997**, *256*, 277–282.

(22) Randall, C. R.; Shu, L.; Chiou, Y.-M.; Hagen, K. S.; Ito, M.; Kitajima, N.; Lachicotte, R. J.; Zang, Y.; Que, L. X-ray Absorption Pre-Edge Studies of High-spin Iron(II) Complexes. *Inorg. Chem.* **1995**, *34*, 1036–1039.

(23) Lee, D.; Bois, J. D.; Petasis, D.; Hendrich, M. P.; Krebs, C.; Huynh, B. H.; Lippard, S. J. Formation of Fe(III)Fe(IV) Species from the Reaction between a Diiron(II) Complex and Dioxygen: Relevance to Ribonucleotide Reductase Intermediate X. *J. Am. Chem. Soc.* **1999**, *121*, 9893–9894.

(24) LeCloux, D. D.; Barrios, A. M.; Mizoguchi, T. J.; Lippard, S. J. Modeling the Diiron Centers of Non-Heme Iron Enzymes. Preparation of Sterically Hindered Diiron(II) Tetracarboxylate Complexes and Their Reactions with Dioxygen. *J. Am. Chem. Soc.* **1998**, *120*, 9001–9014.

(25) Lee, D.; Krebs, C.; Huynh, B. H.; Hendrich, M. P.; Lippard, S. J. Valence-Delocalized Diiron(II,III) Cores Supported by Carboxylate-Only Bridging Ligands. *J. Am. Chem. Soc.* **2000**, *122*, 5000–5001.

(26) Friedle, S.; Kodanko, J. J.; Fornace, K. L.; Lippard, S. J. 9-Triptycenecarboxylate-bridged diiron(II) complexes: Capture of the paddlewheel geometric isomer. *J. of Mol. Struct.* **2008**, *890*, 317–327.

(27) Cotton, F. A.; Daniels, L. M.; Falvello, L. R.; Matonic, J. H.; Murillo, C. A. Trigonal-lantern dinuclear compounds of diiron(I,II): The synthesis and characterization of two highly paramagnetic Fe-2(amidinato)(3) species with short metal-metal bonds .1. *Inorg. Chim. Acta* **1997**, *256*, 269–275.

(28) Cotton, F. A.; Daniels, L. M.; Maloney, D. J.; Matonic, J. H.; Murillo, C. A. Divalent metal chloride formamidine complexes, M11 = Fe, Co and Pt. syntheses and structural characterization. *Polyhedron* **1994**, *13*, 815–823.

(29) He, L. P.; Yao, C. L.; Naris, M.; Lee, J. C.; Korp, J. D.; Bear, J. L. Molecular structure and chemical and electrochemical reactivity of Co2(dpb)4 and Rh2(dpb)4 (dpb=N,N'-Diphenylbenzamidinate). *Inorg. Chem.* **1992**, *31*, 620–625.

(30) Zall, C. M.; Zherebetskyy, D.; Dzubak, A. L.; Bill, E.; Gagliardi, L.; Lu, C. C. A Combined Spectroscopic and Computational Study of a High-Spin S = 7/2 Diiron Complex with a Short Iron–Iron Bond. *Inorg. Chem.* **2012**, *51*, 728–736.

(31) Bencini, A.; Gatteschi, D. *EPR of Exchange Coupled Systems*; Springer Verlag:

Berlin, 1990.

(32) Nippe, M.; Turov, Y.; Berry, J. F. Remote Effects of Axial Ligand Substitution in Heterometallic Cr≡Cr···M Chains. *Inorg. Chem.* **2011**, *50*, 10592–10599.

(33) Robin, M. B.; Day, P. Mixed Valence Chemistry - A Survey and Classification. *Adv. Inorg. Chem. Radiochem.* **1967**, *10*, 247–422.

(34) Glover, S. D.; Lear, B. J.; Salsman, J. C.; Londergan, C. H.; Kubiak, C. P. Electron transfer at the class II/III borderline of mixed valency: dependence of rates on solvent dynamics and observation of a localized-to-delocalized transition in freezing solvents. *Phil. Trans. R. Soc. A.* **2008**, *366*, 177–185.

(35) Andres, H.; Bominaar, E. L.; Smith, J. M.; Eckert, N. A.; Holland, P. L.; Münck, E. Planar Three-Coordinate High-Spin FeII Complexes with Large Orbital Angular Momentum: Mössbauer, Electron Paramagnetic Resonance, and Electronic Structure Studies. *J. Am. Chem. Soc.* **2002**, *124*, 3012–3025.

(36) Stoian, S. A.; Yu, Y.; Smith, J. M.; Holland, P. L.; Bominaar, E. L.; Münck, E. Mössbauer, Electron Paramagnetic Resonance, and Crystallographic Characterization of a High-Spin Fe(I) Diketiminate Complex with Orbital Degeneracy. *Inorg. Chem.* **2005**, *44*, 4915–4922.

(37) Hendrich, M. P.; Gunderson, W.; Behan, R. K.; Green, M. T.; Mehn, M. P.; Betley, T. A.; Lu, C. C.; Peters, J. C. On the feasibility of N2 fixation via a single-site FeI/FeIV cycle: Spectroscopic studies of FeI(N2)FeI, FeIV N, and related species. *Proc. Natl. Acad. Sci, USA.* **2006**, *103*, 17107–17112.

(38) Neese, F. ORCA version 2.8-20.

(39) Sinnecker, S.; Slep, L. D.; Bill, E.; Neese, F. Performance of Nonrelativistic and Quasi-Relativistic Hybrid DFT for the Prediction of Electric and Magnetic Hyperfine Parameters in 57Fe Mössbauer Spectra. *Inorg. Chem.* **2005**, *44*, 2245–2254.

(40) Römelt, M.; Ye, S.; Neese, F. Calibration of Modern Density Functional Theory Methods for the Prediction of 57Fe Mössbauer Isomer Shifts: Meta-GGA and Double-Hybrid Functionals. *Inorg. Chem.* **2008**, *48*, 784–785.

(41) Kuppuswamy, S.; Bezpalko, M. W.; Powers, T. M.; Turnbull, M. M.; Foxman, B. M.; Thomas, C. M. Utilization of Phosphinoamide Ligands in Homobimetallic Fe and Mn Complexes: The Effect of Disparate Coordination Environments on Metal–Metal Interactions and Magnetic and Redox Properties. *Inorg. Chem.* **2012**, *51*, 8225–8240.

(42) Zhao, Q.; Harris, T. D.; Betley, T. A. [(HL)2Fe6(NCMe)m]n+ (m= 0, 2, 4, 6; n= −1, 0, 1, 2, 3, 4, 6): An Electron-Transfer Series Featuring Octahedral Fe6

Clusters Supported by a Hexaamide Ligand Platform. *J. Am. Chem. Soc.* **2011**, *133*, 8293–8306.

(43) Zhao, Q.; Betley, T. A. Synthesis and Redox Properties of Triiron Complexes Featuring Strong Fe-Fe Interactions. *Angew. Chem. Int. Ed.* **2011**, *50*, 709–712.

(44) Cotton, F. A.; Feng, X. Density Functional Theory Study of Transition-Metal Compounds Containing Metal−Metal Bonds. 1. Molecular Structures of Dinuclear Compounds by Complete Geometry Optimization. *J. Am. Chem. Soc.* **1997**, *119*, 7514–7520.

(45) Hall, M. B. Problems in the theoretical description of metal-metal multiple bonds or how I learned to hate the electron correlation problem. *Polyhedron* **1987**, *6*, 679–684.

(46) Nippe, M.; Goodman, S. M.; Fry, C. G.; Berry, J. F. Chemically Reversible Four-Electron Oxidation and Reduction Utilizing Two Inorganic Functional Groups. *J. Am. Chem. Soc.* **2011**, *133*, 2856–2859.

(47) Heyduk, A. F.; Nocera, D. G. Hydrogen Produced from Hydrohalic Acid Solutions by a Two-Electron Mixed-Valence Photocatalyst. *Science* **2001**, *293*, 1639–1641.

(48) Fontecilla-Camps, J. C.; Volbeda, A.; Cavazza, C.; Nicolet, Y. Structure/Function Relationships of [NiFe]- and [FeFe]-Hydrogenases. *Chem. Rev.* **2007**, *107*, 4273–4303.

(49) Cotton, F. A.; Daniels, L. M.; Maloney, D. J.; Murillo, C. A. An unusual iron-oxo tetranuclear species: Li2(HDPhF)2Fe4O4(DPhF)6·4toluene. A ubiquitous side product in the chemistry of iron/formamidine compounds. *Inorg. Chim. Acta* **1996**, *252*, 293–298.

(50) Brown, K.; Tegoni, M.; Prudêncio, M.; Pereira, A. S.; Besson, S.; Moura, J. J.; Moura, I.; Cambillau, C. A novel type of catalytic copper cluster in nitrous oxide reductase. *Nature Structural Biology* **2000**, *7*, 191.

(51) Paraskevopoulos, K.; Antonyuk, S. V.; Sawers, R. G.; Eady, R. R.; Hasnain, S. S. Insight into Catalysis of Nitrous Oxide Reductase from High-resolution Structures of Resting and Inhibitor-bound Enzyme from Achromobacter cycloclastes. *J. Mol. Biol.* **2006**, *362*, 55–65.

(52) Aresta, M. Carbon Dioxide Reduction and Uses as a Chemical Feedstock. In *Activation of Small Molecules*; Tolman, W. B., Ed. Wiley-VCH: Weinheim, 2006; pp. 1–41.

(53) Pauling, L. Atomic Radii and Interatomic Distances in Metals. *J. Am. Chem. Soc.*

1947, *69*, 542–553.

(54) Connelly, N. G.; Geiger, W. E. Chemical Redox Agents for Organometallic Chemistry. *Chem. Rev.* **1996**, *96*, 877–910.

(55) Lin, Z.-S.; Chiou, T.-W.; Liu, K.-Y.; Hsieh, C.-C.; Yu, J.-S. K.; Liaw, W.-F. A Dinitrosyliron Complex within the Homoleptic Fe(NO)4 Anion: NO as Nitroxyl and Nitrosyl Ligands within a Single Structure. *Inorg. Chem.* **2012**, *51*, 10092–10094.

(56) Tsai, M.-C.; Tsai, F.-T.; Lu, T.-T.; Tsai, M.-L.; Wei, Y.-C.; Hsu, I.-J.; Lee, J.-F.; Liaw, W.-F. Relative Binding Affinity of Thiolate, Imidazolate, Phenoxide, and Nitrite Toward the {Fe(NO)2} Motif of Dinitrosyl Iron Complexes (DNICs): The Characteristic Pre-Edge Energy of {Fe(NO)2}9 DNICs. *Inorg. Chem.* **2009**, *48*, 9579–9591.

(57) McCleverty, J. A. Chemistry of Nitric Oxide Relevant to Biology. *Chem. Rev.* **2004**, *104*, 403–418.

Chapter 3 References

(1) Fontecilla-Camps, J. C.; Volbeda, A.; Cavazza, C.; Nicolet, Y. Structure/Function Relationships of [NiFe]- and [FeFe]-Hydrogenases. *Chem. Rev.* **2007**, *107*, 4273–4303.

(2) Kung, Y.; Drennan, C. L. A role for nickel–iron cofactors in biological carbon monoxide and carbon dioxide utilization. *Curr. Opin. Chem. Biol.* **2011**, *15*, 276–283.

(3) Jeoung, J.-H.; Dobbek, H. Structural Basis of Cyanide Inhibition of Ni, Fe-Containing Carbon Monoxide Dehydrogenase. *J. Am. Chem. Soc.* **2009**, *131*, 9922–9923.

(4) Spatzal, T.; Aksoyoglu, M.; Zhang, L.; Andrade, S. L. A.; Schleicher, E.; Weber, S.; Rees, D. C.; Einsle, O. Evidence for Interstitial Carbon in Nitrogenase FeMo Cofactor. *Science* **2011**, *334*, 940–940.

(5) Seefeldt, L. C.; Hoffman, B. M.; Dean, D. R. Mechanism of Mo-Dependent Nitrogenase. *Annu. Rev. Biochem.* **2009**, *78*, 701–722.

(6) Jiang, W.; Yun, D.; Saleh, L.; Barr, E. W.; Xing, G.; Hoffart, L. M.; Maslak, M. A.; Krebs, C.; Bollinger, J. M. A Manganese(IV)/Iron(III) Cofactor in Chlamydia trachomatis Ribonucleotide Reductase. *Science* **2007**, *316*, 1188–1191.

(7) Voevodskaya, N.; Lendzian, F.; Ehrenberg, A.; Gräslund, A. High catalytic activity achieved with a mixed manganese–iron site in protein R2 of Chlamydia ribonucleotide reductase. *FEBS Letters* **2007**, *581*, 3351–3355.

(8) Krebs, C.; Matthews, M. L.; Jiang, W.; Bollinger, J. M. AurF from Streptomyces thioluteus and a Possible New Family of Manganese/Iron Oxygenases. *Biochemistry* **2007**, *46*, 10413–10418.

(9) Schenk, G.; Gahan, L. R.; Carrington, L. E.; Mitić, N.; Valizadeh, M.; Hamilton, S. E.; de Jersey, J.; Guddat, L. W. Phosphate forms an unusual tripodal complex with the Fe–Mn center of sweet potato purple acid phosphatase. *Proc. Natl. Acad. Sci. U. S. A.* **2005**, *102*, 273–278.

(10) Schenk, G.; Elliott, T. W.; Leung, E.; Carrington, L. E.; Mitić, N.; Gahan, L. R.; Guddat, L. W. Crystal structures of a purple acid phosphatase, representing different steps of this enzyme's catalytic cycle. *BMC Struct. Biol.* **2008**, *8*, 6.

(11) Ferreira, K. N.; Iverson, T. M.; Maghlaoui, K.; Barber, J.; Iwata, S. Architecture of the Photosynthetic Oxygen-Evolving Center. *Science* **2004**, *303*, 1831–1838.

(12) Sproviero, E. M.; Gascón, J. A.; McEvoy, J. P.; Brudvig, G. W.; Batista, V. S. A

Model of the Oxygen-Evolving Center of Photosystem II Predicted by Structural Refinement Based on EXAFS Simulations. *J. Am. Chem. Soc.* **2008**, *130*, 6728–6730.

(13) Blackburn, N. J.; Barr, M. E.; Woodruff, W. H.; van der Ooost, J.; de Vries, S. Metal-Metal Bonding in Biology: EXAFS Evidence for a 2.5 Å Copper-Copper Bond in the CuA Center of Cytochrome Oxidase. *Biochemistry* **1994**, *33*, 10401–10407.

(14) Kanady, J. S.; Tsui, E. Y.; Day, M. W.; Agapie, T. A Synthetic Model of the Mn3Ca Subsite of the Oxygen-Evolving Complex in Photosystem II. *Science* **2011**, *333*, 733–736.

(15) Tsui, E. Y.; Tran, R.; Yano, J.; Agapie, T. Redox-inactive metals modulate the reduction potential in heterometallic manganese–oxido clusters. *Nature Chem.* **2013**, *5*, 293–299.

(16) Kanady, J. S.; Mendoza-Cortes, J. L.; Tsui, E. Y.; Nielsen, R. J.; Goddard, W. A., III; Agapie, T. Oxygen Atom Transfer and Oxidative Water Incorporation in Cuboidal Mn 3MOn Complexes Based on Synthetic, Isotopic Labeling, and Computational Studies. *J. Am. Chem. Soc.* **2013**, *135*, 1073–1082.

(17) Voevodskaya, N.; Lendzian, F.; Sanganas, O.; Grundmeier, A.; Graslund, A.; Haumann, M. Redox Intermediates of the Mn-Fe Site in Subunit R2 of Chlamydia trachomatis Ribonucleotide Reductase: An X-Ray Absorption and EPR Study. *J. Biol. Chem.* **2008**, *284*, 4555–4566.

(18) Vincent, J. B.; Averill, B. A. An enzyme with a double identity: purple acid phosphatase and tartrate-resistant acid phosphatase. *FASEB J.* **1990**, *4*, 3009–3014.

(19) Wang, D. L.; Holz, R. C.; David, S. S.; Que, L.; Stankovich, M. T. Electrochemical properties of the diiron core of uteroferrin and its anion complexes. *Biochemistry* **1991**, *30*, 8187–8194.

(20) Kim, B.-E.; Nevitt, T.; Thiele, D. J. Mechanisms for copper acquisition, distribution and regulation. *Nat. Chem. Biol.* **2008**, *4*, 176–185.

(21) Wang, J.; Pantopoulos, K. Regulation of cellular iron metabolism. *Biochem. J.* **2011**, *434*, 365–381.

(22) Li, Y.; Zamble, D. B. Nickel Homeostasis and Nickel Regulation: An Overview. *Chem. Rev.* **2009**, *109*, 4617–4643.

(23) Bullock, R. M.; Casey, C. P. Heterobimetallic compounds linked by heterodifunctional ligands. *Acc. Chem. Res.* **1987**, *20*, 167–173.

(24) Thomas, C. M. Metal-Metal Multiple Bonds in Early/Late Heterobimetallic Complexes: Applications Towards Small Molecule Activation and Catalysis. *Comments Inorg. Chem.* **2011**, *32*, 14–38.

(25) Bauer, J.; Braunschweig, H.; Dewhurst, R. D. Metal-Only Lewis Pairs with Transition Metal Lewis Bases. *Chem. Rev.* **2012**, *112*, 4329–4346.

(26) Krogman, J. P.; Foxman, B. M.; Thomas, C. M. Activation of CO2 by a Heterobimetallic Zr/Co Complex. *J. Am. Chem. Soc.* **2011**, *133*, 14582–14585.

(27) Rudd, P. A.; Planas, N.; Bill, E.; Gagliardi, L.; Lu, C. C. Dinitrogen Activation at Iron and Cobalt Metallalumatranes. *Eur. J. Inorg. Chem.* **2013**, *2013*, 3898–3906.

(28) Harakas, G. N.; Whittlesey, B. R. Xenophilic Metal Clusters: Preparation and Crystal Structure of {μ-Mn(THF) 2} 2Fe 2(CO) 8(THF = Tetrahydrofuran). *J. Am. Chem. Soc.* **1996**, *118*, 4210–4211.

(29) Gade, L. H. "Strangelove" in Cluster Chemistry: A New Class of Open-Shell Transition Metal Clusters. *Angew. Chem. Int. Ed.* **1996**, *35*, 2089–2090.

(30) Uehara, K.; Hikichi, S.; Inagaki, A.; Akita, M. Xenophilic Complexes Bearing a TpR Ligand, [TpRMM'Ln] [TpR=TpiPr2, Tp# (TpMe2,4-Br); M=Ni, Co, Fe, Mn; M'Ln=Co(CO)4, Co(CO)3(PPh3), RuCp(CO)2]: The Two Metal Centers are Held Together not by Covalent Interaction but by Electrostatic Attraction. *Chem. Eur. J.* **2005**, *11*, 2788–2809.

(31) Krämer, T.; Lin, Z.; McGrady, J. E. Exchange coupling through diamagnetic [Fe(CO)4]2− bridging ligands in a xenophilic cluster. *Dalton Trans.* **2011**, *40*, 927–932.

(32) Kuppuswamy, S.; Cooper, B. G.; Bezpalko, M. W.; Foxman, B. M.; Powers, T. M.; Thomas, C. M. Synthesis and Structural Characterization of High Spin M/Cu (M = Mn, Fe) Heterobimetallic and Fe/Cu2 Trimetallic Phosphinoamides. *Inorg. Chem.* **2012**, *51*, 1866–1873.

(33) Kuppuswamy, S.; Bezpalko, M. W.; Powers, T. M.; Turnbull, M. M.; Foxman, B. M.; Thomas, C. M. Utilization of Phosphinoamide Ligands in Homobimetallic Fe and Mn Complexes: The Effect of Disparate Coordination Environments on Metal–Metal Interactions and Magnetic and Redox Properties. *Inorg. Chem.* **2012**, *51*, 8225–8240.

(34) Kuppuswamy, S.; Powers, T. M.; Johnson, B. M.; Bezpalko, M. W.; Brozek, C. K.; Foxman, B. M.; Berben, L. A.; Thomas, C. M. Metal–Metal Interactions in C3-Symmetric Diiron Imido Complexes Linked by Phosphinoamide Ligands. *Inorg. Chem.* **2012**, 121224071404005.

(35) Mathialagan, R.; Kuppuswamy, S.; De Denko, A. T.; Bezpalko, M. W.; Foxman, B. M.; Thomas, C. M. Metal–Metal Bonding in Low-Coordinate Dicobalt Complexes Supported by Phosphinoamide Ligands. *Inorg. Chem.* **2013**, *52*, 701–706.

(36) Eames, E. V.; Hernández Sánchez, R.; Betley, T. A. Metal Atom Lability in Polynuclear Complexes. *Inorg. Chem.* **2013**, *52*, 5006–5012.

(37) Eames, E. V.; Betley, T. A. Site-Isolated Redox Reactivity in a Trinuclear Iron Complex. *Inorg. Chem.* **2012**, *51*, 10274–10278.

(38) Cotton, F. A.; Daniels, L. M.; Falvello, L. R.; Murillo, C. A. A new class of dinuclear compounds: The synthesis and x-ray structural characterization of tris([mu]-diphenyl-formamidinato) diiron. *Inorg. Chim. Acta* **1994**, *219*, 7–10.

(39) Cotton, F. A.; Daniels, L. M.; Falvello, L. R.; Matonic, J. H.; Murillo, C. A. Trigonal-lantern dinuclear compounds of diiron(I,II): The synthesis and characterization of two highly paramagnetic Fe2(amidinato)3 species with short metal-metal bonds. *Inorg. Chim. Acta* **1997**, *256*, 269–275.

(40) Cotton, F. A.; Daniels, L. M.; Maloney, D. J.; Murillo, C. A. Tri-bridged amidinato compounds of dicobalt 1: Co2[PhNC(R)NPh]3 with R = H and C6H5. *Inorg. Chim. Acta* **1996**, *249*, 9–11.

(41) Cotton, F. A.; Daniels, L. M.; Maloney, D. J.; Matonic, J. H.; Murillo, C. A. Dicobalt trigonal lanterns: Compounds containing the Co2(3+) core Co2RC(NPh)(2)(3) (R=H, C6H5) and an oxidized compound {Co2HC(NPh)(2)(3)(CH3CN)(2)}PF6 *Inorg. Chim. Acta* **1997**, *256*, 283–289.

(42) Lucas, R. L.; Zart, M. K.; Murkerjee, J.; Sorrell, T. N.; Powell, D. R.; Borovik, A. S. A Modular Approach toward Regulating the Secondary Coordination Sphere of Metal Ions: Differential Dioxygen Activation Assisted by Intramolecular Hydrogen Bonds. *J. Am. Chem. Soc.* **2006**, *128*, 15476–15489.

(43) Ray, M.; Hammes, B. S.; Yap, G. P. A.; Rheingold, A. L.; Borovik, A. S. Structure and Physical Properties of Trigonal Monopyramidal Iron(II), Cobalt(II), Nickel(II), and Zinc(II) Complexes. *Inorg. Chem.* **1998**, *37*, 1527–1532.

(44) Jones, M. B.; MacBeth, C. E. Tripodal Phenylamine-Based Ligands and Their CoII Complexes. *Inorg. Chem.* **2007**, *46*, 8117–8119.

(45) Cotton, F. A. Chromium Compounds. In *Multiple Bonds Between Metal Atoms*; Cotton, F. A.; Murillo, C. A.; Walton, R. A., Eds. Springer US: New York, 2005; pp. 35–68.

(46) Cotton, F. A.; Hillard, E. A.; Murillo, C. A.; Zhou, H.-C. After 155 Years, A

Crystalline Chromium Carboxylate with a Supershort Cr−Cr Bond. *J. Am. Chem. Soc.* **2000**, *122*, 416–417.

(47) Cotton, F. A.; Daniels, L. M.; Feng, X.; Maloney, D. J.; Matonic, J. H.; Murilio, C. A. The use of CoCl2(amidine)2 compounds in the synthesis of tetragonal lantern dicobalt compounds: synthesis, structures and theoretical studies of Co2(DPhF)4 and the oxidized species [Co2(DPhBz)4]+ (DPhF = N,N′-diphenylformamidinate, DPhBz = N,N′-diphenylbenzamidinate). *Inorg. Chim. Acta* **1997**, *256*, 291–301.

(48) Freedman, D. E.; Han, T. H.; Prodi, A.; Müller, P.; Huang, Q.-Z.; Chen, Y.-S.; Webb, S. M.; Lee, Y. S.; McQueen, T. M.; Nocera, D. G. Site Specific X-ray Anomalous Dispersion of the Geometrically Frustrated Kagomé Magnet, Herbertsmithite, ZnCu 3(OH) 6Cl 2. *J. Am. Chem. Soc.* **2010**, *132*, 16185–16190.

(49) Betley, T. A. Personal communication.

(50) Allen, F. The Cambridge Structural Database: a quarter of a million crystal structures and rising. *Acta Cryst. Sect. B* **2002**, *58*, 380–388.

(51) WanTao, Z.; Go-Shin; Syu-Tin, S. *Russ. J. Inorg. Chem.* **1997**, *42*, 1107.

(52) Glaser, T.; Beissel, T.; Bill, E.; Weyhermüller, T.; Schünemann, V.; Meyer-Klaucke, W.; Trautwein, A. X.; Wieghardt, K. Electronic Structure of Linear Thiophenolate-Bridged Heterotrinuclear Complexes [LFeMFeL]n+ (M = Cr, Co, Fe; n = 1−3): Localized vs Delocalized Models. *J. Am. Chem. Soc.* **1999**, *121*, 2193–2208.

(53) Matsumoto, K.; Sekine, N.; Arimura, K.; Ohba, M.; Sakiyama, H.; Okawa, H. μ-Acetato-di-μ-phenolato-metal(II)cobalt(II) (Metal = Fe, Co, Ni, Cu, Zn) Complexes with Low-Spin Co(II): Synthesis, Structures, and Magnetism. *Bull. Chem. Soc. Jpn.* **2004**, *77*, 1343–1351.

(54) Miller, D.; Lu, C. C. Unpublished Work.

(55) Roos, B. O.; Taylor, P. R.; Si gbahn, P. E. M. A complete active space SCF method (CASSCF) using a density matrix formulated super-CI approach. *Chem. Phys.* **1980**, *48*, 157–173.

(56) Andersson, K.; Malmqvist, P. Å.; Roos, B. O. 2nd-order perturbation-theory with a complete active space self-consistent field reference function. *J. Chem. Phys.* **1992**, *96*, 1218–1226.

(57) Briggs, B. N.; McMillin, D. R.; Todorova, T. K.; Gagliardi, L.; Poineau, F.; Czerwinski, K. R.; Sattelberger, A. P. First emission studies of Tc2X82- systems

(X = Cl, Br). *Dalton Trans.* **2010**.

(58) Ferrante, F.; Gagliardi, L.; Bursten, B. E.; Sattelberger, A. P. Multiconfigurational theoretical study of the octamethylidimetalates of Cr(II), Mo(II), W(II), and Re(III): Revisiting the correlation between the M-M bond length and the delta-delta* transition energy. *Inorg. Chem.* **2005**, *44*, 8476–8480.

(59) Gagliardi, L.; Roos, B. O. The electronic spectrum of Re2Cl82-: A theoretical study. *Inorg. Chem.* **2003**, *42*, 1599–1603.

(60) Poineau, F.; Forster, P. M.; Todorova, T. K.; Gagliardi, L.; Sattelberger, A. P.; Czerwinski, K. R. Structural, Spectroscopic, and Multiconfigurational Quantum Chemical Investigations of the Electron-Rich Metal−Metal Triple-Bonded Tc2X4(PMe 3) 4(X = Cl, Br) Complexes. *Inorg. Chem.* **2010**, *49*, 6646–6654.

(61) Perdew, J. P.; Zunger, A. Self-interaction correction to density-functional approximations for many-electron systems. *Phys. Rev. B* **1981**, *23*, 5048–5079.

(62) TURBOMOLE V6.1 2010.

(63) Ahlrichs, R.; Bar, M.; Haser, M.; Horn, H.; Kolmel, C. Electronic-Structure Calculations on Workstation Computers - the Program System Turbomole. *Chem. Phys. Letters* **1989**, *162*, 165–169.

(64) Aquilante, F.; De Vico, L.; Ferré, N.; Ghigo, G.; Malmqvist, P. Å.; Pedersen, T.; Pitonak, M.; Reiher, M.; Roos, B. O.; Serrano-Andrés, L.; Urban, M.; Veryazov, V.; Lindh, R. Software News and Update MOLCAS 7: The Next Generation. *J. Comput. Chem.* **2010**, *31*, 224–247.

(65) Roos, B. O.; Lindh, R.; Malmqvist, P. Å.; Veryazov, V.; Widmark, P. O. Main group atoms and dimers studied with a new relativistic ANO basis set. *J. Phys. Chem. A* **2004**, *108*, 2851–2858.

(66) Roos, B. O.; Lindh, R.; Malmqvist, P. Å.; Veryazov, V.; Widmark, P. O. New relativistic ANO basis sets for transition metal atoms. *J. Phys. Chem. A* **2005**, *109*, 6575–6579.

(67) Hess, B. A. Relativistic Electronic-Structure Calculations Employing a 2-Component No-Pair Formalism with External-Field Projection Operators. *Physical Review A* **1986**, *33*, 3742–3748.

(68) Aquilante, F.; Pedersen, T. B.; Lindh, R. Low-cost evaluation of the exchange Fock matrix from Cholesky and density fitting representations of the electron repulsion integrals. *J. Chem. Phys.* **2007**, *126*, 11.

(69) Aquilante, F.; Pedersen, T. B.; Lindh, R.; Roos, B. O.; De Meras, A. S.; Koch, H. Accurate ab initio density fitting for multiconfigurational self-consistent field

methods. *J. Chem. Phys.* **2008**, *129*, 8.

(70) Forsberg, N.; Malmqvist, P. Å. Multiconfiguration perturbation theory with imaginary level shift. *Chem. Phys. Lett.* **1997**, *274*, 196–204.

Chapter 4 References

(1) Hammes-Schiffer, S.; Benkovic, S. J. Relating Protein Motion to Catalysis. *Annu. Rev. Biochem.* **2006**, *75*, 519–541.

(2) Unden, G.; Bongaerts, J. Alternative respiratory pathways of Escherichia coli: energetics and transcriptional regulation in response to electron acceptors. *Biochimica et Biophysica Acta (BBA) - Bioenergetics* **1997**, *1320*, 217–234.

(3) Pollak, N.; Dölle, C.; Ziegler, M. The power to reduce: pyridine nucleotides – small molecules with a multitude of functions. *Biochem. J.* **2007**, *402*, 205.

(4) Zhu, X.-Q.; Tan, Y.; Cao, C.-T. Thermodynamic Diagnosis of the Properties and Mechanism of Dihydropyridine-Type Compounds as Hydride Source in Acetonitrile with "Molecule ID Card." *J. Phys. Chem. B* **2010**, *114*, 2058–2075.

(5) Zheng, C.; You, S.-L. Transfer hydrogenation with Hantzsch esters and related organic hydride donors. *Chem. Soc. Rev.* **2012**, *41*, 2498–2518.

(6) Pac, C.; Ihama, M.; Yasuda, M.; Miyauchi, Y.; Sakurai, H. Tris(2,2'-bipyridine)ruthenium(2+)-mediated photoreduction of olefins with 1-benzyl-1,4-dihydronicotinamide: a mechanistic probe for electron-transfer reactions of NAD(P)H-model compounds. *J. Am. Chem. Soc.* **1981**, *103*, 6495–6497.

(7) Adembri, G.; Camparini, A.; Donati, D.; Fusi, S.; Ponticelli, F.; Scotton, M. Photodimerization of N-benzyl-1,4-dihydronicotinamide. *Tetrahedron Lett.* **1983**, *24*, 5399–5402.

(8) Roston, D.; Kohen, A. Elusive transition state of alcohol dehydrogenase unveiled. *Proc. Natl. Acad. Sci. U.S.A.* **2010**, *107*, 9572–9577.

(9) Reichenbach-Klinke, R.; Kruppa, M.; König, B. NADH Model Systems Functionalized with Zn(II)-Cyclen as Flavin Binding SiteStructure Dependence of the Redox Reaction within Reversible Aggregates. *J. Am. Chem. Soc.* **2002**, *124*, 12999–13007.

(10) Koizumi, T.; Tanaka, K. Reversible Hydride Generation and Release from the Ligand of [Ru(pbn)(bpy)2](PF6)2 Driven by a pbn-Localized Redox Reaction. *Angew. Chem. Int. Ed.* **2005**, *44*, 5891–5894.

(11) Polyansky, D.; Cabelli, D.; Muckerman, J.; Fujita, E.; Koizumi, T. A.; Fukushima, T.; Wada, T.; Tanaka, K. Photochemical and Radiolytic Production of an Organic Hydride Donor with a RuII Complex Containing an NAD+ Model Ligand. *Angew. Chem. Int. Ed.* **2007**, *46*, 4169–4172.

(12) Polyansky, D. E.; Cabelli, D.; Muckerman, J. T.; Fukushima, T.; Tanaka, K.; Fujita, E. Mechanism of Hydride Donor Generation Using a Ru(II) Complex Containing an NAD+ Model Ligand: Pulse and Steady-State Radiolysis Studies. *Inorg. Chem.* **2008**, *47*, 3958–3968.

(13) McSkimming, A.; Bhadbhade, M. M.; Colbran, S. B. Bio-Inspired Catalytic Imine Reduction by Rhodium Complexes with Tethered Hantzsch Pyridinium Groups: Evidence for Direct Hydride Transfer from Dihydropyridine to Metal-Activated Substrate. *Angew. Chem. Int. Ed.* **2013**, *52*, 3411–3416.

(14) Miller, D.; Lu, C. C. Unpublished Work.

(15) Ostovic, D.; Lee, I.-S. H.; Roberts, R. M. G.; Kreevoy, M. M. Hydride transfer and oxyanion addition equilibria of NAD+ analogs. *J. Org. Chem.* **1985**, *50*, 4206–4211.

(16) Zhu, X. Q.; Liu, Q. Y.; Chen, Q.; Mei, L. R. Hydride, Hydrogen, Proton, and Electron Affinities of Imines and Their Reaction Intermediates in Acetonitrile and Construction of Thermodynamic Characteristic Graphs (TCGs) of Imines as a "Molecule ID Card." *J. Org. Chem.* **2010**, *75*, 789–808.

(17) Parenty, A. D. C.; Smith, L. V.; Cronin, L. An unusual substitution reaction directed by an intramolecular re-arrangement. *Tetrahedron* **2005**, *61*, 8410–8418.

(18) Parenty, A. D. C.; Smith, L. V.; Pickering, A. L.; Long, D.-L.; Cronin, L. General One-Pot, Three-Step Methodology Leading to an Extended Class of N-Heterocyclic Cations: Spontaneous Nucleophilic Addition, Cyclization, and Hydride Loss. *J. Org. Chem.* **2004**, *69*, 5934–5946.

(19) Richmond, C. J.; Parenty, A. D. C.; Song, Y.-F.; Cooke, G.; Cronin, L. Realization of a "Lockable" Molecular Switch via pH- and Redox-Modulated Cyclization. *J. Am. Chem. Soc.* **2008**, *130*, 13059–13065.

(20) Ellis, W. W.; Raebiger, J. W.; Curtis, C. J.; Bruno, J. W.; DuBois, D. L. Hydricities of BzNADH, C5H5Mo(PMe3)(CO)2H, and C5Me5Mo(PMe3)(CO)2H in Acetonitrile. *J. Am. Chem. Soc.* **2004**, *126*, 2738–2743.

(21) Ellis, W. W.; Miedaner, A.; Curtis, C. J.; Gibson, D. H.; DuBois, D. L. Hydride Donor Abilities and Bond Dissociation Free Energies of Transition Metal Formyl Complexes. *J. Am. Chem. Soc.* **2002**, *124*, 1926–1932.

(22) Muckerman, J. T.; Achord, P.; Creutz, C.; Polyansky, D. E.; Fujita, E. Calculation of thermodynamic hydricities and the design of hydride

donors for CO2 reduction. *Proc. Natl. Acad. Sci. U.S.A.* **2012**, *109*, 15657–15662.

(23) Jurčík, V.; Nolan, S. P.; Cazin, C. S. J. Hydrogenation of C-C Multiple Bonds Mediated by [Pd(NHC)(PCy_3)] (NHC = N-Heterocyclic Carbene) under Mild Reaction Conditions. *Chem. Eur. J.* **2009**, *15*, 2509–2511.

(24) Fantasia, S.; Egbert, J. D.; Jurčík, V.; Cazin, C. S. J.; Jacobsen, H.; Cavallo, L.; Heinekey, D. M.; Nolan, S. P. Activation of Hydrogen by Palladium(0): Formation of the Mononuclear Dihydride Complex trans-[Pd(H)2(IPr)(PCy3)]. *Angew. Chem. Int. Ed.* **2009**, *48*, 5182–5186.

(25) Espenson, J. H. *Chemical Kinetics and Reaction Mechanisms*; Second Edition. McGraw-Hill: New York, 2002; pp. 253–272.

(26) Grushin, V. V. Hydrido Complexes of Palladium. *Chem. Rev.* **1996**, *96*, 2011–2034.

(27) Ozin, G. A.; Garcia-Prieto, J. Pd(eta1-H2) and Pd(eta2-H2): ligand-free end-on and side-on bonded molecular dihydrogen complexes. *J. Am. Chem. Soc.* **1986**, *108*, 3099–3100.

(28) Andrews, L.; Manceron, L.; Alikhani, M. E.; Wang, X. Observed and Calculated Infrared Spectrum of Pd(H2) in Solid Argon: A Ligand-Free Side-Bonded Molecular Hydrogen Complex. *J. Am. Chem. Soc.* **2000**, *122*, 11011–11012.

(29) Andrews, L.; Wang, X.; Alikhani, M. E.; Manceron, L. Observed and Calculated Infrared Spectra of Pd(H2) 1,2,3 Complexes and Palladium Hydrides in Solid Argon and Neon. *J. Phys. Chem. A* **2001**, *105*, 3052–3063.

(30) Collman, J. P. Patterns of organometallic reactions related to homogeneous catalysis. *Acc. Chem. Res.* **1968**, *1*, 136–143.

(31) Ugo, R. The coordinative reactivity of phosphine complexes of platinum(0), palladium(0) and nickel(0). *Coord. Chem. Rev. 3*, 319–344.

(32) Harrod, J. F.; Chalk, A. J. Homogeneous Catalysis. I. Double Bond Migration in n-Olefins, Catalyzed by Group VIII Metal Complexes. *J. Am. Chem. Soc.* **1963**, *86*, 1776–1779.

(33) Cramer, R.; Lindsey, R. V. The Mechanism of Isomerization of Olefins with Transition Metal Catalysts. *J. Am. Chem. Soc.* **1966**, *88*, 3534–3544.

(34) Sprengers, J. W.; Wassenaar, J.; Clement, N. D.; Cavell, K. J.; Elsevier, C. J. Palladium-(N-Heterocyclic Carbene) Hydrogenation Catalysts. *Angew.*

Chem. Int. Ed. **2005**, *44*, 2026–2029.

(35) van Laren, M. W.; Elsevier, C. J. Selective Homogeneous Palladium(0)-Catalyzed Hydrogenation of Alkynes to (Z)-Alkenes. *Angew. Chem. Int. Ed.* **1999**, *38*, 3715–3717.

(36) SMART V5.054, Bruker Analytical X-ray Systems, Madison, Wi (2001).

(37) An empirical correction for absorption anisotropy. **1995**, *51 (Pt 1)*, 33–38.

(38) SAINT+ V6.45, Bruker Analytical X-ray Systems, Madison, WI (2003).

(39) SHELXTL V6.14, Bruker Analytical X-ray Systems, Madison, WI (2000).